



UNIVERSITAT DE
BARCELONA

Design and synthesis of photoswitchable coordination complexes

Jorge Salinas Uber

ADVERTIMENT. La consulta d'aquesta tesi queda condicionada a l'acceptació de les següents condicions d'ús: La difusió d'aquesta tesi per mitjà del servei TDX (www.tdx.cat) i a través del Dipòsit Digital de la UB (diposit.ub.edu) ha estat autoritzada pels titulars dels drets de propietat intel·lectual únicament per a usos privats emmarcats en activitats d'investigació i docència. No s'autoritza la seva reproducció amb finalitats de lucre ni la seva difusió i posada a disposició des d'un lloc aliè al servei TDX ni al Dipòsit Digital de la UB. No s'autoritza la presentació del seu contingut en una finestra o marc aliè a TDX o al Dipòsit Digital de la UB (framing). Aquesta reserva de drets afecta tant al resum de presentació de la tesi com als seus continguts. En la utilització o cita de parts de la tesi és obligat indicar el nom de la persona autora.

ADVERTENCIA. La consulta de esta tesis queda condicionada a la aceptación de las siguientes condiciones de uso: La difusión de esta tesis por medio del servicio TDR (www.tdx.cat) y a través del Repositorio Digital de la UB (diposit.ub.edu) ha sido autorizada por los titulares de los derechos de propiedad intelectual únicamente para usos privados enmarcados en actividades de investigación y docencia. No se autoriza su reproducción con finalidades de lucro ni su difusión y puesta a disposición desde un sitio ajeno al servicio TDR o al Repositorio Digital de la UB. No se autoriza la presentación de su contenido en una ventana o marco ajeno a TDR o al Repositorio Digital de la UB (framing). Esta reserva de derechos afecta tanto al resumen de presentación de la tesis como a sus contenidos. En la utilización o cita de partes de la tesis es obligado indicar el nombre de la persona autora.

WARNING. On having consulted this thesis you're accepting the following use conditions: Spreading this thesis by the TDX (www.tdx.cat) service and by the UB Digital Repository (diposit.ub.edu) has been authorized by the titular of the intellectual property rights only for private uses placed in investigation and teaching activities. Reproduction with lucrative aims is not authorized nor its spreading and availability from a site foreign to the TDX service or to the UB Digital Repository. Introducing its content in a window or frame foreign to the TDX service or to the UB Digital Repository is not authorized (framing). Those rights affect to the presentation summary of the thesis as well as to its contents. In the using or citation of parts of the thesis it's obliged to indicate the name of the author.

DESIGN AND SYNTHESIS OF PHOTOSWITCHABLE COORDINATION COMPLEXES

Universitat de Barcelona

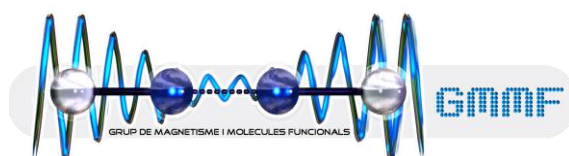
Facultat de Química

Departament de Química Inorgànica i Orgànica

(Secció de Química Inorgànica)

Programa de Doctorat: Química Inorgànica Molecular

Grup de Magnetisme i Molècules Funcionals



Jorge Salinas Uber

Director: Dr. Guillem Aromí Bedmar
Departament de Química Inorgànica i Orgànica

Tutor: Dr. Eliseo Ruiz Sabin
Departament de Química Inorgànica i Orgànica

Guillem Aromí Bedmar, Professor del Departament de Química Inorgànica i Orgànica (Secció de Química Inorgànica) de la Facultat de Química de la Universitat de Barcelona,

CERTIFICA: que el treball titulat “Design and Synthesis of Photoswitchable Coordination Complexes” que presenta el Jorge Salinas Uber per optar al grau de Doctor per la Universitat de Barcelona, ha estat realitzat sota la seva direcció al Departament de Química Inorgànica i Orgànica (Seccio de Química Inorgànica) d’aquesta Facultat.

Barcelona, juny de 2016

Dr. Guillem Aromí Bedmar

Eliseo Ruiz Sabin, Catedràtic del Departament de Química Inorgànica i Orgànica (Secció de Química Inorgànica) de la Facultat de Química de la Universitat de Barcelona,

CERTIFICA: que ha estat el tutor responsable dels estudis de Doctorat realitzats dins del programa de Doctorat de Química Inorgànica Molecular pel Jorge Salinas Uber.

Barcelona, juny de 2016

Dr. Eliseo Ruiz Sabin

Para mis *niñas*

CONTENTS

CHAPTER 1: INTRODUCTION

1.1 Introduction	3
1.2 Photochromic molecules	4
1.2.1 Dithienylethenes.....	8
1.3 Molecular Magnetism	14
1.3.1 Quantum computing (QC).....	16
1.3.2 Single Molecular Magnets (SMMs).....	19
1.3.3 Spin crossover (SCO).....	23
1.4 Diaryethenes and magnetism	28
1.4.1 Others systems combining photochromism and magnetism	34
1.5 Aim of the thesis	35
1.6 References	37

CHAPTER 2: STRUCTURE AND INTERMOLECULAR INTERACTIONS VS PHOTOCHROMISM

2.1 Introduction	49
2.2 Synthesis and characterization	51
2.2.1 Synthesis of 1,2-(5-carboxy-2-methyl-thiophen-3-yl)-cyclopentene (H ₂ L1).....	51
2.2.2 Synthesis and description of [Cu(L)(py) ₃] (1).....	52
2.3 Photoswitching Properties.....	58
2.3.1 Reflectivity Measurements.....	58
2.3.2 Raman spectroscopy.....	66
2.4 Bulk magnetic measurements.....	68
2.5 Copper compounds using blocking ligands.....	70
2.5.1 Synthesis and crystal structure of [Cu ₂ (L1)(Phen) ₄](NO ₃) ₂ ·nMeOH (2)	71
2.5.2 Synthesis and crystal structure of [Cu ₇ (L1) ₄ (Phen) ₇](NO ₃) ₆ ·nMeOH (3)	73
2.5.3 Synthesis and crystal structure of [Cu ₂ (L1)(ByPy) ₄](NO ₃) ₂ ·nMeOH (4)	76
2.6 Photochromic activity	79
2.7 Conclusions	81
2.8 Experimental	82
2.8.1. Ligands and precursors.....	82
2.8.2. Coordination complexes.....	83
2.9 References	85

CHAPTER 3: TOWARDS PHOTOSWITCHABLE 2-QUBIT SYSTEMS

3.1 Introduction	93
3.2 Synthesis and characterization	94
3.2.1 Synthesis of [1,2-bis-(5-(3-oxo-3-(2-hydroxyphenyl)-propanoyl)-2-methylthien-3-yl) cyclopentene] (H ₄ L2)	94
3.2.2 Crystal structure and ¹ HMRN of H ₄ L2.	95
3.2.3 Photochromic properties of H ₄ L2.....	98
3.2.4 Synthesis of 1,2-bis-(5-(3-oxo-3-(2-hydroxynaphthyl)-propanoyl)-2-methylthien-3-yl) cyclopentene (H ₄ L3)	101
3.2.5 Photochromic behavior of H ₄ L3.....	103
3.2.6 Fluorescence of H ₄ L3.....	105
3.3 Synthesis of coordination compounds.....	107
3.3.1 Homometallic pairs of dimers [MM'···MM]. Synthesis and crystal structures	107
3.3.2 Magnetic properties of [M ₄ (L2) ₂ (py) ₆] complexes.....	112
3.4 Heterometallic pair of dimers [MM'···M'M]	116
3.4.1 Synthesis and crystal structures.....	116
3.4.2 Magnetic properties of [M ₂ M' ₂ (L2) ₂ (py) ₆] complexes.....	121
3.4.3 Theoretical studies of the heterometallic compounds	126
3.4.4 Quantum coherence in the heterometallic clusters	127
3.5 Photochromic behavior	135
3.7 Conclusions	140
3.8 Experimental	141
3.8.1 Ligands.....	141
3.8.2 Coordination compounds.	143
3.9 References	146

CHAPTER 4: EXPLORING THE SMM BEHAVIOR OF LANTHANIDES COMPLEXES CONTAINING PHOTOCROMIC LIGANDS

4.1 Introduction	154
4.2 Synthesis and characterization	155
4.2.1 Synthesis and crystal structure of of 1,2-bis-(5-(N'-(2-hydroxybenzylidene) hydrazide)-2-methylthien-3-yl) cyclopentene (H ₄ L7).....	155
4.2.2 Synthesis of 1,2-bis-(5-(N'-(pyridine-2-ylmethylene)hydrazide)-2-methylthien-3-yl) cyclopentene (H ₂ L8)	158
4.2.3 Photochromism of H ₄ L7 and H ₂ L8	158
4.3 Synthesis and crystal structures of H ₄ L7 and H ₂ L8	160
4.3.1 Synthesis and crystal structure of [Ln ₂ L ₇ 2(CO ₃) ₂ Na ₆ Py ₁₀] (Ln: Tb (14); Dy (15))..	160

4.3.2	Synthesis and crystal structure of $[\text{Ln}_4\text{L}_8\text{Cl}_4(\text{H}_2\text{O})_5]\cdot n\text{Py}$ (Ln: Tb (16); Dy (17)).	163
4.3.3	Synthesis and crystal structure of $[\text{Ln}_4\text{L}_7\text{Na}_4(\text{H}_2\text{O})_2(\text{CO}_3)_2(\text{Py})_6(\text{acac})_4]\cdot 9\text{Py}$ (Ln: Tb (18); Dy (19)).	167
4.4	Introduction to magnetic properties on lanthanides	171
4.4.1	Magnetic properties of $[\text{Tb}_2\text{L}_7\text{L}_2(\text{CO}_3)_2\text{Na}_6\text{Py}_{10}]$ (14)	172
4.4.2	Magnetic properties of $[\text{Ln}_4\text{L}_8\text{Cl}_4(\text{H}_2\text{O})_5]\cdot n\text{Py}$ (16 and 17)	173
4.4.3	Magnetic properties of $[\text{Ln}_4\text{L}_7\text{Na}_4(\text{H}_2\text{O})_2(\text{CO}_3)_2(\text{Py})_6(\text{acac})_4]\cdot 9\text{Py}$ (18 and 19)	174
4.4.4	Single molecule magnet behavior	175
4.5	Coordination compounds with copper	177
4.5.1	Synthesis and crystal structure of $[\text{Cu}_2\text{L}_7(\text{Py})_2](\text{MeOH})$ (20)	177
4.5.2	Synthesis and crystal structure of $[\text{Cu}_2\text{L}_7(\text{Phen})_2](\text{H}_2\text{O})_3$ (21)	179
4.6	Magnetic properties of $[\text{Cu}_2\text{L}_7(\text{Py})_2](\text{MeOH})$ and $[\text{Cu}_2\text{L}_7(\text{Phen})_2](\text{H}_2\text{O})_3$	181
4.7	Photochromism behavior	182
4.8	Conclusions	184
4.9	Experimental	185
4.9.1	Ligands	185
4.9.2	Coordination compounds	186
4.10	References	189

CHAPTER 5: PHOTOCROMIC HELICAL ASSEMBLY OF Fe(II) FEATURING SCO

5.1	Introduction	196
5.2	Synthesis and characterization	197
5.2.1	Synthesis and design of 1,2-bis-(5-(2-pyrazol)-pyridin-2-methylthien-3-yl) cyclopentene (H_2L_9)	197
5.2.2	Photochromic behavior and fluorescence of H_2L_9	198
5.3	Synthesis and crystal structure of $[\text{Fe}_2(\text{L}_9)_3](\text{ClO}_4)_4$ (22)	201
5.4	Photochromic properties of $[\text{Fe}_2(\text{L}_9)_3](\text{ClO}_4)_4$ (22)	205
5.5	Magnetic properties of $[\text{Fe}_2(\text{L}_9)_3](\text{ClO}_4)_4$ (22)	207
5.6	Solution studies	209
5.6.1	Fluorescence of $[\text{Fe}_2(\text{L}_9)_3](\text{ClO}_4)_4$ (22)	209
5.6.2	Magnetic properties in solution of $[\text{Fe}_2(\text{L}_9)_3](\text{ClO}_4)_4$ (22)	211
5.7	Conclusions	217
5.8	Experimental	218
5.8.1	Ligands and precursors	218
5.8.2	Coordination complex	220
5.9	References	221

CHAPTER 6: CONCLUSIONS

6.1 Concluding remarks 230

APPENDIX I: UV-Vis spectra for 6, 7, 9, 10, 11 and 13 236

APPENDIX II: Physical techniques 240

APPENDIX III : List of Publications 244

AGRADECIMIENTOS

CHAPTER 1: INTRODUCTION

1.1 Introduction	3
1.2 Photochromic molecules	4
1.2.1 Dithienylethenes	8
1.3 Molecular Magnetism	14
1.3.1 Quantum computing (QC).....	16
1.3.2 Single Molecular Magnets (SMMs).....	19
1.3.3 Spin crossover (SCO).....	23
1.4 Diaryethenes and magnetism	28
1.4.1 Others systems combining photochromism and magnetism	34
1.5 Aim of the thesis	35
1.6 References	37

1.1 Introduction

In recent years, the study and use of molecular systems as prototypes of molecular devices, has been established as one of the most active part of the science, due to the potential implementation of these devices into a new generation of electronic systems^{1,2}. The synergy of different fields such as physics, biology, chemistry, nanotechnology, among others, is also an important factor in that success. In this context, chemistry plays indeed a critical role because it is itself the major source of the actual components of these new devices, thus, the study of new molecular switches has become an exciting area in chemistry.

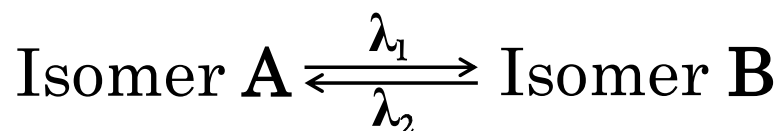
Magnetic compounds are perhaps the most studied compounds given their implementation in conventional computational systems, thanks to the potential to control their spin state by applying magnetic stimuli or charges³. An intensively studied class of magnetic molecules is constituted by the so-called single molecule magnets⁴. These systems are characterized by a slow relaxation of magnetization at low T and by giving rise to magnetic hysteresis of pure molecular origin. Hysteresis is also characteristic of other bi-stable magnetic molecular systems, the spin crossover compounds⁵, resulting from a change from an active magnetic state to an inactive one. The origin of this hysteresis is however completely different (see below). Recently, magnetic spin-engineering research is focused in the study and use of the quantum mechanics to perform tasks of information processes^{6,7}.

The continuous search of new materials to improve the performance of these magnetic devices includes, among others, the use of external photo-, thermo- or piezo stimuli. The synergy between the switching behavior and the spin engineering, should provide the conditions for storing information and bring about read-out processes in a single molecules⁸.

As a large class of molecular switches⁹, extensive research has been devoted to the study of systems where light is used as external stimulus to switch their physical and chemistry properties. Such modulation is observed in photochromic systems which have been used in photo-optical technology and will be the main theme in this thesis, in combination with the magnetic properties of metallic atoms within molecules.

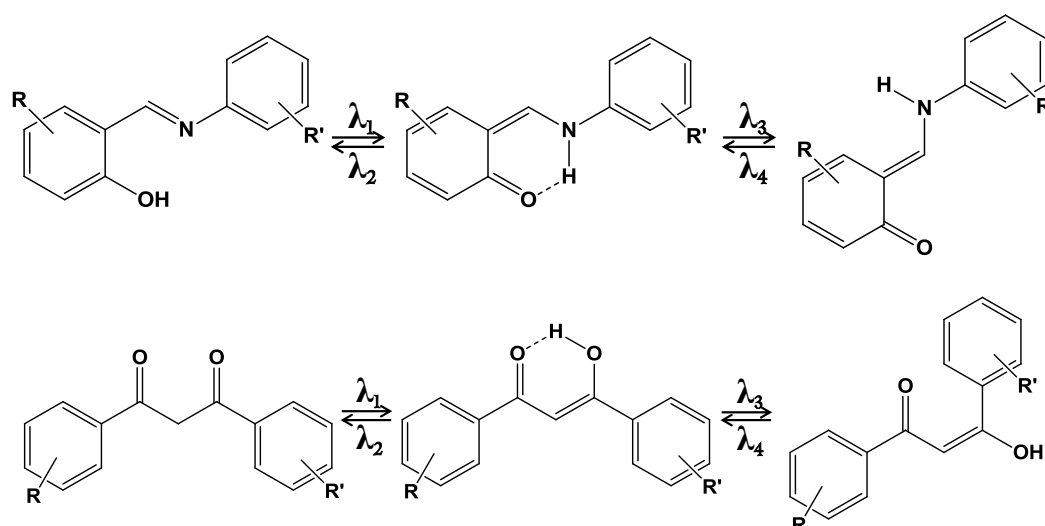
1.2 Photochromic molecules

Photochromism¹⁰ is the reversible transformation of a chemical species between two forms by the absorption of electromagnetic radiation, where the two forms have different absorption spectra. It is often characterized by a reversible color change between two isomers upon photoirradiation, using different wavelengths for each direction of the process (Scheme 1). Both isomers not only differ in their absorption spectra, but usually in other interesting features, such as geometrical structure, fluorescence, oxidation/reduction potentials, etc. These changes between isomers can take place through different processes: tautomerization¹¹, cis-trans isomerizations¹² or photocyclization^{13,14}.



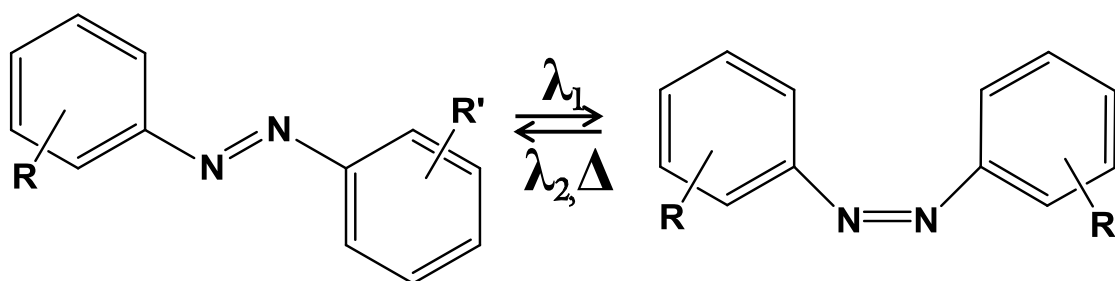
Scheme 1.1: Photochromic switch.

The main examples of photochromic tautomerism occur by hydrogen transfer. In this regard, the best known light-induced hydrogen transfer systems are those involving salicylidene-anilines and keto-enol equilibria¹⁵. In those cases, after irradiation with UV light, a prototropic rearrangement from one isomer to other occurs that can be also followed by a cis-trans isomerization, as scheme 1.2 shows.



Scheme 1.2: Photochromic tautomerization in salicylidene-anilines (upper part) and a similar process for a keto-enol equilibrium (bottom part). In both cases, cis-trans isomerization occurs.

In the case of cis-trans isomerizations, the equilibrium of azocompounds (scheme 1.3) is perhaps the most studied system since it is the most convenient for photochemical studies¹⁶. The molecules go from a trans configuration to a cis configuration via a $n\pi^*$ -transition triggered by UV irradiation. The reversion of the reaction takes place upon irradiation with visible light or thermally. This reversible switch between cis and trans forms has made azocompounds the most widely used photoswitch in the areas of physics, bio-chemistry, and materials science¹⁷⁻²¹. Optomechanical applications exploit the fact that going from cis to trans the molecule substantially expands by 2.4 Å in length. Attempts to design molecular nanomachines and optomechanical cycles that convert light into mechanical work have been based on this principle. This can be used also in photo-addressable image storage media²².

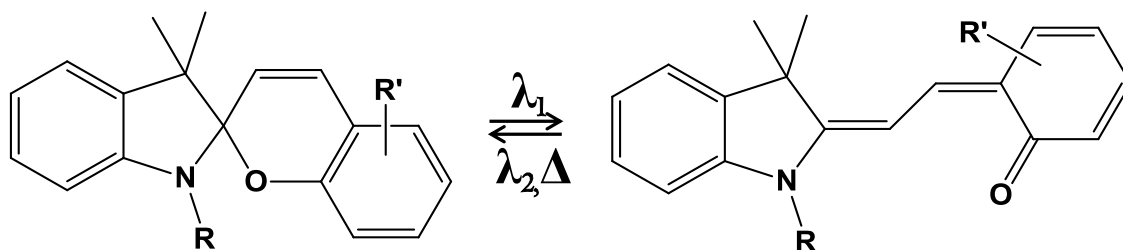


Scheme 1.3: Cis-trans isomerization of azocompounds

Another type of transformation in molecular switches, are electrocyclic reactions^{13,14}. For example, a 1,3,5-hexatriene derivative undergoes a photocyclization to 1,3-cyclohexadiene derivative upon irradiation. According to the Woodward-Hoffmann rule based on π -orbital symmetries for 1,3,5-hexatriene, a con-rotator cyclization reaction is brought about by light and a disrotatory cyclization occurs by heat, in a way that the resulting compound would have its substituents in trans or cis position, respectively. The most studied compounds performing these reactions are spiropyrans²³, fulgides²⁴ and diarylethenes^{9,25}.

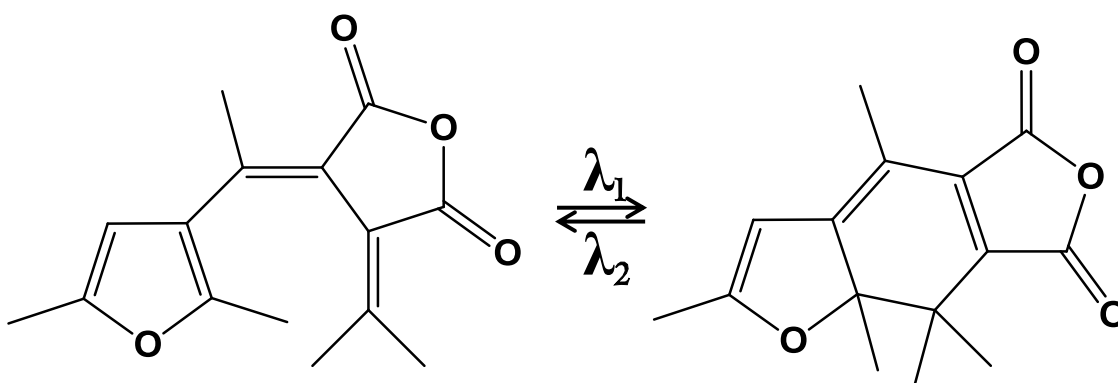
There is wide interest in the spiropyrans, which have been known since the beginning of the twentieth century, when their reversible thermochromic properties were discovered, and their importance has increased greatly as their photochromic properties became known²⁶ (Scheme 1.4). Spiropyrans finds widespread use as molecular logic devices, and are used for the production of nanostructured photochromic films from

biopolymers, photochromic and electrooptical devices, molecular and supramolecular logic switches and multifunctional artificial receptors^{27,28}.



Scheme 1.4: general structure of spiropyranes.

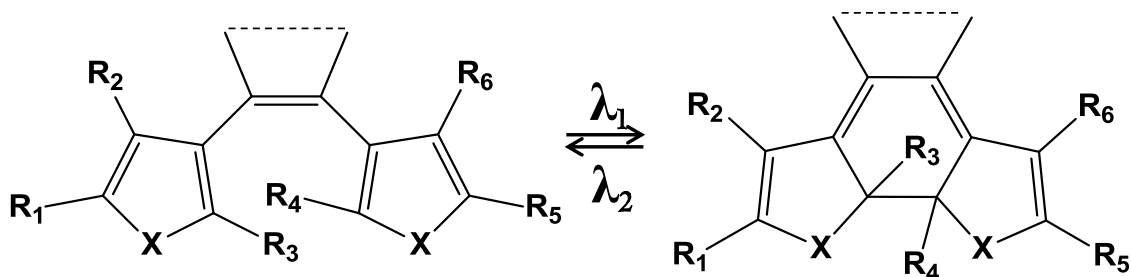
Fulgides were synthesized for the first time by Stobbe at the beginning of the past century, and like to the spiropyranes, their photochromic properties were discovered several years later. To be photochromic, fulgides need at least one aromatic ring on the exo-methylene carbon atom, so that they form a 1,3,5-hexatriene structure that may undergo 6π -electrocyclization²⁴. Upon irradiation with UV, the colorless isomer of the fulgide changes into a deeply colored compound, due to the extended conjugation achieved through the electrocyclization (Scheme 1.5). This process is photoreversible. The large fatigue resistance, the thermal irreversibility and the high conversion efficiency make fulgides highly attractive for potential applications as optical recording media (for example, fulgide-based nanodots were recently presented as a promising nanotechnological approach to the fabrication of organic memory devices) and molecular photoswitches^{27,29,30}.



Scheme 1.5: Fulgide having a furane as an aromatic ring.

Another example, and one of the most used recently, are the diarylethene derivatives^{9,10,25}. Diarylethenes are known as one of the most important classes of thermally irreversible photochromic compounds. The photochromic reaction with UV light of the colorless open-form of diarylethenes is based on the photochemical conrotatory 6π -electrocyclization of the 1,3,5-hexatriene moiety that takes place along the C₂-symmetric helical structure because of the steric hindrance. The closed form is thermally stable and upon irradiation with visible light, the system returns to the initial open form. There are a large number of types of diarylethenes depending on the substituents. For the aryl rings, the most use are thiophenes, but also furanes or thiazoles are employed. The ethene moiety is always embedded in a ring because it provides more rigidity to the complex, being the cyclopentene the most used, usually found in two derivatives (perhydrocyclopentene or perfluorocyclopentene). This photochromic system is amenable to numerous chemical modifications via the incorporation of different substituents, which allows to introduce various functionalities (Scheme 1.6).

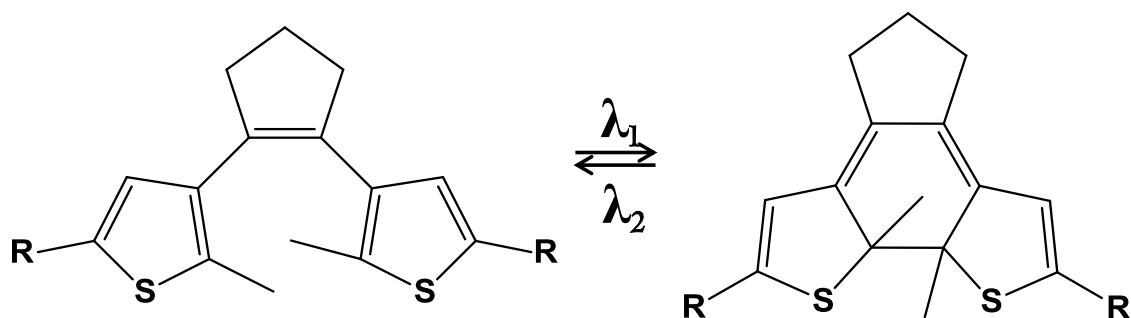
The most important properties of these excellent switchable compounds are thermal stability, large fatigue resistance, high quantum yields or gate reactivity, among others, and will be discussed in the next section. These compounds will be the building blocks of the new functional compounds in this presented thesis.



Scheme 1.6: General structure of diarylethenes with the reversible chemical transformation between both isomers upon photoirradiation.

1.2.1 Dithienylethenes

As previously mentioned, diarylethene-based systems are very useful because their excellent switching properties. One sub-class of these derivatives are dithienylethenes, which have a thiophene ring as the aryl group. The combination with a perhydrocyclopentene unit gives the general name to these compounds of dithienylperhydrocyclopentenenes (Scheme 1.7).



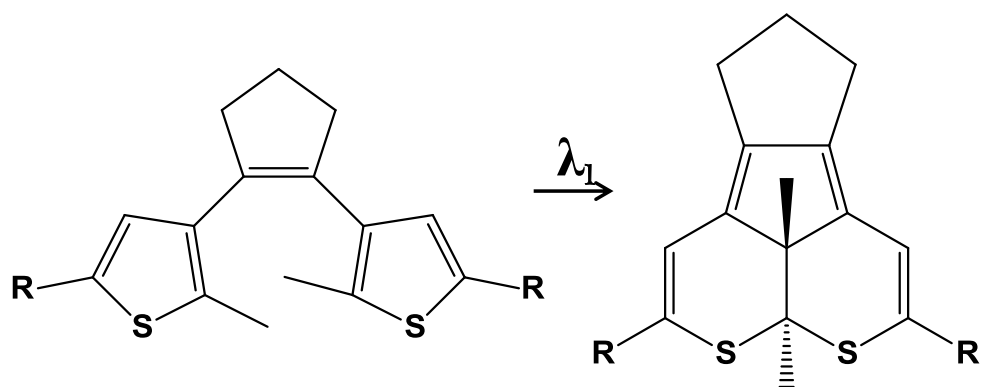
Scheme 1.7: General scheme of a dithienylperhydrocyclopentene with the reversible chemical transformation upon photoirradiation.

The direct and reverse processes occur with light of different wavelength, which make these compounds very useful and interesting. UV light is used for the cyclization process, while the reversion of the process is done using Visible light. These differences can be used to read the state of the isomer. The system has other advantages such as, thermal stability, large fatigue resistant, high quantum yields or the gate reactivity, among others.

The synthesis of dithienylcyclopentene derivatives occurs through a Suzuki cross coupling, which is more favorable for the perhydrocyclopentene moieties than for the perfluorocyclopentene analog³¹. For the latter, the synthesis employs a very volatile compound, the octafluorocyclopentene, giving low reaction yields. The use of dithienylcyclopentenenes reveals similar behavior on terms of photoconversion and quantum yields, but with less thermal stability and fatigue resistance than the perfluoro complexes. Nevertheless, they can undergo a high number of cycles without decomposition or side reactions.

Among the requirements, the most important one is the thermal stability of both isomers, necessary for their use as read-out switches. Very often, photogenerated colored isomers are thermally unstable and return to the initial isomers in the dark. These thermally reversible compounds are classified as T-type compounds (azobenzenes and spiropyranes, for example). In contrast, compounds with both isomers stable in the dark are called P-type compounds. Diarylethenes with heterocyclic aryl groups belong to these thermally irreversible (P-type) photochromic compounds. They are stable even above 100°C.

The resistance to the fatigue is related to the number of cycles that the molecule can undergo without degradation. Side reactions can appear depending on the substituents, but maybe the most damaging for the photochromic process is the irreversible formation of a condensed species which occurs after long exposure to UV light (scheme 1.8). This species was first isolated by the group of Branda and characterized crystallographically³².



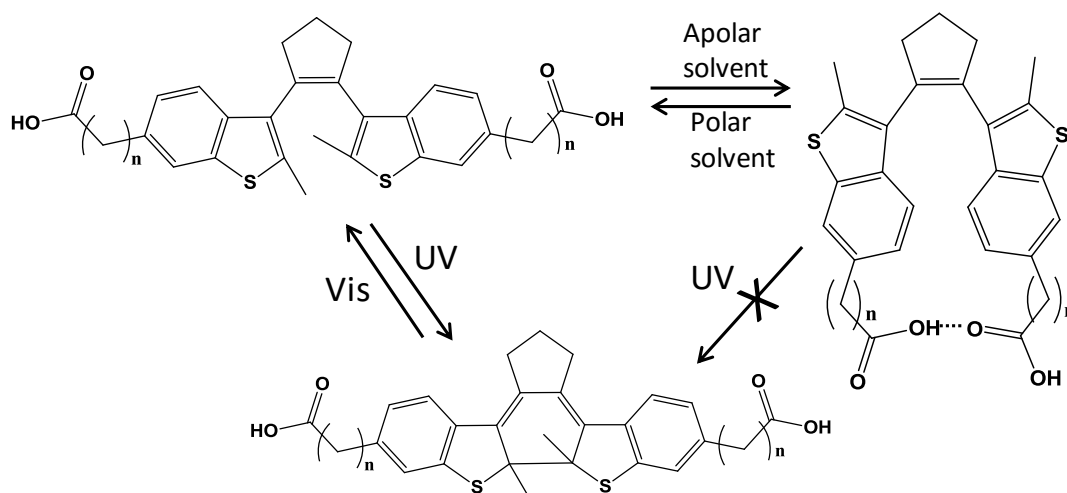
Scheme 1.8: The byproduct formation is the main fatigue process of dithienylethenes.

Several studies show that introducing bulky substituents in the thiophene ring prevents rearrangement of these thiophene to the six-membered condensed ring^{33,34}. The byproducts can be detected via absorption spectroscopy, due to the presence of other absorption peaks in the visible range from the by-products, also conjugated.

Another important parameter is the quantum yield of the photoconversion and generally is defined as the number of defined events occurring per photon absorbed by the system. In our case could be translate as the number of molecules which isomerizes when the sample is irradiated. In terms of the diarylethenes conformation for isomerization, there are two possible situations, where the substituents are pointed to the same direction

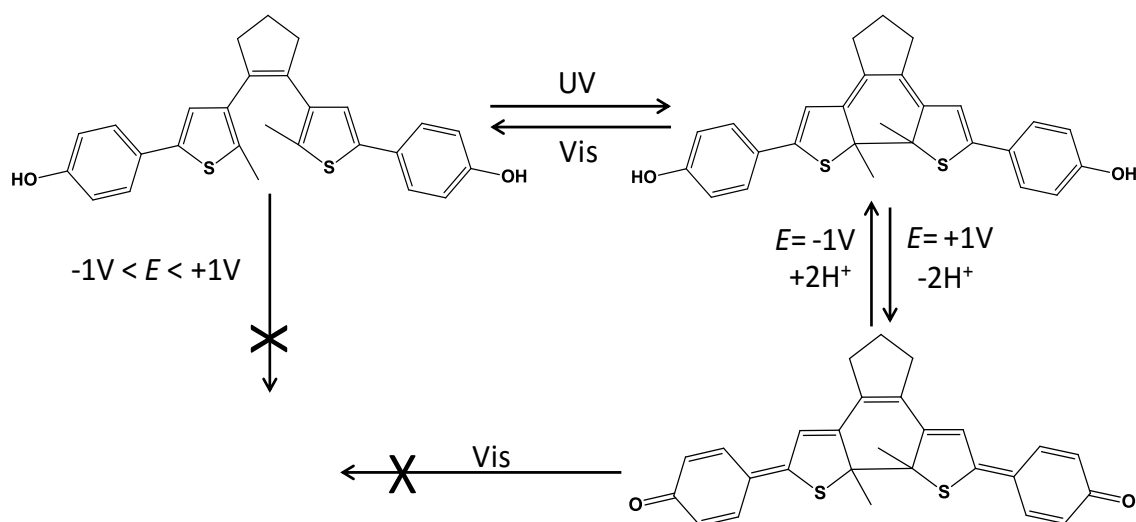
(parallel conformation), or the antiparallel position, which is the opposite case. Only the latter can experience the photocyclization, due to the conrotatory mechanism of the transformation. In solution, the ratio of these conformers is 1:1 and fluctuates continuously. Different approaches have been used to increase the ratio of the antiparallel configuration. One of them is the introduction of bulky substituents in the thiophene ring in order to cause steric impediments, forcing the antiparallel configuration. This consideration should be taken with caution, because some bulky substituents can create interactions between them, provoking the opposite effect. That is the case where the substituents have aromatic rings, causing π - π staking between them or groups that can create hydrogen bonds.

The fact that each direction of the isomerization uses a different type of light, makes these compounds good candidates for optical switches because of the nondestructive read-out behavior. This offers also the possibility to store information, using the gated-reactivity of these compounds³⁵. Thus, the above explained parallel conformation can be used as gated-reactivity agent. If we can interconvert the conformers with other stimuli, we can open or close the possibility to perform the cyclization. One example was reported by Irie's group. It is a diarylethene that in apolar solvent forms intramolecular hydrogen bonds between the substituents, favoring the parallel conformer. The addition of ethanol into the media, breaks the hydrogen bonds. The more ethanol is added, the higher the concentration of antiparallel configuration (Scheme 1.9)^{36,37}.



Scheme 1.9: Gate-reactivity due to the intramolecular hydrogen bonding.

The introduction of substituents controllable electrochemically also can be used as gated-reactivity agent. Lehn's group synthesized a molecule capable of perform photochromism and electrochromism. Depending on the light or voltage used, the system can toggle between three states (Scheme 1.10)^{38,39}.



Scheme 1.10: Gated reactivity behavior depending on the conditions.

Perhaps, the most impressive and useful behavior is the color change of the isomers. The isomer in the open form has all the π electrons localized in the thiophene ring and the ethene double bond. In general, the open-ring isomers of diarylethenes have absorption bands at short wavelengths. Upon irradiation with UV light, new absorption bands appear at longer wavelengths, which are ascribed to the closed-ring isomers where the electrons are delocalized through the conjugation of double bonds by the condensation of the thiophenes with the central sp^2 moiety. The closed form owing to destabilization of the ground state and lowering of the HOMO/ LUMO gap, exhibits distinct absorption spectra, always featuring a large band in the visible region, which provides color to this isomer. The differences on colors between different systems are due the substituents linked to the thiophene rings. Not only the absorption spectra is modified upon isomerization, also the fluorescence emission is affected⁴⁰. Fluorescence is highly sensitive to the electronic structure and can be used as a nondestructive read-out if there are differences in the emission spectra in both isomers and the light used for excitation of the fluorescence does not affect the cyclization/ring opening processes. In general, the open form isomer is more fluorescent than the closed isomer, thus the luminiscence of the compound can be switched ON and OFF.

Also fascinating is the photochromism in the solid state (Figure 1.1)⁴¹. When the photochromic reaction can proceed in the solid state and both isomers are stable, the system can be used potentially as part of devices. It is important that the crystalline compound show the antiparallel configuration. Nevertheless, the photochromic reaction in the solid state, also depends on the distance between the reactive carbons; distances above 4Å, inhibit the photocromism of the compound⁴¹.

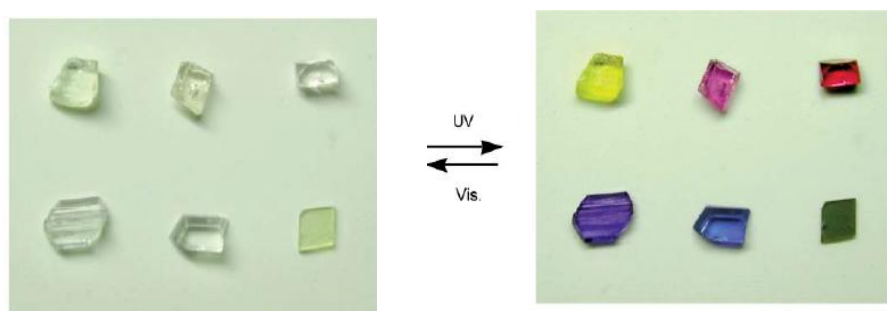


Figure 1.1: Compounds showing the wide possibilities of colors in the crystal state.

The change in the solid state is also accompanied by a change in the size of the crystals (Figure 1.2). Thus, this behavior can be used in the fabrication of actuators, which are systems that mechanical movement exhibit at the macro-scale based on the photochromic reactions^{42–45}.

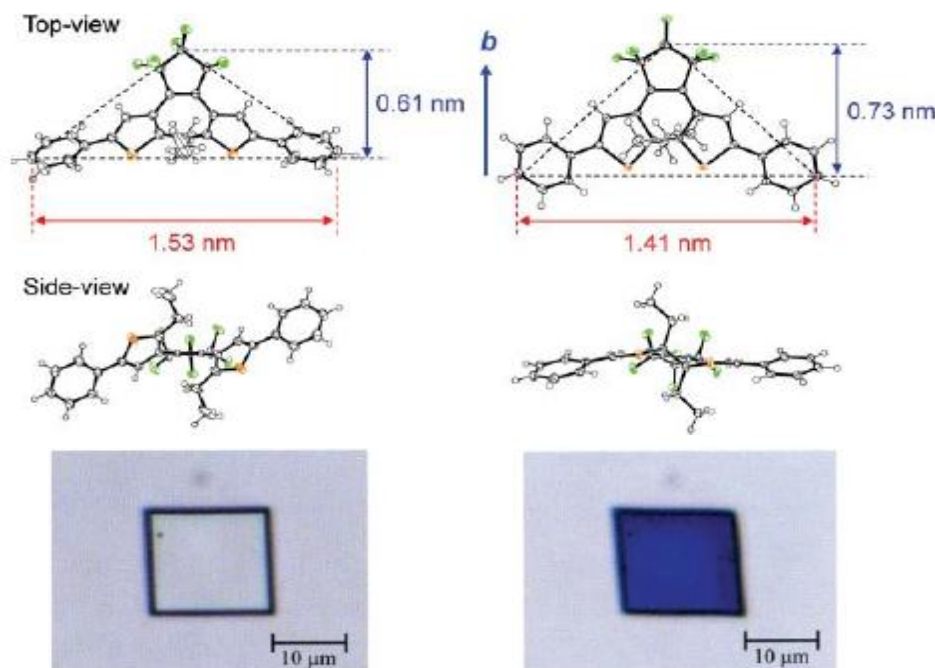


Figure 1.2: Structural changes upon cyclization.

Different applications related to electron transport and surface deposition (e.g. Au-nanoparticles), are currently under investigation with very promising results in the field of optoelectronic devices. Molecules that can be reversibly switched between a high and a low conductance state represent the ideal building blocks for molecular electronics^{8,46}.

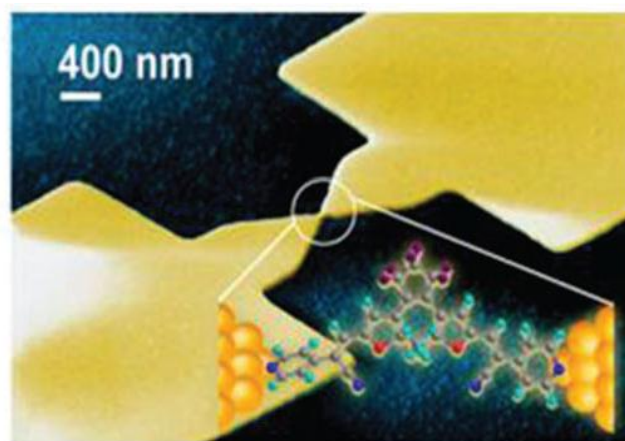


Figure 1.3: SEM image of the single molecule device and a schematic illustration of a single diarylethene molecule bridged between two gold electrodes

Indeed, the closed isomer possesses a higher conductance than the open isomer due to its continuous π -conjugation along the current pathway. This indicates that the charge transport in the molecules is dramatically influenced by the optically induced molecular isomerization (Figure 1.3)⁴⁷.

On a different application, switching of host–guest interactions by photoirradiation potentially enables active transportation of guest molecules or detection of certain chemical species. The photochromic properties of diarylethenes can also be exploited for such purposes as their switching unit may be modified with appropriate functional groups suitable for interacting with a chemical guest. This behavior has potentially utility in biological and environmental applications, such as drug delivery, cellular indicator or in the analysis of water waste^{27,48–54}.

1.3 Molecular Magnetism⁵⁵⁻⁵⁷

The most important property on molecular magnetism is the magnetization (M). It is the magnetic field induced within a material by a homogeneous external magnetic field (H). This property also can be expressed as a susceptibility (χ).

In classical mechanics, when a sample is perturbed by an external field, its magnetization is related to its energy variation through:

$$M = -\delta E / \delta H \quad \text{or} \quad \chi = \delta M / \delta H$$

In quantum mechanics, each molecule exhibits a number of energy states, E_n ($n=1,2,3\dots$), in the presence of a magnetic field. For each energy level it is possible to attribute a microscopic magnetization, μ_n , which can be expressed as:

$$\mu_n = -\delta E_n / \delta H$$

The macroscopic molar magnetization is then obtained by summing the microscopic magnetization according to the Boltzmann distribution law, which leads to:

$$M = N \sum_n \mu_n P_n = \left(\frac{N \sum_n \left(-\frac{\delta E_n}{\delta H} \right) \exp \left(-\frac{E_n}{kT} \right)}{\sum_n \exp \left(-\frac{E_n}{kT} \right)} \right)$$

where T is the temperature, k the Boltzmann constant and N Avogadro's number. Although this formula is general, it is often difficult to apply. Indeed it requires knowledge on the $E_n = f(H)$ variations for all the thermally populated states to calculate the $\delta E_n / \delta H$ derivatives. In 1932, Van Vleck proposed a simplification based on a few approximations⁵⁸. The first decompose the energy of each state, following a perturbation method according to the increasing powers of H:

$$E_n = E_n^{(0)} + E_n^{(1)}H + E_n^{(2)}H^2 + \dots$$

where $E_n^{(0)}$ is the energy of level n in zero field, while $E_n^{(1)}$ and $E_n^{(2)}$ are the first- and second-order Zeeman coefficients respectively. The second approximation is that H/kT

is very small respect to the unit. From these two approximations and applying the definition of the magnetic molar susceptibility, $\chi_M = \delta M / \delta H$, the Van Vleck formula up to the second order is defined as:

$$\chi_M = \frac{N \sum_n \left(\frac{E_n^{(1)2}}{kT} - 2E_n^{(2)} \right) \exp\left(\frac{-E_n^{(0)}}{kT}\right)}{\sum_n \exp\left(\frac{-E_n^{(0)}}{kT}\right)}$$

The formula can be simplified when the external magnetic field and temperature are sufficiently small. Applying these approximations the susceptibility leads as:

$$\chi_M = \frac{Ng^2 \beta^2 \sum_n S(S+1)(2S+1) \exp\left(\frac{-E_n^{(0)}}{k_B T}\right)}{3kT \sum_n (2S+1) \exp\left(\frac{-E_n^{(0)}}{k_B T}\right)}$$

where β is the Bohr factor, g the gyromagnetic factor and S the total spin angular momentum. The *Curie law* can be extracted from the above equation for a system with only one paramagnetic center or with a ground state well separated from the excited states. In these cases, the χ_M value is constant for all the range of temperature:

$$\chi_M = \frac{C}{T}$$

This behavior is usually modified in situations where the first order spin orbit coupling affects the energy state and splits the Zeeman multiplets in zero field. In these cases, the above equation is modified with the introduction of a new term, thus describing the *Curie-Weiss law*:

$$\chi_M = \frac{C}{T - \theta}$$

In cases where there are more than one magnetic center, the interaction between the electronic spins may be considered. The exchange interaction between these spins is used to describe the magnetic behavior of the system and can be expressed by the Heisenberg-Dirac-Van Vleck Hamiltonian:

$$\hat{H} = - \sum_{i,j} J_{ij} \hat{S}_i \hat{S}_j \quad \text{or} \quad \hat{H} = -2 \sum_{i,j} J_{ij} \hat{S}_i \hat{S}_j$$

The notation of this equation depends on the convention used. J is the exchange between the spins S . In this thesis, we will use the second one.

From this equation, the value of the exchange given by J may reflect a ferromagnetic or antiferromagnetic character, if J is larger than zero or lower than zero, respectively.

If the Hamiltonian has analytical solutions for the eigenstates and energies, these can be substituted in the Van Vleck formula, thus the fitting of the mentioned equation will give us the value of the exchange coupling values between the magnetic centers as parameters. Otherwise, a numerically iterative procedure involving the full diagonalization of the spin Hamiltonian will be necessary.

As mentioned, this fascinating field is of great interest due to the possibility to use molecular magnetic compound in systems capable to act as switches or storage devices. Several of these areas have been relevant to this thesis. Thus a brief introduction on these fields will follow. These topics are quantum computing (QC), single molecule magnets (SMM) and spin crossover phenomena (SCO).

1.3.1 Quantum computing (QC)

The future of Nanotechnology depends inevitably on the creation of molecular devices capable of performing crucial functions. One of the most exciting prospects in this respect is the realization of Quantum Computing (QC) where the use of laws of quantum mechanics should allow the processing of information⁵⁹⁻⁶³. In QC the bit of information is encoded by microstates of a quantum system (for example $|1\rangle$ and $|0\rangle$) and is termed qubit. One of the main particularities of qubits is that they can encode information in form of any superposition of two states (for example, $|\phi\rangle = \alpha|0\rangle + \beta|1\rangle$), widening enormously the potential of QC over classical computation (Figure 1.4). The other ingredient to realize QC is the logic gates or logic operations. A set of universal logic gates is a set that, combined, allow to realize any algorithm. Two very important logic operations of QC are the *controlled-NOT* gate (CNOT) and the SWAP. Any of them, combined with the single rotations of a qubit constitute a set of universal logic gates⁵⁹. Both need a double qubit (*2qubit*) for their realization. The CNOT operation inverts the state of one qubit (*target qubit*) depending on the state of the other (*control qubit*). The SWAP inverts the states of both qubits, which must come with opposite values (Figure 1.4).

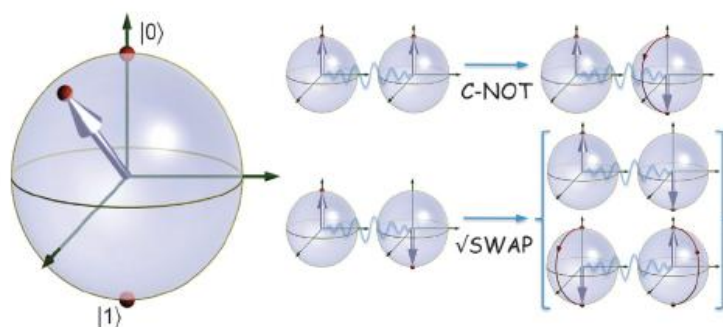


Figure 1.4: Representation of the quantum operations via the Bloch sphere.

Among the most attractive candidates to become the physical realization of qubits in future quantum computers are electronic spins^{64–66}. The electronic spin of magnetic coordination compounds may constitute in fact a true two-level system, so it can act as 0 or 1, depending on the state in which it is found. Interestingly, this change between states is easily done using electromagnetic pulses³ (Figure 1.5).

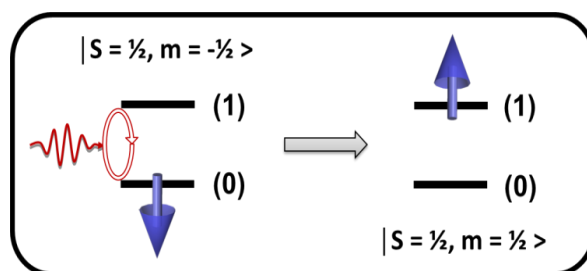


Figure 1.5: Levels of the electronic spin and its changes via electromagnetic pulse.

Pulsed EPR has been the primary tool for investigating and characterizing the coherent spin dynamics of molecular spin systems.

For the chemical design of Quantum Gates it is very important to take into account, the decoherence time⁶ (τ) that characterizes the quantum dynamics of a qubit in contact with its environment. It is the time during which the quantum information stored in a qubit is maintained before it is lost because of the interaction with the surroundings.

It is also interesting, that not only a pure $S=1/2$ spin can act as qubit, but any system that can embody a pure two spin states, for example an isolated $S=1/2$ ground state of antiferromagnetically coupled spin moments⁶⁷, or a highly anisotropic lanthanide ion with a two level ground state (effective $S=1/2$ state)⁶⁸. In that regard, the group has demonstrated the utility using of two different lanthanide ions as a prototype of a two-qubits system, for the realization of quantum operations⁶⁹ (Figure 1.6).

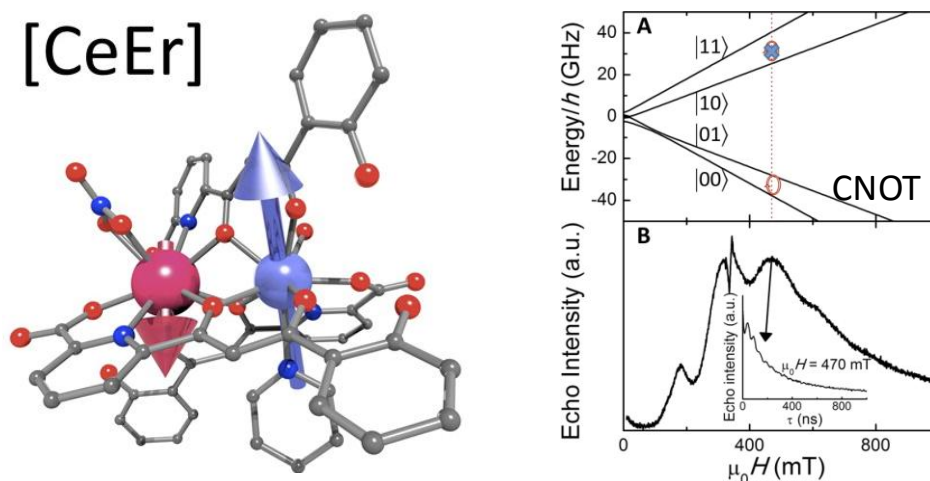


Figure 1.6. Crystal structure of the [CeEr] compound and pulsed EPR which allows quantum operation.

This dinuclear [LnLn'] molecule presents coherent spin dynamics when irradiated with electromagnetic pulses, which ensures that the magnetic levels shown in the upper graph are maintained for a given time. If the measurements are carried out in the resonance range corresponding to the CNOT operation, it is possible to extract the coherence time of this resonance, by fitting the decay with an exponential decay function. Even though the coherence time is not large enough to perform quantum operations, the future synthesis design could improve this time. Nevertheless, this research confirms the utility of the magnetic spin for future quantum information storage.

A widely featured system in this context is made by the antiferromagnetic Cr₇Ni rings^{7,70-74}. Indeed, these compounds have a ground state of S=1/2, which constitutes the realization of a qubit. The facility to obtain many derivatives from these compounds relies on the low reactivity of chromium in front of the nickel, offering a vast spectrum of complexes for the study of their implementation in quantum computing. In addition, the individual clusters may be linked via different approaches, which enable to tune the communication between heterometallic rings. These approaches are i) introduction of an ion-pair interaction supported by hydrogen-bonding interactions ii) functionalization of the exterior of the AF-ring, so that it will act as a Lewis base and iii) creation of a vacancy on one site of the AF-ring, and then, using the ring as a Lewis acid (Figure 1.7)

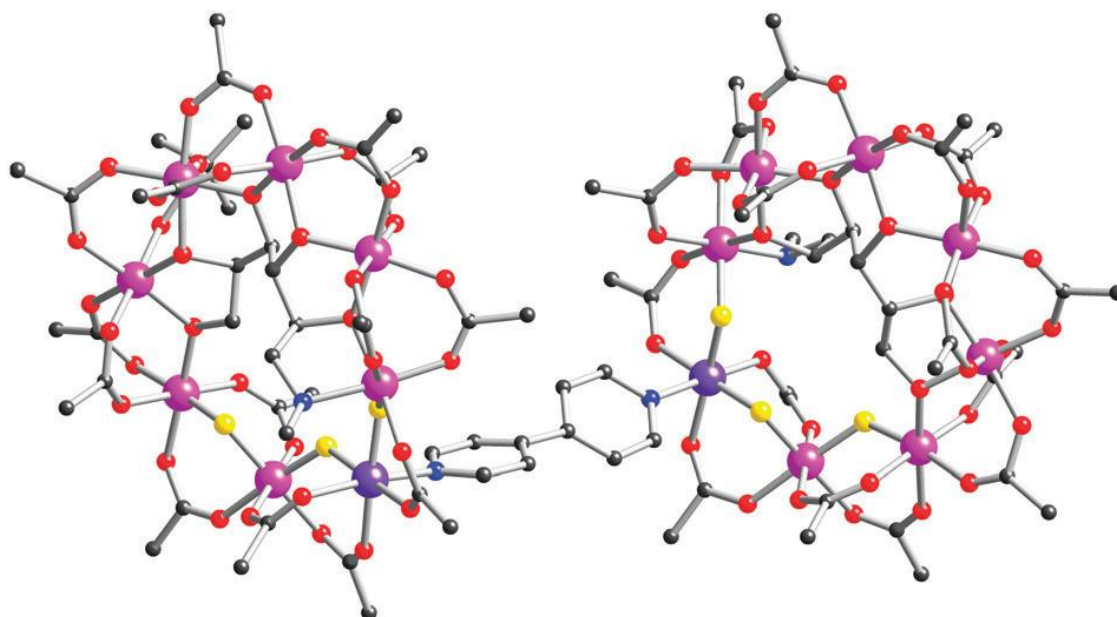


Figure 1.7: Two Cr₇Ni ring linked via bipyridine, using the third approach⁷¹.

It is also possible to change the bridging group, thus it is possible to tune the exchange interaction between the heterometallic rings. Indeed, the longer the bridge, the weaker the interaction. Pulsed EPR measurements established that the coherence times are sufficient for spin manipulation. The Spin entanglement between the rings was experimentally demonstrated below 50 mK using magnetic susceptibility as entanglement witness, in agreement with theoretical calculations. Thus, the Cr₇Ni system appears to be a molecular two-level system very promising for qubit encoding.

1.3.2 Single Molecular Magnets (SMMs)

SMMs were discovered in 1993⁷⁵. These are molecules that exhibit, individually, slow relaxation of the magnetization with time. Since their discovery, SMMs have attracted much attention because of their possible technological applications, for example as systems in which each molecule behaves like a magnet. This behavior shows great promise as they could replace alloys for memory storage with a substantial reduction in size, by replacing a magnetic domain of an alloy (~ 300 nm) for a single molecule (~ 1 nm). The slow relaxation of the magnetization in SMMs is related to the presence of magnetic anisotropy of the ground state, which breaks the degeneracy of the multiplet and originates a barrier which impedes the random orientation of the magnetization vector (Figure 1.8). There are several mechanisms leading to the relaxation of the magnetic moment⁵⁷, i) the thermally activated mechanism: the system reaches excited levels through interaction with molecular vibrations and overcomes the energy barrier.

This mechanism depends on the thermal energy available and can be verified through determination of the relaxation time as a function of temperature, which normally follows an exponential relationship of the Arrhenius law, where is possible to extract the barrier of the demagnetization (commonly referred U_{eff}), ii) Relaxation by tunneling through the ground state: This mechanism is a direct process and independent of temperature and is important at low temperatures, where it is not possible to populate excited states that allow overcoming the energy barrier and iii) Relaxation by thermally assisted by tunneling : A combination of the two above mechanisms , the system can absorb energy and populate excited levels that can cross the barrier by tunneling anisotropy and eventually decay to the ground state in the opposite side of the potential well, also known as an Orbach mechanism, iv) Raman mechanism: Similar to the Orbach process excepting the exitacion goes through an imaginarium exited level.

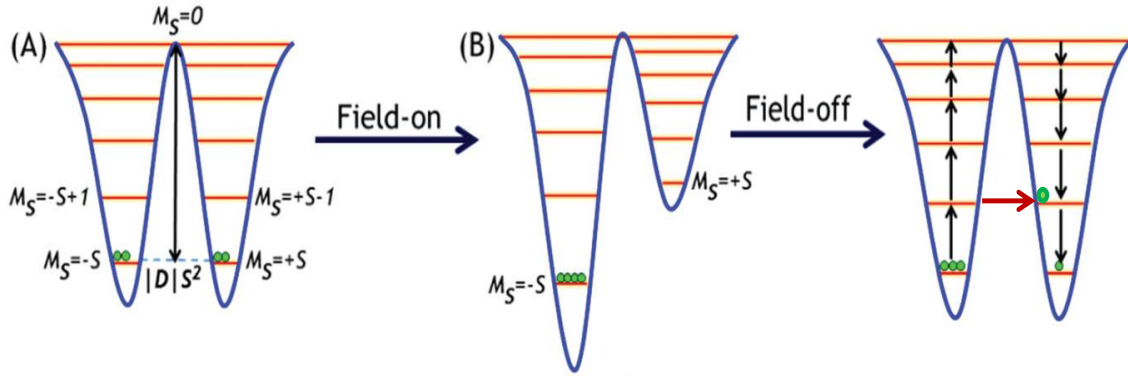


Figure 1.8: Effects of the field on the potential wells in a SMM. The black arrows correspond to thermally activated process while the red one is a tunneling relaxation process.

The experimental technique used in most studies on SMM is the measurement of the magnetic susceptibility in the presence of an alternating magnetic field at different frequencies⁴. In a SMM will be a dependency of the susceptibility with respect to the frequency of the oscillating field that allows the calculation of the relaxation time of the magnetization (τ). A convenient way to calculate experimentally τ is by adjusting the Cole – Cole equation.

$$\chi(\omega) = \chi_s + \frac{\chi_T - \chi_s}{1 + (i\omega\tau)^{1-a}}$$

where χ_T he isothermal susceptibility, χ_s the adiabatic susceptibility, ω the frequency of the ac field and a that is related to the broadness of the distribution of relaxation times that characterize the process. If the demagnetization occurs through a thermally

activated mechanism, the relaxation time will decrease with increasing temperature due to the higher probability of crossing the energy barrier that. As mentioned above, there is an exponential relationship between relaxation time and temperature, which allows evaluation of the energy of the barrier through the adjustment of the relaxation times obtained at different temperatures using the Arrhenius equation:

$$\tau = \tau_0 \exp(-E_a/kT)$$

where E_a is the activation energy of the process (the high of the barrier), τ_0 is the pre-exponential factor, k is the Boltzmann constant and T is the temperature .

The height of the energy barrier depends on the value of the ground state spin parameter and zero field splitting parameter by the following equations, depending if S is integer or half-integer, respectively:

$$U = |D|S^2 \text{ or } U = |D|(S^2-1/4)$$

This barrier is imposed by the magnetic anisotropy regardless of the relaxation mechanism. In systems with additional relaxation mechanisms, the effective barrier experimentally determined (U_{eff}) is usually lower than that the one calculated by the Arrhenius equation. At the beginning, the effort to obtain large energy barriers was based in the building of clusters with high nuclearity and many unpaired electrons as a way to increase S_T in addition with high anisotropy. This strategy was found to be incorrect, since it was later established that as S increases, D decreases. Currently, the efforts are based in the synthesis of compounds with high orbital angular momentum, such as lanthanides, because this situation stabilizes the ground state and its sublevels are strongly split by the crystal field⁷⁶.

One key feature of SMMs is the presence of hysteresis of the magnetization with the external field. Of particular interest is the observation of regular steps and plateaus in magnetic hysteresis loop at well defined intervals. These steps correspond to points of enhanced relaxation of the magnetization as a result of the quantum tunneling⁷⁷. Relaxation efficiency through tunneling depends on the magnetic anisotropy of the system and the presence of other magnetic interactions of smaller magnitude (intermolecular dipolar interaction, interacting spin-nuclei, intermolecular coupling, vibronic coupling).

Molecular slow magnetic relaxation was first observed on a mixed-valence manganese compound commonly referred Mn_{12} ⁷⁸ (Figure 1.9, left) comprising four cations of

Mn(IV) forming a central cubane (green) and eight cations Mn(III), forming an external crown (orange) that are joined together through bridging oxo ligands and carboxylates. There is a relatively strong antiferromagnetic coupling between these two units, so that the spin $S = 16$ ($S = 2$ each Mn(III)) of the outer ring is partially cancelled by the spin $S = 6$ ($S = 3/2$ each Mn(IV)) of central cubane, producing a total spin ground state of $S = 10$, with a $D = -46 \text{ cm}^{-1}$. A strong evidence of the bistability of this compound, is the opening of hysteresis loops depending on the magnetic field (Figure 1.9, right). The observed jumps in the hysteresis loops corresponding to magnetic fields where the variation of the magnetization occurs fast are ascribed to quantum tunneling. This additional relaxation mechanism is the reason why the measured energy barrier (U_{eff}) is smaller than the theoretically calculated one.

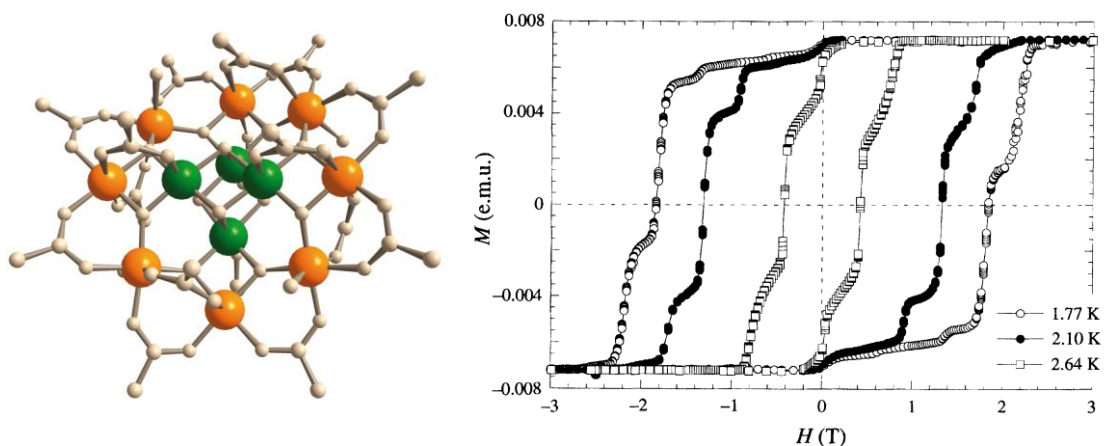


Figure 1.9: Left. Crystal structure of $[\text{Mn}]_{12}$. The Mn(IV) are marked in green and Mn(III) are marked in orange. Right. Hysteresis loops at different temperatures exhibiting the typical steps caused by the quantum tunneling⁷⁷.

In recent years, the relevance SMMs has increased coinciding with the raise of molecular spintronics^{79,80}. This field exploits the fact that an electron current is composed of spin-up and spin-down carriers, thus carrying information encoded in their spin state and interacting differently with magnetic materials. Information encoded in spins persists when the device is switched off, can be manipulated without using magnetic fields and can be written using low energies, here in form of weak electric field. In that regard, SMMs could act as magnets at low temperature which can persist during a long time, while the organic surrounding can be functionalized to link those molecules to surfaces. In addition, its ligand field can preserve and isolate the electronic spin in well defined ground states. That is the case for the case of the molecule TbPC₂, a SMM, which consists in a coordination compound of terbium sandwiched between two

phthalocyanines (Figure 1.10)^{81,82}. In that case, this compound was located between two gold electrodes and the current through its nuclear spin levels was tested with applying electric fields pulses. This was possible due to the well separated ground state of the electronic spin, split in two levels ($J \pm 6$), and the hyperfine coupling with the nuclei spin ($I=3/2$) splits the electronic in four quantum states. Off diagonal terms in the spin Hamiltonian lead to avoided energy level crossings enabling tunneling of the electronic spin.

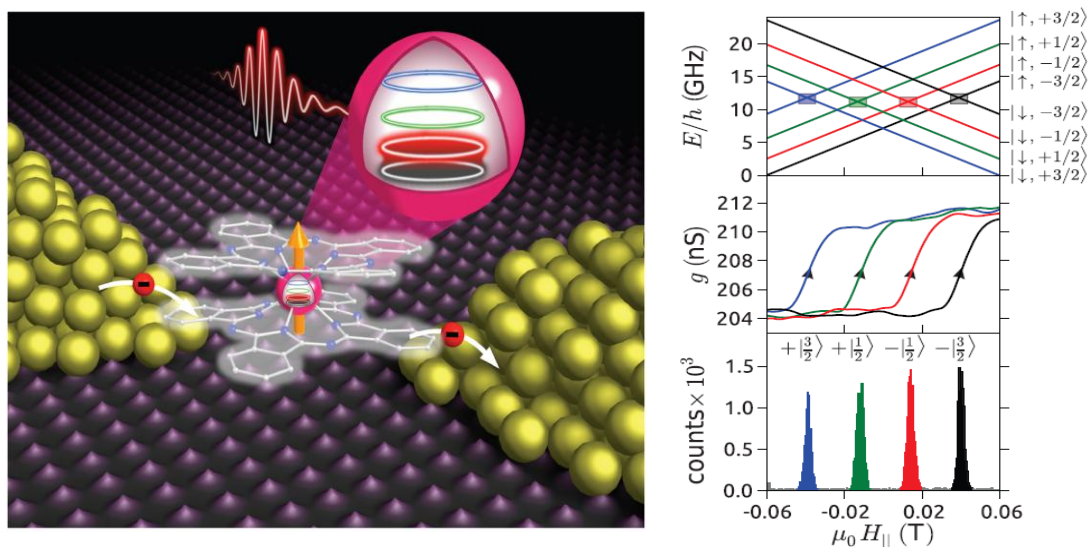


Figure 1.10: Figure scheme of a spin qubit transistor (left). Hyperfine Zeeman diagram of the TbPc2 molecular magnet, as a function of the external magnetic field and the level allowed for tunneling of the electron spin. (Right, up). The jumps of the conductance during magnetic-field sweeps are nuclear-spin dependent (Right, middle). Conductance jumps can be assigned to a nuclear spin state (Right, bottom).

1.3.3 Spin crossover (SCO)

The rational design of new functional materials is now a main area on chemistry research, as the so called top-down approach is reaching its limits of miniaturisation⁸³. This bottom-up approach is another alternative, based on the idea that this miniaturisation limit of an electronic function is the molecule.

Spin crossover (SCO) systems could be exploited in this sense, since they can work as a molecular switches or memory storage media^{84,85}. These compounds are able to pass from a low spin state (LS) to a high spin state (HS) by means of external stimuli⁸⁶, which is sometimes followed by a thermochromic effect, making these systems valuable for optical-storage devices.

Systems which can present this behavior are usually based on metal complexes of octahedral symmetry with a d^4 to d^7 electronic configuration⁸⁷ in addition with the proper ligand field strength. While less common, other coordination geometries may also present SCO in specific configurations. The most common compounds are Fe(II)⁵ systems, but also Fe(III)⁸⁸⁻⁹⁰, Co(II)^{91,92} or Mn(III)^{93,94} can undergo spin crossover phenomena.

The effect of the temperature^{5,86} is the main factor in the crossover but also pressure⁹⁵, application of an external field⁹⁶, light⁹⁷⁻⁹⁹ or the insertion of guest molecules¹⁰⁰⁻¹⁰² can modify this behavior. As previously mentioned, the transition is accompanied with changes of color, but maybe the most interesting feature is the change in the magnetic behavior, passing from a diamagnetic compound in the LS to a paramagnetic compound at HS or viceversa. Indeed, in the case of Fe(II) the transition causes the electrons of the complete orbital t_{2g} at LS, to go to the antibonding orbitals e_g in the HS, from diamagnetic state with $S=0$ to a paramagnetic state with $S=2$.

Also the crystal field influences the magnetic state¹⁰³. For weak ligand field strength, the splitting between the orbitals e_g and t_{2g} will be small, thus electrons will fill up the orbitals following the Hund's rule favouring the paramagnetic state and the HS state. On the contrary, stronger ligand field favours bigger splitting of the orbitals and the electrons prefer to be at the t_{2g} orbital, thus suppressing the magnetic character typical of the LS. For compound with an intermediate ligand field strength are the appropriate complexes where a spin transition can be induced just provoking one of the external stimuli mentioned before.

The condition required for a thermal spin transition can be seen then in Figure 1.11.

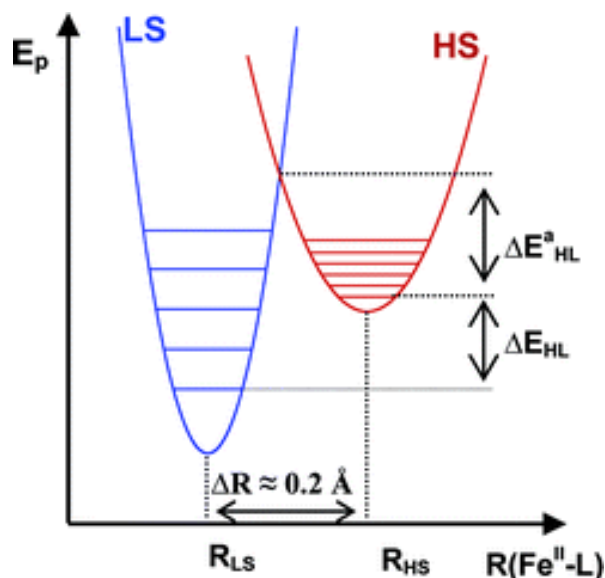


Figure 1.11: Configuration coordinate diagram for Fe(II) expressed along the totally symmetric metal-ligand stretch vibration, $R(\text{Fe-L})$ ¹⁰³.

These conditions are that the zero point energy difference, ΔE_{HL} has to be of the order of thermally accessible energies, therefore in the order of $k_{\text{B}}T$, and also positive. The transition takes place because of the entropy of the HS state, which is larger due to its degeneracy and its higher density of vibrational states.

The relative displacements of the minima the potential wells for the LS and HS states correspond to the difference in metal-ligand bond distance upon SCO (around 0.2\AA). This is because in passing from the LS to the HS two electrons go from non-bonding orbitals to antibonding orbitals.

All these changes and conditions for the spin transition behavior can be summarized in Figure 1.12.

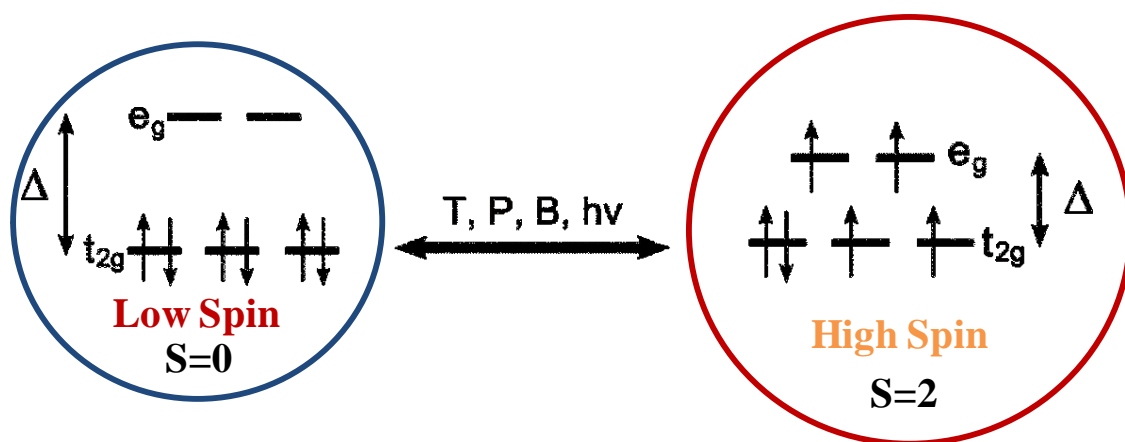


Figure 1.12: Different conditions which affect the spin transition phenomena.

Depending on the crystal lattice where the SCO species belongs, different shapes in the thermal magnetic curves can be seen. The temperature where half of the iron centers are in LS and the other half at HS is called $T_{1/2}$. The transition can be gradual, abrupt, incomplete, but maybe the most desired behavior is the presence of thermal hysteresis. In that case we have two distinct $T_{1/2}$, depending on the pathway: one for the cooling mode and another for the heating mode. That situation leads to a bistable region where the compound lies either in the LS or the HS state, depending on the sample history and this can be used as an indicator of “ON” and “OFF” states in future devices¹⁰⁴.

The synergy with SCO properties with other physical properties such as fluorescence or electrical conductivity, has been studied in search of new hybrid materials^{105–110}. In that sense, the deposition of these compounds on surfaces is crucial. Different examples can be seen in the area of nanoparticles, thin films and fibers.

The example shown below is in fact a study where a spin crossover compound ($[\text{Fe}(\text{trz})(\text{Htrz})_2][\text{BF}_4]$) with a bi-stable region, is inserted in a highly organic conducting matrix. This matrix is formed by polypyrrole, which is known because it changes in conductivity with pressure. Because the SCO involves a volume changes, the internal pressure is affected, therefore, influencing the conducting regime. In fact, the conductivity also features a hysteresis loop, showing more conductivity in the region where the system is in the HS, where the pressure is larger (Figure 1.13)¹¹¹.

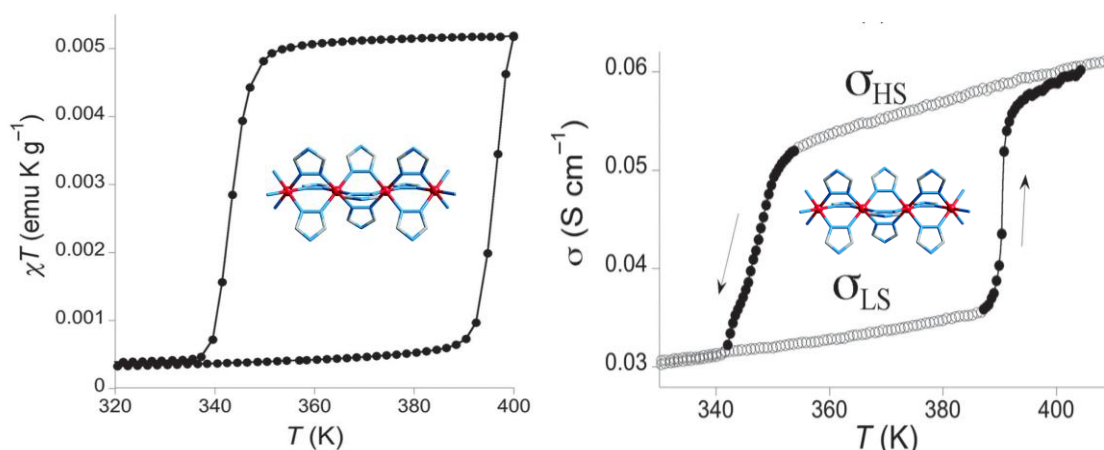


Figure 1.13: Synergy of the SCO and conductivity.

A similar behavior can be observed when studying the fluorescence in a similar spin crossover compound, imbedded together with a matrix of a cellulose fiber and orange acridine (Figure 1.14)¹⁰⁸.

Here there is a change in fluorescence depending on the spin state. Like in the example before, the fluorescence was measured in the same range of the SCO phenomena occurs, showing the same hysteresis loop. The fluorescence is increased when the compound is in the high spin state while it decreases at the low spin. The reason of this behavior is that if the separation between a pair of energy levels associated with the luminophore matches closely the energy level spacing of the SCO center (in a given spin state) the excited state energy can be transferred to the latter, thus quenching the luminescence. When this happens, the luminescence varies dramatically and similar to the above example, can be used as “ON” or “OFF” mechanisms.

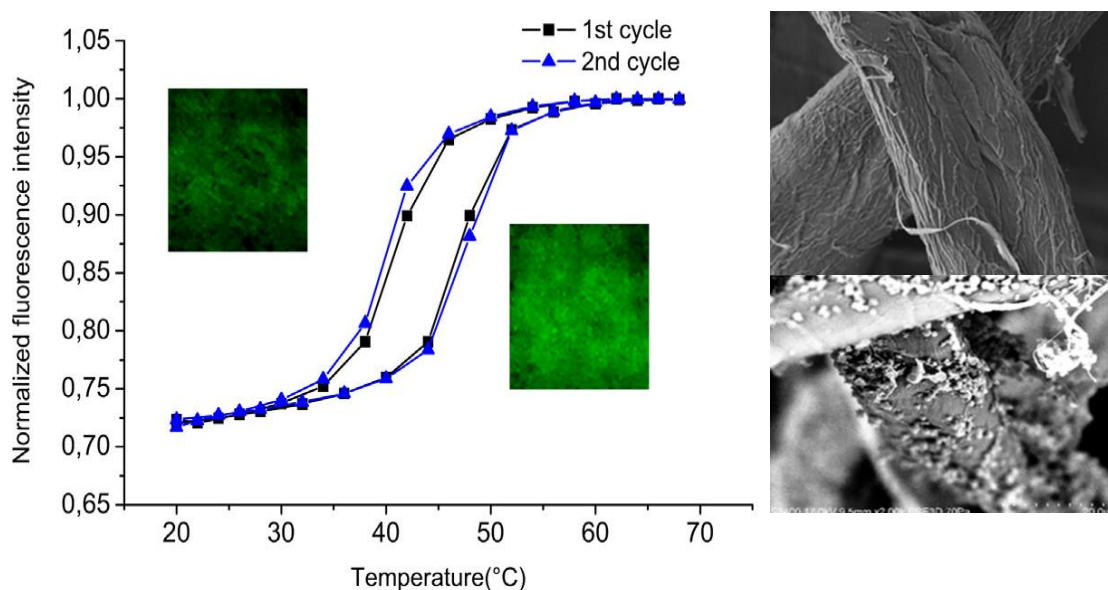


Figure 1.14: Synergy between the SCO and fluorescence. TEM images of the fibers.

The same experiment can be carried out in depositing this mixture of SCO materials with luminophores on nickel nanowires¹¹², the temperature of which can be changed when a DC field is applied. First, it was demonstrated the temperature dependence of the fluorescence intensity of the luminophores around room temperature. Thus, the different temperature provoked by the DC field induces also spin transition on the iron centers therefore it can be followed by the luminescence emission of the luminophore, because in fact, the ON and OFF state coincides with the SCO.

Those examples added to others, show how the properties of one material can be switched via the spin transition phenomena, creating a wide variety of new devices based on this principle.

1.4 Diaryethenes and magnetism

There are very few examples in the literature where a diarylethene molecule is binding metal ions, and even less regarding the exploitation of the magnetic properties.

The first experiments were done with dissymmetric diarylethene ligands containing perfluorocyclopentene (Figure 1.15)¹¹³, having a coordination pocket to link copper ions in one part of the ligand and a nitroxyl radical in the other. The exchange interaction difference between the open and closed-ring isomers was estimated from EPR spectral changes.

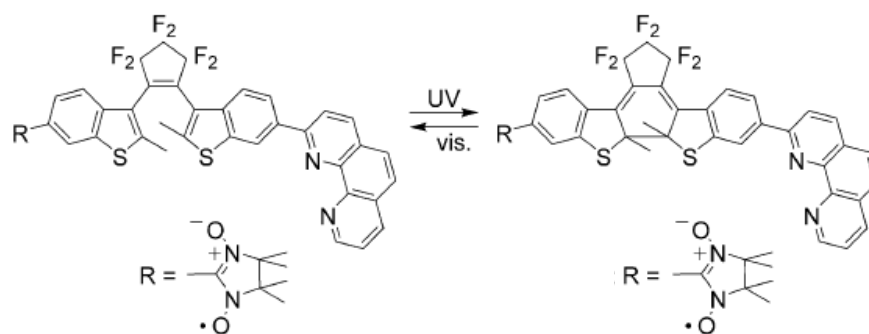


Figure 1.15: Schematic representation of the ligand.

Similar EPR experiments were conducted in different polymer complexes based in two different diarylethenes containing a pyridine moiety (Figure 1.16, left)¹¹⁴ and carboxylates on the other polymer (Figure 1.16, right)¹¹⁴. The complexes underwent reversible photochromic reactions in the single-crystalline phase as well as in solution. The complexation with metal ions does not prevent the photochromic reactions in the single-crystalline phase. The EPR spectra concluded that photochromic the reaction of the ligand caused a change to the coordination geometry of the metal.

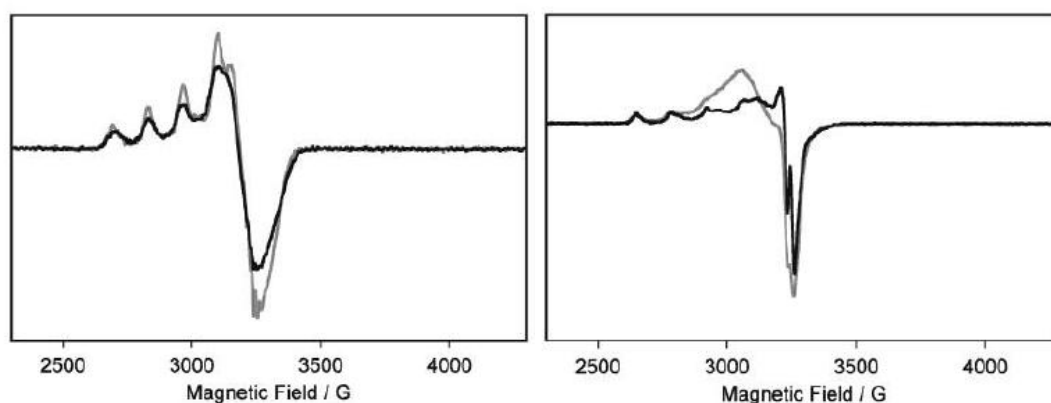


Figure 1.16: EPR experiments for two different compound before (black line) and after UV irradiation (grey line).

More recently Yamashita and Irie prepared different compounds containing a perfluorodiarylethene ligand with two carboxylates (Figure 1.17) has to test its ability to switch the single molecule magnet behavior.

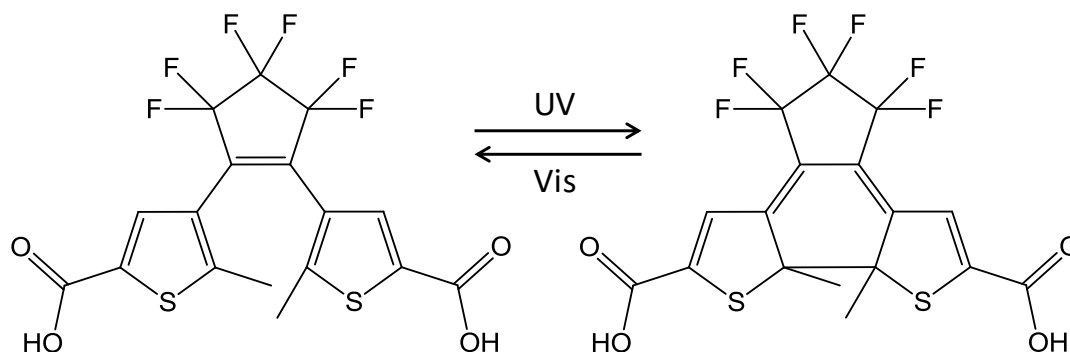


Figure 1.17: Ligand used in the building of SMM.

The first compound showing SMM behavior introducing a photochromic ligand was a polymer composed by the diarylethene of in Figure 1.17 and a double cuboidal Mn^{4+} . DC and AC magnetic measurements on **1o** (polymer with the open isomer) and **1c** (polymer with the closed isomer) showed that they behaved as SMMs. **1o** underwent photocyclization upon irradiation with UV to produce the closed-ring form and photocycloreversion with visible light. No significant changes in the magnetic properties were observed when **1o** was photocyclized. In contrast, photocycloreversion of **1c** by visible irradiation leads to **1c-vis** accompanied by a drastic change in the magnetic behavior (Figure 1.18). The difference in the photoresponsive behaviors of **1o** and **1c** was attributed to the difference in the packing structures of the polymers in the crystals.

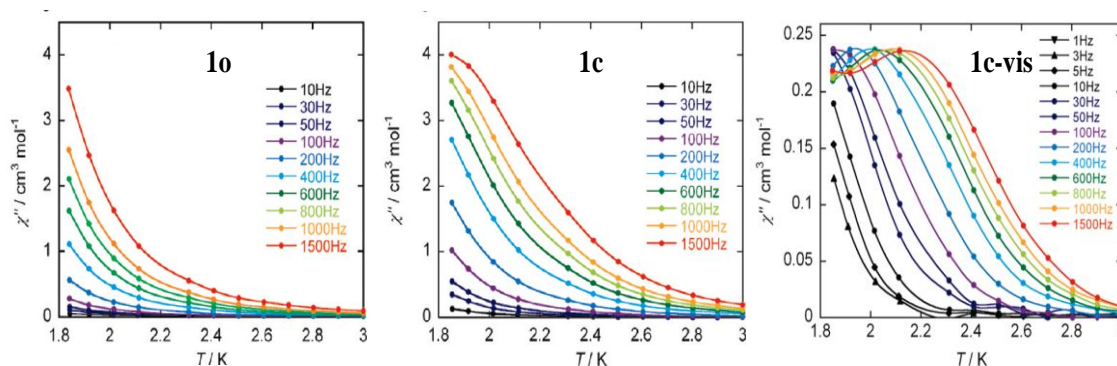


Figure 1.18: **1o**, **1c** and **1c-vis** measured at several frequencies in a zero dc field and a 3 Oe oscillating ac field.

The same behavior was observed in a copper-terbium complex¹¹⁶. Two compounds were synthesized, one using the open isomer (**2o**) and the other with the closed one (**2c**). Each compound presents different crystal packing: while the compound with the open ligand was a discrete molecule, the other was a 2D network.

The magnetic behavior shows ferromagnetic interaction in both complexes in addition to single molecule magnet behavior. When **2o** was irradiated with UV light, no changes were detected to the magnetic behavior whereas the magnetic behavior of **2c** changed. The distinct change of magnetic properties in the ladder-system can be thought of as the change of intermolecular interactions, as in the previous example.

Recently, different complexes of Dy had been synthesized presenting single molecule magnet behavior^{117,118}. In all cases, the photoswitching properties show that the irreversibility of the process cannot be achieved or is incomplete, because the cyclization of the ligand causes the sample to become irreversibly amorphous. In all the cases, the crystal structure reveals a 2D network, where the Dy atoms are linked through the diarylethene moieties in the way shown in Figure 1.19.

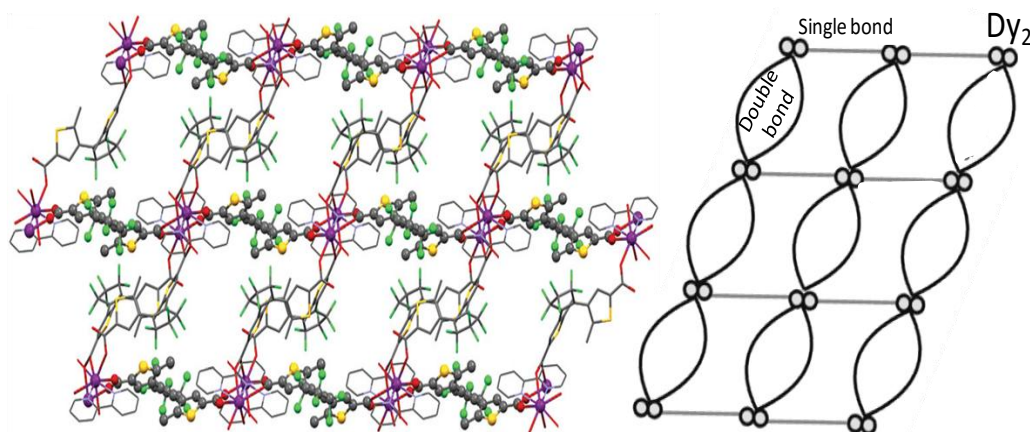


Figure 1.19: Left. Crystal structure taken from pairs of Dy. Right. Schematic 2D network of the explained compounds using the dicarboxylic ligand

This type of network is the cause why the reversibility of the process can not be reached. Probably, when the cyclisation occurs, the large number of diarylethene molecules coordinated to the dysprosium, creates a very big distortion on the crystal lattice which prevents the recovery of the initial conformation after visible light irradiation. Nevertheless, the presence of the single molecule magnet behavior make these type of photochromic molecules good candidates as switches, and future efforts will lead to new system able to perform the required photoreversion.

Also the use of diarylethenes in the field of spin crossover is very attractive due the possibility to encode different responses depending on different factors, such as light, temperature or magnetism.

The first experiment was carried out by the group of Feringa, using the photochromic ligand shown in Figure 1.20 on an Fe(II) coordination complex¹¹⁹.

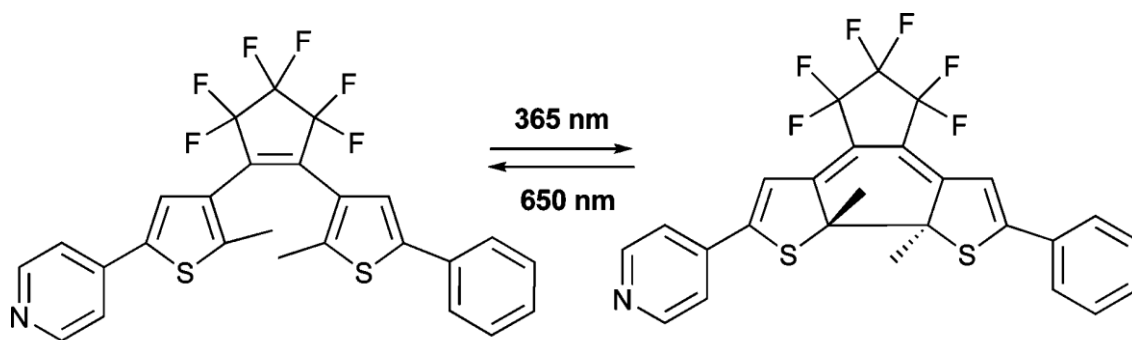


Figure 1.20: Schematic representation of the ligand used by Feringa's group.

The crystal structure of the complex shows an octahedral Fe(II) metal surrounded by the pyridine group of four ligands in the equatorial positions, while the axial ones were occupied by thiocyanate ions. The susceptibility of the sample indicates a high spin state of the complex in all the temperature range. Nevertheless, a small change in the magnetization is observed after irradiation the sample with UV. This change can be followed in time after a long exposure to UV light, as Figure 1.21 shows.

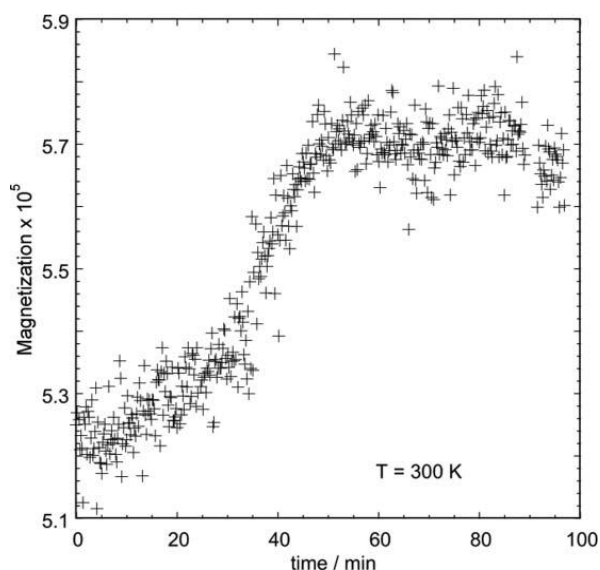


Figure 1.21: Magnetization vs. the time of irradiation for the crystalline sample at r.t.

In the last years, two different groups have been studied separately the spin crossover phenomena in the complex shown in Figure 1.22^{120–122}.

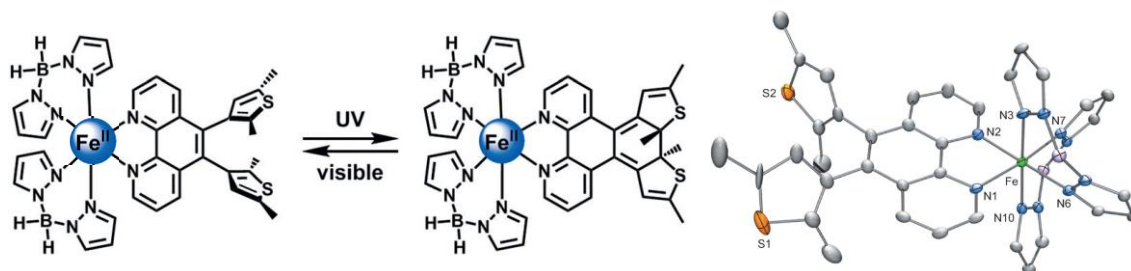


Figure 1.22: Left. Cyclization of the complex. Right. Crystal structure of the complex.

The first publication indicates differences to the spin transition in solution. The crystal structure of the complex reveals a parallel configuration of the thiophene rings, thus explaining the incapacity to perform photocyclization in the solid state. The SCO behavior of **1-o** and **1-c** in butyronitrile was investigated by means of variable-temperature UV/Vis absorption spectroscopy in the temperature range 293–163 K, following the changes in the MLCT of the complexes in the visible region (Figure 1.23, left). This temperature dependence of the absorption spectra was due to the occurrence of thermal spin conversion. Even though the photochromic process cannot be performed in solid, a spin change can be observed when the complex is irradiated with light (637 nm) at 5K, suggesting the occurrence of LIESST from the LS to a metastable HS state. A reverse-LIESST effect, a light-induced conversion from the metastable HS back to the ground LS state, was also confirmed by irradiation (808 nm), thus this compound shows magnetic bistability through LIESST and reverse-LIESST below 52 K in the solid state. (Figure 1.23, right)

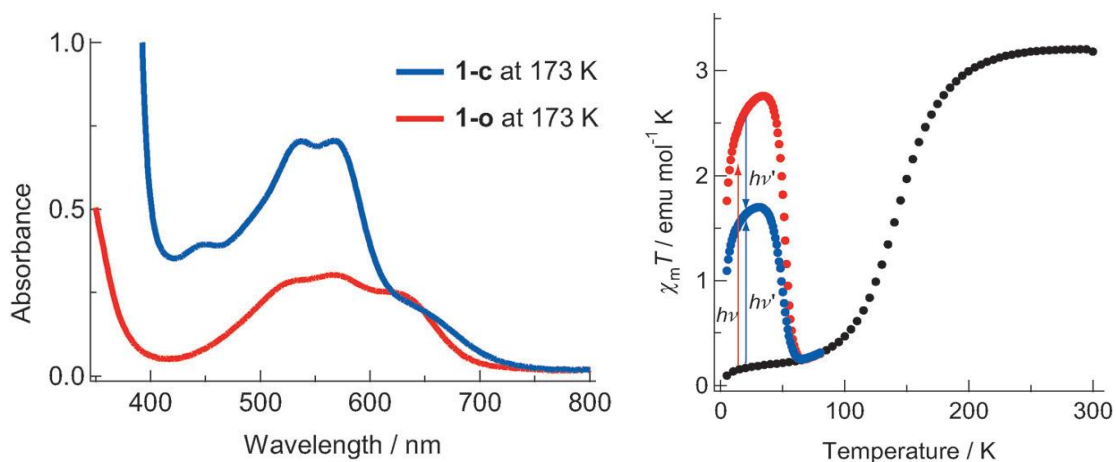


Figure 1.23: Left. Different changes on the UV-Vis after irradiation. Right. LIESST effect on the solid compound¹²⁰.

Other studies show that the use of different crystallization solvents, leads to mixtures of parallel form and antiparallel form in the crystal lattice¹²². It was shown that X-ray photoelectron spectroscopy (XPS) combined with near-edge X-ray absorption fine structure (NEXAFS) spectroscopy represents a useful tool for monitoring ligand-driven SCO quantitatively. In fact, XPS was used to follow the aromatic character of the thiophen groups at the S 2p core. Changes in the XPS spectra can be seen after 12h of UV irradiation (Figure 1.24, left). The photomagnetic behavior was followed by NEXAFS, where the different occupation of the t_{2g} and e_g orbitals in the HS and LS states can be probed as a function of the intensity of excitation from the Fe 2p core levels into the unoccupied d orbitals, thus allowing the determination of the spin state (Figure 1.24, right). The experiment where done in the same conditions, 12 hours of UV and 8 hours for Visible irradiation. The studies reveal that the number of molecules that undergo the spin transition are around the 32% of the sample.

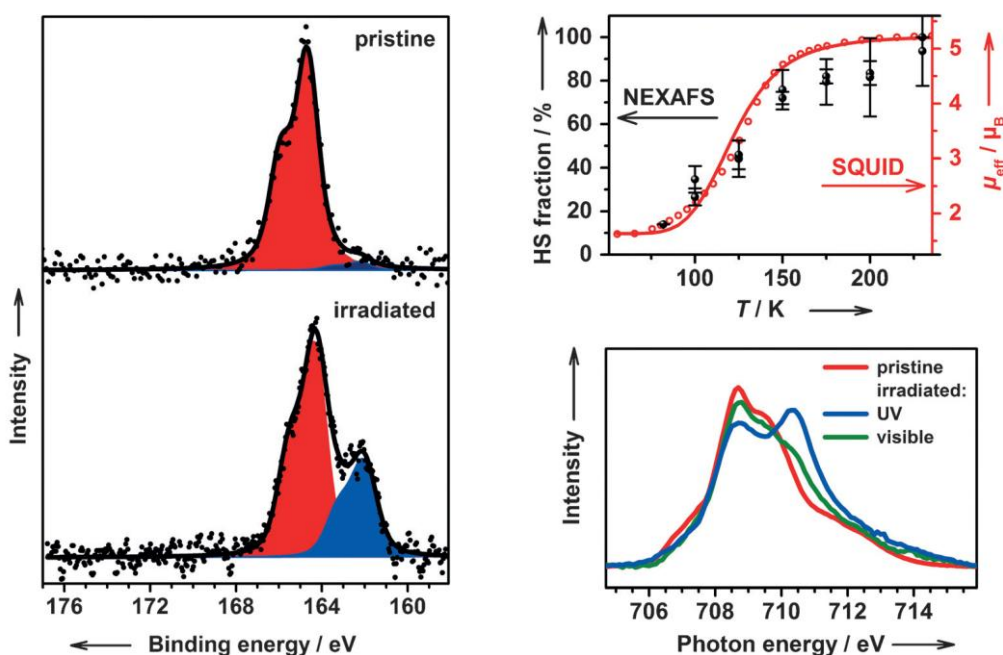


Figure 1.24: Left. Sulfur 2p XPS spectra at room temperature initial complex and after UV irradiation at room temperature. the fit areas in blue correspond to the closed-ring isomer (32%). Right Up. Quantification of the HS fraction from temperature-dependent NEXAFS data (black circles), as compared with magnetic susceptibility measurements performed with a SQUID magnetometer. Right, Down. NEXAFS spectra acquired at room temperature on the initial sample, after UV irradiation, and after subsequent irradiation with visible light.

1.4.1 Others systems combining photochromism and magnetism

Not only diarylethenes have been used for switching of the magnetic character of clusters. The easy synthesis of derivatives of azobenzenes makes this family as good candidates for optical devices. Several examples proof that magnetic and optical bistability can be made to coexist in the same material.

One of these examples is based in Fe(III) metals surrounded by an azobenzene derivative ligand. According to DC magnetic data and EPR spectra, the spin value and the anisotropy parameters in the ground state are unmodified upon dispersion the iron compound inside a polymer and upon irradiation with UV light. Nevertheless, photoisomerization has a feeble, but clearly detectable effect on the dynamics of the magnetization, affording a slightly faster relaxation of the magnetization¹²³.

Another example which is now at being investigated, is based on a modified porphyrine with a pyridine based-azobenzene substituent, which can coordinate in a square geometry to a nickel atom. This geometry results in a diamagnetic low spin state. Irradiation of the complex, leads to a cis isomerization of the azobenzene moiety that now is able to coordinate the nickel through the pyridine substituent, leading now to a pentacoordinate configuration which causes a spin change of the nickel, passing from a diamagnetic to a paramagnetic state. Furthermore, the magnetic state can be reversed upon irradiation of the sample again, with a different wavelength (Figure 1.25)¹²⁴.

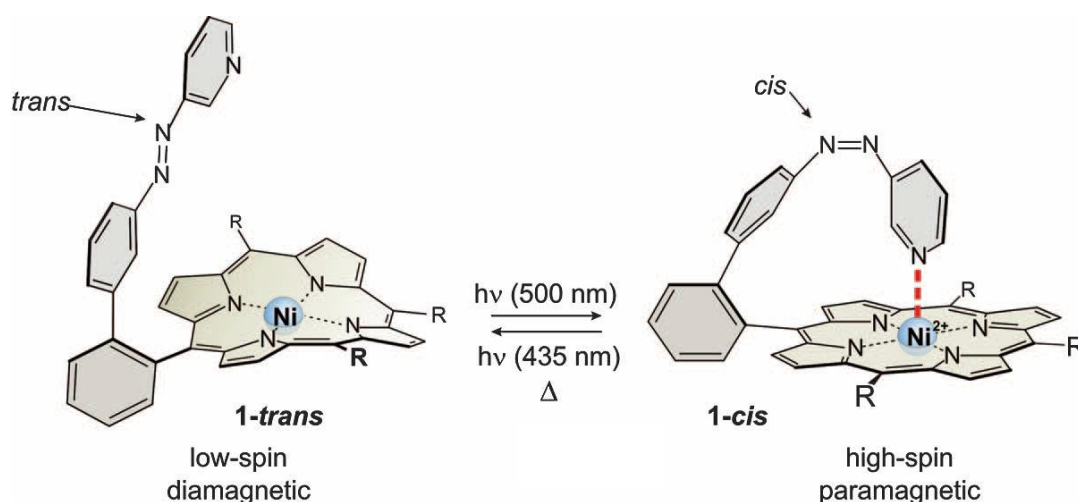


Figure 1.25: Reversible light-induced magnetic switching of azopyridine.

1.5 Aim of the thesis

Despite the large number of diarylethene compounds that can be found in the literature, only few of them are able to coordinate metal atoms. Therefore, this thesis proposes the design and synthesis of new photochromic ligands that can accommodate metal ions in their molecular framework. The building block that will be employed is shown in Figure 1.26.

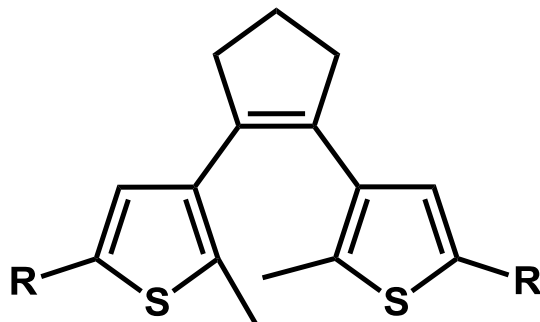


Figure 1.26: Building block.

The initial step will be the development of strategies for the synthesis of functionalized diarylethene ligands, followed by the synthesis of their metal complexes. Of great importance will be the determination of their crystallographic structure, in order to understand their photochromic properties, either in the solid or in solution. The understanding of the photochromic process is the main objective of Chapter 2, where the photoconversion is explained in light of the structural information.

As previously shown, important areas are related with the study of the magnetic behavior of these new systems: Quantum Computing (QC), Single Molecule Magnets (SMMs) and Spin CrossOver (SCO). Thus, different approaches will be needed.

The synthesis of pairs of clusters with a weak magnetic coupling between them, will be the basis for building pairs of Qbits. The following step will be to control the coupling between them by using light. For the synthetic approach, the synthesis of multidentate β -diketones will be an important goal. Related systems have been widely used in the group for already the synthesis of various types of molecular cluster assemblies. Indeed, these systems are able of featuring two well defined coordination pockets gathering metals into clusters that could represent ideal systems for embodying quantum bits. Chapter 3 explains the synthetic route for two new ligands, with their metal complexes, and all the physical characterization to prove their utility as candidates for new Qbit systems.

Chapter 4 presents a synthetic approach to find new photochromic ligands with large chelating pockets able to coordinate atoms which can present slow relaxation of the magnetization, such as Dysprosium and Terbium. Those new ligands are based on hydrazones with two different coordination pockets, one with an environment of the $[\text{NO}_2]$ type and the other one with a $[\text{N}_2\text{O}]$ environment, which lead to different types of clusters. Also the preparation of transition metal complexes using copper is detailed in this chapter.

The synthesis of a photochromic ligand with a complete nitrogen chelating pocket is the main approach, since this environment is well known to produce a crystal field effect that can induce SCO in a octahedral configuration of Fe(II) centers. A dinuclear iron compound presenting SCO behavior is characterized in Chapter 5.

Chapter 6 contains the conclusions drawn from the chemistry of the new photochromic ligands applied to molecular magnetism, as well as some general comments and possible future prospects.

1.6 References

1. Selzer, Y. & Allara, D. L. Single-Molecule Electrical Junctions. *Annu. Rev. Phys. Chem.* **57**, 593–623 (2006).
2. Tao, N. J. Electron transport in molecular junctions. *Nat. Nanotechnol.* **1**, 173–181 (2006).
3. Ardavan, a. & Blundell, S. J. Storing quantum information in chemically engineered nanoscale magnets. *J. Mater. Chem.* **19**, 1754 (2009).
4. Gatteschi, D., Sessoli, R., Villain, J. *Molecular Nanomagnets*. (2006).
5. Gütlich, P., Garcia, Y. & Goodwin, H. a. Spin crossover phenomena in Fe(II) complexes. *Chem. Soc. Rev.* **29**, 419–427 (2000).
6. Affronte, M. Molecular nanomagnets for information technologies. *J. Mater. Chem.* **19**, 1731 (2009).
7. Wedge, C. J. *et al.* Chemical engineering of molecular qubits. *Phys. Rev. Lett.* **108**, 1–5 (2012).
8. Zhang, J. L. *et al.* Towards single molecule switches. *Chem. Soc. Rev.* **44**, - (2015).
9. Feringa, B. L. *Molecular Switches*. **3**, (2001).
10. Bouas-Laurent, H. & Dürr, H. *Photochromism : Molecules and systems*. Elsevier (2003).
11. El'tsov, A. V, Ponyaev, A. I., Zakhs, É. R., Klemm, D. & Klemm, E. in 177–228 (Springer US, 1990).
12. Hammond, G. S. *et al.* Mechanisms of Photochemical Reactions in Solution. XXII.' Isomerization Photochemical. *J. Am. Chem. Soc.* **86**, 3197–3217 (1964).
13. Hoffmann, R. B. W. and R. *The Conservation of Orbital Symmetry*. *Journal of Chemical Information and Modeling* (1971).
14. Hoffmann, R. & Woodward, R. B. Conservation of orbital symmetry. *Acc. Chem. Res.* **1**, 17–22 (1968).
15. Dürr, H. Photochromic Nitrogen Containing Compounds. *Science* (2003)
16. Tamai, N. & Miyasaka, H. Ultrafast Dynamics of Photochromic Systems. *Chem. Rev.* **100**, 1875–1890 (2000).
17. Aemissegger, A. & Hilvert, D. Synthesis and application of an azobenzene amino acid as a light-switchable turn element in polypeptides. *Nat. Protoc.* **2**, 161–167 (2007).
18. Böckmann, M., Doltsinis, N. L. & Marx, D. Azobenzene photoswitches in bulk materials. *Phys. Rev. E - Stat. Nonlinear, Soft Matter Phys.* **78**, 1–4 (2008).

19. Mahimwalla, Z. *et al.* Azobenzene photomechanics: Prospects and potential applications. *Polymer Bulletin* **69**, (2012).
20. Park, J., Sun, L. B., Chen, Y. P., Perry, Z. & Zhou, H. C. Azobenzene-functionalized metal-organic polyhedra for the optically responsive capture and release of guest molecules. *Angew. Chemie - Int. Ed.* **53**, 5842–5846 (2014).
21. Abellán, G. *et al.* Photo-switching in a hybrid material made of magnetic layered double hydroxides intercalated with azobenzene molecules. *Adv. Mater.* **26**, 4156–4162 (2014).
22. Song, H., Jing, C., Ma, W., Xie, T. & Long, Y.-T. Reversible photoisomerization of azobenzene molecules on a single gold nanoparticle surface. *Chem. Commun.* **52**, 2984–2987 (2016).
23. Lukyanov, B. S. & Lukyanova, M. B. Spiroyrans: Synthesis, Properties, and Application. (Review). *Chem. Heterocycl. Compd.* **41**, 281–311 (2005).
24. Yokoyama, Y. Fulgides for Memories and Switches. *Chem. Rev.* **100**, 1717–1740 (2000).
25. Irie, M. Diarylethenes for Memories and Switches. *Chemical Reviews* **100**, (2000).
26. Maafi, M. Useful spectrokinetic methods for the investigation of photochromic and thermo-photochromic spiropyrans. *Molecules* **13**, 2260–2302 (2008).
27. Natali, M. & Giordani, S. Molecular switches as photocontrollable ‘smart’ receptors. *Chem. Soc. Rev.* **41**, 4010 (2012).
28. Darwish, N., Aragonés, A. C., Darwish, T., Ciampi, S. & Díez-Pérez, I. Multi-responsive photo- and chemo-electrical single-molecule switches. *Nano Lett.* **14**, 7064–7070 (2014).
29. Rath, S., Heilig, M., Port, H. & Wrachtrup, J. Periodic organic nanodot patterns for optical memory. *Nano Lett.* **7**, 3845–3848 (2007).
30. Tomasello, G., Bearpark, M. J., Robb, M. A., Orlandi, G. & Garavelli, M. Significance of a zwitterionic state for fulgide photochromism: Implications for the design of mimics. *Angew. Chemie - Int. Ed.* **49**, 2913–2916 (2010).
31. Lucas, L. N., Jong, J. J., Esch, J. H., Kellogg, R. M. & Feringa, B. L. Syntheses of Dithienylcyclopentene Optical Molecular Switches. *Eur. J. Org. Chem.* **2003**, 155–166 (2003).
32. Peters, A. & Branda, N. R. Limited photochromism in covalently linked double 1,2-dithienylethenes. *Adv. Mater. Opt. Electron.* **10**, 245–249 (2000).
33. Uchida, K., Tsuchida, E., Aoi, Y., Nakamura, S. & Irie, M. Substitution Effect on the Coloration Quantum Yield of a Photochromic Bisbenzothienylethene. *Chem. Lett.* 63–64 (1999).

34. Uchida, K. *et al.* Thermally Reversible Photochromic Systems. Photochromism of a Dipyrrolylperfluorocyclopentene. *Chem. Lett.* 835–836 (1999).
35. Mausella, B. M. J., Fu, D. & Swager, T. M. *Advanced materials.* 145–147 (1995).
36. Irie, M., Miyatake, O., Uchida, K. & Eriguchi, T. Photochromic Diarylethenes with Intralocking Arms. *J. Am. Chem. Soc.* **116**, 9894–9900 (1994).
37. Irie, M., Miyatake, O. & Uchida, K. Blocked photochromism of diarylethenes. *J. Am. Chem. Soc.* **114**, 8715–8716 (1992).
38. Kawai, S. H., Gilat, S. L. & Lehn, J.-M. A dual-mode optical-electrical molecular switching device. *J. Chem. Soc. Chem. Commun.* 1011–1013 (1994).
39. Kawai, S. H., Gilat, S. L., Ponsinet, R. & Lehn, J.-M. A Dual-Mode Molecular Switching Device: Bisphenolic Diarylethenes with Integrated Photochromic and Electrochromic Properties. *Chem. - A Eur. J.* **1**, 285–293 (1995).
40. Tsivgoulis, G. M. & Lehn, J. M. Photoswitched and functionalized oligothiophenes: Synthesis and photochemical and electrochemical properties. *Chem. - A Eur. J.* **2**, 1399–1406 (1996).
41. Kobatake, S. & Irie, M. Single-Crystalline Photochromism of Diarylethenes. in *Bulletin of the Chemical Society of Japan* **77**, 195–210 (2004).
42. Morimoto, M., Kobatake, S. & Irie, M. Crystal engineering of photochromic diarylethene single crystals. *Chem. Rec.* **4**, 23–38 (2004).
43. Irie, M. Photochromism of diarylethene single molecules and single crystals. *Photochem. Photobiol. Sci.* **9**, 1535–42 (2010).
44. Morimoto, M. & Irie, M. A diarylethene cocrystal that converts light into mechanical work. *J. Am. Chem. Soc.* **132**, 14172–14178 (2010).
45. Terao, F., Morimoto, M. & Irie, M. Light-driven molecular-crystal actuators: Rapid and reversible bending of rodlike mixed crystals of diarylethene derivatives. *Angew. Chemie - Int. Ed.* **51**, 901–904 (2012).
46. Sandler, T. *et al.* Light-Induced Switching of Tunable Single-Molecule Junctions. *Adv. Sci.* (2015).
47. Kim, Y. *et al.* Charge transport characteristics of diarylethene photoswitching single-molecule junctions. *Nano Lett.* **12**, 3736–3742 (2012).
48. Han, M. *et al.* Light-triggered guest uptake and release by a photochromic coordination cage. *Angew. Chemie - Int. Ed.* **52**, 1319–1323 (2013).
49. Szymanski, W., Beierle, J. M., Kistemaker, H. A. V., Velema, W. A. & Feringa, B. L. Reversible photocontrol of biological systems by the incorporation of molecular photoswitches. *Chemical Reviews* **113**, 6114–6178 (2013).
50. Luo, F. *et al.* Photoswitching CO₂ Capture and Release in a Photochromic Diarylethene Metal-Organic Framework. *Angew. Chem. Int. Ed. Engl.* 9298–9301 (2014).

51. Van Herpt, J. T., Areephong, J., Stuart, M. C. A., Browne, W. R. & Feringa, B. L. Light-controlled formation of vesicles and supramolecular organogels by a cholesterol-bearing amphiphilic molecular switch. *Chem. - A Eur. J.* **20**, 1737–1742 (2014).
52. Zhang, J., Wang, J. & Tian, H. Taking orders from light: progress in photochromic bio-materials. *Mater. Horizons* **1**, 169 (2014).
53. Presa, A. *et al.* Photoswitching the Cytotoxic Properties of Platinum(II) Compounds. *Angew. Chemie Int. Ed.* **54**, 1–6 (2015).
54. Okuda, J. *et al.* Photoinduced cytotoxicity of a photochromic diarylethene via caspase cascade activation. *Chem. Commun.* **51**, 10957–10960 (2015).
55. Kahn, O. *Molecular Magnetism*. (VCH Publishers, 1993).
56. J.Ribas. *Coordination Chemistry, Wiley VCH*. (2008).
57. Carlin, Richard L, Duyneveldt, H. van. *Magnetochemistry*. (1986).
58. Van Vleck, J. The theory of electric and magnetic susceptibilities. *Oxford Univ. Press* 384 pp (1965).
59. Luis, F., Roubeau, O. & Aromí, G. *Architecture and Design of Molecule Logic Gates and Atom Circuits*. (Springer Berlin Heidelberg, 2013).
60. Feynman, R. P. Quantum mechanical computers. *Found. Phys.* **16**, 507–531 (1986).
61. Ladd, T. D. *et al.* Quantum computers. *Nature* **464**, 45–53 (2010).
62. Nielson, M. A., Chuang, I. L., Nielsen, M. A. & Chuang, I. L. Quantum computation and quantum information. 700 (2010).
63. Aromí, G., Aguilà, D., Gamez, P., Luis, F. & Roubeau, O. Design of magnetic coordination complexes for quantum computing. *Chem. Soc. Rev.* **41**, 537 (2012).
64. Meier, F., Levy, J. & Loss, D. 208 Quantum computing with spin cluster qubits. *Phys. Rev. Lett.* **90**, 047901 (2003).
65. Spiller, J. T. and E. M. C. and E. del B. and J. M. H. and T. P. Magnetic qubits as hardware for quantum computers. *Nanotechnology* **12**, 181 (2001).
66. Leuenberger, M. N. & Loss, D. Quantum computing in molecular magnets. *Nature* **410**, 789–793 (2001).
67. Affronte, M., Carretta, S., Timco, G. a & Winpenny, R. E. P. A ring cycle: studies of heterometallic wheels. *Chem. Commun. (Camb)*. 1789–1797 (2007).
68. Luis, F. *et al.* Molecular prototypes for spin-based CNOT and SWAP quantum gates. *Phys. Rev. Lett.* **107**, 1–4 (2011).

69. Aguilà, D. *et al.* Heterodimetallic [LnLn'] Lanthanide Complexes : Towards a Chemical Design of 2-Qubit Molecular Spin Quantum Gates Heterodimetallic [LnLn'] Lanthanide Complexes : Towards a Chemical Design of 2-Qubit Molecular Spin Quantum Gates. (2014).
70. Whitehead, G. F. S. *et al.* The acid test: the chemistry of carboxylic acid functionalised {Cr7Ni} rings. *Chem. Sci.* **5**, 235 (2014).
71. Timco, G. a, Faust, T. B., Tuna, F. & Winpenny, R. E. P. Linking heterometallic rings for quantum information processing and amusement. *Chem. Soc. Rev.* **40**, 3067–3075 (2011).
72. Candini, A. *et al.* Entanglement in supramolecular spin systems of two weakly coupled antiferromagnetic rings (purple-Cr7Ni). *Phys. Rev. Lett.* **104**, 1–4 (2010).
73. Whitehead, G. F. S. *et al.* A ring of rings and other multicomponent assemblies of cages. *Angew. Chemie - Int. Ed.* **52**, 9932–9935 (2013).
74. Schlegel, C., Van Slageren, J., Timco, G., Winpenny, R. E. P. & Dressel, M. Origin of superhyperfine interactions in the antiferromagnetic ring Cr 7Ni. *Phys. Rev. B - Condens. Matter Mater. Phys.* **83**, 5–7 (2011).
75. Caneschi, A. *et al.* Alternating current susceptibility, high field magnetization, and millimeter band EPR evidence for a ground $S = 10$ state in $[\text{Mn}_{12}\text{O}_{12}(\text{CH}_3\text{COO})_{16}(\text{H}_2\text{O})_4] \cdot 2\text{CH}_3\text{COOH} \cdot 4\text{H}_2\text{O}$. *J. Am. Chem. Soc.* **113**, 5873–5874 (1991).
76. Craig, G. A. & Murrie, M. 3D Single-Ion Magnets. *Chem. Soc. Rev.* **44**, 2135–2147 (2015).
77. Thomas, L. *et al.* Macroscopic quantum tunnelling of magnetization in a single crystal of nanomagnets. *Nature* **383**, 145–147 (1996).
78. Lis, T. Preparation, structure, and magnetic properties of a dodecanuclear mixed-valence manganese carboxylate. *Acta Crystallogr. Sect. B* **36**, 2042–2046 (1980).
79. Bogani, L. & Wernsdorfer, W. Molecular spintronics using single-molecule magnets. *Nat. Mater.* **7**, 179–186 (2008).
80. Moro, F. *et al.* Coherent electron spin manipulation in a dilute oriented ensemble of molecular nanomagnets: pulsed EPR on doped single crystals. *Chem. Commun.* **50**, 91–93 (2014).
81. Thiele, S. *et al.* Electrical readout of individual nuclear spin trajectories in a single-molecule magnet spin transistor. *Phys. Rev. Lett.* **111**, 1–5 (2013).
82. Thiele, S. *et al.* Electrically Driven Nuclear Spin Resonance in Single-Molecule Magnets. *Science (80)*. **344**, 1135–1138 (2014).
83. Létard, J.-F., Guionneau, P. & Goux-Capes, L. in 221–249 (Springer Berlin Heidelberg, 2004).
84. Kahn, O. & Martinez, C. J. Spin-Transition Polymers: From Molecular Materials Toward Memory Devices. *Science (80)*. **279**, 44–48 (1998).

85. Kahn, O., Kröber, J. & Jay, C. Spin Transition Molecular Materials for displays and data recording. *Adv. Mater.* **4**, 718–728 (1992).
86. Gütlich, P.; Hauser, A.; Spiering, H. Thermal and Optical Switching of Iron (II) complexes. *Angew. Chem. Int. Ed. Engl.* **33**, 2024–2054 (1994).
87. Murray, K. S. Advances in polynuclear iron(II), iron(III) and cobalt(II) spin-crossover compounds. *Eur. J. Inorg. Chem.* 3101–3121 (2008).
88. Griffin, M. *et al.* A symmetry-breaking spin-state transition in iron(III). *Angew. Chemie - Int. Ed.* **50**, 896–900 (2011).
89. Harding, D. J., Harding, P. & Phonsri, W. Spin Crossover in Iron(III) Complexes. *Coord. Chem. Rev.* **313**, 38–61 (2016).
90. Tang, J. *et al.* Two-step spin-transition iron(III) compound with a wide [high spin-low spin] plateau. *Inorg. Chem.* **48**, 2128–2135 (2009).
91. Zhang, X. *et al.* A cobalt(II) spin-crossover compound with partially charged TCNQ radicals and an anomalous conducting behavior. *Chem. Sci.* **7**, 1569–1574 (2015).
92. Bhar, K. *et al.* Crystallographic evidence for reversible symmetry breaking in a spin-crossover d⁷ cobalt(II) coordination polymer. *Angew. Chemie - Int. Ed.* **51**, 2142–2145 (2012).
93. Pandurangan, K. *et al.* Lattice effects on the spin-crossover profile of a mononuclear manganese(III) cation. *Chem. - A Eur. J.* **18**, 2021–2029 (2012).
94. Martinho, P. N. *et al.* Cooperative spin transition in a mononuclear manganese(III) complex. *Angew. Chemie - Int. Ed.* **51**, 12597–12601 (2012).
95. Shepherd, H. J. *et al.* High-pressure spin-crossover in a dinuclear Fe(ii) complex. *Phys. Chem. Chem. Phys.* **14**, 5265 (2012).
96. Bousseksou, A., Varret, F., Goiran, M., Boukheddaden, K. & Tuchagues, J. P. in 65–84 (Springer Berlin Heidelberg, 2004).
97. Carbonera, C. *et al.* Photomagnetic properties of iron(II) spin crossover complexes of 2,6-dipyrazolylpyridine and 2,6-dipyrazolylpyrazine ligands. *Dalt. Trans.* 3058–3066 (2006).
98. Shih, C.-H. *et al.* The photo-induced commensurate modulated structure in site-selective spin crossover complex trans-[Fe(abpt)₂(NCS)₂]. *Dalton Trans.* **39**, 9794–9800 (2010).
99. Létard, J. F. *et al.* Photomagnetism of a sym-cis-dithiocyanato iron(II) complex with a tetradentate N,N'-bis(2-pyridylmethyl)1,2-ethanediamine ligand. *Chem. - A Eur. J.* **18**, 5924–5934 (2012).
100. Costa, J. S. *et al.* Three-way crystal-to-crystal reversible transformation and controlled spin switching by a nonporous molecular material. *J. Am. Chem. Soc.* **136**, 3869–3874 (2014).

101. Bao, X. *et al.* The effect of an active guest on the spin crossover phenomenon. *Angew. Chemie - Int. Ed.* **52**, 1198–1202 (2013).
102. Bartual-Murgui, C. *et al.* Synergetic effect of host-guest chemistry and spin crossover in 3D hofmann-like metal-organic frameworks [Fe(bpac)M(CN)₄] (M=Pt, Pd, Ni). *Chem. - A Eur. J.* **18**, 507–516 (2012).
103. Hauser, A. Ligand Field Theoretical Considerations. *Top. Curr. Chem* **51**, 49–58 (2004).
104. Gamez, P., Costa, J. S., Quesada, M. & Aromi, G. Iron Spin-Crossover compounds: from fundamental studies to practical applications. *Dalt. Trans.* 7845–7853 (2009).
105. Wang, C. F. *et al.* Synergetic spin crossover and fluorescence in one-dimensional hybrid complexes. *Angew. Chemie - Int. Ed.* **54**, 1574–1577 (2015).
106. Lochenie, C., Wagner, K. G., Karg, M. & Weber, B. Modulation of the ligand-based fluorescence of 3d metal complexes upon spin state change. *J. Mater. Chem. C* **3**, 7925–7935 (2015).
107. Quintero, C. M. *et al.* Hybrid spin-crossover nanostructures. *Beilstein J. Nanotechnol.* **5**, 2230–2239 (2014).
108. Nagy, V. *et al.* Cellulose fiber nanocomposites displaying spin-crossover properties. *Colloids Surfaces A Physicochem. Eng. Asp.* **456**, 35–40 (2014).
109. Quintero, C. M. *et al.* Soft lithographic patterning of spin crossover complexes. Part 1: fluorescent detection of the spin transition in single nano-objects. *J. Mater. Chem.* **22**, 3745 (2012).
110. Bousseksou, A., Molnár, G., Salmon, L. & Nicolazzi, W. Molecular spin crossover phenomenon: recent achievements and prospects. *Chem. Soc. Rev.* **40**, 3313–3335 (2011).
111. Koo, Y. S. & Galán-Mascarós, J. R. Spin crossover probes confer multistability to organic conducting polymers. *Adv. Mater.* **26**, 6785–6789 (2014).
112. Salmon, L. *et al.* A novel approach for fluorescent thermometry and thermal imaging purposes using spin crossover nanoparticles. *J. Mater. Chem.* **20**, 5499 (2010).
113. Takayama, K., Matsuda, K. & Irie, M. Photoswitching of the Magnetic Interaction between a Copper(II) Ion and a Nitroxide Radical by Using a Photochromic Spin Coupler. *Chem. - A Eur. J.* **9**, 5605–5609 (2003).
114. Matsuda, K., Takayama, K. & Irie, M. Photochromism of metal complexes composed of diarylethene ligands and Zn (II), Mn (II), and Cu (II) hexafluoroacetylacetonates. *Inorg. Chem.* **43**, 482–489 (2004).

115. Morimoto, M., Miyasaka, H., Yamashita, M. & Irie, M. Coordination assemblies of [Mn₄] single-molecule magnets linked by photochromic ligands: Photochemical control of the magnetic properties. *J. Am. Chem. Soc.* (2009).
116. Shiga, T., Miyasaka, H., Yamashita, M., Morimoto, M. & Irie, M. Copper(II)-terbium(III) single-molecule magnets linked by photochromic ligands. *Dalton Trans.* (2011).
117. Pinkowicz, D. *et al.* Control of the Single-Molecule Magnet Behavior of Lanthanide-Diarylethene Photochromic Assemblies by Irradiation with Light. *Chem. - A Eur. J.* **20**, 12502–12513 (2014).
118. Cosquer, G. *et al.* Photo-control of the magnetic properties of Dy(III) and Ho(III) homometal coordination polymers bridged by a diarylethene ligand. *Dalt. Trans.* **44**, 5996–6002 (2015).
119. Sénéchal-David, K. *et al.* Combining organic photochromism with inorganic paramagnetism--optical tuning of the iron(II) electronic structure. *Dalton Trans.* 1932–1936 (2008).
120. Nihei, M., Suzuki, Y., Kimura, N., Kera, Y. & Oshio, H. Bidirectional photomagnetic conversions in a spin-crossover complex with a diarylethene moiety. *Chem. - A Eur. J.* **19**, 6946–6949 (2013).
121. Milek, M., Heinemann, F. W. & Khusniyarov, M. M. Spin crossover meets diarylethenes: Efficient photoswitching of magnetic properties in solution at room temperature. *Inorg. Chem.* **52**, 11585–11592 (2013).
122. Rösner, B. *et al.* Reversible Photoswitching of a Spin-Crossover Molecular Complex in the Solid State at Room Temperature. *Angew. Chemie - Int. Ed.* **54**, 12976–12980 (2015).
123. Prasad, T. K. *et al.* Magnetic and optical bistability in tetrairon(III) single molecule magnets functionalized with azobenzene groups. *Dalt. Trans.* **41**, 8368 (2012).
124. Venkataramani, S. Magnetic Bistability of Molecules. *Science (80)*. **445**, 445–449 (2011).

CHAPTER 2: STRUCTURE AND INTERMOLECULAR INTERACTIONS VS PHOTOCROMISM

2.1. Introduction	49
2.2. Synthesis and characterization	51
2.2.1. Synthesis of 1,2-(5-carboxy-2-methyl-thiophen-3-yl)-cyclopentene (H ₂ L1).....	51
2.2.2 Synthesis and description of [Cu(L)(py) ₃] (1).....	52
2.3. Photoswitching Properties.....	58
2.3.1. Reflectivity Measurements.....	58
2.3.2. Raman spectroscopy.....	66
2.4. Bulk magnetic measurements.....	68
2.5. Copper compounds using blocking ligands.....	70
2.5.1 Synthesis and crystal structure of [Cu ₂ (L1)(Phen) ₄](NO ₃) ₂ ·nMeOH (2)	71
2.5.2 Synthesis and crystal structure of [Cu ₇ (L1) ₄ (Phen) ₇](NO ₃) ₆ ·nMeOH (3)	73
2.5.3 Synthesis and crystal structure of [Cu ₂ (L1)(ByPy) ₄](NO ₃) ₂ ·nMeOH (4)	76
2.6. Photochromic activity	79
2.7 Conclusions	81
2.8 Experimental	82
2.8.1. Ligands and precursors.....	82
2.8.2. Coordination complexes.....	83
2.9. References	85

2.1 Introduction

As shown in Chapter 1, diarylethene-based systems are very promising compounds because of their excellent switching properties¹⁻¹⁴, even in the solid state.¹⁵⁻¹⁸ Unlike in solution, molecules within a lattice are interconnected and kept in fixed positions, therefore, their photoconverting properties could be easily influenced by small changes to the intermolecular interactions or to the crystal packing^{19,20}. In this respect, one of the compulsory conditions for the formation of the C–C bond during the ring closure (in the solid state) is that the aryl rings must be in the antiparallel conformation, just to avoid the steric hindrance between their methyl groups upon in this process¹⁵.

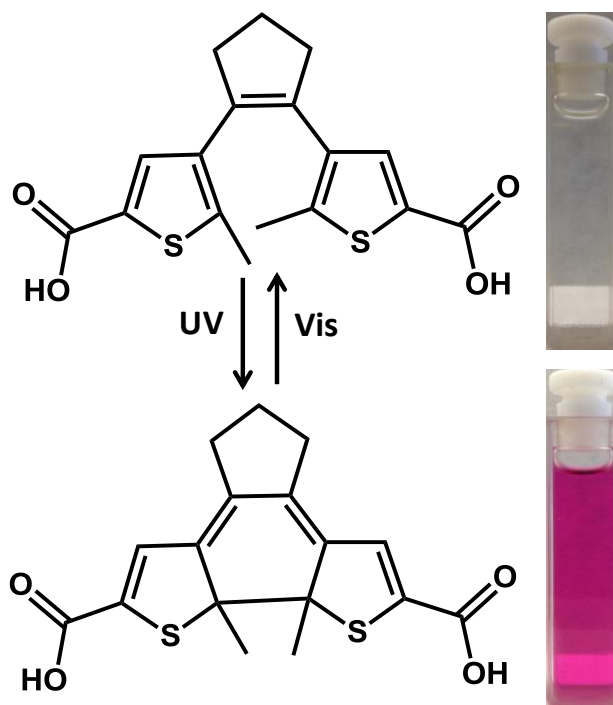
Regarding metal complexes based on diarylethene ligands, most of the work has been devoted to organometallic multifunctional compounds combining the photo and electrochromic properties²¹⁻²³ while little attention has been paid to photo-crystal engineering of coordination systems, in other words to study the crystal packing requirements to perform the photoisomerization in the solid state have been scarcely studied. In this line, some studies report on the photochromism of metal complexes in the crystalline phase^{11,24-31} but no examples are found assessing differences in photoactivity behaviour between two polymorphic compounds.

Despite the abundant research on diarylethene derivatives, it is indeed mainly devoted to the diarylperfluoropentene entity. The synthesis of these compounds is neither trivial nor easy to scale up since the octafluorocyclopentene reagent used is very volatile and expensive while the yields are very low. To solve these problems, Feringa *et al.* reported a new synthetic pathway where a perhydro-cyclopentene unit was used instead of the perfluoro analogue³². Interestingly, although this procedure is cheaper and allows large scale reactions, only few coordination complexes based on these derivatives can be found in the literature^{3,33-36}.

In this chapter we present first two solvatomorphs of a Cu(II) coordination polymer [Cu(L1)(py)₃] (**1**), where **H₂L1** is the fluorine-free photochromic ligand **1,2-(5-carboxy-2-methyl-thiophen-3-yl)-cyclopentene** (Scheme 2.1). Both compounds feature polymeric chains but the crystal packing of these chains is

quite disparate due to the presence of dissimilar guest molecules. As a consequence, although both solvatomorphs are photoactive, the kinetics of the process is drastically different. The reversible photoconversion in the crystalline phase for both complexes has been characterized by means of reflectivity and Raman spectroscopy techniques due to the insolubility of these polymers.

Also a strategy to stop the growth of these polymers has been implemented in order to prepare discrete molecules. It consists in using other chelating ligands to block the coordination positions of the copper ions and it has led to three new coordination compounds. The distinct behaviour of the polymers and the isolated compounds is rationalized in light of the structural information.



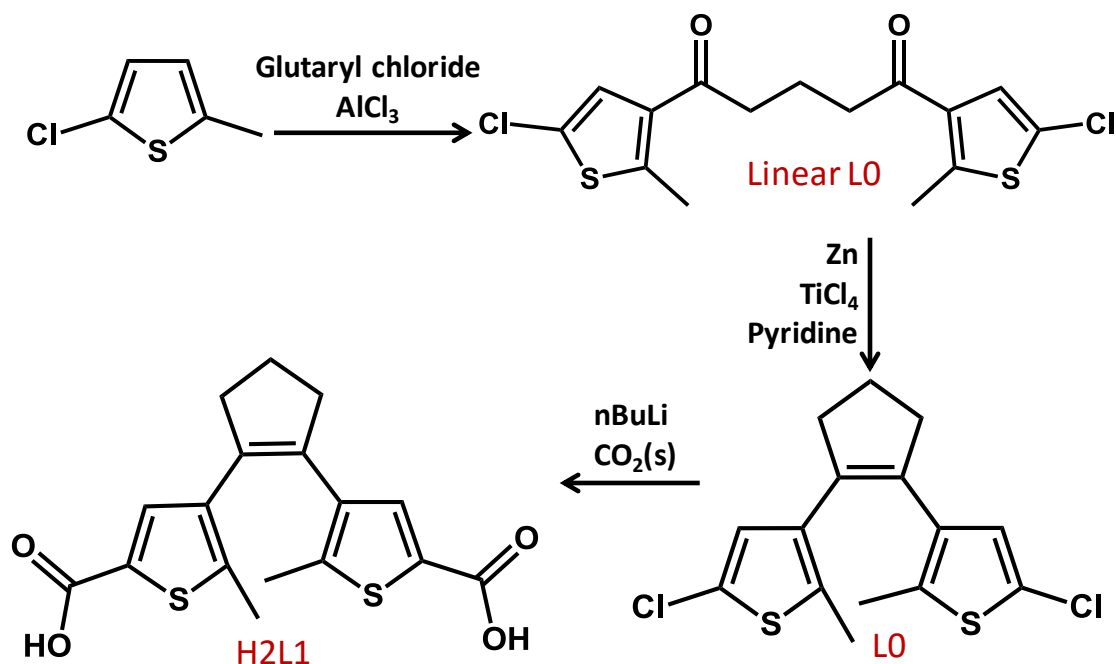
Scheme 2.1: Reversible photocyclization of H_2L1 with its characteristic change of color.

2.2 Synthesis and characterization

2.2.1 Synthesis of 1,2-(5-carboxy-2-methyl-thiophen-3-yl)-cyclopentene (H_2L1)

The ligand H_2L1 was synthesized according to an earlier reported procedure with some modifications^{32,37–39}.

The preparation of the **1,2-bis(5-chloro-2-methyl-3-thienyl)cyclopentene (L0)**, starts from 2-chloro-5-methyl-thiophene which was treated with 0.5 equivalent of glutaryl chloride and 1.2 equivalents of $AlCl_3$ in a Friedel-Crafts acylation reaction to obtain **1,5-bis(5-chloro-2-methylthiophen-3-yl)pentane-1,5-dione (linear L0)** in good yield (69.9%). In the following step, a cyclization reaction of **linear L0** was performed by means of an intramolecular McMurry reaction using Zn as reducing agent, $TiCl_4$ and pyridine, leading after the quenching of the reaction, to light yellow crystals also in good yield (79%). The diacid H_2L1 can be obtained by adding $CO_2(s)$ to a solution of lithiated **L0**. The complete synthesis is presented in Scheme 2.2.



Scheme 2.2: Synthesis of diarylethene based precursor **L0** and H_2L1 .

2.2.2 Synthesis and description of $[\text{Cu}(\text{L})(\text{py})_3]$ (**1**)

Compound **1** was prepared as two solvatomorphs of the same coordination complex, formed as slightly different isomers (see below). The composition of their crystal lattice is $[\text{Cu}(\text{L})(\text{py})_3]\cdot 2\text{py}$ (**1a**) and $[\text{Cu}(\text{L})(\text{py})_3]\cdot 2\text{H}_2\text{O}\cdot 0.5\text{Et}_2\text{O}$ (**1b**), respectively, thus just differing in the nature of the solvent molecules of crystallization.

While both reactions were performed through the exact same procedure and using the same solvents, the only distinction was the initial source of Cu(II) ($\text{Cu}(\text{AcO})_2\cdot\text{H}_2\text{O}$ and $\text{Cu}(\text{NO}_3)_2\cdot 3\text{H}_2\text{O}$ for **1a** and **1b**, respectively). Interestingly however, the varying counter ions are not present in the final products.

Thus, the reaction in pyridine of one equivalent of $\text{Cu}(\text{X})_2\cdot n\text{H}_2\text{O}$ with one equivalent of **H₂L1** and 2.2 equivalents of base leads to blue crystals in the case of **1a** and green crystals for **1b**, after layering both solutions in ether. The asymmetric unit of both compounds is shown in Figure 2.1.

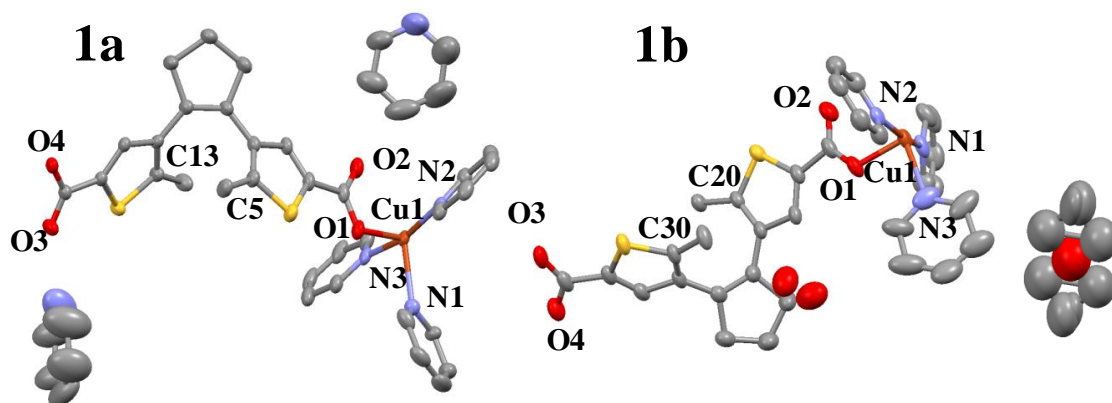


Figure 2.1: ORTEP representations of the asymmetric unit of **1a** and **1b** with heteroatoms labelled (down). Hydrogens atoms have been omitted for clarity.

Therefore, the reasons for a different final composition and solid state arrangement may have to do with the role that AcO^- and NO_3^- play on the equilibria taking place in solution, or with the larger amount of water borne by the nitrate salt. Both procedures were found to be fully reproducible.

Compounds **1a** and **1b** crystallize in the monoclinic space group $P2_1/c$. Table 2.1 compiles the data for both compounds.

Table 2.1. Crystallographic data for compounds 1a and 1b		
	1a	1b
formula	$C_{42}H_{39}CuN_5O_4S_2$	$C_{34}H_{38}CuN_3O_{6.50}S_2$
M_r	805.44	720.33
a [Å]	8.3462(11)	12.2633(3)
b [Å]	17.638(2)	17.5472(4)
c [Å]	26.285(4)	15.7535(4)
$\alpha = \gamma$ [°]	90	90
β [°]	95.725(3)	91.1670(10)
V [Å ³]	3850.2(9)	3389.24(14)
ρ [g cm ⁻³]	1.389	1.412
shape and colour	blue plates	green plates
crystal size [mm ³]	0.35 x 0.21 x 0.08	0.18 x 0.07 x 0.02
μ [mm ⁻¹]	0.725	0.818
reflns	8549	7002
parameters	532	455
restrains	162	66
R_{int}	0.0585	0.0315
R_1 [$I/\sigma(I) > 2$]	0.0556	0.0640
$wR2$ [$I/\sigma(I) > 2$]	0.1643	0.1818
S	1.021	1.001

Their asymmetric unit coincides with their empirical formulae, and the unit cell contains four such units. Both compounds consist of polymeric chains of Cu(II) ions linked by the L^{2-} ligands through their end carboxylate groups acting as monodentate donors (Figure 1 and 2). Thus each metal exhibits two *trans* Cu–O bonds (distances: 1.954 and 1.973 Å, **1a**; 1.950 and 1.954 Å, **1b**). The Cu⋯O distances to the other oxygen atoms of the carboxylate groups diverge more for complex **1a** (2.768 and 3.322 Å) than for **1b** (2.982 and 3.023 Å). Additionally, each metal is coordinated by three solvent pyridine molecules in a *mer* fashion. The Cu(II) ions are thus described as five coordinate (N_3O_2) with slightly distorted square pyramidal geometries. In **1a**, the axial site is occupied by a pyridine molecule that exhibits occupational disorder over two positions (0.73:0.27 ratio). In the isomeric complex **1b** the axial pyridine group is fully ordered. Selected metric parameters are listed in Tables 2.2 and Table 2.3.

Table 2.2. Selected bonds [Å] and angles[°]for **1a**

Cu1-O4	1.954(2)	O4-Cu1-O1	174.59(10)	N2-Cu1-N3	164.06(12)
Cu1-O1	1.973(2)	O4-Cu1-N2	89.73(10)	O4-Cu1-N1	83.6(3)
Cu1-N2	2.016(3)	O1-Cu1-N2	89.75(11)	O1-Cu1-N1	91.3(3)
Cu1-N3	2.021(3)	O4-Cu1-N3	91.73(10)	N2-Cu1-N1	103.9(3)
Cu1-N1	2.356(13)	O1-Cu1-N3	90.25(11)	N3-Cu1-N1	92.1(3)

Table 2.3. Selected bonds [Å] and angles[°]for **1b**

Cu1-O3	1.954(3)	N1-Cu1-N3	99.05(16)	O1-Cu1-N3	86.61(16)
Cu1-O1	1.951(3)	N2-Cu1-N1	161.90(15)	O1-Cu1-O3	178.00(13)
Cu1-N2	2.037(3)	N2-Cu1-N3	98.54(15)	O3-Cu1-N1	92.33(13)
Cu1-N3	2.271(3)	O1-Cu1-N1	86.05(12)	O3-Cu1-N2	91.13(12)
Cu1-N1	2.044(4)	O1-Cu1-N2	90.77(12)	O3-Cu1-N3	92.50(17)

In both compounds, the coordination polyhedron around Cu(II) alternates within the chain between two approximately opposite orientations, the Cu–N_{axial} angle between both orientations being 150.556° and 119.58° for **1a** and **1b**, respectively. The cyclopentene unit of the photochromic spacer alternates as well between two almost opposite orientations. In both cases the chains are not chiral, since both enantiomeric conformers of the ligand L²⁻ are present and alternate within the chains (Figure 2.2).

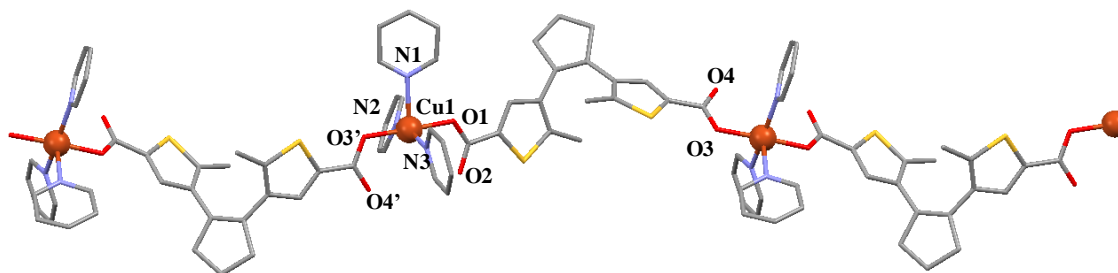


Figure 2.2: Representation of the polymeric chain of **1** with heteroatoms of the asymmetric unit (and some symmetry equivalent) labelled.

The crystal packing of compound **1a** shows a two-dimensional arrangement of the chains linked by π – π stacking interactions between the equatorial pyridine molecules (inter-centroid distance of 3.586 Å; Figure 2.3). Within the sheets, the inter-chain connected Cu centers exhibit the exact same mutual orientation, as do adjacent diarylethene units. The free space available between chains is shaped as infinite channels efficiently occupied by a 1D supramolecular array of pyridine

molecules connected by a combination of π - π stacking and C-H $\cdots\pi$ interactions (Figure 2.4).

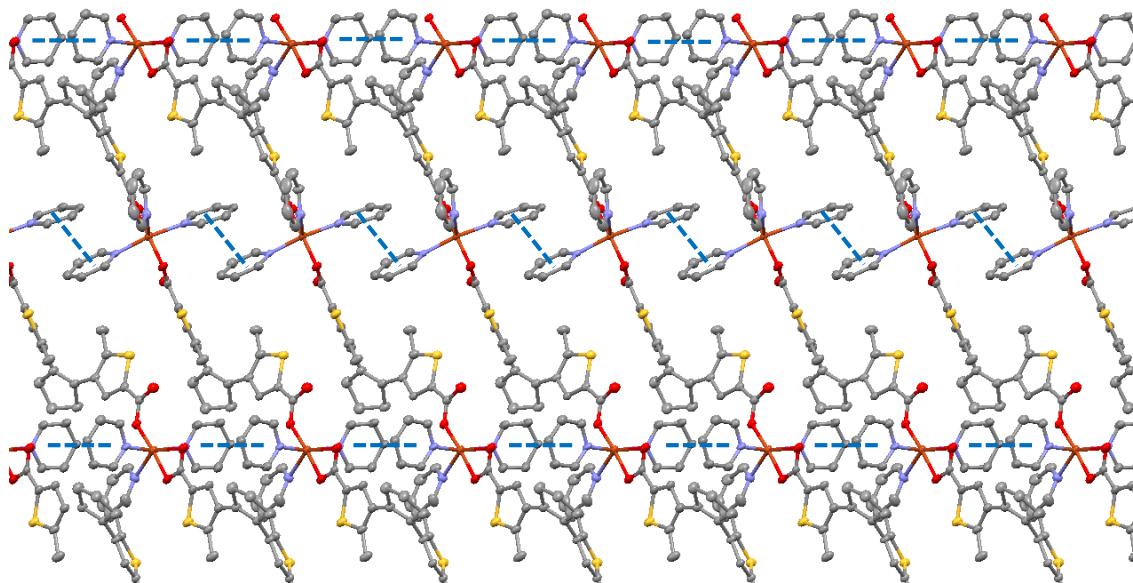


Figure 2.3: Representation of the polymeric chains of **1a** forming sheets *via* π $\cdots\pi$ stacking interactions (shown as blue thick lines joining the centroids) between equatorial pyridine ligands.

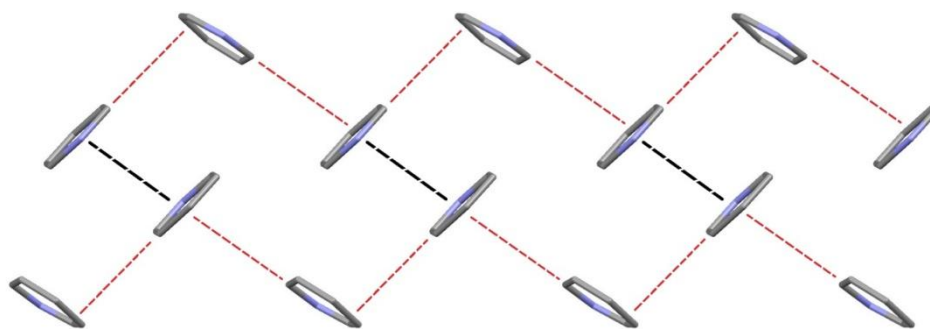


Figure 2.4: Organization of solvate pyridine molecules within the 1D channels of **1a**, interacting *via* π $\cdots\pi$ (black) or C-H $\cdots\pi$ (red) interactions.

In Figure 2.5, a stick representation of several stacks of polymeric chains of **1a** are shown, forming several adjacent sheets and emphasizing the 1D channels parallel to *a* traversing through the middle of the unit cell. The latter are occupied by ordered molecules of pyridine molecules, here in the spacefill style, organized as explained above.

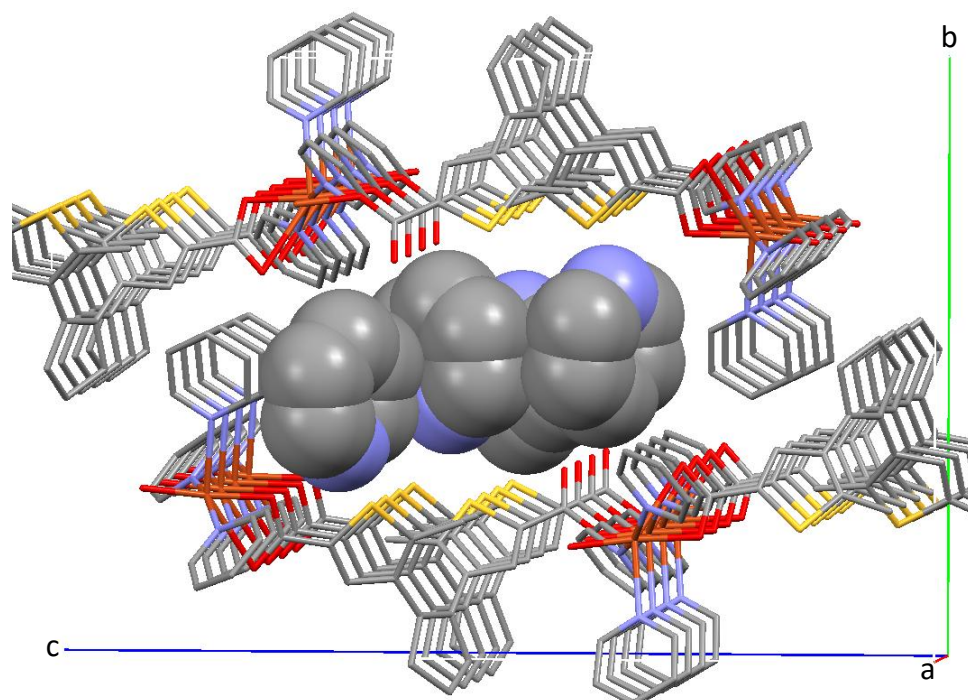


Figure 2.5: Crystal packing of **1a** quasi down the crystallographic a axis.

The chains of **1b** also organize as 2D assemblies through lateral π - π stacking interactions involving equatorial pyridine ligands (inter-centroid distance of 3.663 Å, Figure 2.6). Here however, adjacent Cu(II) ions between chains exhibit opposite orientations, as do adjacent diarylethene units. This arrangement conduces to 2D sheets that are much more corrugated than in **1a** and also prevents the establishment of 1D channels as seen in the other compound. Instead, two types of cavities are formed in between the sheets; *i*) one with a hydrophobic character that contains one half disordered molecule of ether and *ii*) one hydrophilic that sees four non-coordinated carboxylate O-atoms pointing towards its interior forming a total of six hydrogen bonds with four hosted water molecules (Figure 2.7, left).

This network of hydrogen bonds contributes to the cementing of the 2D sheets of **1b** within the tridimensional lattice (Figure 2.7, righth).

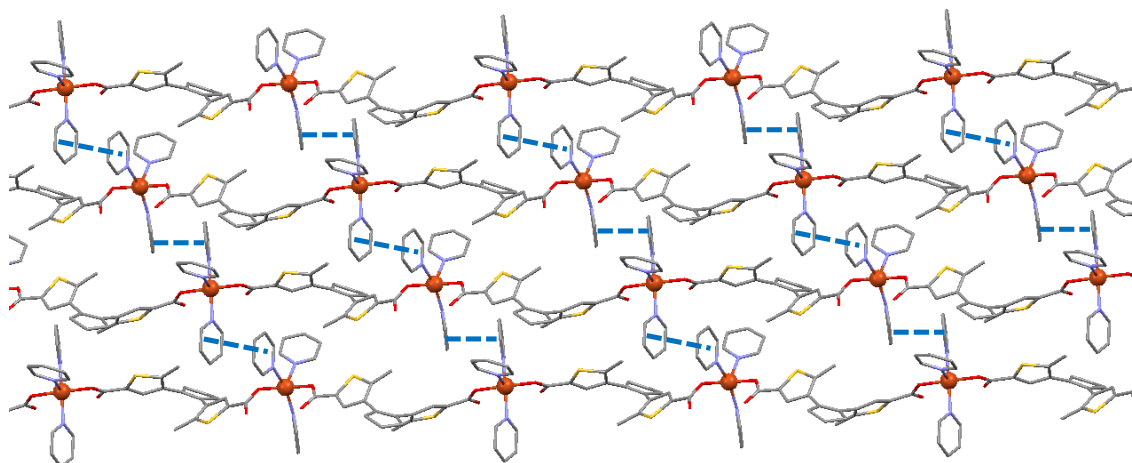


Figure 2.6: Representation of the polymeric chains of **1b** forming sheets *via* $\pi \cdots \pi$ stacking interactions (shown as red thick lines joining the centroids) between equatorial pyridine ligands.

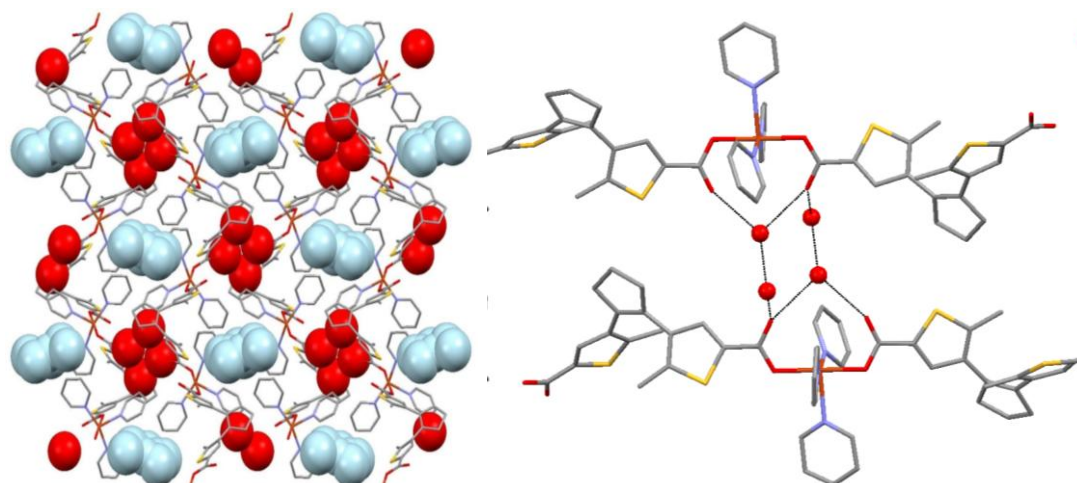
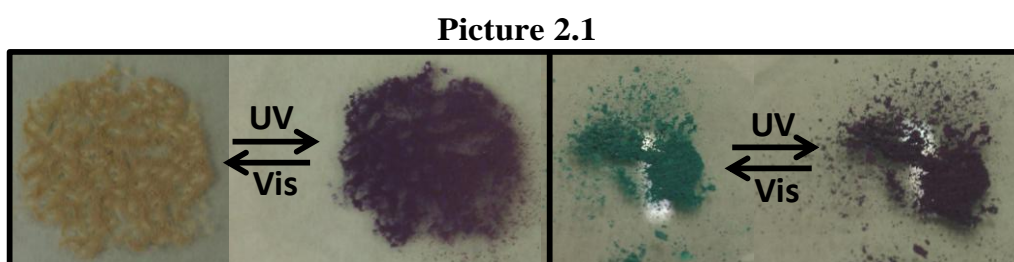


Figure 2.7: (Left) Stick representation of two unit cells of compound **1b** down the *a* axis, showing the hydrophilic and hydrophobic cavities encapsulating respectively, four molecules of water (red) or a disordered half occupied molecule of ether (blue). (Right) Network of hydrogen bonding interactions (black lines) of the hydrophilic cavity.

In both compounds, the thiophenyl rings within the photo switchable unit exhibit an antiparallel arrangement, a necessary condition for the photochromic conversion to proceed. Another important parameter in this respect is the distance between the C-atoms that form a new bond during the cyclisation process, which needs to be shorter than approximately 4 Å⁴⁰. This distance is 3.550 Å and 3.479 Å for **1a** (C5 \cdots C13) and **1b** (C20 \cdots C30), respectively.

2.3 Photoswitching Properties

The photoisomerization properties of compounds **H₂L1**, **1a** and **1b** in the solid state were examined through reflectivity and Raman measurements. Of particular interest was to know whether the differences in the crystallographic arrangements had an effect on the dynamics of the photoactivity. In the Picture 2.1, the color change upon reversible photoisomerization of **H₂L1** (left) and compound **1a** (right) is shown.



2.3.1 Reflectivity Measurements

The photoswitching properties of **H₂L1** were first investigated by optical reflectivity in the solid state. As a preliminary experiment on ligand **H₂L1**, its variable temperature reflectivity was determined (Figure 2.8), which showed almost no spectral variations with temperature. When a powdered sample of **H₂L1** is irradiated continuously with UV light (365 nm) at 290 K, the pale brown solid turns deep violet (Picture 2.1). Then, the thermal variation of the reflectivity properties of the irradiated product was also studied (Figure 2.9), and showed again almost no variation with temperature.

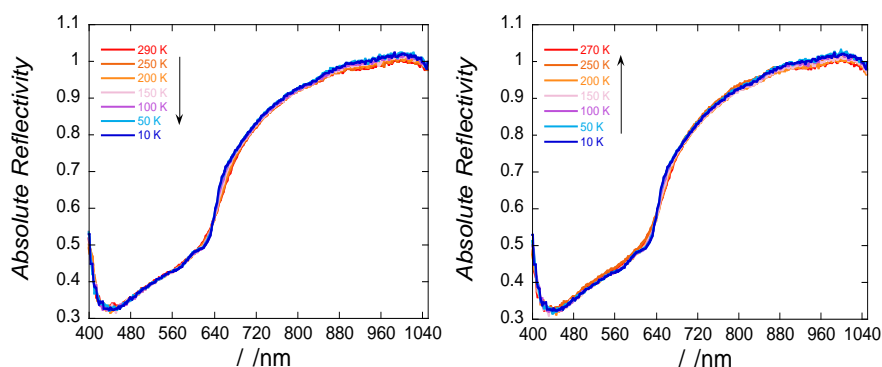


Figure 2.8: Absolute reflectivity of **H₂L1** in its open form at various temperatures, showing its thermal stability from room temperature down to 10 K (left) and then upon warming again to 270 K (right).

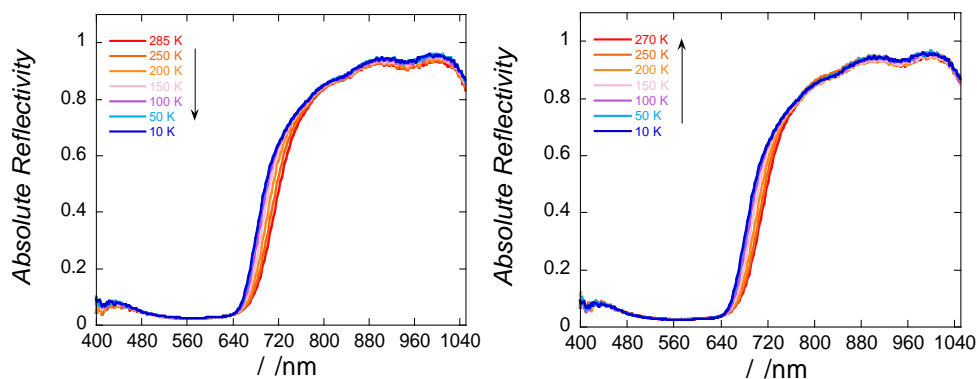


Figure 2.9: Absolute reflectivity of **H₂L1** in its closed form at various temperatures, showing its thermal stability from room temperature down to 10 K (left) and then upon warming again to 270 K (right).

This change of colour can be followed during approximately 2 hours as a clear decrease of the absolute reflectivity, most noticeable in the 500 to 650 nm region (Figure 2.10). After 4.5 hours of irradiation, practically no further evolution had been observed. If the compound is then irradiated with visible light (455 nm), the photoconversion of **H₂L1** is fully reversed, as followed again through absolute reflectivity (Figure 2.11).

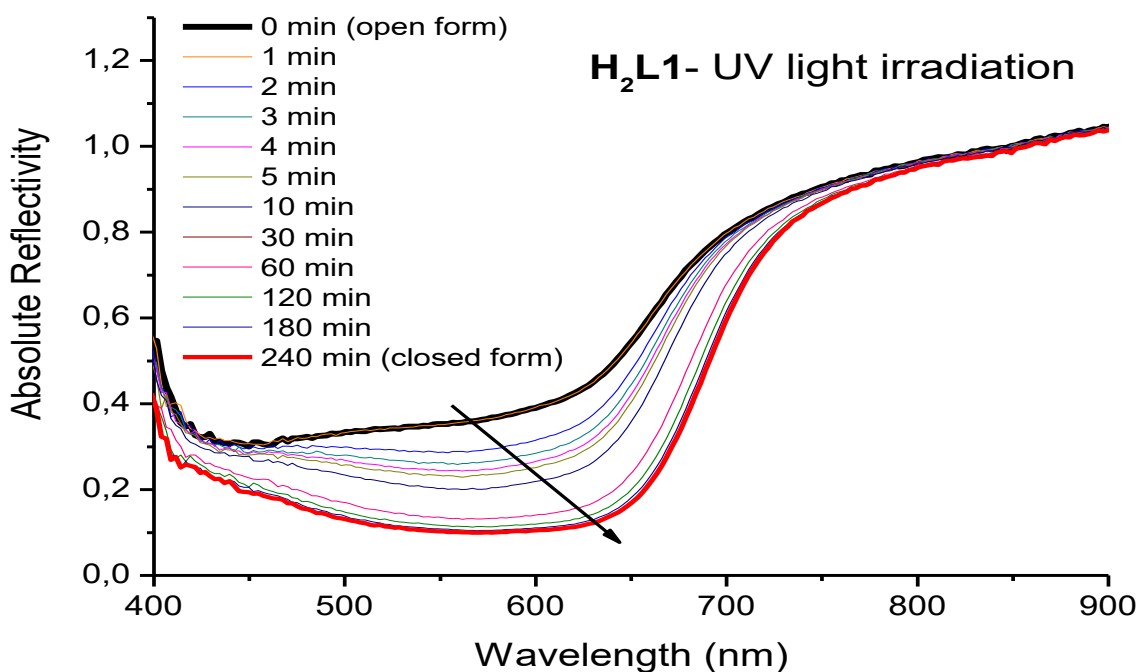


Figure 2.10: Evolution of the behaviour of **H₂L1**, followed by absolute reflectivity measurements, upon continuous laser irradiation of 365 nm.

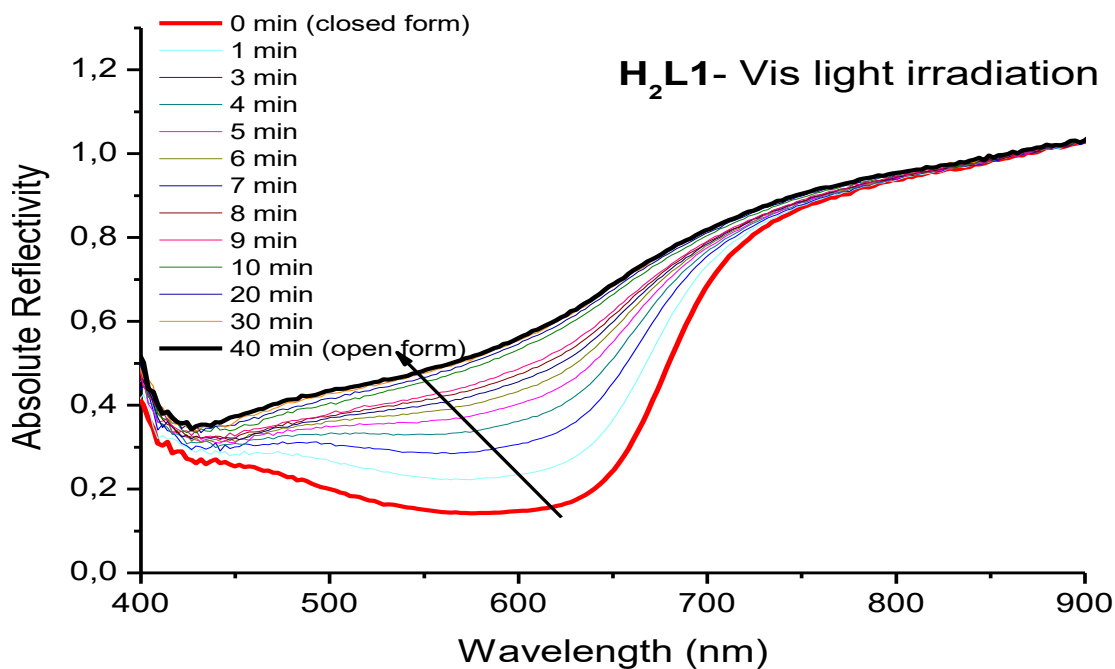


Figure 2.11: Evolution of the behaviour of **H₂L1**, followed by absolute reflectivity measurements, upon continuous laser irradiation of 455 nm

The kinetics and reversibility of both photochromic reactions were studied through the time dependence of the absolute reflectivity at a specific wavelength (selected here at 500 nm), irradiating with light of 365 nm for the direct process and of 405 nm for the reverse isomerization (Figure 2.12). The absolute reflectivity at 500 nm rapidly decreases from 0.40 to 0.06 under 365 nm excitation, while it increases again upon excitation with 455 nm light, to reach in 50 min the value of 0.36.

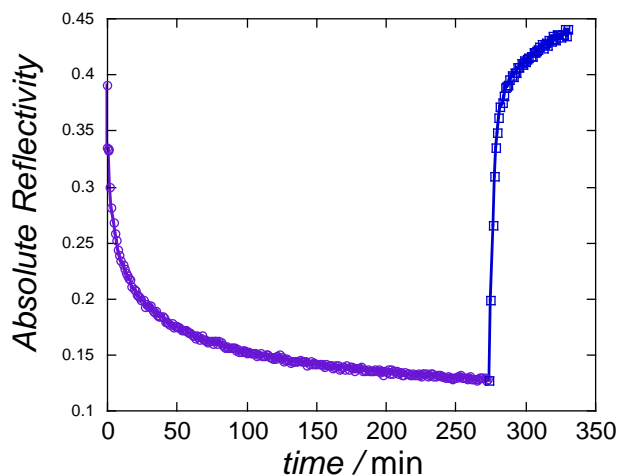


Figure 2.12: Data plotted at 500 nm during the two consecutive irradiations at r.t.

To the best of our knowledge, the optical properties of **H₂L1** in the solid state have not been previously reported. Nevertheless, the noticeable decrease of reflectivity of this compound in the 500-650 nm range is consistent with previously observed changes to its solution absorption spectra upon irradiation with UV light. The latter mainly consist on the development of a broad band centred at 530 nm attributed to $\pi \cdots \pi^*$ transitions of the photochromic products³². Indeed, the solution and solid state spectral behaviour may not change significantly, as could be ascertained on the molecule analogous to **H₂L1**, with a perfluoropentene instead of a pentene unit²⁰.

The same experimental protocol was carried out for compounds **1a** and **1b**. First, reflectivity experiments were performed with white light in order to determine the temperature dependence of the spectra of both complexes. More pronounced changes than observed for **H₂L1** were detected now, especially above 700 nm (**1a**) or near 600 nm (**1b**), reflecting on a larger influence of the near infrared transitions, more enhanced for **1b** (Figures 2.13 and 2.14).

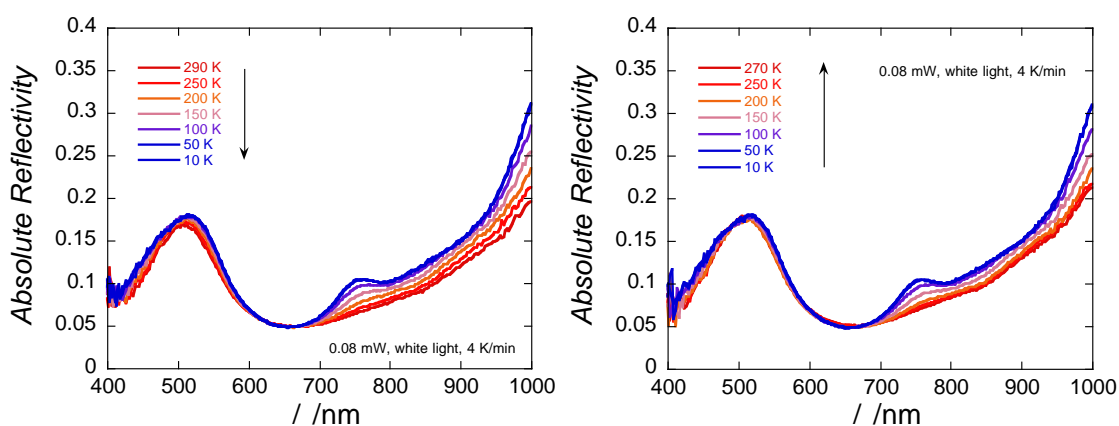


Figure 2.13: Absolute reflectivity of **1a** (open form) in cooling (left) and heating modes (right).

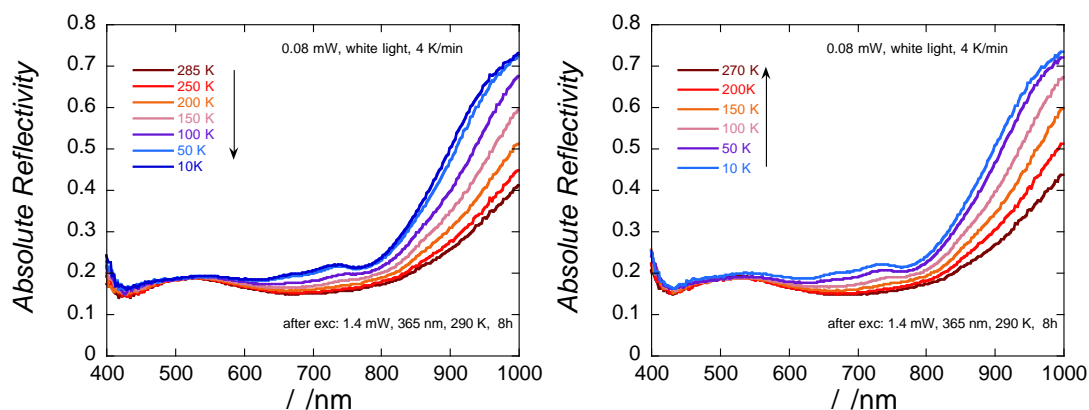


Figure 2.14: Absolute reflectivity of **1b** (open form) in cooling (left) and heating modes (right).

All these thermal changes were fully reversible. For complex **1a**, irradiation with UV light ($\lambda = 365$ nm) causes a decrease of the reflectivity that is most obvious in the approximately 450-600 nm range (Figure 2.15), which may be attributed to the formation of the closed form isomer. A steady state was reached after approximately 90 minutes of irradiation.

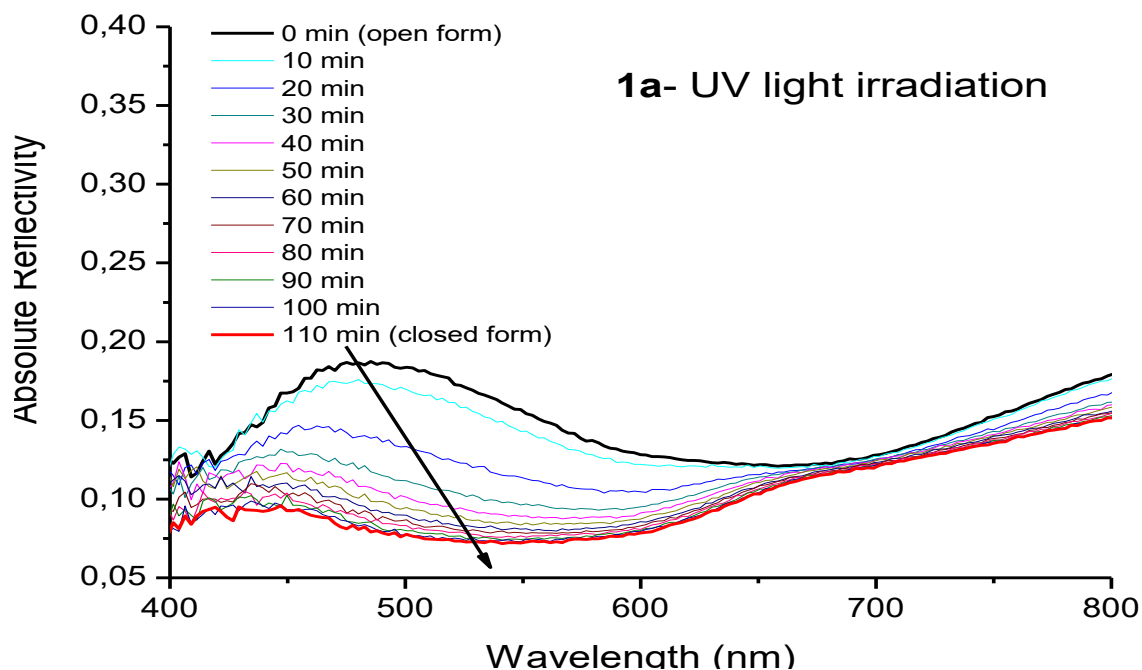


Figure 2.15: Evolution of the behaviour of **1a**, followed by absolute reflectivity measurements, upon continuous laser irradiation of 365 nm.

Subsequently, the photoconversion to the original form was brought about by using green light ($\lambda = 530$ nm). Interestingly, the maximum of the reflectivity

spectra after this process was found to be red shifted from approximately 485 to 509 nm (Figure 2.16). The reversibility of the thermal changes to the reflectivity properties of the closed form, similar to these seen for the open form, was also confirmed (Figure 2.17). It is conceivable that the first isomerization causes changes to the crystal lattice that prevent the restoration of the exact original system. Actually, time dependence studies of the absolute reflectivity during the excitation-de-excitation cycle exhibits only partial reversibility as the initial absolute reflectivity is not fully recovered (Figure 2.18).

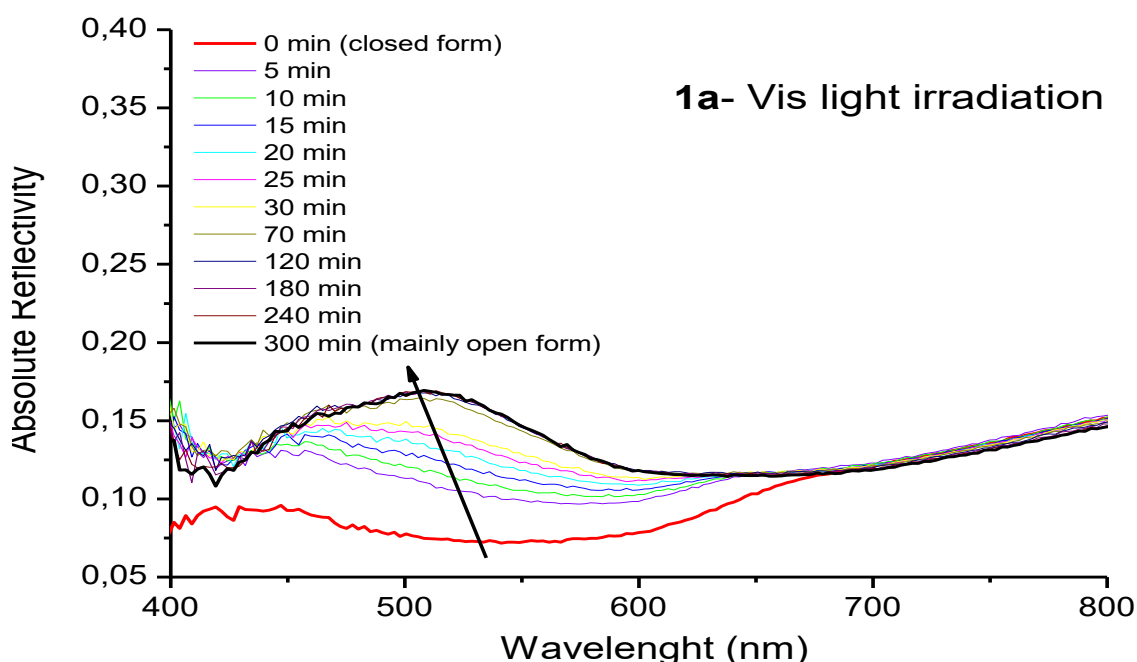


Figure 2.16: Evolution of the behaviour of **1a**, followed by absolute reflectivity measurements, upon continuous laser irradiation of 530 nm.

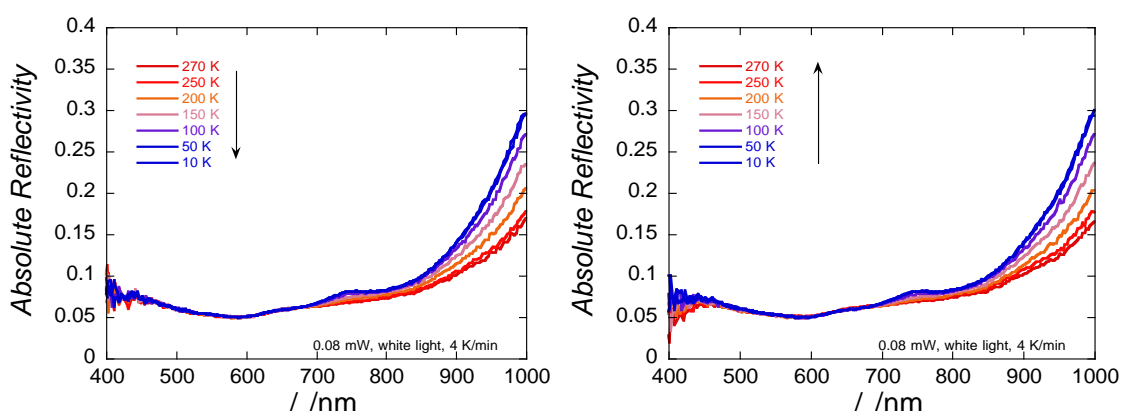


Figure 2.17: Absolute reflectivity of **1a** after photoisomerization with 365-nm (closed form) in cooling (left) and heating modes (right).

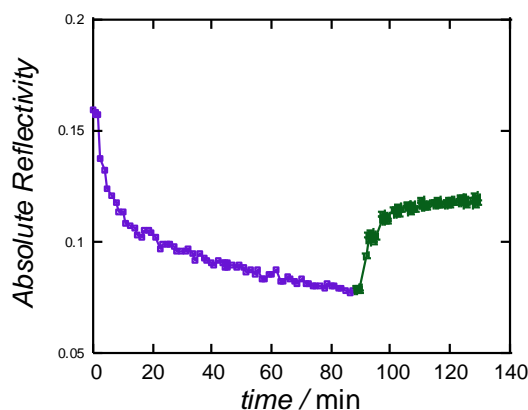


Figure 2.18: Data plotted at 500 nm during the two consecutive irradiations at r.t.

Quite remarkably, complex **1b** shows a totally different behaviour. First, it requires fivefold longer UV irradiation times (approximately eight hours) than **1a** to reach a photostationary state, presumably corresponding to the closed form (Figure 2.19). Secondly, the associated reverse process was not observed (Figure 2.20). Note that several attempts with other wavelengths near the visible light did not lead to (full) reversibility in none of both complexes. In the case of **1b**, the failure to cause any reverse conversion may be attributed to changes to the structure after the closure of the diarylethene, blocking the process.

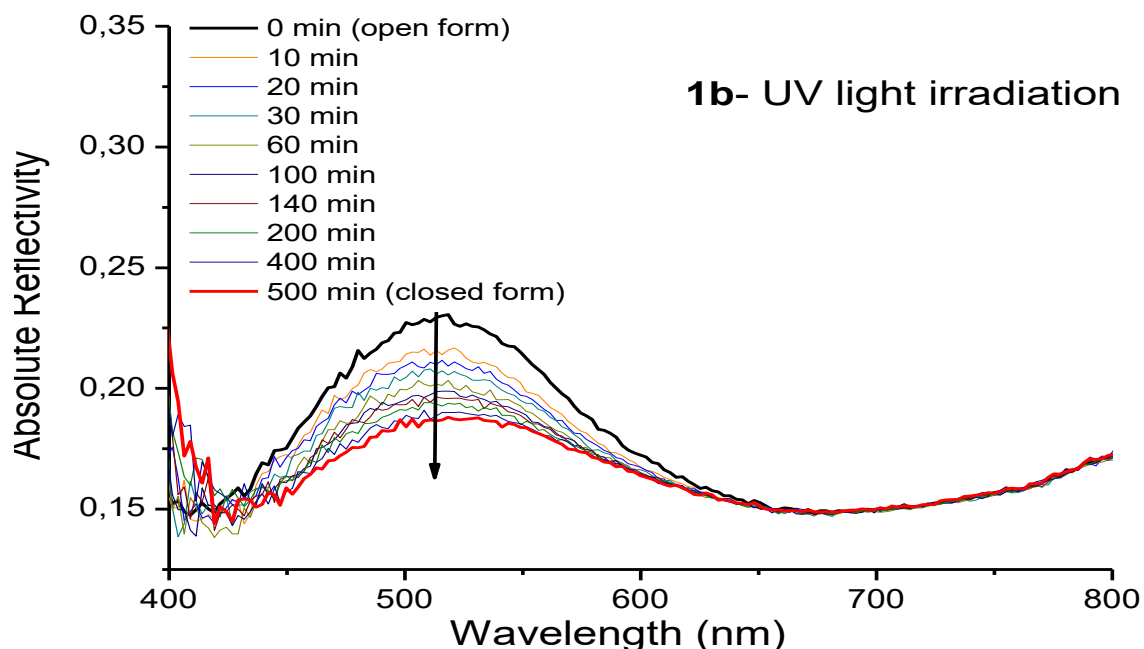


Figure 2.19: Evolution of the behaviour of **1b**, followed by absolute reflectivity measurements, upon continuous laser irradiation of (left) 365 nm and subsequently (right) of 530 nm.

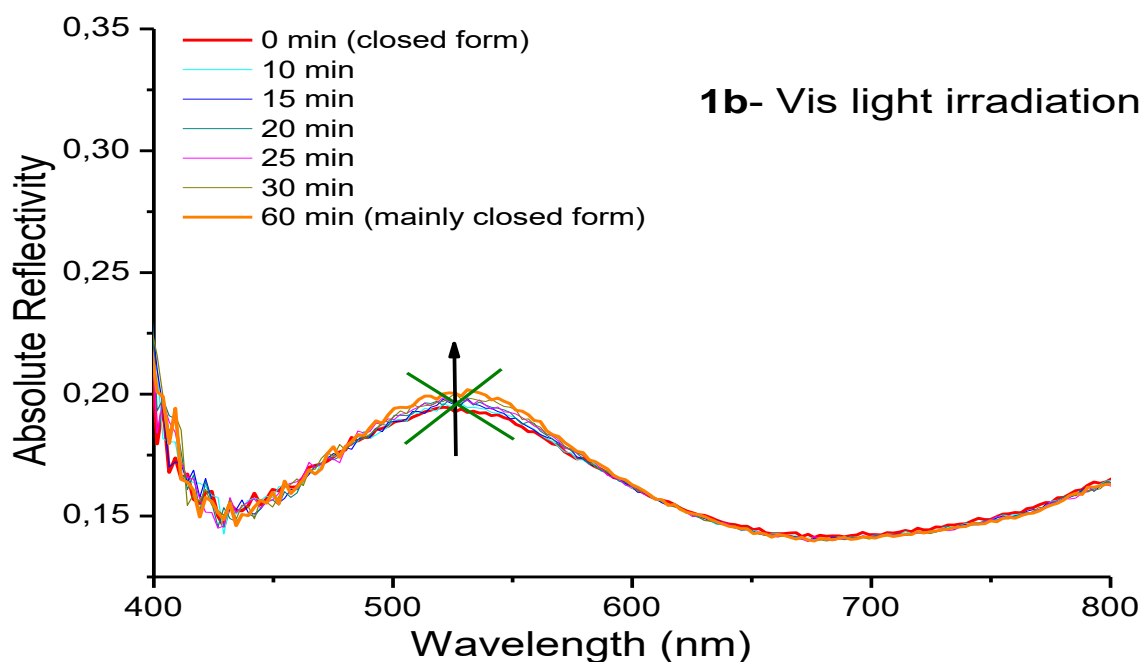


Figure 2.20: Evolution of the behaviour of **1b**, followed by absolute reflectivity measurements, upon continuous laser irradiation of (left) 365 nm and subsequently (right) of 530 nm.

The resulting system also exhibits a thermal dependence of the absolute reflectivity (Figure 2.21) similar to that of the original sample and to both forms of **1a**.

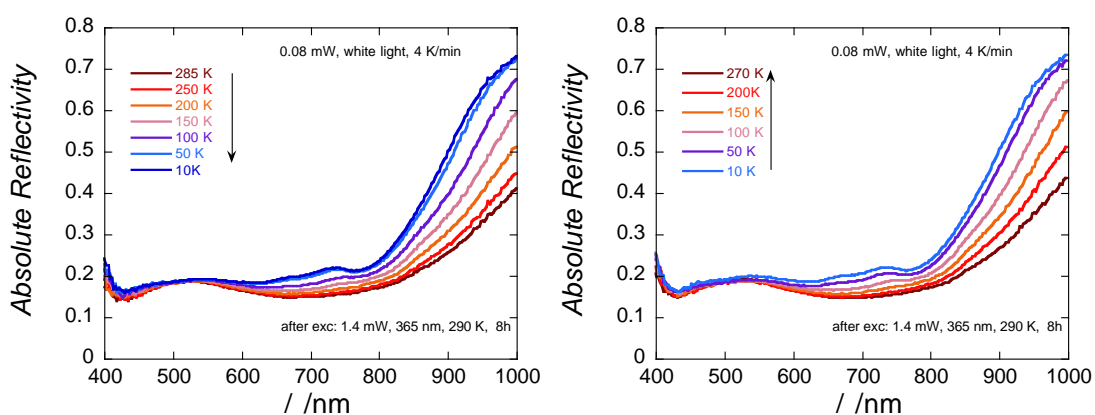


Figure 2.21: Absolute reflectivity of **1b** after photoisomerization with 365-nm (closed form) in cooling and heating modes

The dramatic difference to the kinetics of the photoactivity exhibited by both coordination polymers must be rooted on their crystalline arrangement. One difference is that the layers of chains in **1b** are packed through a network of H-bonding interactions (mediated by water molecules) that is absent in **1a**. This may render the molecular rearrangement inherent to the photocyclization more difficult for **1b** than for **1a**, as a consequence of the enhanced rigidity of the lattice in the former. It is possible that the parallel disposition of adjacent chains in **1a** (*vide supra*) compared to the alternating arrangement in **1b** facilitates the concerted atomic movement throughout the lattice required for the reversible photoconversion.

It must be noted that, to the best of our knowledge, there are no reported studies about the role of the supramolecular arrangement on the photochromic properties of metal complexes assembled by diarylethene ligands. However, some papers report on the quenching or the appearance of photoconversion in diarylethene single crystals depending on the exact crystal structure. For instance, an increase of the quantum yield of up to 100 % can be achieved by introducing guest molecules (favouring the antiparallel arrangement of thiophenyls via intermolecular interactions) into the lattice^{19,20,41}.

2.3.2 Raman spectroscopy

Ligand **H₂L1** and complex **1a** exhibit Raman spectra similar to that of other previously studied bithiophenylethene derivatives^{42,43}. Spectra on powdered samples of both compounds were then recorded after subsequent and repeated cycles of continuous UV light irradiation (< 425 nm) (Figure 2.22). During the course of this irradiation, the colour of the illuminated area changes in the same way as was observed during the reflectivity experiments. This process however, does not result in large spectral Raman changes. However, as seen on previous compounds⁴⁴, the appearance of a distinct band near 1500 cm⁻¹ upon isomerization is very obvious and constitutes a marker of the ring closure.

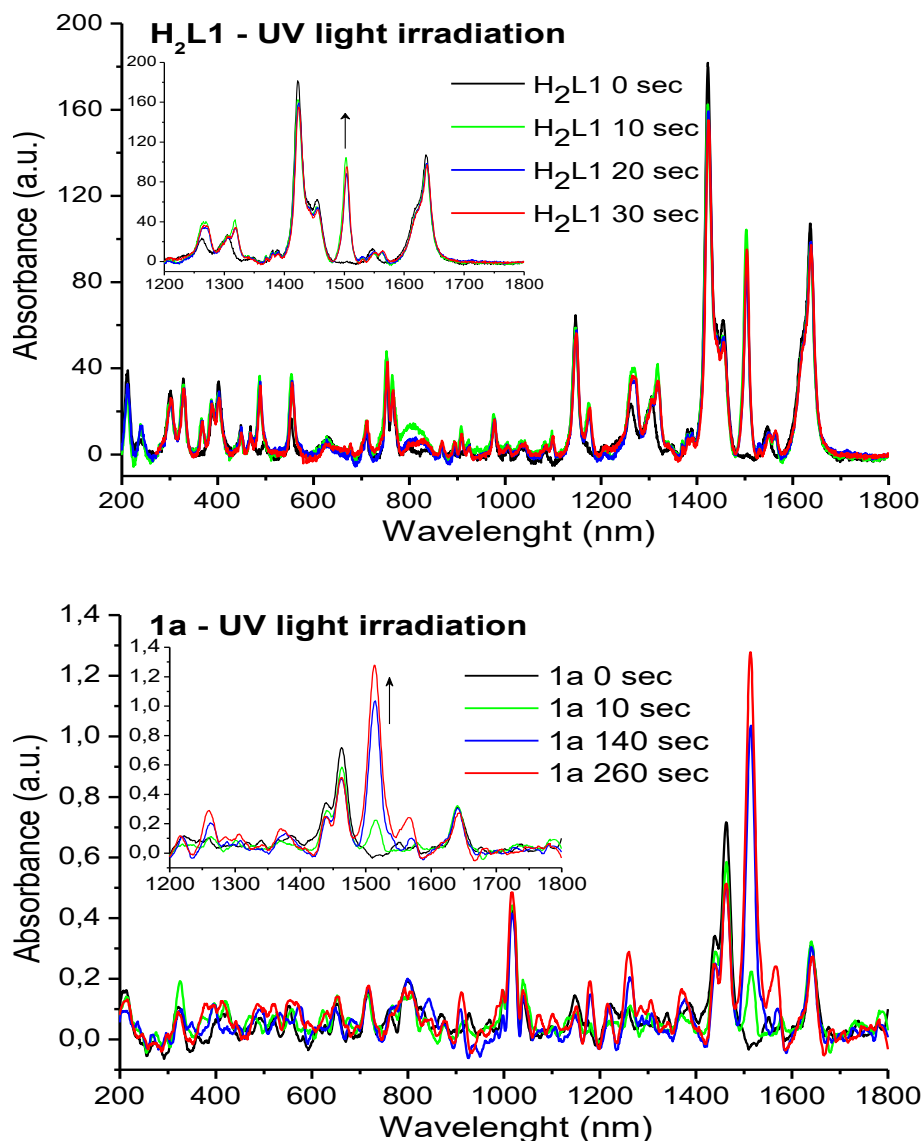


Figure 2.22: Evolution of the Raman spectra of ligand **H₂L1** (up), and complex **1a** (down) upon continuous irradiation with UV-light ($\lambda < 425$ nm)

Importantly, the reversal of the process by illumination with visible light (> 430 nm) takes place indeed with complete disappearance of this marker, which is consistent with the reflectivity results (Figure 2.23). This peak is attributed to a C=C stretching vibration of the thiophene unit when it becomes embedded within the extended conjugated polyenic structure of the closed form⁴³⁻⁴⁵. Regarding complex **1b**, the experiments were hampered by the weakness of the signal. This is ascribed to the instability of the sample under the Raman beam excitation. This confirms once again the dramatic differences in photo-responsive behaviour of both solvatomorphs.

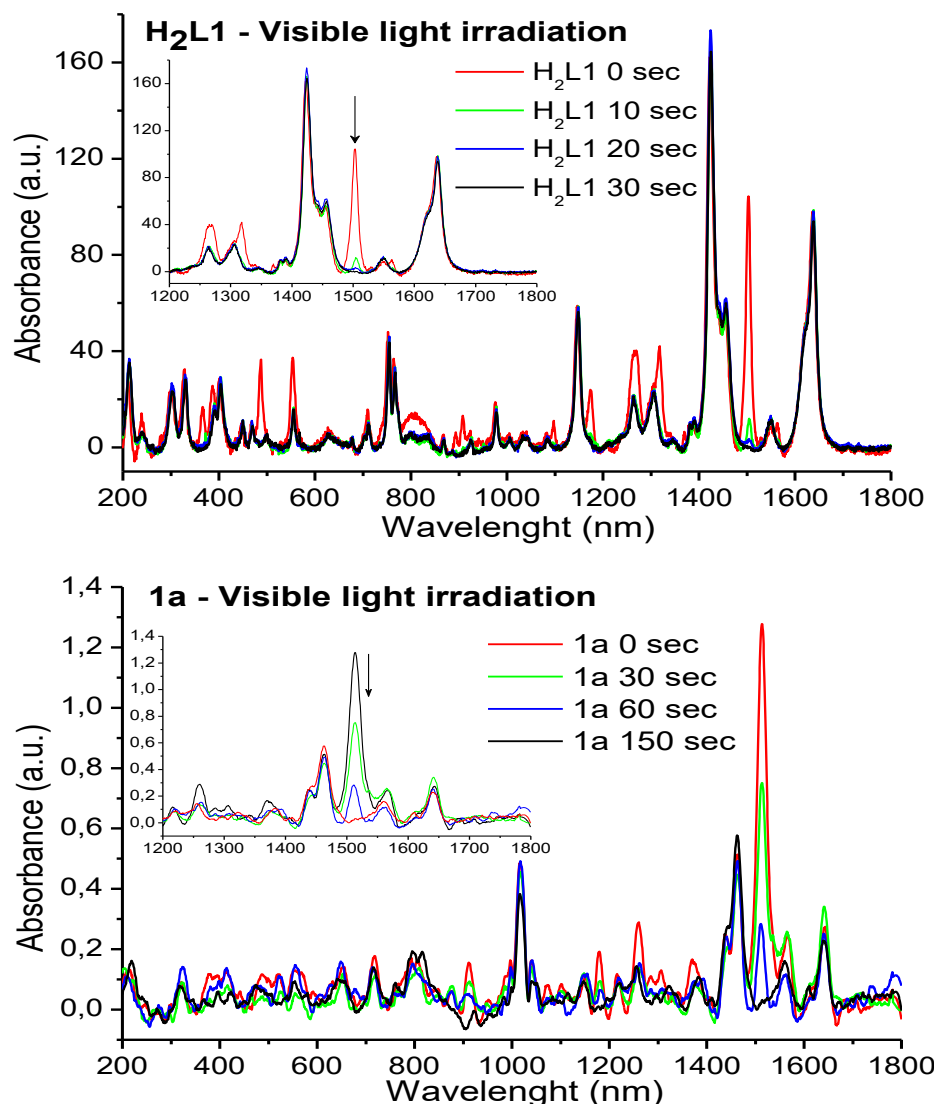


Figure 2.23: Evolution of the Raman spectra of ligand **H₂L1** (up), and complex **1a** (down) upon continuous irradiation with visible light ($\lambda > 430$ nm).

2.4 Bulk magnetic measurements

The variable temperature bulk magnetic susceptibility of complexes **1a** and **1b** before and after UV light irradiation was measured on powdered microcrystalline samples under a constant magnetic field. The $\chi_M T$ vs T plots of compounds **1a** and **1b** as synthesized (thus, in the open form) show that in all cases, the susceptibility follows a Curie law along the whole temperature range in agreement with non-interacting $S = \frac{1}{2}$ systems (a constant value of $0.44 \text{ cm}^3 \text{ K mol}^{-1}$ for both, **1a** and **1b**, before irradiation and of $0.43 \text{ cm}^3 \text{ K mol}^{-1}$ for both complexes after the irradiation with UV light). This indicates that the diaryl

ethane spacer, as expected, does not mediate any significant magnetic exchange between the metal ions. The irradiation of powdered samples of both compounds with UV light ($\lambda = 385 \text{ nm}$, $P = 3 \text{ mW/cm}^2$) using the same LEDs than the ones used for the reflectivity measurements, causes a change of color from green to deep violet. The absence of changes to the magnetic susceptibility in the resulting samples may be a consequence that upon ring closure, the diarylethene spacer H₂L1 does not increase in any efficient way the Cu...Cu exchange interactions. In addition, one must also consider that the photoisomerization in solid state may not have taken place throughout the entire bulk of the sample but only down to a certain depth below the surface. Both experiments, for 1a and 1b are shown in Figure 2.24 and Figure 2.25.

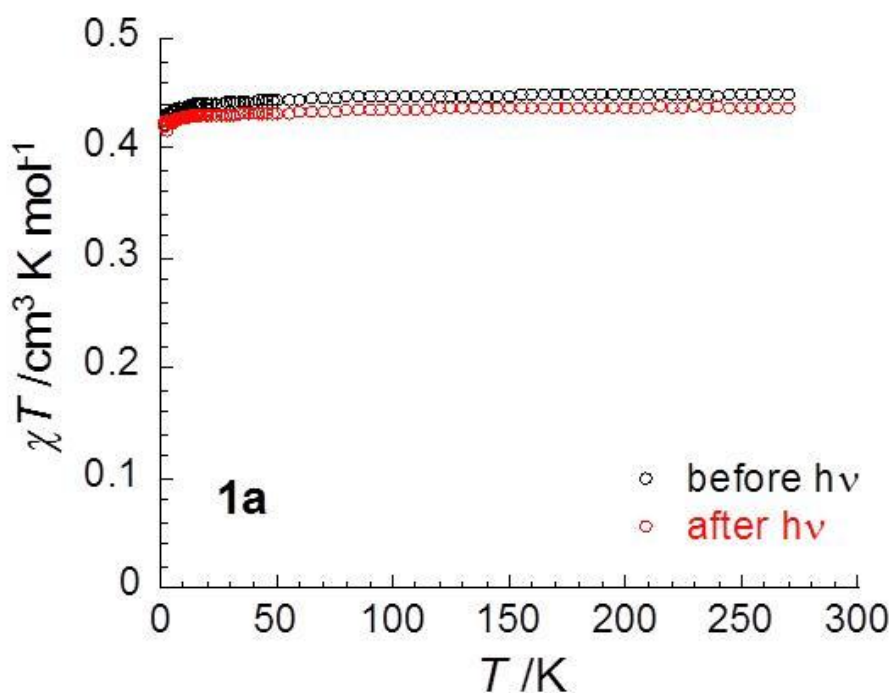


Figure 24: Plots of χT versus T for compound **1a** before (black), and after (red), UV light irradiation.

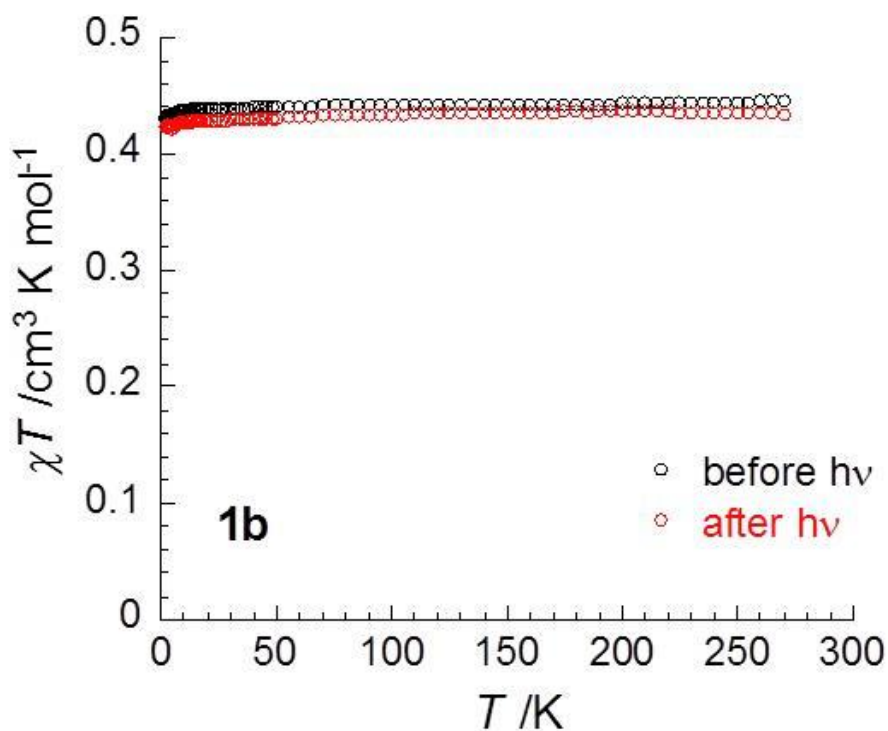


Figure 25: Plots of χT versus T for compound **1b** before (black), and after (red), UV light irradiation.

2.5 Copper compounds using blocking ligands

As we have seen, the polymeric character of compounds **1a** and **1b**, prevents the study of its photochromic properties in solution.

To open this possibility, a new synthetic strategy was used consisting in the addition of blocking ligands into the coordination sphere of the metal centre, in order to stop the growth of the polymers. Here, the substitution of the pyridine ligands with chelating agents, such as 2,2'-bipyridine and 1,10-phenanthroline, was attempted.

Three discrete complexes were obtained in this way as described below using **H₂L1**. The three structures show a very fast loss of crystallinity after exposure to the air and should be resolved better. Nevertheless, the crystal core of the three compounds can be described with enough accuracy.

2.5.1 Synthesis and crystal structure of $[\text{Cu}_2(\text{L1})(\text{Phen})_4](\text{NO}_3)_2 \cdot n\text{MeOH}$ (**2**)

Mixing a solution of one equivalent of $\text{H}_2\text{L1}$ and two equivalents of triethylamine in methanol to another containing one equivalent of $\text{Cu}(\text{NO}_3)_2 \cdot 3\text{H}_2\text{O}$ and two equivalents of 1,10-phenanthroline in methanol leads to a green solution. Blue crystals of **2** suitable for X-ray diffraction were obtained in 5 days after slow evaporation of the solvent (Figure 2.26).

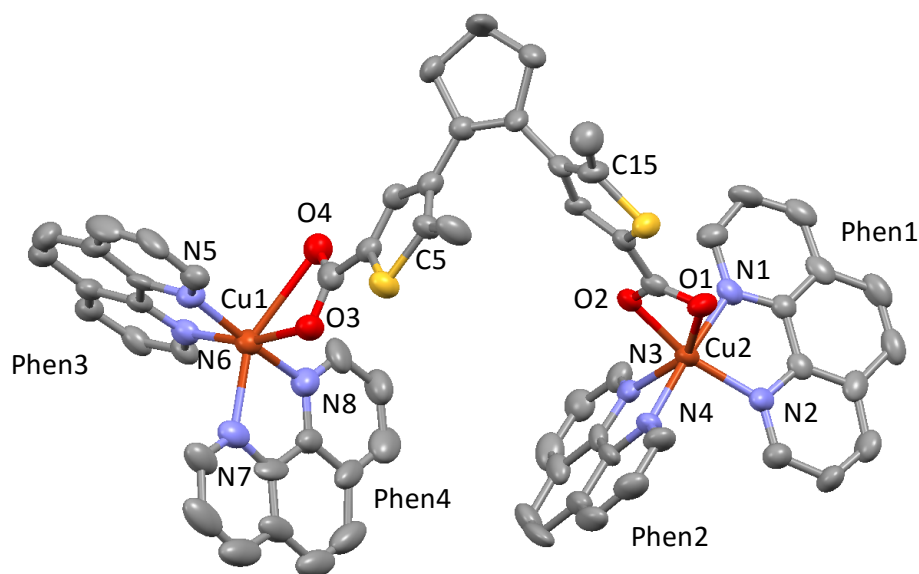


Figure 2.26: Crystal structure of **2**. Solvent, contraions and hydrogens are omitted for clarity.

The asymmetric unit consists on a dimer of copper (II) linked by the L1^{2-} ligand through the carboxylate groups, acting as a bischelating moiety. To complete the coordination sphere, four phenathroline ligands, two for each copper ion, are disposed nearly perpendicular to each other with a mutual angle of 77.99 and 81.3° for Cu1 and Cu2 respectively. The Cu(II) ions are thus described as six coordinate (N_4O_2) with highly distorted octahedral geometry.

To neutralize the charge of the complex, two molecules of NO_3^- are found in the lattice, one of them disordered in two positions due to a symmetry operation. The distance between the metal of the complex is 8.445 \AA inside the moiety. The methyl groups of the thiophene rings within the photo switchable unit exhibit a parallel configuration with a C-C bond distance of 4.126 \AA (Figure 2.26). As a result, photochromic behaviour in the solid state could not be observed. Crystallographic data and selected angles and bonds are listed in Table 2.4 and Table 2.5.

The crystal packing of this compound shows that each phenantroline ligand is connected via $\pi \cdots \pi$ stacking interactions with the same phenantroline from a neighbouring asymmetric unit (Figure 2.27). The distances between the planes for each phenantroline are: Phen1: 3.581 Å, Phen2: 3.393 Å, Phen3: 3.336 Å and Phen4: 3.425 Å.

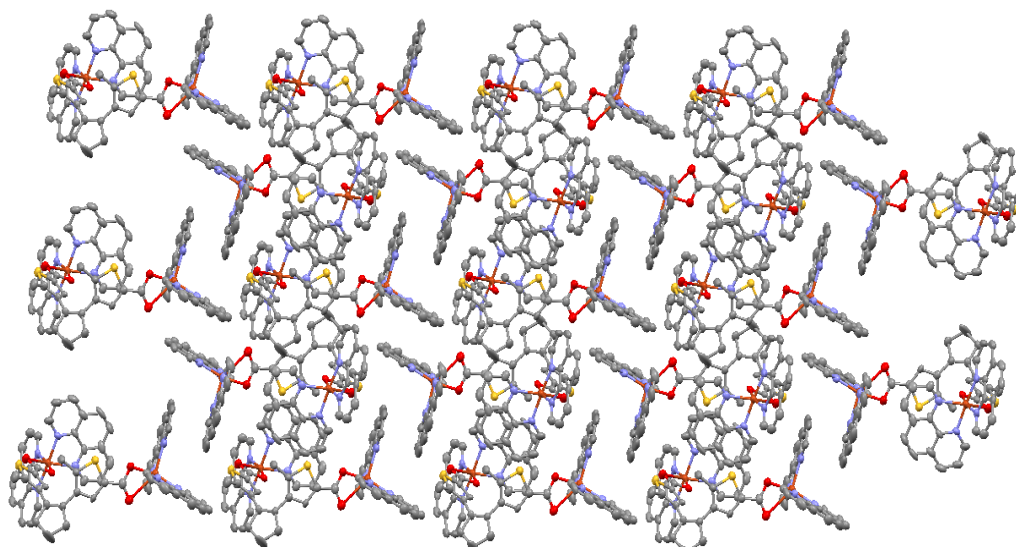


Figure 2.27: Crystal packing of **2** showing the $\pi \cdots \pi$ stacking interactions with Phen1 and Phen2 with its corresponding neighbours Phen1' and Phen2'.

Table 2.4. Crystallographic data for 2	
formula	$C_{65}H_{46}Cu_2N_{10}O_{10}S_2$, nMeOH
M_r	1260,55 + nMeOH
Crystal system	Triclinic
space group	P-1
a [Å]	14.0468(8)
b [Å]	16.5926(9)
c [Å]	16.9533(9)
α [°]	115.977(4)
β [°]	90.070(3)
γ [°]	109.330(3)
V [Å ³]	3301.75
Z	2
shape; colour	Blue blocks
R_1	0.1001
wR_2	0.2956
S	1.218

Cu1-O3	1.984(5)	O3-Cu1-N6	163.5(3)	O1-Cu2-N2	163.9(3)
Cu1-O4	2.540(8)	O3-Cu1-N7	91.1(3)	O1-Cu2-N3	93.3(3)
Cu1-N5	1.997(8)	O3-Cu1-N8	96.4(3)	O1-Cu2-N4	94.7(3)
Cu1-N6	2.022(6)	O4-Cu1-N5	90.6(3)	O2-Cu2-N1	87.6(3)
Cu1-N7	2.022(7)	O4-Cu1-N6	107.7(3)	O2-Cu2-N2	110.3(3)
Cu1-N8	2.225(9)	O4-Cu1-N7	88.9(3)	O2-Cu2-N3	89.6(3)
Cu2-O1	1.979(9)	O4-Cu1-N8	151.1(3)	O2-Cu2-N4	148.1(3)
Cu2-O2	2.653(7)	N5-Cu1-N6	81.2(3)	N1-Cu2-N2	81.2(3)
Cu2-N1	2.004(5)	N5-Cu1-N7	176.2(3)	N1-Cu2-N3	173.1(3)
Cu2-N2	2.03(1)	N5-Cu1-N8	102.8(3)	N1-Cu2-N4	104.9(3)
Cu2-N3	2.028(6)	N6-Cu1-N7	95.4(3)	N2-Cu2-N3	93.8(3)
Cu1-Cu2	10.036(1)	N6-Cu1-N8	99.6(3)	N2-Cu2-N4	100.7(3)
C5-C15	4.126(1)	N7-Cu1-N8	79.3(3)	N3-Cu2-N4	80.7(4)
O3-Cu1-O4	57.1(2)	O1-Cu2-O2	55.4(3)	Phen1-2hen2	77.99(1)
O3-Cu1-N5	91.8(3)	O1-Cu2-N1	90.3(3)	Phen3-Phen4	81.30(1)

2.5.2 Synthesis and crystal structure of $[\text{Cu}_7(\text{L1})_4(\text{Phen})_7](\text{NO}_3)_6 \cdot n\text{MeOH}$ (**3**)

The reaction in the previous section, using two equivalents of $\text{Cu}(\text{NO}_3)_2 \cdot 3\text{H}_2\text{O}$ and four equivalents of Phenantroline, gives green crystals of **3** after two weeks following the slow evaporation of the solvent (Figure 2.28).

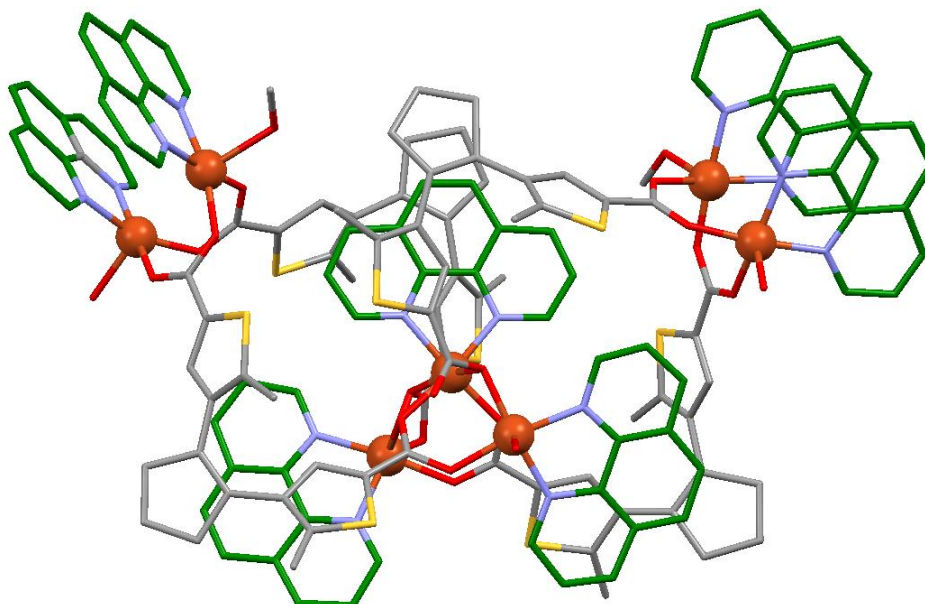


Figure 2.28: Crystal structure of **3**. Solvent, contraions and hydrogens are omitted for clarity. Phenantrolines are marked in green also for clarity.

Compound **3** crystallizes in the triclinic space group P-1. The crystal lattice consists in a heptamer cluster of copper containing three well defined cavities hosting two similar dimers and one trimer of copper ions. Four fully deprotonated $L1^{2-}$ are present in the structure, all of them with the methyl groups pointing to the same direction, suppressing any possibility to perform photochromic activity in the solid state.

Both dimers (Figure 2.29, left) are not symmetric but they present the same five coordination environment (N_2O_3). The copper ions are connected via two carboxylates from the ligand in a *syn-syn* mode I (Scheme 2.3), occupying two equatorial positions per metal, while the other equatorial positions are filled by two molecules of phenantroline. The latter are disposed almost parallel and the distances between the copper ions are 3.050 and 3.087 Å. The axial metal positions are completed with one molecule of water for one copper and one molecule of methanol for the other one.

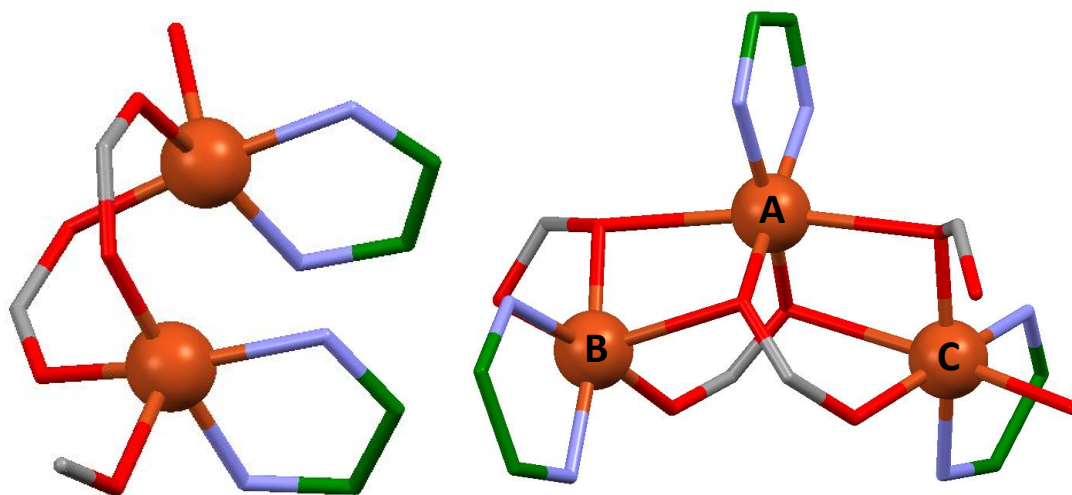
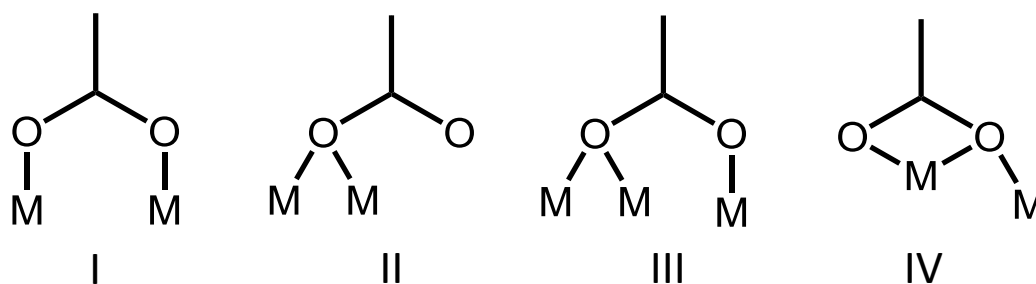


Figure 2.29: Crystal core of the copper dimer (left) and the trimer (right)

With regard to the trimer (Figure 29, right), the three coppers are six coordinate (N_2O_4). Each copper has a phenantroline molecule coordinated at the equatorial position. For copper A, the coordination sphere is completed with the carboxylates of four different ligands, which feature three different coordination modes (II, 2xIII, IV); (Scheme 2.3). Copper B are surrounded by three different carboxylates in two modes (2xIII, IV); (Scheme 2.3), while copper C also coordinates to three different ligands via carboxylate groups in modes II and 2xIII. In addition, C completes its coordination sphere with one molecule of water.



Scheme 2.3: Different carboxylate modes found in the crystal structure of **3**.

The inter metallic distances are 3.176 Å (CuA-CuB), 3.225 Å (CuA-CuC) and 5.012 Å (CuB-CuC), leading to an isosceles triangle with an obtuse angle having as a vertex copper A and a value of 103.06°, while the other two angles are 38.12° and 38.82°, having as vertex copper B and C, respectively.

Owing to the large number of interactions, only the crystallographic data for **3** are summarized in Table 2.6.

Table 2.6. Crystallographic data for 3	
formula	$C_{153}H_{128}Cu_7N_{20}O_{40}S_8, nMeOH$
M_r	3585.99 + nMeOH
Crystal system	Triclinic
space group	P-1
a [Å]	17.661(3)
b [Å]	21.370(6)
c [Å]	27.083(6)
α [°]	97.524(15)
β [°]	105.559(15)
γ [°]	111.828(15)
V [Å ³]	8806.65
Z	2
shape; colour	Blue blocks
R_{int}	0.0809
R_1	0.096
wR_2	0.2696
S	1.037

2.5.3 Synthesis and crystal structure of $[\text{Cu}_2(\text{L1})(\text{ByPy})_4](\text{NO}_3)_2 \cdot n\text{MeOH}$ (**4**)

The reaction performed with one equivalent of $\text{H}_2\text{L1}$ and two equivalents of triethylamine in methanol added to a solution containing two equivalents of $\text{Cu}(\text{NO}_3)_2 \cdot 3\text{H}_2\text{O}$ and four equivalents of 2,2'-bipyridine in methanol leads to a green solution. Blue crystals of **4** suitable to X-ray diffraction were obtained in 5 days via the slow evaporation of the solvent (Figure 2.30).

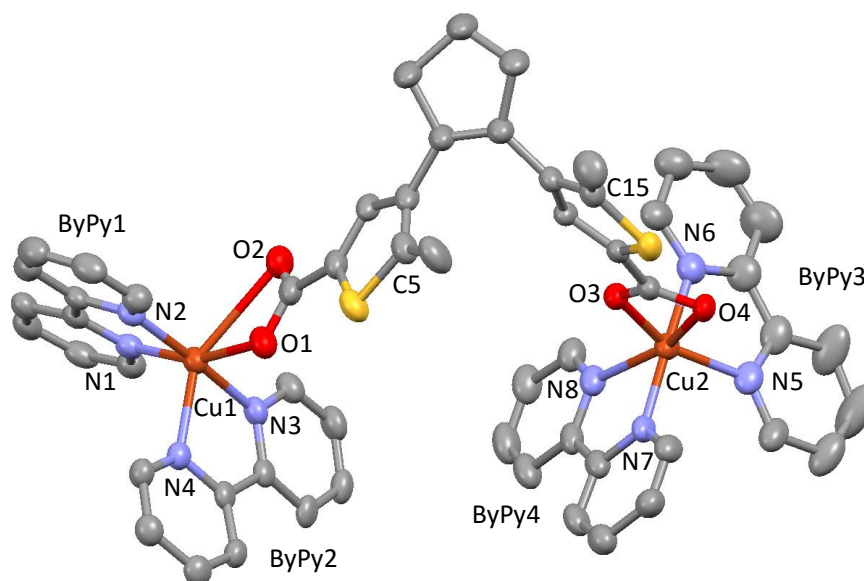


Figure 2.30: Crystal structure of **4**. Solvent, contraions and hydrogens are omitted for clarity.

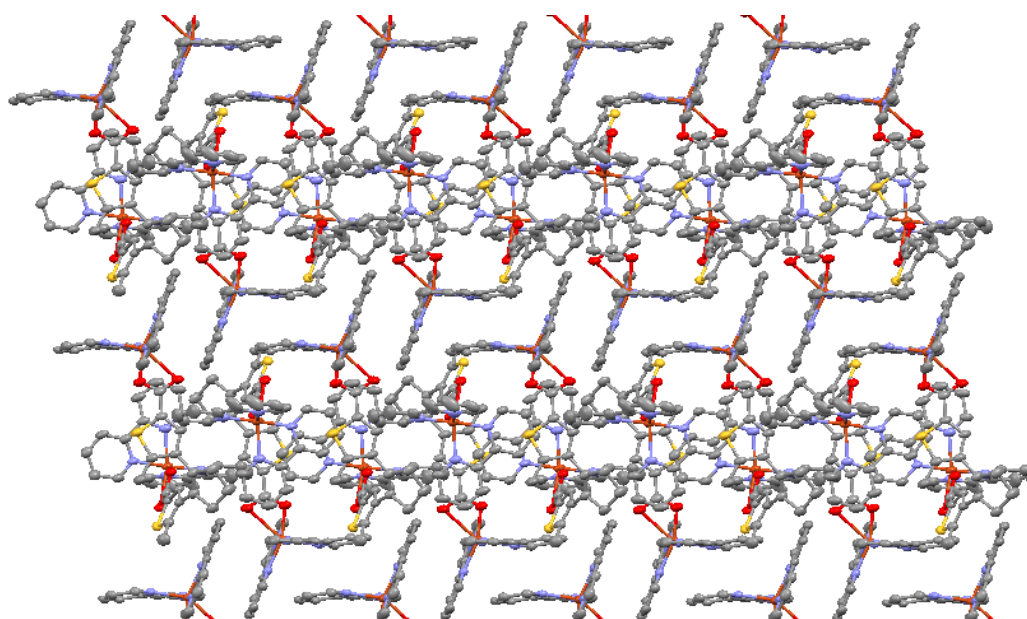


Figure 2.31: Crystal packing showing the $\pi \cdots \pi$ stacking interactions with ByPy1 and ByPy2 with its corresponding neighbours ByPy1' and ByPy2'

Compound **4** crystallizes in the triclinic space group P-1, with two molecules per asymmetric unit. Crystallographic data are given in Table 2.7 and selected bond lengths and angles are listed in Table 2.8. Each copper(II) ion is hexacoordinated and adopts a highly distorted octahedral arrangement, with two oxygens from the carboxylate group and four nitrogens coming from two bipyridine ligands. The distance between copper ions is 9.988 Å, while the reactive carbons are 4.221 Å apart and also present the parallel configuration.

Compound **4** presents the same $\pi\cdots\pi$ stacking motif as **2** and a similar crystal packing. The charge in **4** is neutralized with two molecules of nitrate, but here, these anions play a more important role in the packing of the structure, providing the same $\pi\cdots\pi$ stacking of the bipyridines with the same neighbour, excepting in the ByPy3 which cannot form this contacts (Figure 2.32). Here, the anions are making a clear separation between layers of cations, unlike compound **2**, where the layers of cations are more packed, allowing the formation of $\pi\cdots\pi$ interactions with all the phenantrolines. In compound **4**, these interactions cannot be achieved for ByPy3. The comparison between both compounds and the position of the nitrates can be seen in Figure 2.32.

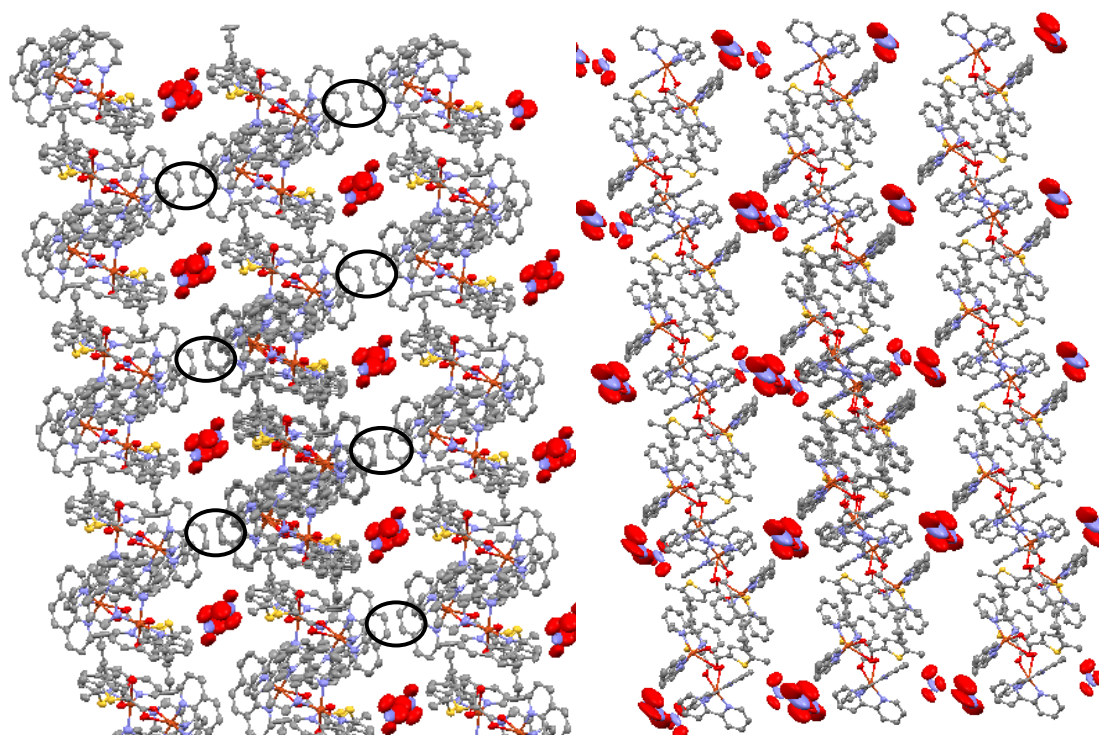


Figure 2.32: Crystal packing showing the nitrates, localized between layers of cations creating a different lattice for **2** (left) and **4** (right). The $\pi\cdots\pi$ stacking between Phen3 are marked with circles in compound **2**. This stacking in ByPy3 is not possible due the disposition of the nitrates between the layers.

Table 2.7. Crystallographic data for **4**

formula	$C_{57}H_{46}Cu_2N_{10}O_{10}S_2 \cdot nMeOH$
M_r	1222.24 + nMeOH
Crystal system	Triclinic
space group	P-1
a [Å]	13.497(19)
b [Å]	15.007(17)
c [Å]	15.756(5)
α [°]	86.293(18)
β [°]	86.539(17)
γ [°]	79.398(10)
V [Å ³]	3126.3
Z	2
shape; colour	Blue blocks
R_{int}	0.0761
R_1	0.096
wR_2	0.2220
S	1.006

Table 2.8. Selected bonds [Å] and angles[°]for **4**

Cu1-O1	1.975(3)	O1-Cu1-N2	92.3(1)	O3-Cu2-N6	91.2(1)
Cu1-O2	2.735(3)	O1-Cu1-N3	90.4(1)	O3-Cu2-N7	92.5(1)
Cu1-N1	1.997(3)	O1-Cu1-N4	93.0(1)	O3-Cu2-N8	100.7(1)
Cu1-N2	1.986(3)	O2-Cu1-N1	108.6(1)	O4-Cu2-N5	103.1(1)
Cu1-N3	2.001(3)	O2-Cu1-N2	96.4(1)	O4-Cu2-N6	97.6(1)
Cu1-N4	2.185(3)	O2-Cu1-N3	88.3(1)	O4-Cu2-N7	86.1(1)
Cu2-O3	1.979(3)	O2-Cu1-N4	144.3(1)	O4-Cu2-N8	149.5(1)
Cu2-O4	2.744(4)	N1-Cu1-N2	81.1(1)	N5-Cu2-N6	81.5(2)
Cu2-N5	2.026(4)	N1-Cu1-N3	96.9(1)	N5-Cu2-N7	95.8(1)
Cu2-N6	1.987(4)	N1-Cu1-N4	106.4(1)	N5-Cu2-N8	104.4(1)
Cu2-N7	2.006(4)	N2-Cu1-N3	176.9(1)	N6-Cu2-N7	175.9(2)
Cu2-N8	2.182(4)	N2-Cu1-N4	99.4(1)	N6-Cu2-N8	99.1(1)
C5-C15	4.221(1)	N3-Cu1-N4	78.9(1)	N7-Cu2-N8	78.6(1)
O1-Cu1-O2	53.6(1)	O3-Cu2-O4	53.6(1)	ByPy1-ByPy2	65.4(1)
O1-Cu1-N1	160.3(1)	O3-Cu2-N5	154.7(1)	ByPy3-ByPy4	81.47(1)

2.6 Photochromic activity

The crystal structure of **2** and **4** reveals the unsuitable configuration of the reactive carbons in the solid state. Nevertheless the photochromic activity of these compounds can be followed in solution. The experiments were performed in $1 \times 10^{-5} \text{M}$ solutions of DMSO:H₂O (1:99) and followed by UV-Vis spectrometry with UV light for cyclization (<425nm, left) and Visible light for ring opening (>430nm, right).

First, the photochromic behavior of **H₂L1** was studied in the same conditions as the two complexes, for the purpose of compare the results (Figure 2.33).

H₂L1 presents a big and sharp band similar to the complexes which can be related to the solvent. The important signal which is related to the photochromic unit, is the one centered at 255nm, assigned to π - π transitions. This band decreases in intensity when the colorless solution is irradiated with UV light (<425nm), while two new bands at 346 and 525 nm appear due to the cyclization of the ligand. The process reaches the PSS in 60 seconds, and the reversibility can be followed leading to the initial isomer in 300 seconds.

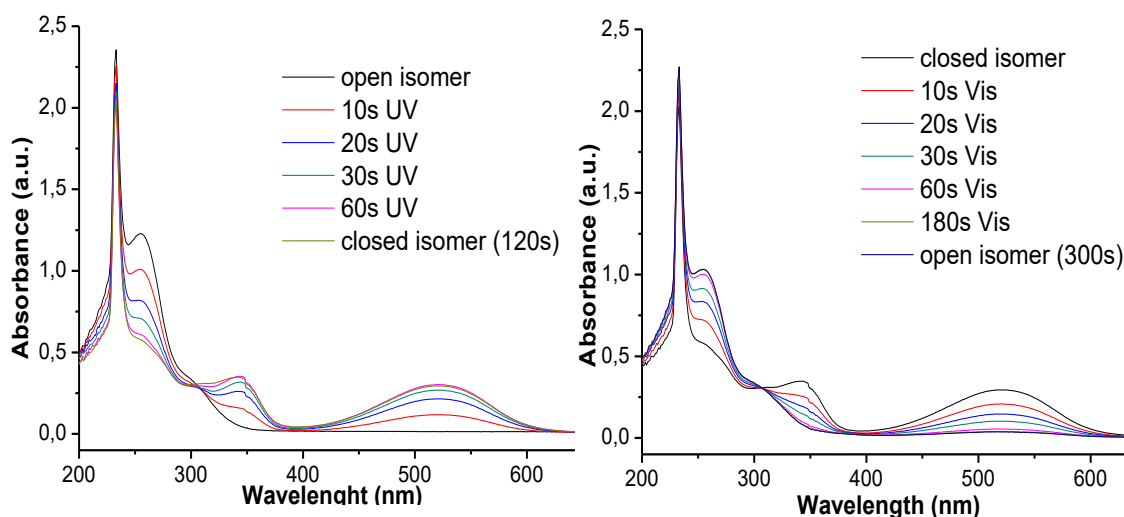


Figure 2.33: UV-Vis spectra of **H₂L1** with UV (<425nm, left) and Visible (>430nm, right).

The photochromic activity of both compound, **2** (Figure 2.34) and **4** (Figure 2.35), is quite weak, but still obvious. Irradiation of light greenish solutions of **2** and **4** with UV light (<425nm) led to purple solutions and new absorption bands at 343 and 520nm in the UV-Vis spectrum, due to the enlargement of the π -electronic delocalization. In the

case of **2**, these bands develop at the expense of the band observed one at 270 nm. The band that decreases in intensity for compound **4** is the one centered at 242nm, while the bands at 297 and 309nm are not affected by the UV light irradiation.

For both compounds, the reversibility of the process is complete, as shown by spectroscopy. The rates of the reactions are quite fast: both compounds reaching the PSS in 120 seconds, while the inverse process only takes 180 and 120 seconds, respectively, for **2** and **4**.

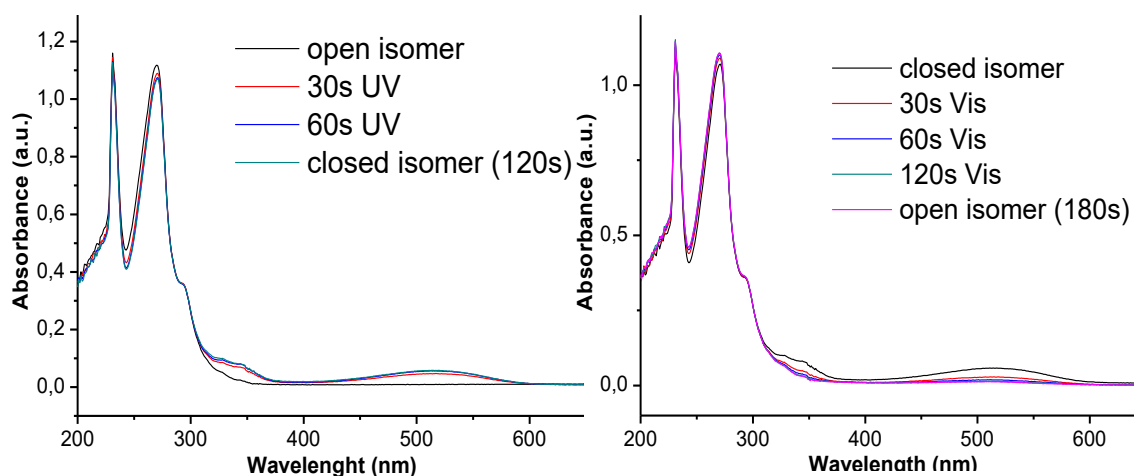


Figure 2.34: UV-Vis spectra of **2** with UV (<425nm, left) and Visible (>430nm, right).

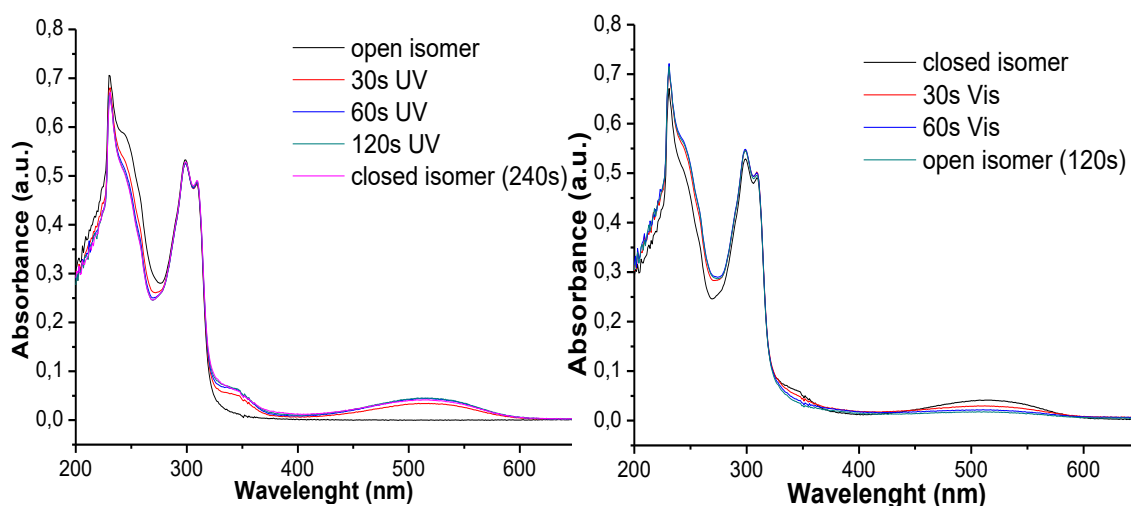


Figure 2.35: UV-Vis spectra of **4** with UV (<425nm, left) and Visible (>430nm, right).

2.7 Conclusions

As we have seen, the diarylethene photochromic dicarboxylate ligand (**H₂L1**), can be exploited for the use in the synthesis of new coordination compound featuring different coordination modes and configurations.

The reaction of a **H₂L1** with two different Cu(II) salts produces two solvatomorphs of the polymeric complex [Cu(L)(py)₃] (**1**). The nature of the solvent of crystallization (pyridine or H₂O/Et₂O) gives rise to significantly different organizations in the crystal lattice. Quite remarkably, these differences result in remarkable differing photochromic properties for these two systems. Thus, the pyridine solvate exhibits reversible solid state ring closure photoisomerism, whereas this process is significantly hampered for the other system and seems to be irreversible. The complexity generally associated to solid state photochemistry has attracted attention recently, so these results show that the subtleties of crystal engineering may constitute an avenue for modulating the kinetics of the solid state photoactivity, with potential for the understanding of these intriguing functional materials and for the design of future single crystal photochromic systems.

Even though the rational use of secondary chelating ligands, leads to the block of the growth of polymers, is not possible to escape to the serendipity of these processes, and all the attempts to obtain the photoactive isomers (in the solid state) were not possible as the crystal structures of **2**, **3** and **4** show. Nevertheless, the photochromic behaviour can be followed in solution.

All the efforts to obtain the crystal structure of the closed isomer also were unsuccessful.

Although ligand **H₂L1** is well known, the use in coordination chemistry is not so common, and different applications in areas such MOFs or in bioinorganics systems will be very useful.

2.8 Experimental

2.8.1. Ligands and precursors

1,5-bis-(5-chloro-2-methylthien-3-yl)pentane-1,5-dione (linear L0)

Under vigorous stirring, crushed AlCl_3 (0.225 mol, 30.01g) was added in portions to an ice cooled solution of 2-chloro-5-methylthiophene (0.189mol, 25g) and glutaryl chloride (0.094 mol, 15.78g) in 250ml of nitromethane. After complete addition of AlCl_3 , the solution was stirred for 3hours. Cold water (150ml) was added carefully to quench the reaction mixture and stirred for 2 hours, till a brown precipitate appears. This precipitate was filtered and dried yielding 1,5-bis(5-chloro-2-methylthiophen-3-yl)pentane-1,5-dione as a light brown powder (23.68g, 69.9%). $^1\text{H-NMR}$ (CDCl_3 , 400 MHz): δ (ppm): 2.06 (m, 2H, Cp), 2.66 (s, 6H, Me), 2.86 (t, 4H, Cp), 7.18 (s, 2H, Tph). MS (ESI+): m/z 360.98 ($[\text{C}_{15}\text{H}_{14}\text{Cl}_2\text{O}_2\text{S}_2 + \text{H}]^+$).

1,2-bis-(5-chloro-2-methylthien-3-yl) cyclopentene (L0)

Zn dust (3.8 g; 0,056mol) were placed in a schlenk flask under nitrogen in 100ml of dry THF. The solution was cooled with an ice bath and TiCl_4 (3.07 mL, 0.028 mol) was added very cautiously. The solution turned yellow and immediately grey-blue. The solution was mixed for 30 min and then refluxed 2,5h. After this, the solution was cooled to r.t. and Pyridine (2.25ml; 0.028mol) was added to the solution and mixed for 10 min. Then, **Linear L0** (5g; 0.014mol) was dissolved in THF (25 ml) and this solution was added in portions to the first one. This mixture was refluxed in the dark overnight. The solution was cooled and quenched with K_2CO_3 2M (25 ml). The precipitate was filtered over a glass filter. The precipitate was washed with Diethyl Ether (3 x 50ml) and the organic phase was separated and cooled in the fridge. White crystals appear after 2-4 hours and were separated (not the product). After this, the organic solution was washed with H_2O (5 x 500 ml), dried (Na_2SO_4) and the solvent was removed in vacuo yielding a light yellow brown oil (3.66g; 79%), that crystallizes in the fridge overnight. $^1\text{H-NMR}$ (CDCl_3 , 400 MHz): δ (ppm): 1.88 (s, 6H, Me), 2.02 (m, 2H, Cp), 2.71 (t, 4H, Cp), 6.57 (s, 2H, Tph). MS (ESI+): m/z 328.99 ($[\text{C}_{15}\text{H}_{14}\text{Cl}_2\text{S}_2 + \text{H}]^+$).

1,2-bis-(5-carboxy-2-methylthien-3-yl) cyclopentene (H₂L1)

nBuLi (5 mL of a 2.5M solution in hexane, 11.5 mmol) was added to a stirred solution of **L0** (2 g, 5.75 mmol) in anhydrous THF (15 mL) under nitrogen at room temperature. After 1 h, solid CO₂ (excess) was added. After 30 min, water (15 mL) was added. The water layer was washed with diethyl ether and then acidified with HCl until pH 1 was reached. The precipitated product was filtered with care and washed with water and ether to remove some impurities yielding a white solid. ¹H-NMR ([D₆]DMSO, 400 MHz): δ (ppm): 1.91 (s, 6H, Me), 1.95_2.05 (m, 2 H, Cp), 2.77 (t, 4 H, Cp), 7.40 (s, 2H, Tph). MS (ESI⁺): m/z 349.13 ([C₁₇H₁₆O₄S₂ + H]⁺).

2.8.2. Coordination complexes.**[Cu(L1)(py)₃]·2py (1a)**

A solution of **H₂L1** (50 mg, 0.143 mmol) and NaH (11.46 mg, 0.286 mmol) in pyridine (15 mL) was added to a solution of Cu(AcO)₂·H₂O (28.66 mg, 0.143 mmol) in pyridine (15 mL). The resulting green solution was stirred for 2 hours, filtered and the filtrate was layered with ether (30 mL). After one day, blue crystals were obtained (92mg, yield 78%). IR (KBr pellet, cm⁻¹): 3439, 3108, 3065, 2904, 2843, 1600, 1465, 1447, 1378, 1334, 1213, 1147, 1069, 769, 695. Anal., found (calc% for **1a**·3H₂O–2py): C, 54.80 (55.25); H, 5.03 (4.70); N, 5.99 (5.38).

[Cu(L1)(py)₃]·2H₂O·0.5Et₂O (1b)

A solution of **H₂L1** (50 mg, 0.143 mmol) and NaH (11.46 mg, 0.286 mmol) in pyridine (15 mL) was added to a solution of Cu(NO₃)₂·3H₂O (33.26 mg, 0.143 mmol) in pyridine (15 mL). The resulting green solution was mixed for 2 hours, filtered and the filtrate was layered with ether (30 mL). After five days, green crystals were collected (67 mg, yield 66%). IR (KBr pellet, cm⁻¹): 3400, 2969, 2908, 2834, 1605, 1460, 1378, 1343, 1216, 1150, 1044, 875, 804, 773, 695. Anal., found (calc% for **1b**–0.5Et₂O): C, 56.24 (56.60); H, 4.88 (4.75); N, 6.15 (6.15).

[Cu₂(L1)(Phen)₄](NO₃)₂·nMeOH (2)

A solution of **H₂L1** (30 mg, 0.086 mmol) and triethylamine (24 μl, 0.18 mmol) in methanol (10 mL) was added to a solution of Cu(NO₃)₂·3H₂O (20.77 mg, 0.086 mmol) and phenantroline (31 mg, 0.18 mmol) in methanol (10 mL). The resulting green

solution was mixed for 2 hours, filtered and the filtrate was slowly evaporated. After one day, blue crystals were collected (72 mg, yield 67%). IR (KBr pellet, cm^{-1}): 3421, 3056, 2939, 1586, 1517, 1426, 1382, 1143, 1100, 852, 778, 721, 639. Anal., found (calc% for $2 \cdot 2.25\text{H}_2\text{O} \cdot 0.5\text{Cu}(\text{NO}_3)_3$): C, 52.96 (52.62); H, 4.11 (3.43); N, 11.54 (10.86).

[Cu₇(L1)₄(Phen)₇](NO₃)₆·nMeOH (3)

A solution of **H₂L1** (30 mg, 0.086 mmol) and triethylamine (24 μl , 0.18 mmol) in methanol (10 mL) was added to a solution of $\text{Cu}(\text{NO}_3)_2 \cdot 3\text{H}_2\text{O}$ (41.54 mg, 0.18 mmol) and phenantroline (62 mg, 0.36 mmol) in methanol (10 mL). The resulting green solution was mixed for 2 hours, filtered and the filtrate was slowly evaporated. After two weeks, green crystals were collected. IR (KBr pellet, cm^{-1}): 3426, 3052, 2943, 2913, 2839, 1569, 1517, 1430, 1382, 1147, 1108, 852, 765, 721, 639. Anal., found (calc% for $3 \cdot 10\text{H}_2\text{O}$): C, 48.7 (49.22); H, 3.46 (3.98); N, 7.26 (7.31).

[Cu₂(L1)(ByPy)₄](NO₃)₂·nMeOH (4)

A solution of **H₂L1** (30 mg, 0.086 mmol) and triethylamine (24 μl , 0.18 mmol) in methanol (10 mL) was added to a solution of $\text{Cu}(\text{NO}_3)_2 \cdot 3\text{H}_2\text{O}$ (41.54 mg, 0.18 mmol) and 2,2'-bipyridine (53.6 mg, 0.36 mmol) in methanol (10 mL). The resulting green solution was mixed for 2 hours, filtered and the filtrate was slowly evaporated. After one day, blue crystals were collected (59 mg, yield 57%). IR (KBr pellet, cm^{-1}): 3426, 3060, 2917, 2847, 1578, 1465, 1439, 1378, 1239, 1147, 1030, 973, 769, 734, 647. Anal., found (calc% for $4 \cdot 7.2\text{H}_2\text{O} \cdot 2\text{NO}_3$): C, 55.34 (55.75); H, 4.29 (4.96); N, 8.46 (9.13).

2.9. References

1. Feringa, B. L. *Molecular Switches*. **3**, (2001).
2. Zhang, J., Wang, J. & Tian, H. Taking orders from light: progress in photochromic bio-materials. *Mater. Horizons* **1**, 169 (2014).
3. Murguly, E., Norsten, T. B. & Branda, N. R. Nondestructive data processing based on chiroptical 1,2-dithienylethene photochromes. *Angew. Chemie - Int. Ed.* **40**, 1752–1755 (2001).
4. Singer, M. & Jäschke, A. Reversibly photoswitchable nucleosides: Synthesis and photochromic properties of diarylethene-functionalized 7-deazaadenosine derivatives. *J. Am. Chem. Soc.* **132**, 8372–8377 (2010).
5. Zhang, J., Zou, Q. & Tian, H. Photochromic materials: More than meets the eye. *Advanced Materials* **25**, 378–399 (2013).
6. Park, J., Sun, L. B., Chen, Y. P., Perry, Z. & Zhou, H. C. Azobenzene-functionalized metal-organic polyhedra for the optically responsive capture and release of guest molecules. *Angew. Chemie - Int. Ed.* **53**, 5842–5846 (2014).
7. Bianchi, A., Delgado-Pinar, E., García-España, E., Giorgi, C. & Pina, F. Highlights of metal ion-based photochemical switches. *Coordination Chemistry Reviews* **260**, 156–215 (2014).
8. Kim, D. *et al.* Flexible molecular-scale electronic devices composed of diarylethene photoswitching molecules. *Adv. Mater.* **26**, 3968–3973 (2014).
9. Falenczyk, C. *et al.* Chromo-pharmacophores: photochromic diarylmaimide inhibitors for sirtuins. *Chem. Sci.* **5**, 4794–4799 (2014).
10. Abellán, G. *et al.* Photo-switching in a hybrid material made of magnetic layered double hydroxides intercalated with azobenzene molecules. *Adv. Mater.* **26**, 4156–4162 (2014).
11. Morimoto, M., Miyasaka, H., Yamashita, M. & Irie, M. Coordination assemblies of [Mn4] single-molecule magnets linked by photochromic ligands: Photochemical control of the magnetic properties. *J. Am. Chem. Soc.* (2009).
12. Katsonis, N. *et al.* Reversible conductance switching of single diarylethenes on a gold surface. *Adv. Mater.* **18**, 1397–1400 (2006).
13. Peters, A. & Branda, N. R. Electrochromism in photochromic dithienylcyclopentenes. *J. Am. Chem. Soc.* **125**, 3404–3405 (2003).
14. Irie, M., Fukaminato, T., Sasaki, T., Tamai, N. & Kawai, T. Organic chemistry: a digital fluorescent molecular photoswitch. *Nature* **420**, 759–760 (2002).
15. Kobatake, S. & Irie, M. Single-Crystalline Photochromism of Diarylethenes. in *Bulletin of the Chemical Society of Japan* **77**, 195–210 (2004).

16. Irie, M. Photochromism of diarylethene single molecules and single crystals. *Photochem. Photobiol. Sci.* **9**, 1535–42 (2010).
17. Irie, M. Photochromism of diarylethene molecules and crystals. *Proc. Jpn. Acad. Ser. B. Phys. Biol. Sci.* **86**, 472–483 (2010).
18. Irie, M. Diarylethenes for Memories and Switches. *Chemical Reviews* **100**, (2000).
19. Morimoto, M., Kobatake, S. & Irie, M. Crystal engineering of photochromic diarylethene single crystals. *Chem. Rec.* **4**, 23–38 (2004).
20. Morimoto, M. & Irie, M. Photochromic reactions of diarylethenes in single crystals with intermolecular O-H···N hydrogen-bonding networks. *Chem. - A Eur. J.* **12**, 4275–4282 (2006).
21. Lin, Y. *et al.* Syntheses and properties of binuclear ruthenium vinyl complexes with dithienylethene units as multifunction switches. *Organometallics* **28**, 6402–6409 (2009).
22. Motoyama, K., Koike, T. & Akita, M. Remarkable switching behavior of bimodally stimuli-responsive photochromic dithienylethenes with redox-active organometallic attachments. *Chem. Commun. (Camb)*. 5812–4 (2008).
23. Tan, W., Zhang, Q., Zhang, J. & Tian, H. Near-infrared photochromic diarylethene iridium (iii) complex. *Org. Lett.* **11**, 161–164 (2009).
24. Han, J. *et al.* Photochromism of novel metal coordination polymers with 1,2-Bis(2'-methyl-5'-(carboxylic acid)-3'-thienyl)perfluorocyclopentene in the crystalline phase. *Inorg. Chem.* **46**, 3313–3321 (2007).
25. Munakata, M. *et al.* A MLCT-switched photochromic copper(II) coordination polymer with 1,2-bis(2'-methyl-5'-(4"-pyridyl)-3'-thienyl)perfluorocyclopentene in crystalline phase. *Inorganica Chim. Acta* **360**, 2792–2796 (2007).
26. Pinkowicz, D. *et al.* Control of the Single-Molecule Magnet Behavior of Lanthanide-Diarylethene Photochromic Assemblies by Irradiation with Light. *Chem. - A Eur. J.* **20**, 12502–12513 (2014).
27. Shiga, T., Miyasaka, H., Yamashita, M., Morimoto, M. & Irie, M. Copper(II)-terbium(III) single-molecule magnets linked by photochromic ligands. *Dalton Trans.* (2011).
28. Sénéchal-David, K. *et al.* Combining organic photochromism with inorganic paramagnetism--optical tuning of the iron(II) electronic structure. *Dalton Trans.* 1932–1936 (2008).
29. Cosquer, G. *et al.* Photo-control of the magnetic properties of Dy(III) and Ho(III) homometal coordination polymers bridged by a diarylethene ligand. *Dalt. Trans.* **44**, 5996–6002 (2015).

30. Munakata, M. *et al.* Syntheses, structures and photochromism of two novel copper(II) complexes with 1,2-bis(2'-methyl-5'-(2"-pyridyl)-3'-thienyl)perfluorocyclopentene. *Polyhedron* **25**, 3519–3525 (2006).
31. Matsuda, K., Takayama, K. & Irie, M. Photochromism of metal complexes composed of diarylethene ligands and Zn (II), Mn (II), and Cu (II) hexafluoroacetylacetonates. *Inorg. Chem.* **43**, 482–489 (2004).
32. Lucas, L. N., Jong, J. J., Esch, J. H., Kellogg, R. M. & Feringa, B. L. Syntheses of Dithienylcyclopentene Optical Molecular Switches. *Eur. J. Org. Chem.* **2003**, 155–166 (2003).
33. Motoyama, K. *et al.* The future of metal–organic frameworks. *Dalt. Trans.* **40**, 10311 (2011).
34. Guan, J.-T., Yu, G.-A., Yin, J., Lin, Y. & Liu, S.-H.)-5-Ferrocenylvinyl-2-Methylthien-3-Yl]Cyclopentene. *Acta Crystallogr. Sect. E Struct. Reports Online* **63**, m1499–m1500 (2007).
35. Guan, J.-T., Yu, G.-A., Yin, J., Meng, X.-G. & Liu, S.-H. 5-Ferrocenylvinyl-2-methylthien-3-yl]-2-(5-formyl-2-methylthien-3-yl)cyclopentene. *Acta Crystallogr. Sect. E Struct. Reports Online* **63**, m1515–m1516 (2007).
36. Qin, B., Yao, R. & Tian, H. One-dimensional structure of a photochromic coordination polymer composed of 1,2-bis[2-methyl-5-(4-pyridyl)-3-thienyl]cyclopentene and Zn(II) chloride. *Inorganica Chim. Acta* **357**, 3382–3384 (2004).
37. Wissler, J., Mulder, A., Tampé, R. & Bolte, M. 1,2-Bis(5-chloro-2-methyl-3-thienyl)cyclopentene. *Acta Crystallogr. Sect. E Struct. Reports Online* **62**, (2006).
38. Duan, X. F., Zeng, J., Lü, J. W. & Zhang, Z. Bin. Insights into the general and efficient cross McMurry reactions between ketones. *J. Org. Chem.* **71**, 9873–9876 (2006).
39. Migulin, V. A. *et al.* Synthesis and characterization of nonsymmetric cyclopentene-based dithienylethenes. *J. Org. Chem.* **77**, 332–340 (2012).
40. Kobatake, S., Uchida, K., Tsuchida, E. & Irie, M. Single-crystalline photochromism of diarylethenes: reactivity–structure relationship. *Chem. Commun.* **2**, 2804–2805 (2002).
41. Nakashima, T., Fujii, R. & Kawai, T. Regulation of folding and photochromic reactivity of terarylenes through a host-guest interaction. *Chem. - A Eur. J.* **17**, 10951–10957 (2011).
42. Zhou, X. H. *et al.* Raman spectra study of photochromic diarylethene in a single crystalline phase. *J. Photochem. Photobiol. A Chem.* **171**, 205–208 (2005).
43. Yasukuni, R. *et al.* Specific and nondestructive detection of different diarylethene isomers by NIR-SERS. *J. Phys. Chem. C* **116**, 16063–16069 (2012).

44. de Jong, J. J. D. *et al.* Raman scattering and FT-IR spectroscopic studies on dithienylethene switches--towards non-destructive optical readout. *Org. Biomol. Chem.* **4**, 2387–92 (2006).
45. Saita, K. *et al.* Raman spectroscopic study on isomers of photochromic 1,2-bis(2,5-dimethyl-3-thienyl)perfluorocyclopentene in crystal and stability of the closed-ring forms in the open-ring forms. *Chem. Phys. Lett.* **454**, 42–48 (2008).

CHAPTER 3: TOWARDS PHOTOSWITCHABLE 2-QUBIT SYSTEMS

3.1 Introduction	93
3.2 Synthesis and characterization	94
3.2.1 Synthesis of [1,2-bis-(5-(3-oxo-3-(2-hydroxyphenyl)-propanoyl)-2-methylthien-3-yl) cyclopentene] (H_4L2)	94
3.2.2 Crystal structure and 1H RMN of H_4L2	95
3.2.3 Photochromic properties of H_4L2	98
3.2.4 Synthesis of 1,2-bis-(5-(3-oxo-3-(2-hydroxynaphthyl)-propanoyl)-2-methylthien-3-yl) cyclopentene (H_4L3)	101
3.2.5 Photochromic behavior of H_4L3	103
3.2.6 Fluorescence of H_4L3	105
3.3 Synthesis of coordination compounds.....	107
3.3.1 Homometallic pairs of dimers $[MM \cdots MM]$. Synthesis and crystal structures	107
3.3.2 Magnetic properties of $[M_4(L2)_2(py)_6]$ complexes.....	112
3.4 Heterometallic pair of dimers $[MM' \cdots M'M]$	116
3.4.1 Synthesis and crystal structures.....	116
3.4.2 Magnetic properties of $[M_2M'_2(L2)_2(py)_6]$ complexes.....	121
3.4.3 Theoretical studies of the heterometallic compounds	126
3.4.4 Quantum coherence in the heterometallic clusters	127
3.5 Photochromic behavior	135
3.7 Conclusions	140
3.8 Experimental	141
3.8.1 Ligands.....	141
3.8.2 Coordination compounds.	143
3.9 References	146

3.1 Introduction

The design and synthesis of new polydentate ligands is a good strategy to obtain compounds with predetermined topologies and properties

In this regard, our group is experienced in the design and synthesis of ligands containing different coordination pockets, combining beta-diketones with other chelating groups. The judicious use of these ligands leads to the synthesis of a large family of coordination clusters, in form of metallocycles, polynuclear cages, polymers, as well as metallohelicates linear arrays of metals¹. This versatility has been recently exploited in our group for the synthesis of good candidates of 2-qubit systems². Qubits are quantum systems with two quantum microstates. These states emulate the values of the classical bits, 1 and 0, but also can exist as all the superpositions of them^{3,4}. In this project, we have used the electronic spin of magnetic coordination compounds to embody the qubits, because in fact, the electric spin can provide a true two level system that can define the two states of a qubit. The spin up or down can be related to the states 0 or 1. To perform quantum operations we need to change from one state to the other. Using the electronic spins, this change can be carried out using an electromagnetic pulse⁵. To perform these operations and manipulate the spins, we need long decoherence times (T_2). This is related to the time over which the quantum information stored in a qubit is maintained and depends on the ligand and the environment of the possible qubit⁶. Thus as chemists, we can design molecules that can acomodate spins appropriately and use them to perform quantum operations.

In this chapter therefore, we continue exploiting the properties of the beta-diketones, in order to synthesize new ligands, introducing a photoactive group as spacer between the qubits (seen in the chapter 1). This spacer should exist as two different isomers exchangeable photochemically, and capable of modifying the coupling between the two qubits within a cluster.

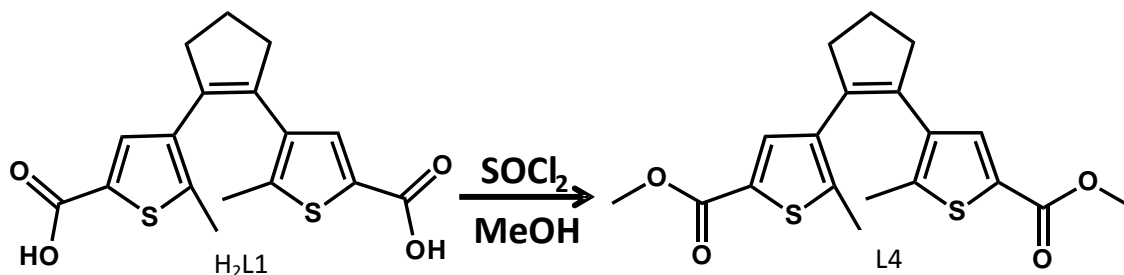
In this context, ligands **H₄L2** and **H₄L3** have been prepared (Schemes 3.3 and 3.4). These ligands have the capacity to induce the formation of tetranuclear species, disposed as two dinuclear units separated by the photochromic moiety. This is achieved through the complete deprotonation of the ligands, thus creating the two potential well defined qubits.

3.2 Synthesis and characterization

3.2.1. Synthesis of [1,2-bis-(5-(3-oxo-3-(2-hydroxyphenyl)-propanoyl)-2-methylthien-3-yl) cyclopentene] (**H₄L₂**)

The new photochromic bis- β -diketone derivative **H₄L₂** was prepared through the functionalization of **H₂L₁**. The latter was synthesized according to a previously reported procedure with some modifications⁷⁻¹⁰ (See Chapter 2).

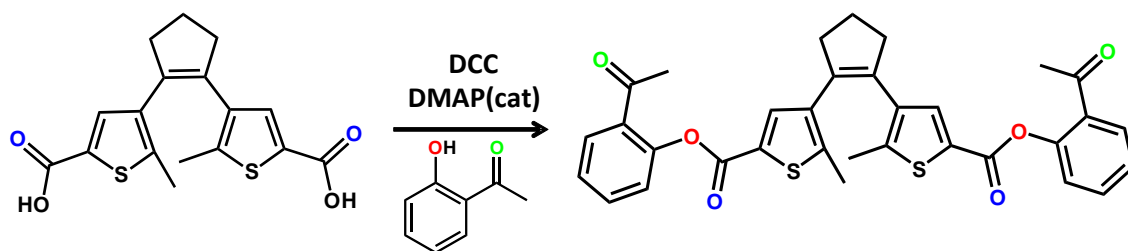
The design of this new ligand was inspired on earlier work carried out in the group, on poly beta-diketone synthesis. The central procedure for the synthesis of beta-diketones is the well known Claisen condensation¹¹, which is the condensation of an ester with a ketone in the presence of a strong base. For this reason, the first goal was to achieve the synthesis of the diester **1,2-bis-(5-methoxycarbonyl-2-methylthien-3-yl) cyclopentene** (**L4**). This was accomplished using an excess of thionyl chloride in a refluxing methanolic solution of **H₂L₁** (Scheme 3.1). Analogous compound **1,2-bis-(5-ethoxycarbonyl-2-methylthien-3-yl) cyclopentene** (**L5**) having an ethanolic diester can be obtained refluxing **H₂L₁** in ethanol.



Scheme 3.1: Synthesis of **L4**

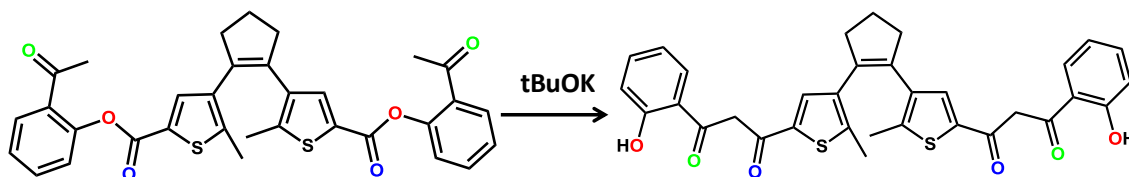
After this, the condensation of **L4** with 2-hydroxyacetophenone using sodium hydride, gives the expected compound **H₂L₁** in a very low yield, as part of a mixture containing the hydrolyzed initial ester and the half hydrolyzed compound. Using different conditions, such as changing solvents, temperature, base or starting materials did not help to improve the outcome. In collaboration with the organic group “Metodología sintética aplicada a productos bioactivos, SMBioCom” of Dr Jordi Garcia Gómez of the UB, a new route was implemented successfully. Thus the concepts of peptide synthesis were used to perform a new route to synthesize an ester which had the possibility to react in an intramolecular way, to form the desired beta-diketone. Thus the so-called Steglich esterification¹² of **H₂L₁** was carried out following three steps, i) the

DMAP (4-dimethylamino pyridine) catalyst removes the acidic protons of the substrate, ii) DCC (dicyclohexyl carbodiimide) activates the carboxylic group turning it into a good leaving group and iii) an alcohol group (in this case 2'-hydroxyacetophene) is added to the carbonyl activated by the DCC. A pure solid, **1,2-bis-(5-((2-acetylphenyl)-carboxylate)-2-methylthien-3-yl) cyclopentene (L2a)**, in excellent yield (over 90 %) is obtained after column chromatography. (Scheme 3.2)



Scheme 3.2: Synthesis of **L2a**.

Finally, upon employing a simultaneously double transposition Baker-Venkataraman rearrangement, a type of intramolecular Claisen condensation, in one-pot reaction in THF at 0°C with a strong base (^tBuOK), the bis-substituted ester turns into the corresponding phenolate in “α” to a beta-diketonate.^{12,13} The latter is protonated during acidic work-up to give the desired **1,2-bis-(5-(3-oxo-3-(2-hydroxyphenyl)-propanoyl)-2-methylthien-3-yl) cyclopentene (H₄L2)** ligand. The product is further purified by recrystallization with acetone (yield of 60 %) (Scheme 3.3).



Scheme 3.3: Synthesis **H₄L2**.

3.2.2. Crystal structure and ¹HMRN of H₄L2.

Figure 3.1 shows a molecular representation of ligand **H₄L2**. The corresponding crystallographic data are summarized in Table 3.1. The system crystallizes in the monoclinic *P2₁/n* space group. The crystal structure comprises two fragments. On the one hand it shows a non-planar central part corresponding to the photochromic unit, where the aryl thiophene rings are in the antiparallel conformation while the C13-C21 distance is shorter than 4 Å (3.612 Å). These two features are necessary conditions for the photocyclization reaction to proceed in the solid state.¹⁵ On the other hand, each aryl

ring is connected to an extended conjugated π system composed by a 1,3-diketone in its enolic form and an hydroxyphenyl ring. Both groups are almost coplanar, which is most probably due to the presence of intramolecular hydrogen bonds between O1-O2 and O2-O3 atoms (Figure 3.1) and extended conjugation. The coplanarity is likely reinforced by intermolecular interactions between neighbouring molecules in the lattice that lead to *zig-zag* chains in the *bc* crystallographic direction (Figure 3.2).

Table 3.1. Crystallographic data for **H₄L2**

Formula	C ₃₆ H ₃₄ O ₇ S ₂
<i>M_r</i>	642.75
Crystal system	Monoclinic
Space group	P2 ₁ / <i>n</i>
<i>a</i> [Å]	8.123(4)
<i>b</i> [Å]	14.639(7)
<i>c</i> [Å]	25.861(13)
α [°]	90
β [°]	90.75 (3)
γ [°]	90
<i>V</i> [Å ³]	3075(3)
ρ [g cm ⁻³]	1.388
shape and colour	Yellow block
<i>Z</i>	4
μ [mm ⁻¹]	0.225
reflns	5040
parameters	414
restrains	0
<i>R</i> _{int}	0.0707
<i>R</i> ₁	0.0578
<i>wR</i> ₂	0.1292
<i>S</i>	0.986

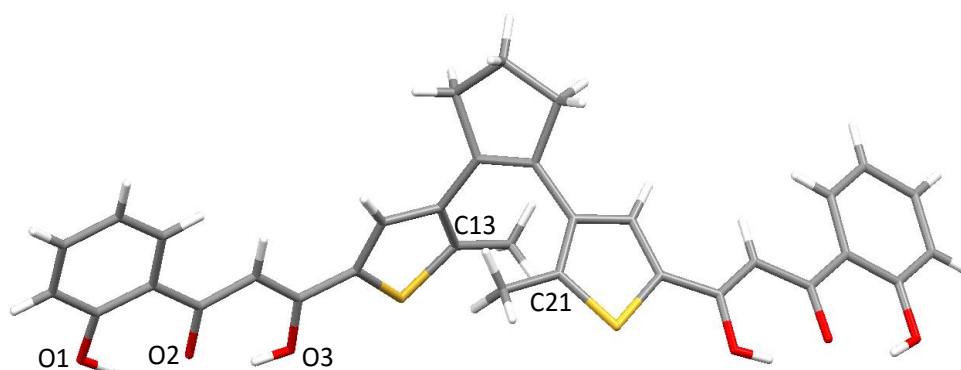


Figure 3.1: Molecular structure of ligand **H₄L2**.

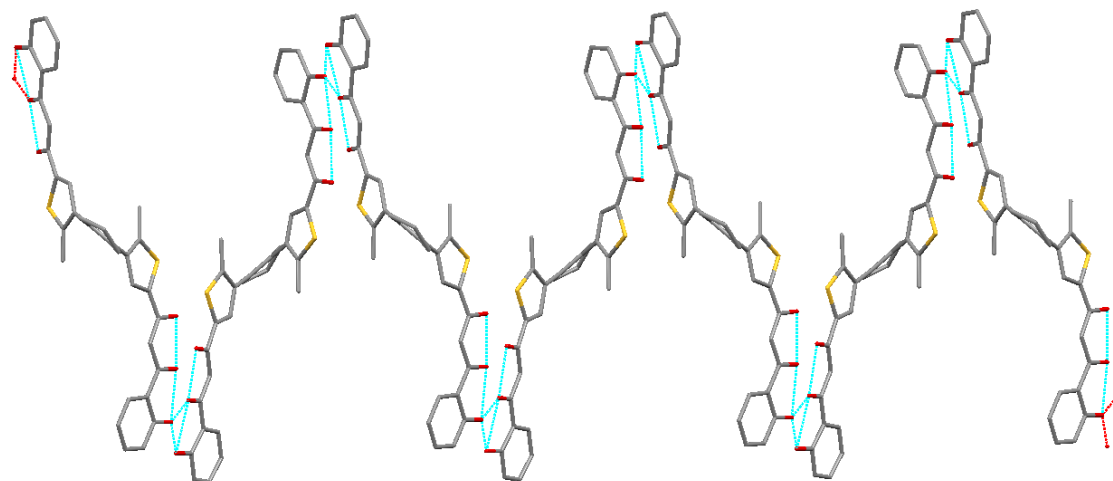


Figure 3.2: zig-zag chains in the *bc* crystallographic direction. Hydrogen bonds are marked in blue.

^1H NMR spectroscopy supports the purity and the enolic form of the new diarylethene molecule. In the Figure 3.3 the assigned spectrum is detailed.

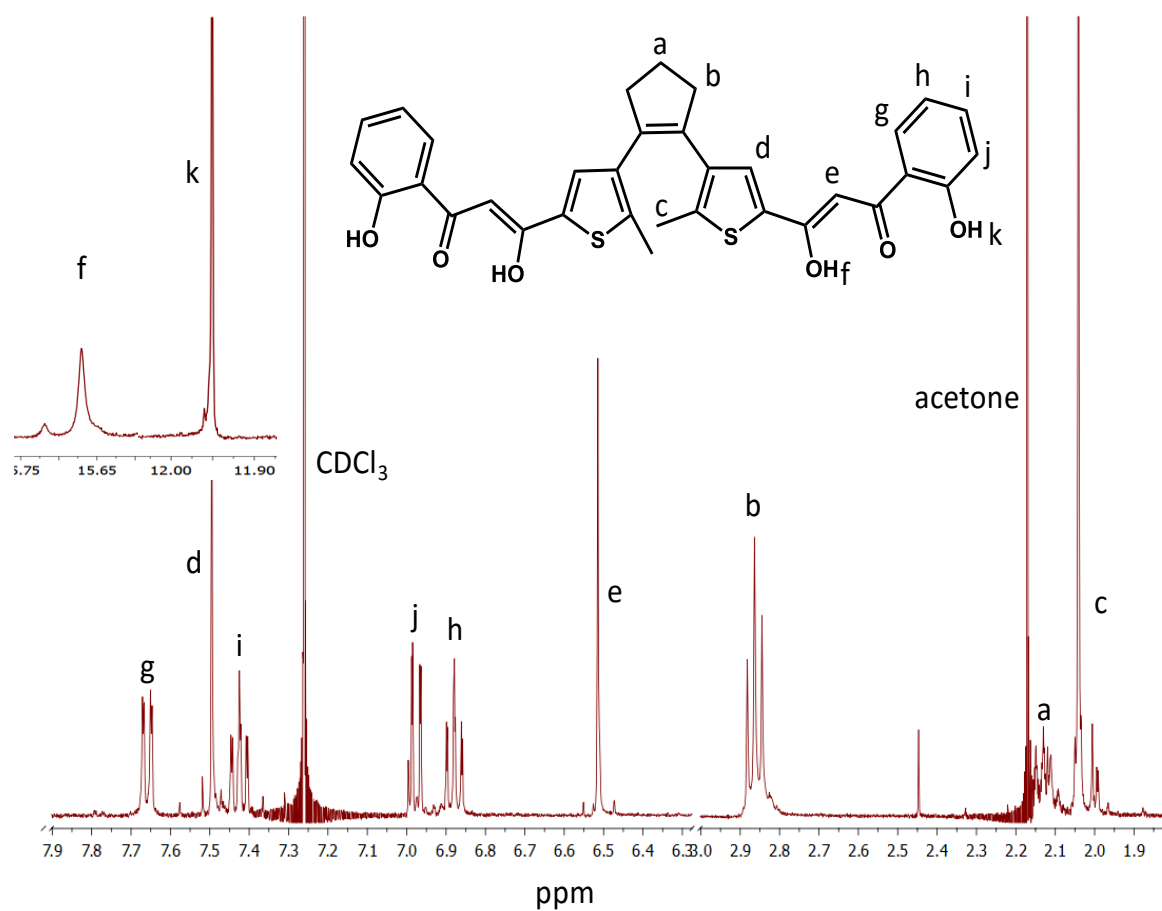


Figure 3.3: ^1H NMR of H_4L_2

3.2.3 Photochromic properties of **H₄L2**.

The photochromic behavior of **H₄L2** was studied by irradiation in solution with a Xenon lamp using pass band filters to select the wavelength and monitoring by UV-Vis spectroscopy. During this process, a photostationary state (PPS) is reached and an equilibrium between the open form and the closed form is established, determined by the quantum yields of ring-closing and ring-opening processes. Indeed, quantum yields obtained for diarylethenes showed that the cyclization is more efficient than the ring-opening¹⁶. Therefore, it can be assumed that the PSS represents essentially the closed form of the diarylethene. The cyclization of the dithienylcyclopentene unit leads to a clear change of colour, from pale yellow to blue (Figure 3.4). Figure 3.5a and 3.5b show the changes in the UV-Vis spectra of ligand **H₄L2** upon irradiation with UV and Visible light, respectively, of a 5×10^{-5} M solution of Toluene/DMSO (1:1). As can be observed, the ligand exhibits bands at 282 and 392 nm, ascribed to π - π^* and n - π^* transitions¹⁷ of the phenol and the diarylethene units respectively in the open form, which decrease after irradiation with UV light. Simultaneously, nearly at 615 nm, a new band attributed to similar transitions is featured by the closed form, progressively appears. Thus the extended polyenic system leads to transitions at longer wavelengths owing to the destabilization of the ground state and lowering of the HOMO/LUMO barrier. Remarkably, both spectra show the reversibility of the photoisomerization by recovering the original colouring upon irradiating the sample with the corresponding energy of light.

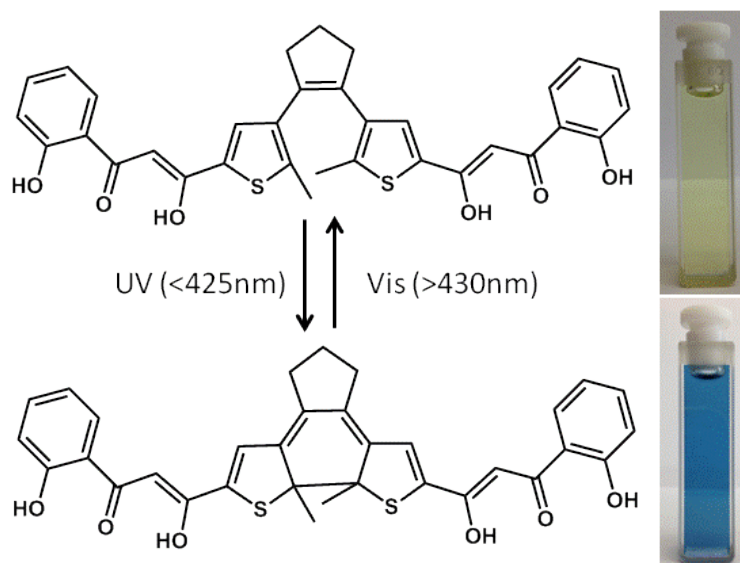


Figure 3.4: Cyclization of ligand **H₄L2** with its corresponding change of color.

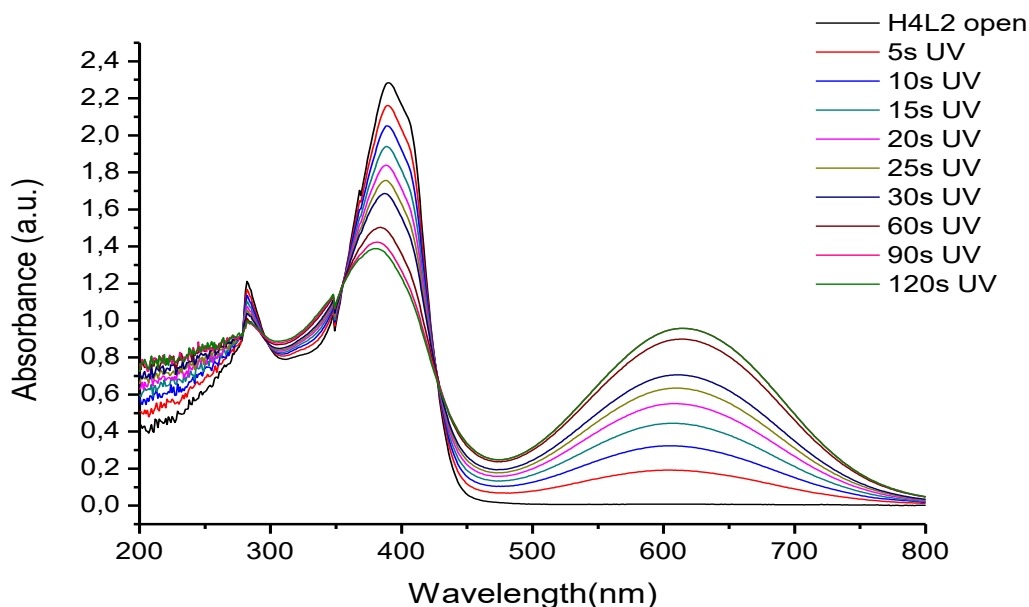


Figure 3.5a: UV-Vis spectra of open **H₄L₂** upon irradiation with UV light (<425nm).

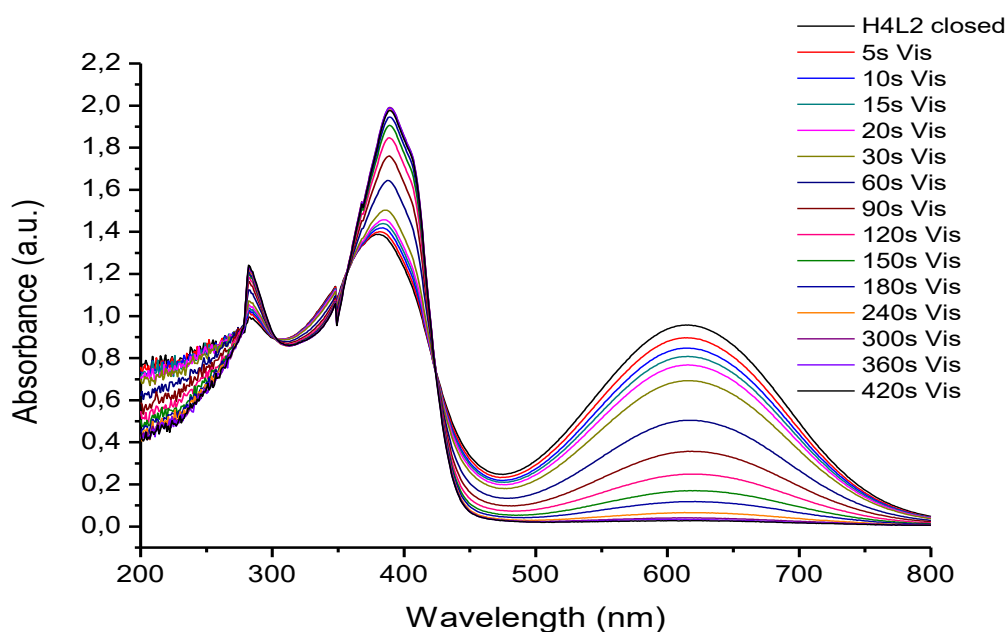


Figure 3.5b: UV-Vis spectra of closed **H₄L₂** upon irradiation with visible light (>430nm).

The occurrence of isosbestic points during the photoswitching processes indicates the presence of solely the two photoisomers at all times, which is crucial for the quantitative quantum yield of the photoreaction.

The spectra show also that the rate of the photochromic reactions are quiet fast: it takes 180s to reach the PSS during the ring closure and 240s to recover the initial state.

Another interesting feature of this ligand as a molecular switch, is its capacity to present fluorescence in the open form, which vanished upon ring closure^{18,19}.

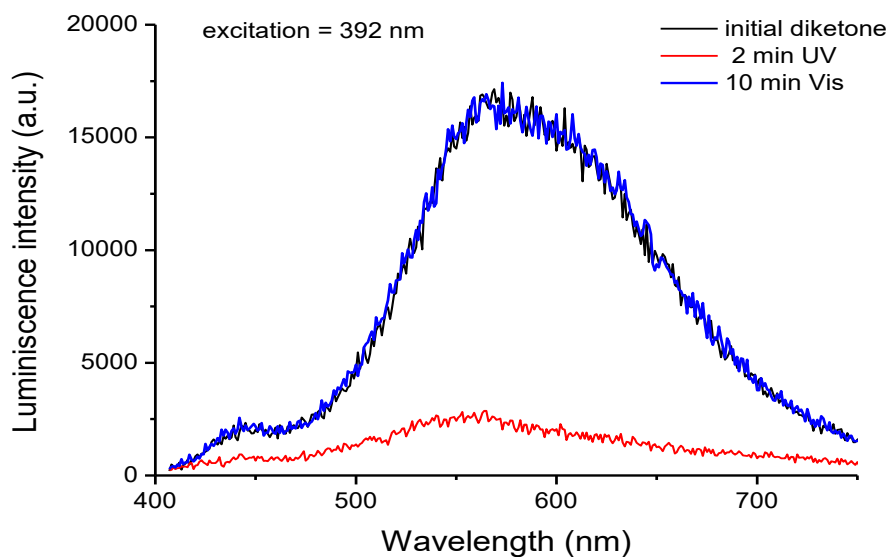


Figure 3.6: Fluorescence spectra for **H₄L₂**

The initial emission spectrum (Figure 3.6; black line) is dominated by a broad signal centered around 565nm when the compound is excited with light of 392 nm (corresponding to the maximum absorbance of the open form). This emission band is significantly decreased (Figure 3.6; red line) when the sample is irradiated during 2 min with UV light (< 425 nm). The fluorescence of the compound can be recovered

completely (Figure 3.6; blue line) after irradiation of the resulting system during 10 min with visible light ($> 430\text{nm}$).

The photochemical ring closure of **H₄L2** in CDCl_3 was observed also by ^1H NMR. Both the chemical shift of the methyl group and the thiophene proton of the photochromic unit before and after irradiation are displayed in Table 3.2. The upfield shift of the thienyl hydrogens by 1.04 ppm is most pronounced, and indicates that the aromatic character of the thiophene moiety is lost.²⁰

δCH_3 open	δCH_3 closed	$\delta\text{thiophene}$ open	$\delta\text{thiophene}$ closed
2.04	2.16	7.5	6.46

Table 3.2: ^1H MN chemical shift data before and after UV irradiation (δ in ppm)

4.2.4. Synthesis of 1,2-bis-(5-(3-oxo-3-(2-hydroxynaphthyl)-propanoyl)-2-methylthien-3-yl) cyclopentene (**H₄L3**)

Following the same approach for **H₄L2**, the use of 1-hydroxy-2-acetonaphone instead the 2-hydroxyacetophenone, leads to the diester **1,2-bis-(5-((2-acetylnaphthyl)-carboxylate)-2-methylthien-3-yl) cyclopentene L3a**. Subsequently, the intramolecular condensation gives compound **1,2-bis-(5-(3-oxo-3-(2-hydroxynaphthyl)-propanoyl)-2-methylthien-3-yl) cyclopentene (**H₄L3**)** (Figure 3.7), which crystallizes with ethyl acetate in the dark due to its sensitivity to light.

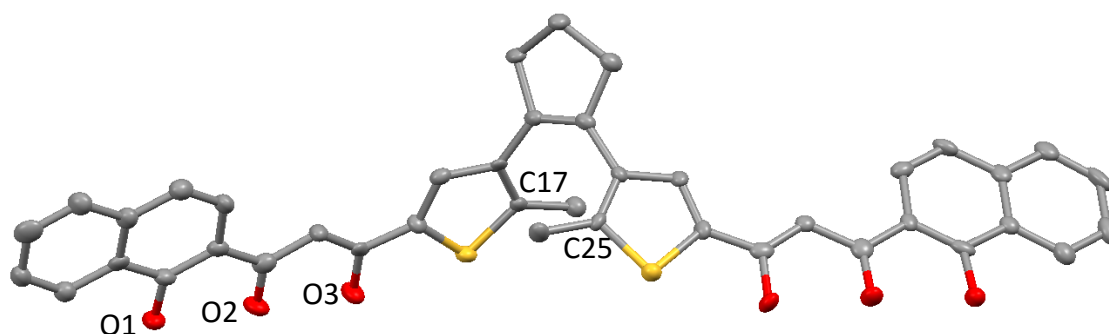


Figure 3.7: Molecular structure of **H₄L3**

H₄L3 has some similarities with **H₄L2** regarding the crystal structure. **H₄L3** crystallizes in the monoclinic space group $P21/n$. The corresponding crystallographic data are summarized in Table 3.2. The representation of figure 7 shows the photochromic

moiety with the methyl groups in the antiparallel conformation, with a distance between the reactive carbons of 3.601 Å. The presence of the same intra and inter molecular hydrogen bonds interactions gives the same type of *zig-zag* motif as before (Figure 3.8).

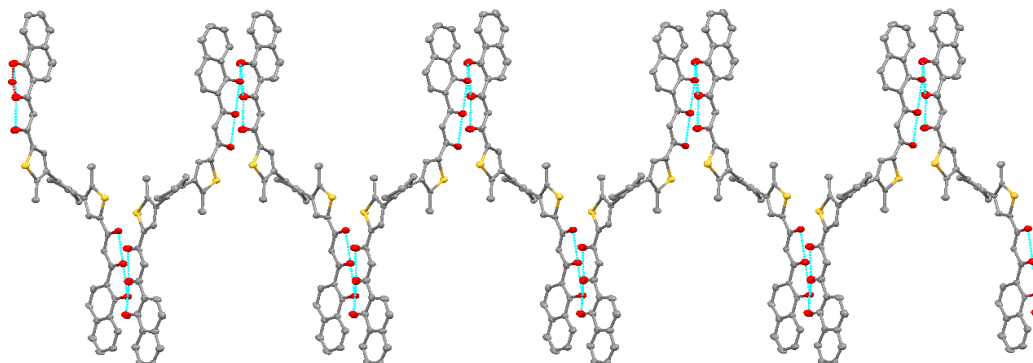


Figure 3.8: *zig-zag* chains in the *bc* crystallographic direction. Hydrogen bonds are marked in blue

In addition, the presence of the naphthyl group produce a more packed structure, thanks to the π - π interactions between them (Figure 3.9). These interactions added to the hydrogen bonds and the conjugation, give a high coplanarity of the naphthyl group and the diketone.

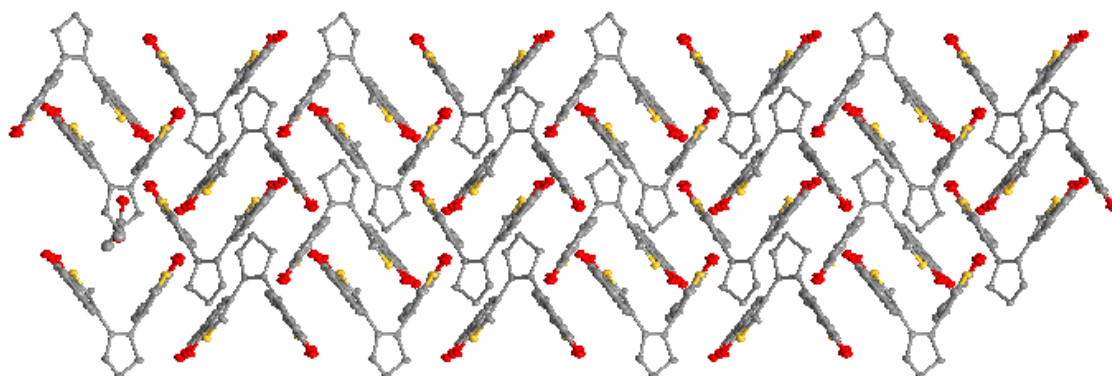


Figure 3.9: Crystal packing trough the *c* axis, showing the interactions between the naphthyl groups

Table 3.2. Crystallographic data for **H₄L3**

Formula	C ₄₅ H ₄₀ O ₈ S ₂
<i>M_r</i>	772.89
Crystal system	Monoclinic
Space group	P2 ₁ / <i>n</i>
<i>a</i> [Å]	8.108(2)

b [Å]	14.787(4)
c [Å]	30.971(9)
α [°]	90
β [°]	92.118 (3)
γ [°]	90
V [Å ³]	3710.6(3)
ρ [g cm ⁻³]	1.384
Color and shape	Yellow plates
Z	4
μ [mm ⁻¹]	0.201
reflns	4125
parameters	504
restrains	0
R_{int}	0.1075
R_1	0.0556
wR_2	0.1150
S	0.999

3.2.5 Photochromic behavior of **H₄L3**

The photochromic behavior of **H₄L3** is quite different in terms of reversibility. The shape of the open form is similar to the one of **H₄L2** (Figure 3.10). In that case, to obtain the spectrum of the pure open isomer, the solution was first irradiated with visible light due to the color change seen even without irradiating with UV light. The latter was evidence of the sensitivity of this compound. Similar to **H₄L2**, **H₄L3** features two bands centered at 281 and 422 nm, respectively related to π - π^* and n - π^* transitions. The redshift of the latter can be ascribed to the higher conjugation of the naphthone group. After irradiation with UV light (<425nm) the band at 422nm starts to decrease giving place to another one at 380 nm, accompanied by the formation of a new broad band centered at 640 nm. The PSS can be reached after 120s of exposure to UV light, as Figure 10 shows. When the solution is irradiated with Visible light (>430nm) (Figure 3.11), the band ascribed to the extended conjugated system, disappears in 600s, a longer time than the same process with ligand **H₄L2**. Moreover, the band at 422 nm cannot be fully recovered while the band at 380 nm is blue shifted to 370 nm. The peak at 280 nm is maintained during the whole process.

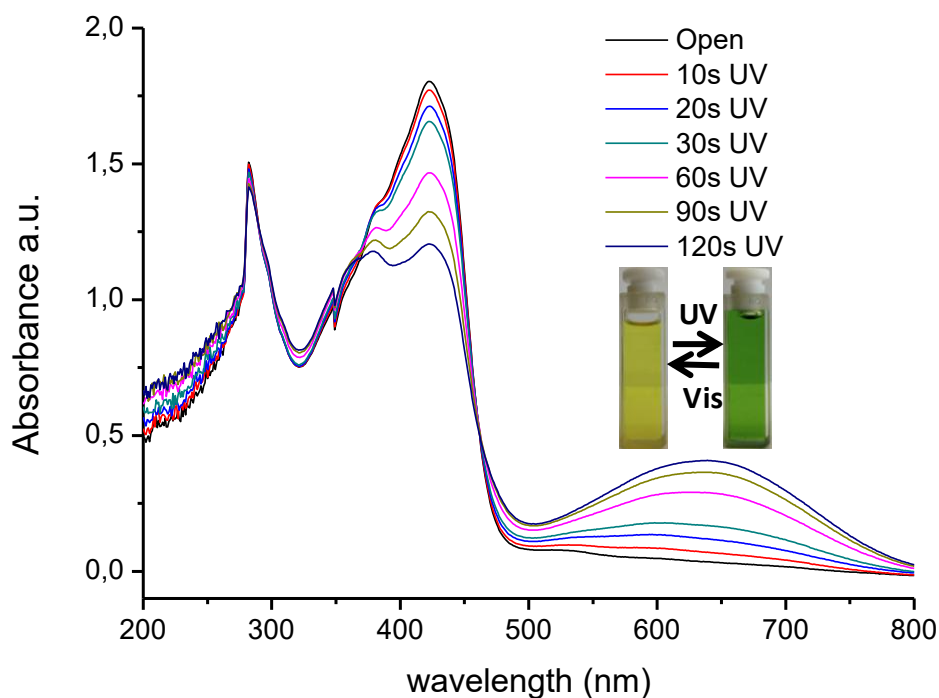


Figure 3.10: UV-Vis spectra of open H₄L3 upon irradiation with UV light (<425nm).

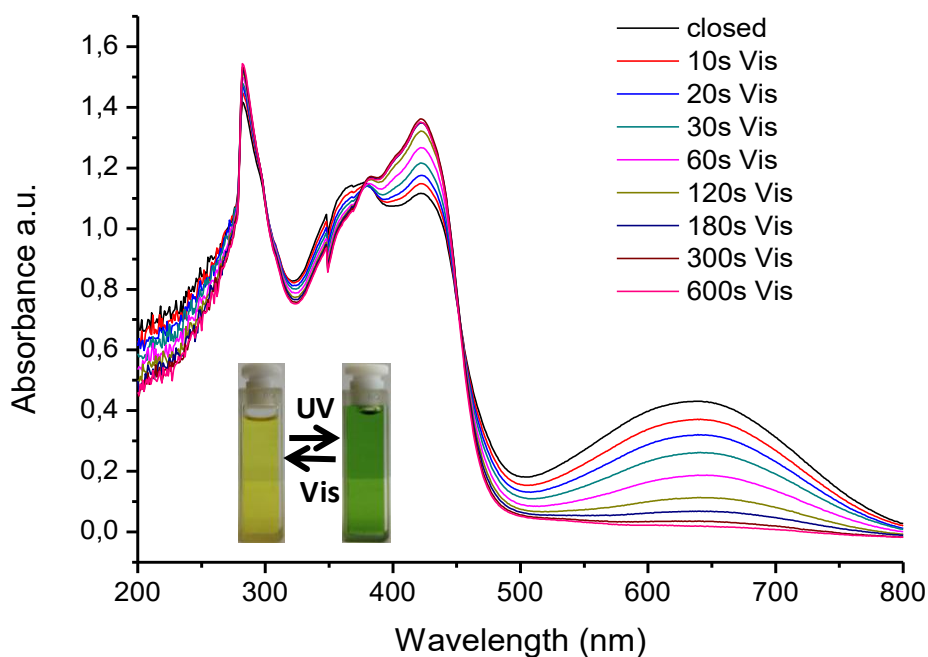


Figure 3.11: UV-Vis spectra of closed H₄L3 upon irradiation with visible light (>430nm).

All these differences are indicative of a change or degradation of the initial compound, thus leading to the formation of new species. A similar situation was described by the group of Branda²¹, where the large exposure to UV light, converts the photochromic unit in a new specie which is not able to turn back into the initial compound. This is

possibly less probable here since this new compound has a much more extended conjugation and a residual band in the visible range should be appear. One possibility could be that the exposure to UV light damages beta-diketone group, via the Norrish type I mechanism, where the diketone can be converted into radicals which can react with each other, forming new compounds²²⁻²⁴. Another hypothesis may have to do with the ketoenolic equilibrium of the beta-diketones. In solution, these tautomers reach an equilibrium that depends on the nature of the solvent. The stabilization of the enol form by intramolecular hydrogen bonding is more pronounced when there is no competition with the solvent. Hence, the proportion of the enolic form is much greater in apolar or polar aprotic solvents than in polar protic solvents. Here, the UV light might also induce changes to this equilibrium, so that the different peaks at 380 and 420 nm are affected²⁴. Taking into account that both processes have isosbestic points, this explanation is the most plausible and further research is thus necessary to clarify this

3.2.6 Fluorescence of **H₄L3**

Similar to ligand **H₄L2**, **H₄L3** presents fluorescence depending on the isomer.

In Figure 3.12 the changes on the luminescence intensity between the isomers is shown.

The open isomer presents a big band centered a 492nm when the compound is excited with 380nm (black line). The intensity starts to decrease (red line) while the compound is irradiated with UV light (<425nm), till complete extinction of fluorescence after 240 seconds of UV irradiation (blue line). The process is totally reversible when the compound is irradiated with Visible light (>430nm), obtaining after 500 seconds the initial fluorescence spectrum of **H₄L3** (pink line).

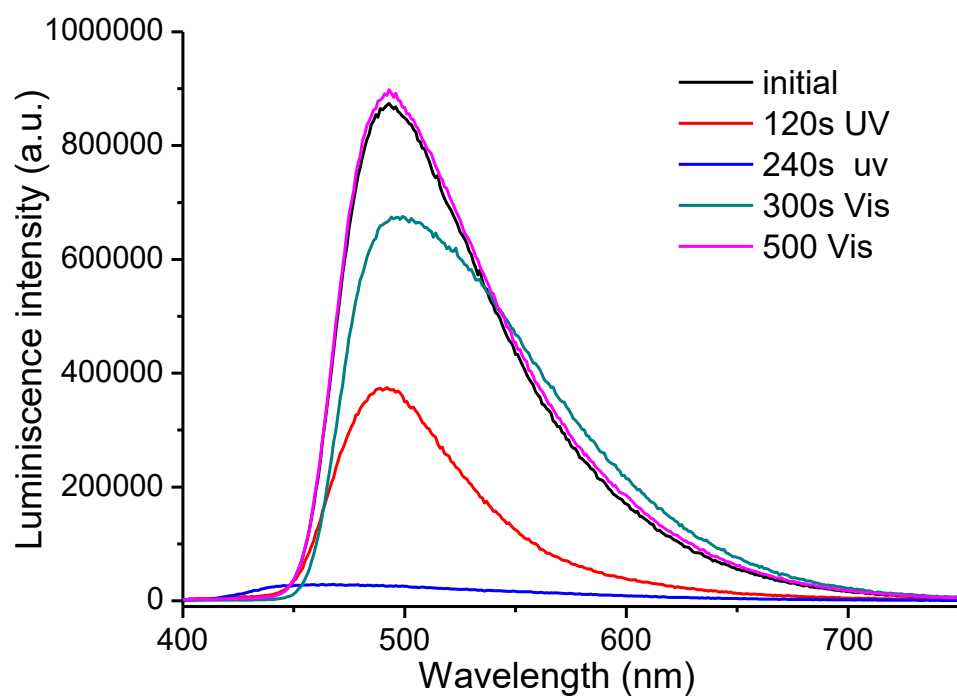


Figure 3.12: Fluorescence spectra for **H₄L3**

3.3. Synthesis of coordination compounds

3.3.1 Homometallic pairs of dimers [MM···MM]. Synthesis and crystal structures

The results obtained previously in our group showed that a beta-diketone in combination with a phenol moiety, with protons of different acidity, can be used to tune the nuclearity of the resulting complexes by simply using the appropriate base strength and amount.^{25,26} Also, we have demonstrated that the combination of a beta-diketones and phenols with a spacer leads to the preparation of pairs of dimers in linear arrays. We intend to use this approach to introduce a photochromic unit as a spacer between the two possible metal dimers. The aim is to switch the coupling between them, using an external stimulus, which in this case is light.

Reaction of **H₄L2** with a metal precursor (metal ion, M^{II} = Cu, Co, Ni, Zn) and NBu₄OH (1:2:4 molar ratio) in pyridine, produces the expected homometallic tetranuclear [MM···MM] complexes: [Cu₄L₂(py)₆]·9(py) (**5**), [Co₄L₂(py)₆]·9(py) (**6**), [Ni₄L₂(py)₆]·9(py) (**7**), [Zn₄L₂(py)₆]·9(py) (**8**). These were obtained as crystals after layering the solutions with different solvents (ether or hexanes).

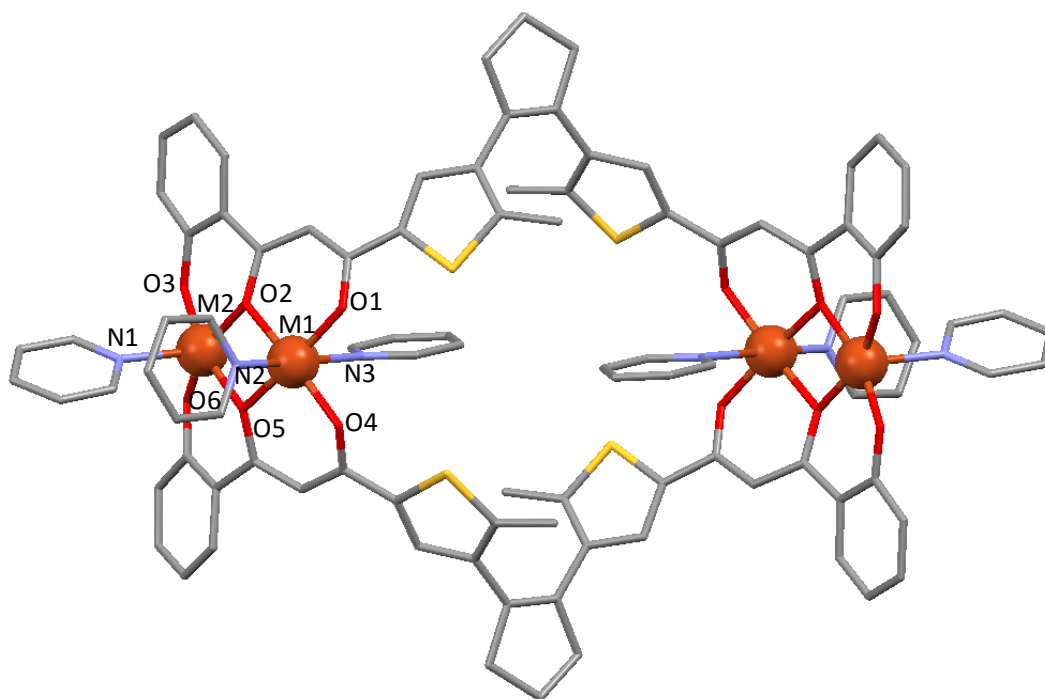


Figure 3.13: Crystal structure of [M₄L₂(py)₆]·9(py). Hydrogen atoms and solvent pyridine molecules were omitted for clarity.

Complexes **5** to **8** are isostructural and crystallize in the orthorhombic space group *Pbca*. All compounds present nine additional lattice molecules of pyridine per asymmetric unit. The structure of these complexes reveals a linear arrangement of four metal ions disposed as two independent metal pairs. The average metal-metal distances within the pairs are 3.133 Å, whereas it is 11.277 Å between the inner metals of different dimers. This arrangement is in agreement with the full deprotonation of two **H₄L2** ligands, which dispose all the oxygen donor atoms at two opposite sides for coordination (Figure 3.13). The latter coordinate the equatorial sites of the metals forming six-member chelate rings (four per ligand and two per metal), leading to a $\eta^6:\mu_4-L^4$ coordination mode. The axial positions are occupied by either two or one pyridine molecules giving rise to six or five-coordinated metals, respectively. This striking difference in coordination environment between the metals was firstly observed in similar compounds with [MM...MM] topologies and β -diketone based ligands related to **H₂L2**.²⁷ In that work the coordination number site-dependence was suggested to be related with the C-C-C angles of the chelating rings (1,3-diketonate versus 2-hydroxybenzoyl) (Figure 3.14).

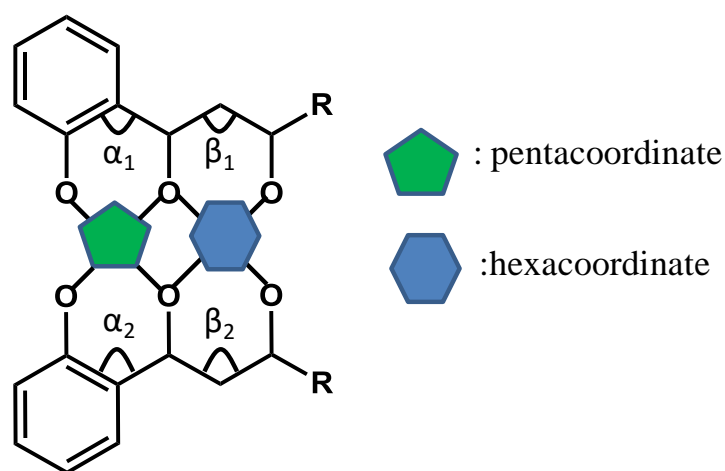


Figure 3.14: site-dependent coordination mode due to the C-C-C angle.

Compound	α_1	α_2	α average(°)	β_1	β_2	β average(°)
Cu ₄	122.31	123.42	122.865	126.96	127.57	127.265
Co ₄	120.19	123.54	121.865	126.70	127.81	127.255
Ni ₄	119.83	123.33	121.58	126.64	127.75	127.195
Zn ₄	121.33	123.52	122.425	128.02	127.08	127.55

Table 3.3: C-C-C angles for the chelating rings.

Interestingly, the latter was some degrees smaller, 122° vs 127° , which was attributed to the stiffness provided by the phenylene moiety where the C-C-C angle was embedded. Hence, an equatorial-square environment is too small for the metals to fit in giving rise to a pyramidalization of the geometry. This distortion hinders the coordination of a ligand in the remaining axial position. The complexes reported in this work exhibit the same angle differences (i.e. average of 122° and 127° , see Table 3.3), thus corroborating the structure correlation earlier observed. The pyramidalization is evidenced by a mean distance average between the metal ion and the equatorial plane of 0.39 \AA (Table 3.4). Another interesting parameter observed is the angle between the two basal planes (average 22.19° , Figure 3.15). Crystallographic and metric parameters are listed in Tables 3.5-3.8.

Compound	τ	Curvature($^\circ$)	Distance to plane(\AA)
Cu4	0.08	23.44	0.298
Co4	0.27	22.94	0.443
Ni4	0.07	20.97	0.354
Zn4	0.17	23.14	0.502

Table 3.4: Distortion data for the homometallic compounds

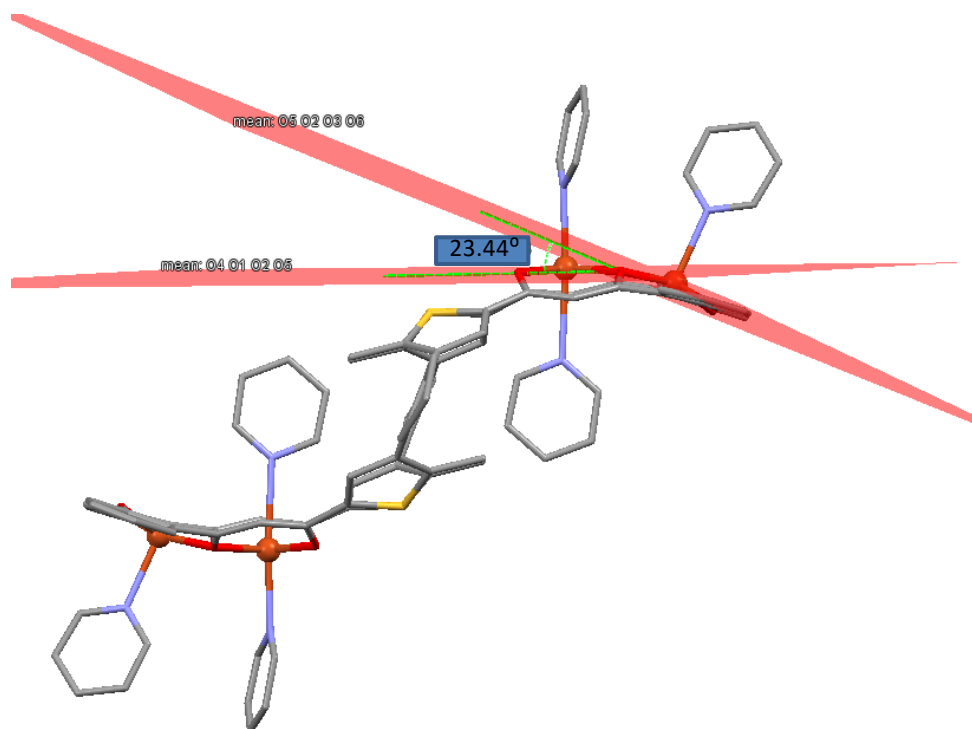


Figure 3.15: Angle between basal planes.

formula	$\text{C}_{141}\text{H}_{123}\text{Cu}_4\text{N}_{15}\text{O}_{12}\text{S}_4$	Cu1-O1	1.929(3)	O2-Cu1-N2	92.6(1)
M_r	2601.94	Cu1-O2	1.978(3)	O2-Cu1-O4	170.5(1)
Crystal system	orthorhombic	Cu1-O4	1.938(3)	O2-Cu1-O5	79.1(1)
space group	Pbca	Cu1-O5	1.968(3)	O2-Cu1-N3	89.2(1)
a [\AA]	24.4217(15)	Cu1-N2	2.266(3)	O4-Cu1-O5	93.4(1)
b [\AA]	16.9289(10)	Cu1-N3	2.554(3)	O4-Cu1-N2	93.8(1)
c [\AA]	29.8588(18)	Cu2-O2	1.982(3)	O4-Cu1-N3	84.8(1)
$\alpha = \beta = \gamma$ [$^\circ$]	90	Cu2-O3	1.906(3)	O5-Cu1-N2	94.4(1)
V [\AA^3]	12344.6(13)	Cu2-O5	1.994(3)	O5-Cu1-N3	89.4(1)
Z	4	Cu2-O6	1.897(3)	O2-Cu2-O3	92.6(1)
ρ [g cm^{-3}]	1.400	Cu2-N1	2.205(3)	O2-Cu2-O5	78.3(1)
shape;colour	orange block	Cu1-Cu2	3.053(1)	O2-Cu2-O6	159.9(1)
μ [mm^{-1}]	0.818	Cu1-Cu1'	11.349(1)	O2-Cu2-N1	102.3(1)
reflns	12599	Cu1-O2-Cu2	100.9(1)	O3-Cu2-O5	164.6(1)
parameters	822	Cu1-O5-Cu2	100.8(1)	O3-Cu2-O6	91.9(1)
restrains	120	O1-Cu1-O2	94.0(1)	O3-Cu2-N1	97.5(1)
R_{int}	0.0973	O1-Cu1-O4	92.9(1)	O5-Cu2-O6	92.6(1)
R_1	0.0530	O1-Cu1-O5	171.0(1)	O5-Cu2-N1	96.6(1)
$wR2$	0.1673	O1-Cu1-N2	91.6(1)	O6-Cu2-N1	96.6(1)
S	1.049	O1-Cu1-N3	84.7(1)	N2-Cu1-N3	176.0(1)

formula	$\text{C}_{141}\text{H}_{123}\text{Co}_4\text{N}_{15}\text{O}_{12}\text{S}_4$	Co1-O1	1.992(4)	O2-Co1-N2	90.3(2)
M_r	2583.50	Co1-O2	2.093(3)	O2-Co1-O4	169.0(1)
Crystal system	orthorhombic	Co1-O4	2.009(4)	O2-Co1-O5	80.3(1)
space group	Pbca	Co1-O5	2.057(4)	O2-Co1-N3	90.6(2)
a [\AA]	24.2449(12)	Co1-N2	2.133(5)	O4-Co1-O5	89.1(1)
b [\AA]	16.6486(8)	Co1-N3	2.215(5)	O4-Co1-N2	92.5(2)
c [\AA]	30.3308(15)	Co2-O2	2.030(4)	O4-Co1-N3	87.2(2)
$\alpha = \beta = \gamma$ [$^\circ$]	90	Co2-O3	1.938(4)	O5-Co1-N2	90.7(2)
V [\AA^3]	12242.8(10)	Co2-O5	2.152(4)	O5-Co1-N3	92.6(2)
Z	4	Co2-O6	1.926(4)	O2-Co2-O3	89.2(1)
ρ [g cm^{-3}]	1.402	Co2-N1	2.053(5)	O2-Co2-O5	79.5(1)
shape;colour	orange plate	Co1-Co2	3.189(1)	O2-Co2-O6	146.5(2)
μ [mm^{-1}]	0.671	Co1-Co1'	11.227(1)	O2-Co2-N1	108.8(2)
reflns	11449	Co1-O2-Co2	101.3(2)	O3-Co2-O5	162.8(1)
parameters	792	Co1-O5-Co2	98.5(1)	O3-Co2-O6	97.8(2)
restrains	148	O1-Co1-O2	89.8(1)	O3-Co2-N1	101.2(2)
R_{int}	0.1138	O1-Co1-O4	100.8(1)	O5-Co2-O6	85.0(1)
R_1	0.0739	O1-Co1-O5	170.0(1)	O5-Co2-N1	94.8(2)
$wR2$	0.2316	O1-Co1-N2	90.1(2)	O6-Co2-N1	101.9(2)
S	1.037	O1-Co1-N3	86.7(2)	N2-Co1-N3	176.7(2)

formula	C ₁₄₁ H ₁₂₃ Ni ₄ N ₁₅ O ₁₂ S ₄	Ni1-O1	1.988(9)	O2-Ni1-N2	89.8(3)
M_r	2582.62	Ni1-O2	2.045(8)	O2-Ni1-O4	172.2(3)
Crystal system	orthorhombic	Ni1-O4	2.012(6)	O2-Ni1-O5	82.5(3)
space group	Pbca	Ni1-O5	2.040(9)	O2-Ni1-N3	91.5(3)
a [Å]	24.365(6)	Ni1-N2	2.073(8)	O4-Ni1-O5	89.9(3)
b [Å]	16.439(4)	Ni1-N3	2.146(8)	O4-Ni1-N2	92.1(3)
c [Å]	30.389(7)	Ni2-O2	2.018(9)	O4-Ni1-N3	87.1(3)
$\alpha = \beta = \gamma$ [°]	90	Ni2-O3	1.953(8)	O5-Ni1-N2	91.0(3)
V [Å ³]	12172(5)	Ni2-O5	2.031(8)	O5-Ni1-N3	92.6(3)
Z	4	Ni2-O6	1.935(9)	O2-Ni2-O3	87.6(3)
ρ [g cm ⁻³]	1.323	Ni2-N1	1.99(1)	O2-Ni2-O5	83.4(3)
shape;colour	orange plate	Ni1-Ni2	3.043(1)	O2-Ni2-O6	157.4(3)
μ [mm ⁻¹]	0.935	Ni1-Ni1'	11.292 (1)	O2-Ni2-N1	106.8(4)
reflns	6907	Ni1-O2-Ni2	97.0(3)	O3-Ni2-O5	161.4(3)
parameters	769	Ni1-O5-Ni2	96.7(3)	O3-Ni2-O6	94.3(3)
restrains	403	O1-Ni1-O2	91.4(3)	O3-Ni2-N1	98.4(4)
R_{int}	0.1637	O1-Ni1-O4	96.2(3)	O5-Ni2-O6	88.1(3)
R_1	0.0963	O1-Ni1-O5	173.7(3)	O5-Ni2-N1	99.7(4)
$wR2$	0.3069	O1-Ni1-N2	90.0(3)	O6-Ni2-N1	95.2(4)
S	1.052	O1-Ni1-N3	86.5(3)	N2-Ni1-N3	176.3(3)

formula	C ₁₄₁ H ₁₂₃ Zn ₄ N ₁₅ O ₁₂ S ₄	Zn1-O1	2.008(3)	O2-Zn1-N2	90.4(1)
M_r	2609.26	Zn1-O2	2.089(3)	O2-Zn1-O4	168.2(1)
Crystal system	orthorhombic	Zn1-O4	2.019(3)	O2-Zn1-O5	79.3(1)
space group	Pbca	Zn1-O5	2.084(3)	O2-Zn1-N3	89.9(1)
a [Å]	24.3925(13)	Zn1-N2	2.141(3)	O4-Zn1-O5	89.3(1)
b [Å]	16.7691(12)	Zn1-N3	2.275(3)	O4-Zn1-N2	92.9(1)
c [Å]	30.2900(19)	Zn2-O2	2.089(3)	O4-Zn1-N3	87.4(1)
$\alpha = \beta = \gamma$ [°]	90	Zn2-O3	1.956(4)	O5-Zn1-N2	91.0(1)
V [Å ³]	12389.8(14)	Zn2-O5	2.142(3)	O5-Zn1-N3	91.7(1)
Z	4	Zn2-O6	1.951(3)	O2-Zn2-O3	87.9(1)
ρ [g cm ⁻³]	1.399	Zn2-N1	2.044(5)	O2-Zn2-O5	78.0(1)
shape;colour	green plate	Zn1-Zn2	3.248(1)	O2-Zn2-O6	146.5(1)
μ [mm ⁻¹]	0.902	Zn1-Zn1'	11.239(1)	O2-Zn2-N1	108.0(2)
reflns	8893	Zn1-O2-Zn2	102.0(1)	O3-Zn2-O5	156.6(1)
parameters	810	Zn1-O5-Zn2	100.5(1)	O3-Zn2-O6	95.6(1)
restrains	163	O1-Zn1-O2	90.1(1)	O3-Zn2-N1	103.1(2)
R_{int}	0.0787	O1-Zn1-O4	101.2(1)	O5-Zn2-O6	86.4(1)
R_1	0.0510	O1-Zn1-O5	169.3(1)	O5-Zn2-N1	99.1(2)
$wR2$	0.1515	O1-Zn1-N2	90.6(1)	O6-Zn2-N1	103.6(2)
S	1.065	O1-Zn1-N3	86.6(1)	N2-Zn1-N3	177.3(1)

3.3.2. Magnetic properties of $[M_4(L2)_2(py)_6]$ complexes

The main goal of this chapter, is the synthesis of systems having two well independent clusters with a weak interaction between them, where each entity will act as a qubit, and its coupling within the molecule switch with light. In relation to this, the magnetic properties of complexes **5-7** have been measured, and the results are presented in the form of $\chi_M T$ versus T plots (χ_M is the molar paramagnetic susceptibility). Complex **8** has not been measured owing to the diamagnetic nature of zinc. The data have been analyzed and fitted by means of PHI program which uses the spin-coupling Hamiltonian convention of $H = -2JS_iS_j$.²⁸ In all complexes the magnetic interaction between the metal centers via the photochromic unit is expected to be very weak due to its extended length. Thus, to a first approximation, these tetranuclear systems can be magnetically treated as pairs of dimers where the main magnetic coupling pathway is through the diketone O double bridge. (Figure 3.16)

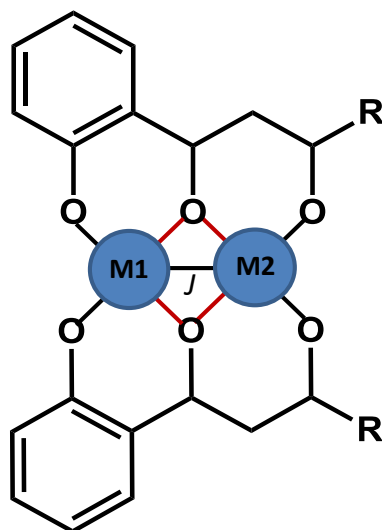


Figure 3.16: Magnetic exchange via the diketone O double bridge.

The $\chi_M T$ versus T plot for complex **5** ($[Cu_2]_2$) (Figure 3.17) clearly shows a sharp decrease of the susceptibility from 300 K to 100 K, where it reaches a plateau near zero. This behavior indicates strong antiferromagnetic coupling within the $[Cu_2]$ pairs. As a consequence $\chi_M T$ values at 300 K ($0.48 \text{ cm}^3 \text{ K mol}^{-1}$) are lower than the expected for a spin-only system ($1.5 \text{ cm}^3 \text{ K mol}^{-1}$, calculated value for four Cu^{II} centers with $S = 1/2$ and $g = 2$).²⁷ This very strong coupling prevents the observation of any possible coupling between the pair of dimers. The data could be fit giving rise to $J = -239 \text{ cm}^{-1}$, $g = 2.02$ and $S = 1/2$ monomer impurity of 0.20.

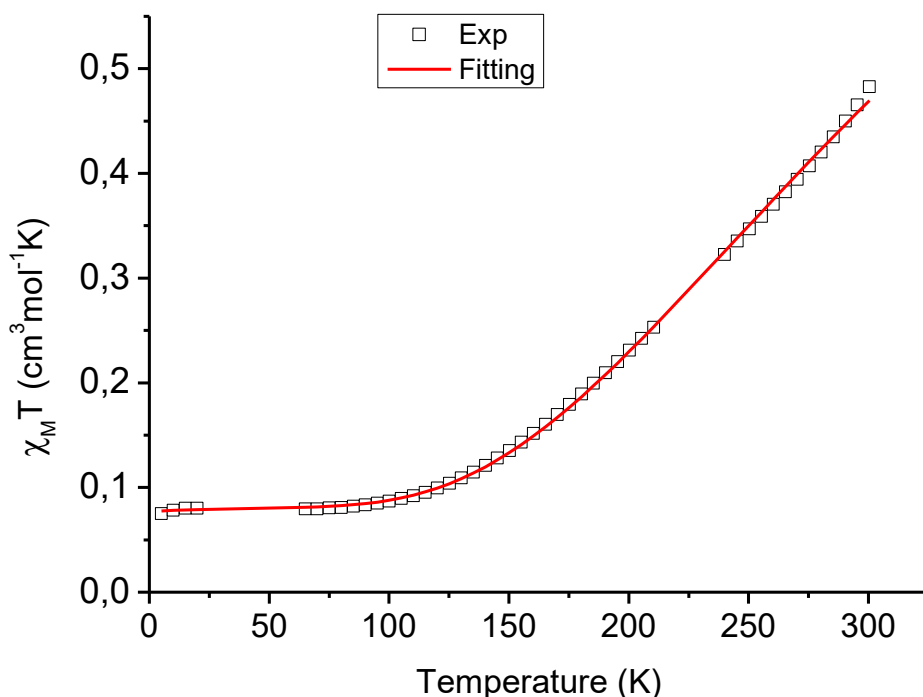


Figure 3.17: Plot of $\chi_M T$ vs T per mol of complex **5** at constant field of 0.5T.

This magnitude for the antiferromagnetic coupling is in line with other similar compounds^{29,30} having these type of interactions with Cu-O-Cu moieties, involving alcoxide bridges, with angles around 100° (Cu1-O2-Cu2: 100.9° ; Cu1-O5-Cu2: 100.8°).

This strong antiferromagnetic coupling, leads to the vanishing of the total spin momentum for each dimer [Cu₂], so this compound has not the possibility to act as a pairs of well defined qubits (at least in the ground state), taking into account the definition of a qubit.

The curve for complex **6** ([Co₂]₂) (Figure 3.18) denotes the occurrence of spin-orbit coupling (SOC) which clearly affects the susceptibility leading to higher values at 300K ($11.11 \text{ cm}^3 \text{ K mol}^{-1}$) with respect to those calculated for four non-interacting $S = 3/2$ centres and $g = 2$ ($7.5 \text{ cm}^3 \text{ K mol}^{-1}$).²⁷ Hence, the magnetic data could not be fit with a spin-only Heisenberg Hamiltonian, instead the orbital reduction and SOC parameters were introduced. The best fit of the data was obtained by fixing the orbital reduction at -1.5 (tabulated value for a Co^{II} free ion with octahedral geometry; see the *User Manual* provided with the PHI code)²⁸ which led to $J = -5 \text{ cm}^{-1}$, $g = 2.03$, a spin-orbit coupling parameter (λ) of -103.5 cm^{-1} and $S = 3/2$ monomer impurity of 0.24. Although λ deviates from the -171.5 cm^{-1} value found for a Co^{II} free ion, it's in line with those recently

reported in the literature.³¹ The non-zero value of $\chi_M T$ at low temperatures may be likely due to the presence of the small amount of paramagnetic impurity.

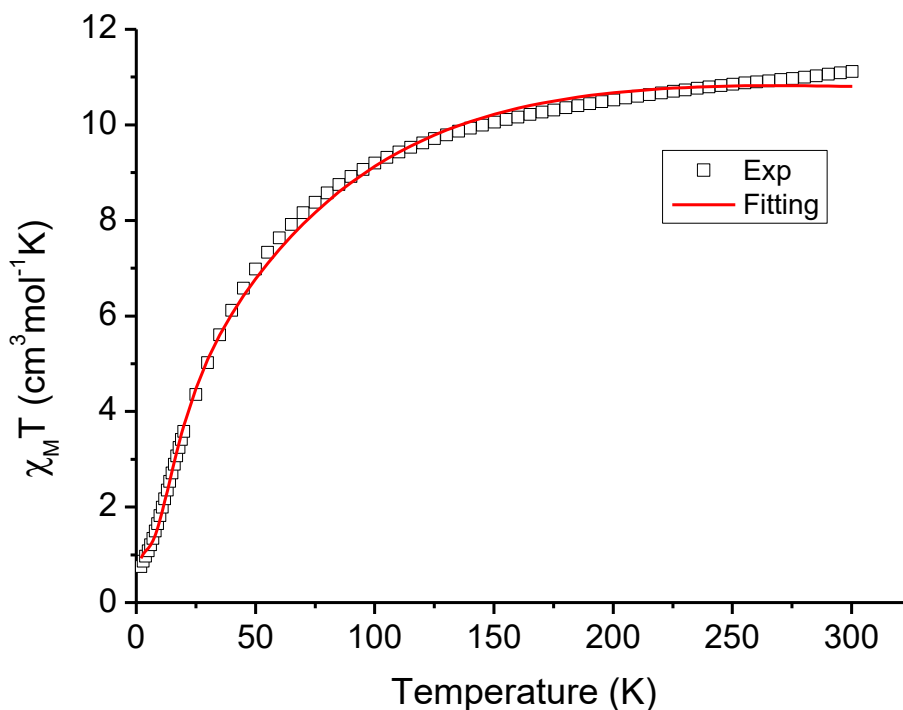


Figure 3.18: Plot of $\chi_M T$ vs T per mol of complex **6** at constant field of 0.5T.

Here again, the total suppression of the spin momentum is achieved, without possibilities to be use in the field of quantum computing.

The results for complex **7** ($[\text{Ni}_2]_2$) (Figure 3.19) show a $\chi_M T$ curve starting at $4.43 \text{ cm}^3 \text{ K mol}^{-1}$ ($4 \text{ cm}^3 \text{ K mol}^{-1}$: calculated value for four magnetically isolated Ni^{II} centres and $g = 2$) which strongly decreases below near 100 K to reach $0.5 \text{ cm}^3 \text{ K mol}^{-1}$ at 2 K. The first data fitting was performed without using the single-ion zero field splitting parameter (ZFS) commonly exhibited by $S = 1$ paramagnetic centres, considering, thus, the overall decreasing profile of the susceptibility solely owing to antiferromagnetically coupled $[\text{Ni}_2]_2$ pairs. The results obtained with $J = -8.9 \text{ cm}^{-1}$ and $g = 2.15$, were slightly modified to $J = -5.5 \text{ cm}^{-1}$ and $g = 2.14$ (with the residual error improved from 4.68 to 1.95) when ZFS reached a value of 70.0 cm^{-1} . However, ZFC falls far from the values encountered in the literature ($\pm 10 \text{ cm}^{-1}$) for compounds containing octahedral Ni^{II} ions.^{32,33} An attempt was then done by fixing ZFS = 10.0 cm^{-1} and $g = 2.5$ and fitting the exchange coupling, the amount $S = 1$ paramagnetic impurities (IM) and intermolecular interactions (ZJ). The results attain gave $J = -2.7 \text{ cm}^{-1}$, IM = 0.19 and ZJ = -1.7 cm^{-1}

(residual error of 1.95), reflect that intermolecular interactions are within the range of J values and can, thus, be masked by the latter. Moreover it's clearly seen that even though the presence of paramagnetic impurities explains the $\chi_M T$ value of $0.5 \text{ cm}^3 \text{ K mol}^{-1}$ at 2 K, their inclusion requires higher g values ($g=2.5$)

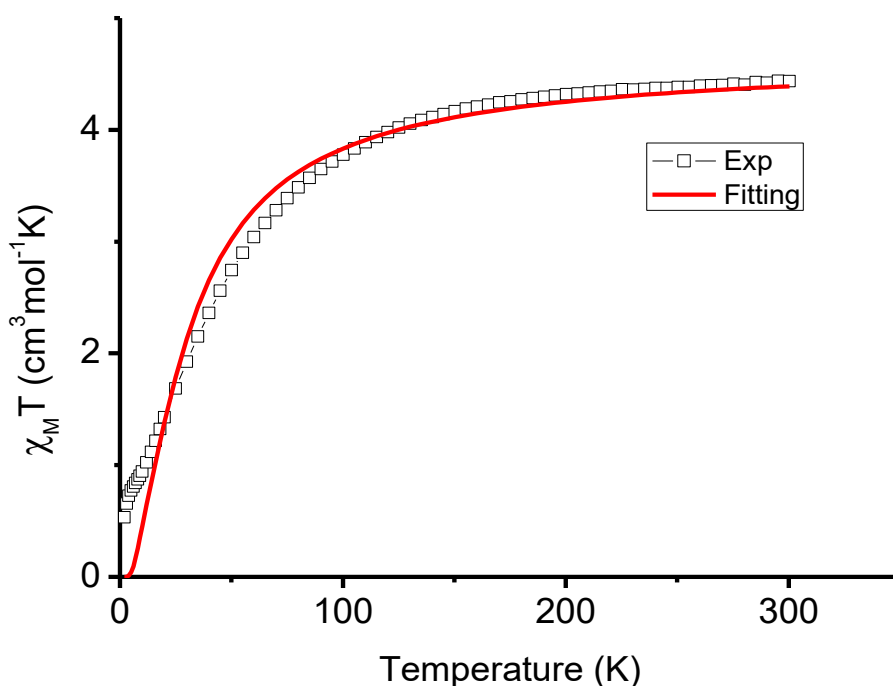


Figure 3.19: Plot of $\chi_M T$ vs T per mol of complex **7** at constant field of 0.5T.

As in the other homometallic compounds, each nickel pair loses its potential as a qubit prototype due to suppression of the spin.

The suppression of the total spin momentum of the studied systems due to the antiferromagnetic interaction within each dimer, prevents to create the desired electronic spin that should act as qubit, hence, the impossibility to evaluate the possible entanglement between the spin wave functions of both parts of the molecule.

Thus, another pathway is needed to search a none zero electronic spin on each side. The site dependent coordination number seen in these structures, could be used to reach this goal.

3.4 Heterometallic pair of dimers [MM'···M'M]

3.4.1 Synthesis and crystal structures

The site-dependent coordination number observed on the previous compounds was exploited to synthesize pure heterometallic clusters based on the different trends of transition metal ions to exhibit either octahedral or square pyramidal geometry.²⁷ This coordination environment selectivity lead to compounds **9** to **13**: [Cu₂Ni₂L₂(py)₆]·9(py) (**9**), [Co₂Ni₂L₂(py)₆]·9(py) (**10**), [Co₂Cu₂L₂(py)₆]·9(py) (**11**), [Cu₂Zn₂L₂(py)₆]·9(py) (**12**) and [Ni₂Zn₂L₂(py)₆]·9(py) (**13**), prepared by mixing with **H₄L2** two dissimilar metal ions in pyridine and using NBU₄OH as base. Crystals were obtained after layering the solutions in different solvents (ether or hexanes). All these compounds are isostructural to the homometallic ones (Figure 3.20), presenting five coordinated geometry for the external metals and six coordination environment at the inner metals with similar behavior on the C-C-C angles of the chelating moieties (Table 3.9) and the curvature of the ligand (Table 3.10; Figure 3.21) as seen before. As the Figure 14 shows, the crystal reveals again the presence of pair of dimmers in the [MM'···M'M] disposition.

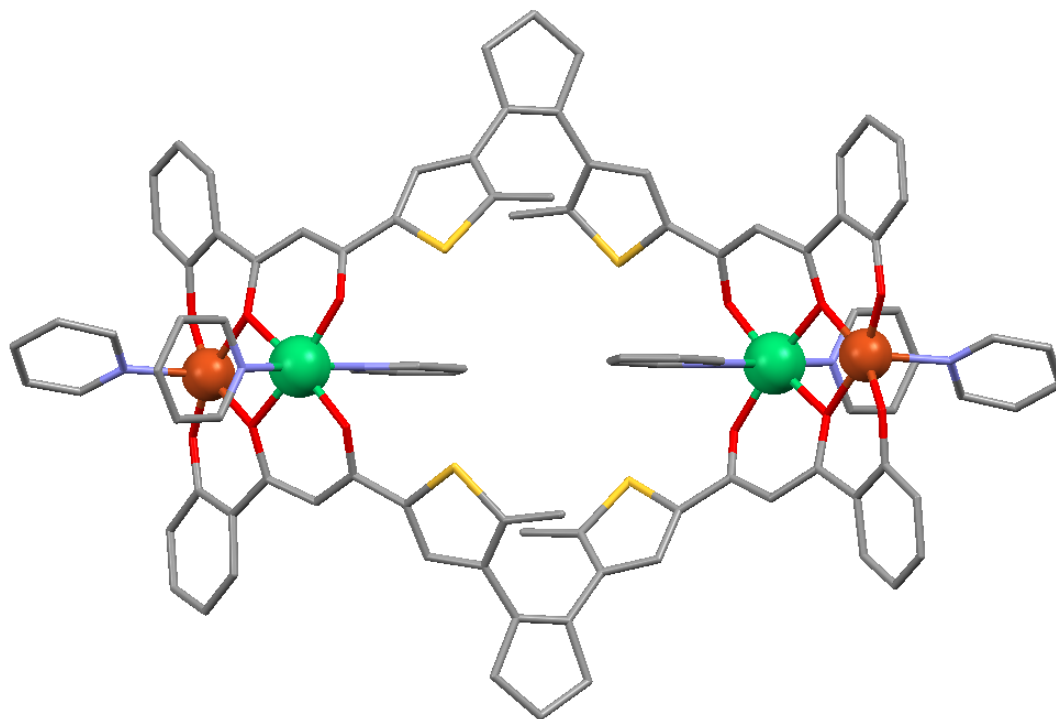


Figure 3.20: Crystal structure of [M₂M'₂L₂(py)₆]·9(py). Hydrogen atoms and pyridine molecules were omitted for clarity.

Compound	α_1	α_2	α average($^\circ$)	β_1	β_2	β average($^\circ$)
Cu ₂ Ni ₂	121.60	122.49	122.045	126.85	127.45	127.15
Co ₂ Ni ₂	121.00	122.81	121.905	125.86	127.30	126.58
Co ₂ Cu ₂	122.86	124.87	123.865	127.71	128.80	128.255
Cu ₂ Zn ₂	121.34	122.61	121.975	126.78	127.58	127.18
Ni ₂ Zn ₂	120.65	122.18	121.415	126.79	127.22	127.005

Table 3.9: C-C-C angles for the chelating groups.

Compound	τ	Curvature($^\circ$)	Distance to plane(\AA)
Cu ₂ Ni ₂	0.06	20.75	0.301
Co ₂ Ni ₂	0.23	22.90	0.454
Cu ₂ Co ₂	0.07	20.48	0.294
Cu ₂ Zn ₂	0.09	22.22	0.350
Ni ₂ Zn ₂	0.13	22.87	0.508

Table 3.10: Distortion data for the heterometallic compounds.

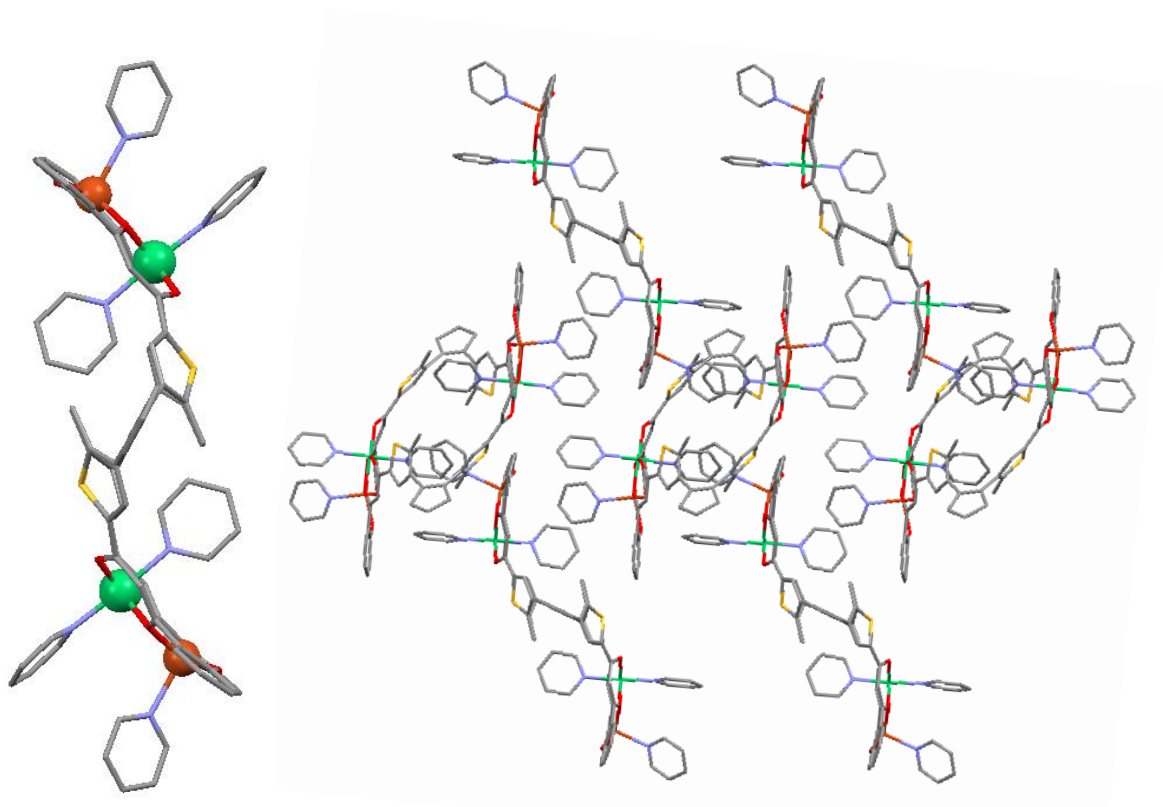


Figure 3.21: Curvature of the metals due to the coordination and the packing.

In all cases the refining procedure of the crystal structures confirmed the exact position of the metal ions since by exchanging their locations or forcing the [MM'···M'M'] and [MM'···M'M] topologies the *R*1 factor considerably increases. The 1/1 metal molar ratio obtained through the refinement of single crystal data was corroborated in the bulk, by measuring polycrystalline samples by through inductively coupled plasma (ICP) (found Cu/Ni (**9**), Cu/Zn (**12**) and Ni/Zn (**13**) molar ratio of 1; Co/Ni (**10**) of 1.05 and Co/Cu (**11**) of 1.05). In addition, theoretical studies confirm those dispositions. The magnetic behavior also corroborates the presence of these pairs of dimmers in the configuration of pure heterometallic pairs. (see later)

The crystallographic data and selected distances and angles are listed in the following tables.

formula	C ₁₄₁ H ₁₂₃ Cu ₂ Ni ₂ N ₁₅ O ₁₂ S ₄	Ni1-O1	1.992(4)	O2-Ni1-N2	89.9(2)
<i>M_r</i>	2592.28	Ni1-O2	2.034(4)	O2-Ni1-O4	170.1(1)
Crystal system	orthorhombic	Ni1-O4	1.989(4)	O2-Ni1-O5	79.1(1)
space group	Pbca	Ni1-O5	2.030(4)	O2-Ni1-N3	91.8(1)
<i>a</i> [Å]	24.254(5)	Ni1-N2	2.071(5)	O4-Ni1-O5	91.2(1)
<i>b</i> [Å]	16.457(3)	Ni1-N3	2.161(3)	O4-Ni1-N2	92.1(2)
<i>c</i> [Å]	30.402(6)	Cu1-O2	1.975(4)	O4-Ni1-N3	86.8(2)
$\alpha = \beta = \gamma$ [°]	90	Cu1-O3	1.919(4)	O5-Ni1-N2	90.9(2)
<i>V</i> [Å ³]	12135(4)	Cu1-O5	1.988(4)	O5-Ni1-N3	92.4(1)
<i>Z</i>	4	Cu1-O6	1.904(4)	O2-Cu1-O3	91.1(2)
ρ [g cm ⁻³]	1419	Cu1-N1	2.202(5)	O2-Cu1-O5	81.5(1)
shape; colour	orange plate	Ni1-Cu1	3.060(1)	O2-Cu1-O6	160.2(2)
μ [mm ⁻¹]	0.996	Ni1-Ni1'	11.166(1)	O2-Cu1-N1	104.2(2)
reflns	10404	Ni1-O2-Cu1	99.4(2)	O3-Cu1-O5	164.1(2)
parameters	756	Ni1-O5-Cu1	99.2(2)	O3-Cu1-O6	91.6(2)
restraints	285	O1-Ni1-O2	91.9(1)	O3-Cu1-N1	97.9(2)
<i>R</i> _{int}	0.0706	O1-Ni1-O4	97.7(1)	O5-Cu1-O6	90.8(2)
<i>R</i> ₁	0.0696	O1-Ni1-O5	171.0(1)	O5-Cu1-N1	97.5(2)
<i>wR</i> ₂	0.2115	O1-Ni1-N2	90.2(2)	O6-Cu1-N1	94.8(2)
<i>S</i>	1.054	O1-Ni1-N3	86.8(2)	N2-Ni1-N3	176.6(2)

Table 3.12. Crystallographic data, Bond distances [Å] and Angles [°] for **(10)**

formula	$C_{141}H_{123}Ni_2Co_2N_{15}O_{12}S_4$	Ni1-O1	2.000(3)	O2-Ni1-N2	90.5(1)
M_r	2583.06	Ni1-O2	2.017(3)	O2-Ni1-O4	173.0(1)
Crystal system	orthorhombic	Ni1-O4	1.991(2)	O2-Ni1-O5	81.2(1)
space group	Pbca	Ni1-O5	2.036(2)	O2-Ni1-N3	92.9(1)
a [Å]	24.257(3)	Ni1-N2	2.079(3)	O4-Ni1-O5	91.8(1)
b [Å]	16.532(2)	Ni1-N3	2.166(3)	O4-Ni1-N2	89.9(1)
c [Å]	30.337(4)	Co1-O2	2.129(3)	O4-Ni1-N3	86.9(1)
$\alpha = \beta = \gamma$ [°]	90	Co1-O3	1.932(3)	O5-Ni1-N2	90.4(1)
V [Å ³]	12166(3)	Co1-O5	2.038(2)	O5-Ni1-N3	90.8(1)
Z	4	Co1-O6	1.948(3)	O2-Co1-O3	86.0(1)
ρ [g cm ⁻³]	1.410	Co1-N1	2.00(1)	O2-Co1-O5	78.6(1)
shape; colour	orange plate	Ni1-Co1	3.146(1)	O2-Co1-O6	161.1(1)
μ [mm ⁻¹]	0.895	Ni1-Ni1'	11.280(1)	O2-Co1-N1	96.2(4)
reflns	13985	Ni1-O2-Co1	98.7(1)	O3-Co1-O5	147.0(1)
parameters	851	Ni1-O5-Co1	101.1(1)	O3-Co1-O6	96.8(1)
restrains	141	O1-Ni1-O2	90.6(1)	O3-Co1-N1	102.1(4)
R_{int}	0.0738	O1-Ni1-O4	96.4(1)	O5-Co1-O6	89.4(1)
R_1	0.0659	O1-Ni1-O5	171.5(1)	O5-Co1-N1	108.3(4)
$wR2$	0.2037	O1-Ni1-N2	92.3(1)	O6-Co1-N1	101.4(4)
S	1.048	O1-Ni1-N3	86.9(1)	N2-Ni1-N3	176.5(1)

Table 3.13. Crystallographic data, Bond distances [Å] and Angles [°] for **(11)**

formula	$C_{141}H_{123}Cu_2Co_2N_{15}O_{12}S_4$	Co1-O1	1.993(6)	O2-Co1-N2	90.0(2)
M_r	2593.72	Co1-O2	2.075(7)	O2-Co1-O4	166.6(2)
Crystal system	orthorhombic	Co1-O4	1.989(7)	O2-Co1-O5	77.6(2)
space group	Pbca	Co1-O5	2.055(6)	O2-Co1-N3	91.2(2)
a [Å]	24.248(4)	Co1-N2	2.137(7)	O4-Co1-O5	89.1(2)
b [Å]	16.646(3)	Co1-N3	2.242(7)	O4-Co1-N2	92.4(2)
c [Å]	30.355(5)	Cu1-O2	1.978(6)	O4-Co1-N3	87.2(2)
$\alpha = \beta = \gamma$ [°]	90	Cu1-O3	1.914(7)	O5-Co1-N2	91.5(2)
V [Å ³]	12252(4)	Cu1-O5	2.013(7)	O5-Co1-N3	91.9(2)
Z	4	Cu1-O6	1.916(6)	O2-Cu1-O3	92.1(3)
ρ [g cm ⁻³]	1.406	Cu1-N1	2.194(7)	O2-Cu1-O5	80.9(2)
shape; colour	orange plate	Co1-Cu1	3.120(1)	O2-Cu1-O6	160.4(3)
μ [mm ⁻¹]	0.748	Co1-Co1'	11.121(1)	O2-Cu1-N1	103.5(3)
reflns	8731	Co1-O2-Cu1	100.6(3)	O3-Cu1-O5	164.9(3)
parameters	796	Co1-O5-Cu1	100.2(3)	O3-Cu1-O6	90.8(3)
restrains	238	O1-Co1-O2	90.1(2)	O3-Cu1-N1	97.9(3)
R_{int}	0.1008	O1-Co1-O4	103.1(2)	O5-Cu1-O6	91.5(2)
R_1	0.0885	O1-Co1-O5	167.6(2)	O5-Cu1-N1	96.7(3)
$wR2$	0.2760	O1-Co1-N2	90.1(3)	O6-Cu1-N1	95.3(3)
S	1.066	O1-Co1-N3	86.7(2)	N2-Co1-N3	176.6(3)

Table 3.14. Crystallographic data, Bond distances [Å] and Angles [°] for **(12)**

formula	$C_{141}H_{123}Cu_2Zn_2N_{15}O_{12}S_4$	Zn1-O1	1.977(2)	O2-Zn1-N2	90.89(9)
M_r	2605.60	Zn1-O2	2.058(2)	O2-Zn1-O4	168.11(8)
Crystal system	orthorhombic	Zn1-O4	1.986(2)	O2-Zn1-O5	78.41(8)
space group	Pbca	Zn1-O5	2.055(2)	O2-Zn1-N3	89.60(9)
a [Å]	24.3653(11)	Zn1-N2	2.173(3)	O4-Zn1-O5	90.32(8)
b [Å]	16.7784(8)	Zn1-N3	2.340(3)	O4-Zn1-N2	93.38(9)
c [Å]	30.1926(13)	Cu1-O2	2.012(2)	O4-Zn1-N3	86.72(9)
$\alpha = \beta = \gamma$ [°]	90	Cu1-O3	1.916(2)	O5-Zn1-N2	92.20(9)
V [Å ³]	12343.1(10)	Cu1-O5	2.031(2)	O5-Zn1-N3	90.75(9)
Z	4	Cu1-O6	1.908(2)	O2-Cu1-O3	90.72(9)
ρ [g cm ⁻³]	1.402	Cu1-N1	2.158(3)	O2-Cu1-O5	80.01(8)
shape; colour	yellow plate	Zn1-Cu1	3.135(1)	O2-Cu1-O6	156.71(9)
μ [mm ⁻¹]	0.862	Zn1-Zn1'	11.204(1)	O2-Cu1-N1	104.16(9)
reflns	14184	Zn1-O2-Cu1	100.77(8)	O3-Cu1-O5	162.37(9)
parameters	877	Zn1-O5-Cu1	100.23(8)	O3-Cu1-O6	92.65(9)
restrains	318	O1-Zn1-O2	90.91(8)	O3-Cu1-N1	99.1(1)
R_{int}	0.0777	O1-Zn1-O4	100.10(9)	O5-Cu1-O6	90.24(9)
R_1	0.0491	O1-Zn1-O5	168.90(8)	O5-Cu1-N1	97.70(9)
$wR2$	0.1422	O1-Zn1-N2	91.01(9)	O6-Cu1-N1	98.0(1)
S	1.062	O1-Zn1-N3	86.07(9)	N2-Zn1-N3	177.0(1)

Table 3.15. Crystallographic data, Bond distances [Å] and Angles [°] for **(13)**

formula	$C_{141}H_{123}Ni_2Zn_2N_{15}O_{12}S_4$	Zn1-O1	2.002(3)	O2-Zn1-N2	90.4(1)
M_r	2596.94	Zn1-O2	2.017(3)	O2-Zn1-O4	173.3(1)
Crystal system	orthorhombic	Zn1-O4	1.991(3)	O2-Zn1-O5	81.2(1)
space group	Pbca	Zn1-O5	2.023(3)	O2-Zn1-N3	92.8(1)
a [Å]	24.438(4)	Zn1-N2	2.077(3)	O4-Zn1-O5	92.1(1)
b [Å]	16.592(3)	Zn1-N3	2.152(3)	O4-Zn1-N2	89.8(1)
c [Å]	30.293(5)	Ni1-O2	2.127(3)	O4-Zn1-N3	87.0(1)
$\alpha = \beta = \gamma$ [°]	90	Ni1-O3	1.940(4)	O5-Zn1-N2	89.7(1)
V [Å ³]	12283(3)	Ni1-O5	2.085(3)	O5-Zn1-N3	91.1(1)
Z	4	Ni1-O6	1.936(3)	O2-Ni1-O3	86.1(1)
ρ [g cm ⁻³]	1.404	Ni1-N1	2.046(4)	O2-Ni1-O5	77.2(1)
shape; colour	orange plate	Zn1-Ni1	3.176(1)	O2-Ni1-O6	155.1(1)
μ [mm ⁻¹]	0.826	Zn1-Zn1'	11.233(1)	O2-Ni1-N1	100.2(1)
reflns	8179	Zn1-O2-Ni1	100.1(1)	O3-Ni1-O5	146.9(1)
parameters	795	Zn1-O5-Ni1	101.3(1)	O3-Ni1-O6	96.8(1)
restrains	0	O1-Zn1-O2	91.2(1)	O3-Ni1-N1	102.5(1)
R_{int}	0.0928	O1-Zn1-O4	95.5(1)	O5-Ni1-O6	87.5(1)
R_1	0.0483	O1-Zn1-O5	172.1(1)	O5-Ni1-N1	108.4(1)
$wR2$	0.1284	O1-Zn1-N2	92.3(1)	O6-Ni1-N1	103.3(1)
S	1.034	O1-Zn1-N3	87.2(1)	N2-Zn1-N3	176.7(1)

In relation to the possible photoswitching properties of these complexes, the conformation of the central part of the ligand (i.e. the photochromic unit) exhibit the necessary conditions¹⁵; the right antiparallel conformation and C-C distances between 3.559 Å and 3.604 Å (Table 3.16).

Compound	Cu ₄	Co ₄	Ni ₄	Zn ₄	Cu ₂ Ni ₂	Co ₂ Ni ₂	Co ₂ Cu ₂	Cu ₂ Zn ₂	Ni ₂ Zn ₂
C-C	3.604	3.583	3.563	3.581	3.559	3.571	3.576	3.592	3.569

Table 3.16: Distances between the reactive carbons.

3.4.2. Magnetic properties of [M₂M'₂(L₂)₂(py)₆] complexes

The relevance of the heterometallic complexes as 2-qubit quantum gates was evaluated through bulk magnetic measurements.

For complex **9** ([CuNi]₂) (Figure 3.21), the $\chi_M T$ profile upon lowering the temperature shows an antiferromagnetic coupling between the Cu^{II} and Ni^{II} ions within each [CuNi] pair. This is firstly confirmed by the presence of a plateau below 50 K with $\chi_M T$ value of, approximately, 1.3 cm³ K mol⁻¹ that is evidence of a net non zero spin and, in turn, corroborates the [CuNi...NiCu] metal ion arrangement. Subsequently, the curve drops sharply at the lowest temperatures probably due to intermolecular or inter dimer interactions. The $\chi_M T$ value at 300 K is 3.39 cm³ K mol⁻¹, being a bit far away from the calculated for two Cu^{II} and Ni^{II} metal centres with an averaged $g = 2$ (2.7 cm³ K mol⁻¹), thus hinting higher g values for those ions. Bearing in mind all the aforementioned signs, the best fit, fixing $g_{Cu} = 2.3$ and $g_{Ni} = 2.6$, yielded to $J = -70.1$ cm⁻¹ and $ZJ = -0.11$ cm⁻¹. The intermolecular interactions model the decrease of $\chi_M T$ at around 5 K. These results are consistent with other reported systems involving [CuNi] units.^{27,34} A fit introducing the ZFS parameter did not considerably affect the above data, yielding a value of -17.6 cm⁻¹ that exceeds a reasonable limit.

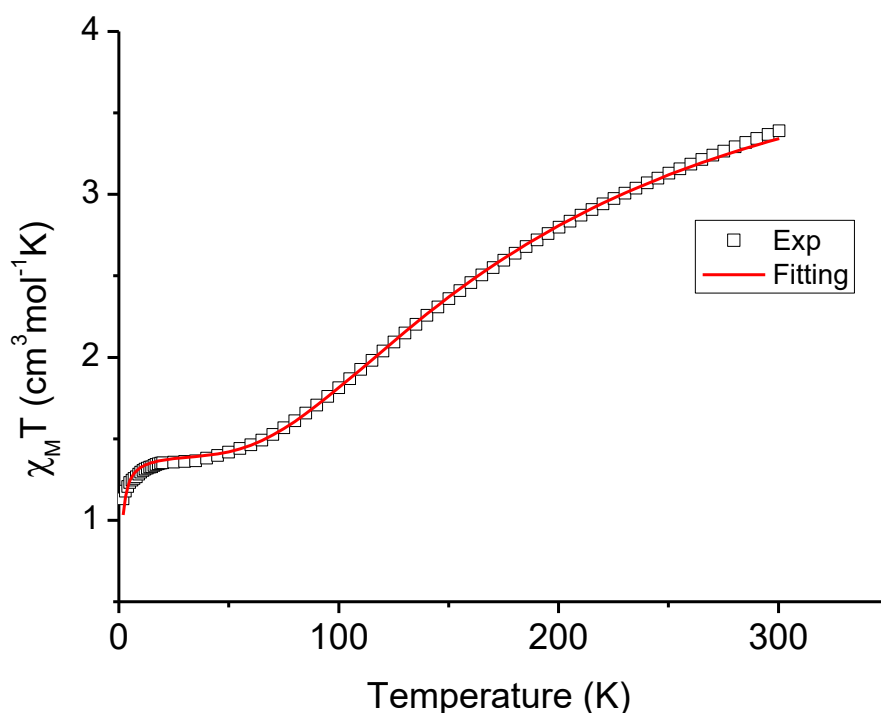


Figure 3.21: Plot of $\chi_M T$ vs T per mol of complex **9** at constant field of 0.5T.

The $\chi_M T$ versus T plots for complex **10** ($[\text{CoNi}]_2$) (Figure 3.22) shows that $\chi_M T$ decreases smoothly from 300 K to 100 K and then drops markedly until 2 K. This behavior clearly agrees with an antiferromagnetic coupling within the $[\text{CoNi}]$ pairs and is further validated by the value of $\chi_M T = 1.05 \text{ cm}^3 \text{ K mol}^{-1}$ at 2 K, which roughly matches with the expected residual $[S = \frac{1}{2}]_2$ ground state of each $[\text{CoNi}]$ pair once the coupling takes place. In analogy to the $[\text{CuNi}]_2$ complex, this residual magnetic moment is consistent with the metal ion distribution shown by the single crystal XRD measurements. The $\chi_M T$ value of $9.6 \text{ cm}^3 \text{ K mol}^{-1}$ is well above the theoretical one corresponding to non-interacting $2(\text{Co}^{\text{II}})$ and $2(\text{Ni}^{\text{II}})$ ions ($5.7 \text{ cm}^3 \text{ K mol}^{-1}$). As mentioned for complex $[\text{Co}_2]_2$ this difference can be certainly ascribed to the intrinsic SOC of Co^{II} free ion with octahedral geometry. The $\chi_M T$ curve was successfully fitted keeping the orbital reduction at -1.5 (a free fitting yields irrational values) and g_{Co} and g_{Ni} at 2.1 and 2.5, respectively. Furthermore, the analysis was performed taking into account the possible ZFS arising from Ni^{II} ions. The results were the following: $J = -5.0 \text{ cm}^{-1}$, $\text{SOC} = -133.0 \text{ cm}^{-1}$, $\text{ZFS} = 8.3 \text{ cm}^{-1}$ and $\text{IM} = 0.08$ (Ni^{II} , $S = 1$, monomeric entity). The calculations without the ZFS parameter and the small amount of paramagnetic impurity led to poor fittings, primarily, at low temperatures.

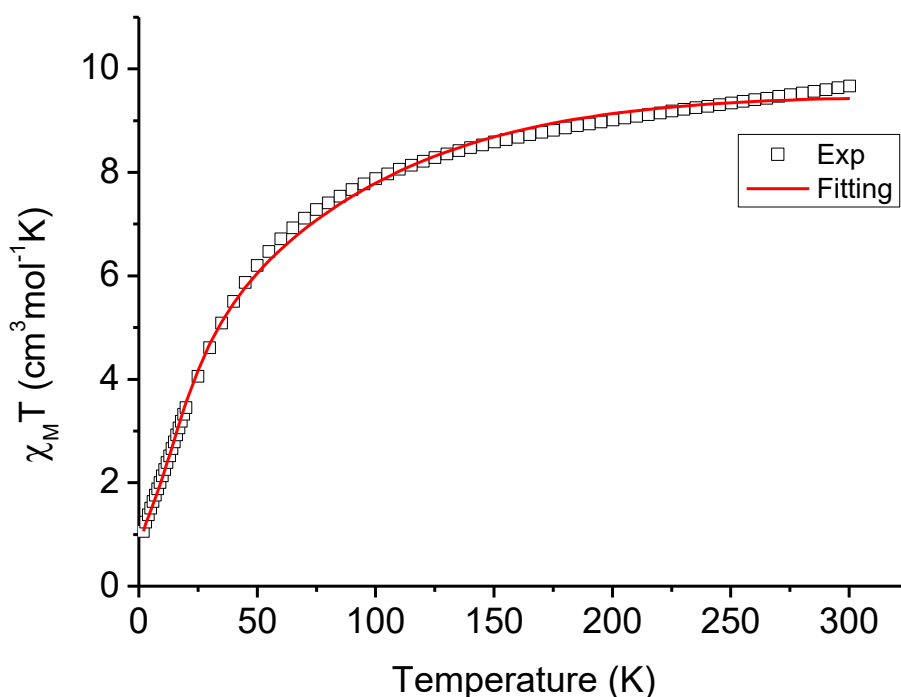


Figure 3.22: Plot of $\chi_M T$ vs T per mol of complex **10** at constant field of 0.5T.

The magnetic susceptibility of (**11**) $[\text{CuCo}]_2$ (Figure 3.23) is found entirely, in between the reading for the corresponding homometallic counterparts, complexes **1** and **2**. The system is again subject to the effects of SOC by Co(II), with a value of χT at 300 K ($6.14 \text{ cm}^3 \text{ K mol}^{-1}$) larger than the calculated for the uncoupled system ($5.4 \text{ cm}^3 \text{ K mol}^{-1}$ for two $S = 3/2$ and two $S = 1/2$ with $g = 2$). The approximate fit using PHI, incorporating the SOC as well as the magnetic exchange, provided an estimate for the magnetic exchange of $J = -44.5 \text{ cm}^{-1}$, fixing for all the metals $g = 2$, $\lambda = -100.0 \text{ cm}^{-1}$ and $\sigma = -1.5$. The very small response at the lowest temperatures ($0.21 \text{ cm}^3 \text{ K mol}^{-1}$ at 2 K), almost diamagnetic, is consistent with the approximation that in this thermal range, only the lowest J state of the Co(II) 4T_1 term is occupied ($J = 1/2$), thus Co(II) exhibits an effective $S = 1/2$ spin state which would vanish in coupling with the neighboring Cu(II) spin.

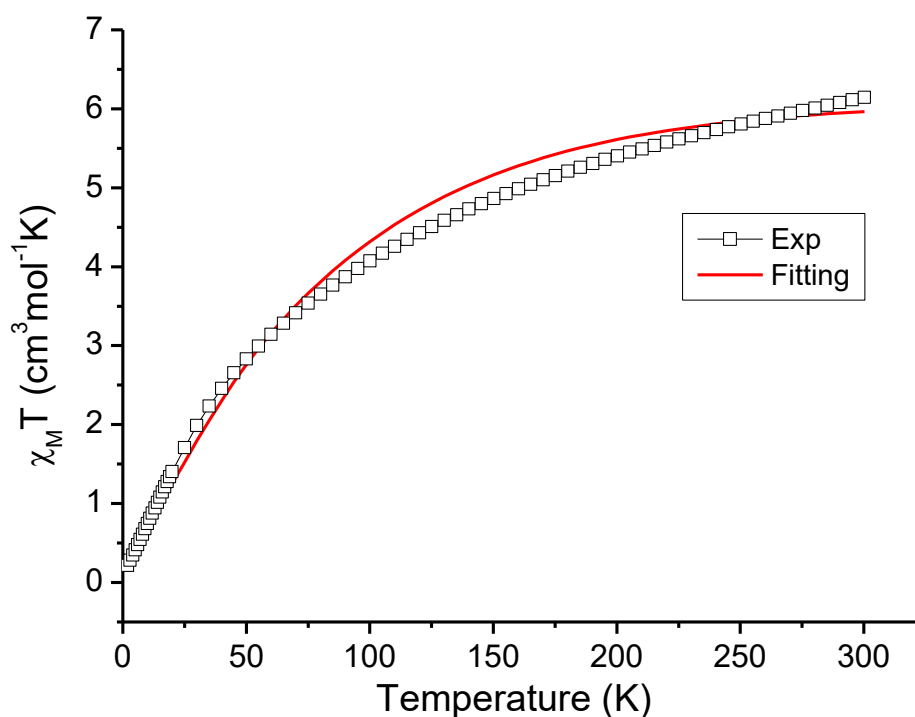


Figure 3.23: Plot of $\chi_M T$ vs T per mol of complex **11** at constant field of 0.5T.

Complexes **12** ($[\text{CuZn}]_2$) (Figure 3.24) and **13** ($[\text{NiZn}]_2$) (Figure 3.25) contain one Zn^{II} ion, which is diamagnetic, at each $[\text{MZn}]$ ($\text{M}^{\text{II}} = \text{Cu}, \text{Ni}$) pair, thus the latter behave, magnetically, as non-interacting M^{II} ions. Hence, the corresponding $\chi_M T$ curves will correspond solely to the magnetic contribution coming from isolated Cu^{II} or Ni^{II} ions respectively and should follow the Curie law over whole the temperature range. As can be observed in the graph, the $\chi_M T$ curve for both complexes starts at 300 K nearly at the theoretical values (0.75_{teor} and 0.65_{exp} $\text{cm}^3 \text{K mol}^{-1}$ for $[\text{CuZn}]_2$ and 2.0_{theor} and 2.6_{exp} for $[\text{NiZn}]_2$) and, as expected, is constant. Nevertheless, $\chi_M T$ decreases from 10 K ($[\text{CuZn}]_2$) and 50 K ($[\text{NiZn}]_2$), fact that can be attributed to either intermolecular interactions or ZFS in the case of $[\text{NiZn}]_2$ compound. Bearing in mind these considerations, the best fit for the $[\text{CuZn}]_2$ complex was achieved with fixed $g = 1.95$ and refined $S = \frac{1}{2}$ impurity of 0.16. Note that by introducing intermolecular interactions the results were worst and the latter ferromagnetic. For complex $[\text{NiZn}]_2$, g was kept at a value of 2.3 whereas ZFC and ZJ were fitted to -0.49 cm^{-1} and -0.14 cm^{-1} , respectively. The presence of a small amount of paramagnetic impurity in complex $[\text{CuZn}]_2$ and the value of $g = 2.3$ for compound $[\text{NiZn}]_2$ are the most plausible reasons for the slight deviations of $\chi_M T$ at 300 K from their tabulated values.

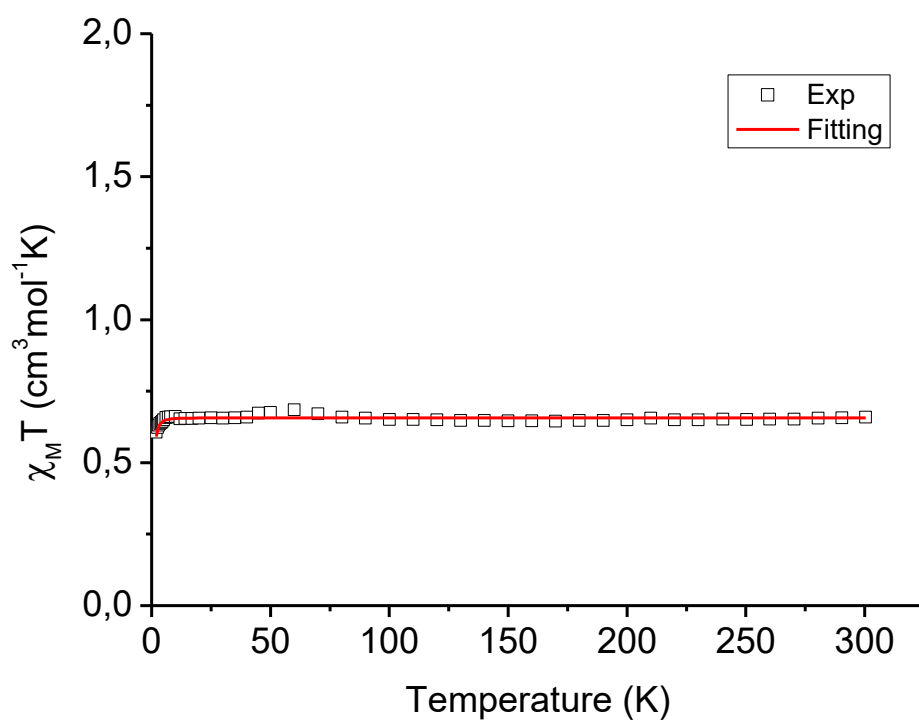


Figure 3.24: Plot of $\chi_M T$ vs T per mol of complex **12** at constant field of 0.5T.

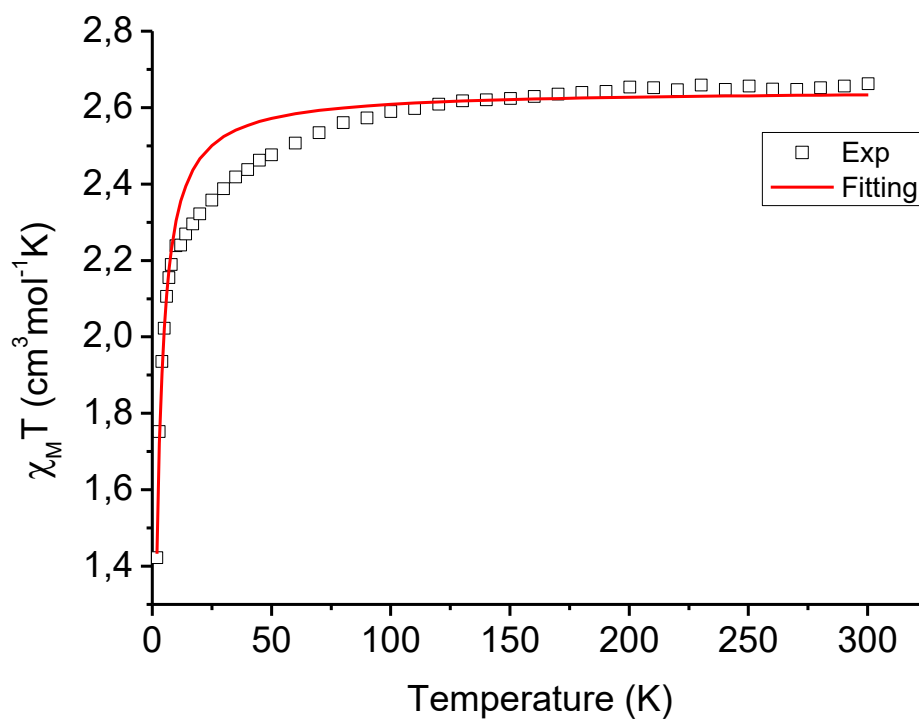
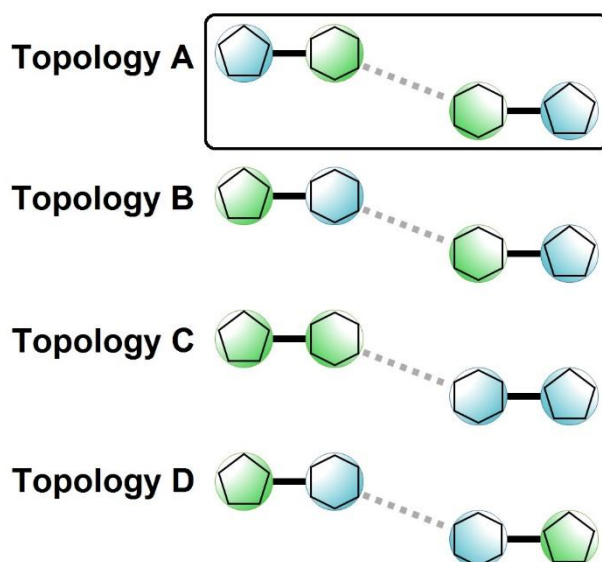


Figure 3.25: Plot of $\chi_M T$ vs T per mol of complex **13** at constant field of 0.5T.

3.4.3 Theoretical studies of the heterometallic compounds

The calculations were conducted by Dr. Jordi Ribas-Ariño, from Universitat de Barcelona. The molecular structure of each heterometallic compound was used to support, by means of DFT calculations, the efficiency of the current coordination system in directing the site-selective organisation of the hexa- and heptacoordinated ions within the molecule. Thus, the topologies A, B, C and D (Scheme 3.4) were investigated for each structure (**9-13**). The computed relative energies of the spin ground state (cm^{-1}) for these topologies are summarized in Table 3.17. Therefore, the stability of the observed by X-Ray diffraction and the magnetic properties, Topology A, is the favoured topology over that immediately above and is of the order of magnitude of a weak covalent bond, demonstrating the stability of this distribution over the rest.

Table 3.17. Energies in cm^{-1} for the different metal topologies				
	Topology A	Topology B	Topology C	Topology D
$[\text{CuNi}]_2$	0	7068	7132	14418
$[\text{CoNi}]_2$	0	2505	2510	5559
$[\text{CuCo}]_2$	0	5207	5303	10409
$[\text{CuZn}]_2$	0	2839	3328	5674
$[\text{ZnNi}]_2$	0	4009	4136	8030



Scheme 3.4: Metal topologies used for DFT calculations for the heterometallic compounds based on the structure data.

3.4.4 Quantum coherence in the heterometallic clusters

Complexes [CuNi]₂ (**9**) and [CuZn]₂ (**12**), exhibit both a pair of spins ½ well defined within the molecule. Thus, they provide good requirements to act as 2-Qubit quantum gates and therefore we decided to measure the quantum coherence of their spin resonances by pulsed EPR. All the experiments were done in the group of Professor Joris van Slageren, in Stuttgart. First experiments were carried out in 1mM solutions of the complex, in a 1:1 mixture of toluene and DMSO. For compound **9**, the pair of [CuNi]₂, the pulsed Q-band (35GHz) echo spectrum is presented in Figure 3.26, showing the echo amplitude as a function of the magnetic field for a constant separation between pulses. The fact that a spin echo is observed at all immediately confirms the existence of measurable quantum coherence. Hence, we have studied in detail the quantum coherence within the pair CuNi in the low temperature range 7–35 K, where again we used the Hahn echo sequence, varying the interpulse distance τ . The measurements were performed at the fixed field position given by the maximum peak of the Hahn echo graph at different temperatures (Figure 3.27).

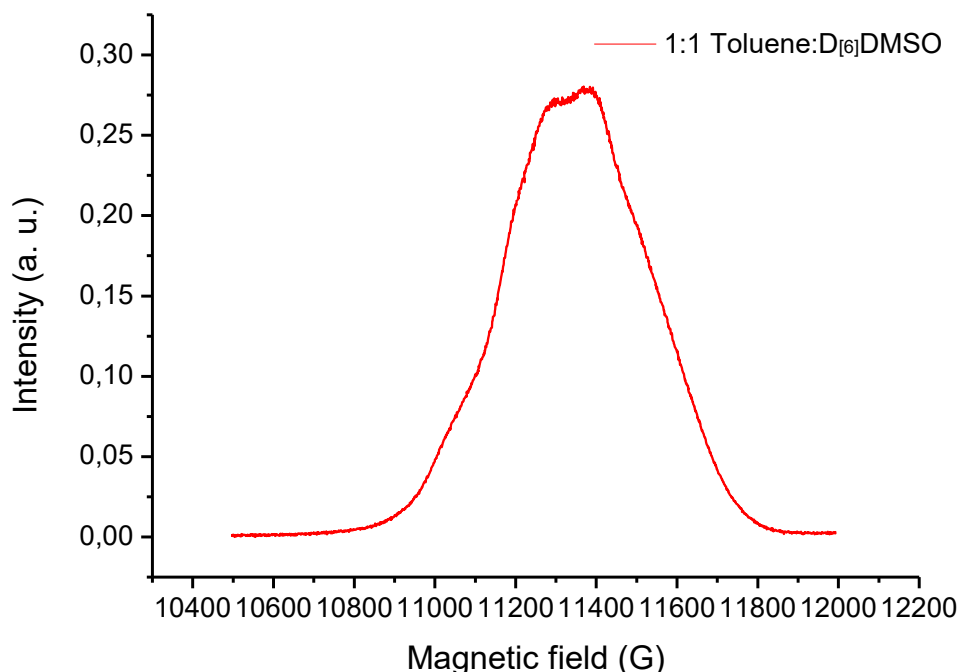


Figure 3.26: Q-band echo detected spectra of **9** in 1mM solutions at 35 GHz, 7 K, 10 ms repetition time, 50 shots per point.

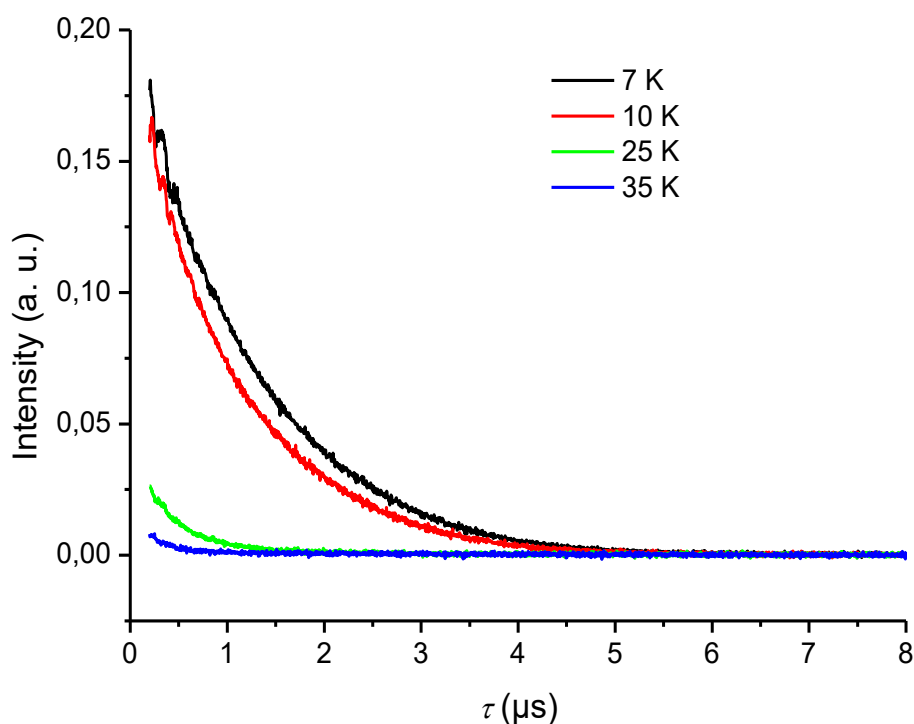


Figure 3.27: Hahn echo decay for **9** in Toluene-H8/DMSO-D6 at different temperatures at 11400 G. Modulation in decay is ESEEM due to deuterium (7.45 MHz at 11400 G).

The tables below show the relaxation times T_1 and T_2 determined by monoexponential fit functions $y=A*\exp(-\tau/T_1)$ and $y=A*\exp(-2\tau/T_2)$ respectively at different temperatures.

Table 3.18. CuNi Toluene-H8/DMSO-D6 1:1 monoexponential fit T_1 at 11400 G

T (K)	A	+/-	T_1 (μ s)	+/- (μ s)	R^2
7	-0.18848	0.00108	1037.9009	9.10356	0.9851
10	-0.1437	8,76E+01	511.4033	4.51766	0.98101
25	-0.02623	3,98E+01	578.723	0.13127	0.88717

Table 3.19. CuNi Toluene-H8/DMSO-D6 1:1 monoexponential fit T_2 at 11400 G

T (K)	A	+/-	T_2 (ns)	+/- (ns)	R^2
7	0.20359	0.00024	2434.74	4.58	0.99882
10	0.19247	0.00021	2095.93	3.38	0.99887
25	0.03843	0.00024	877.57	5.50	0.98101
35	0.01267	0.00036	653.34	15.80	0.77433

As the table shows, good relaxation times for the pair CuNi can be obtained. The oscillations in the echo amplitude are ascribed to the ESEEM effect due to the deuterium. Earlier investigations revealed a strong correlation between the spin–lattice relaxation time T_1 and the coherence time T_2 ^{6,35}. Therefore, we determined T_1 and its temperature dependence by means of the inversion recovery sequence. The results demonstrate that at temperatures higher than 30 K, T_1 and T_2 are indeed essentially the same (Figure 3.28 and Figure 3.29), suggesting that the latter is determined by the former. In addition, there may be a contribution from nuclear spin motions, for example, librational motions of the ligand rings or from the solvent.

In contrast, at low temperatures, decoherence is dominated by the interaction with nuclear spins^{36,37}. Considering the distances from the crystal structure, the strongest (dipolar) hyperfine coupling is expected to be on the nuclei spins of the atoms from the ligand or the coordinated solvents. Since the complete deuterated ligand is not available, we used deuterated Toluene to see if there were some differences in the quantum coherence.

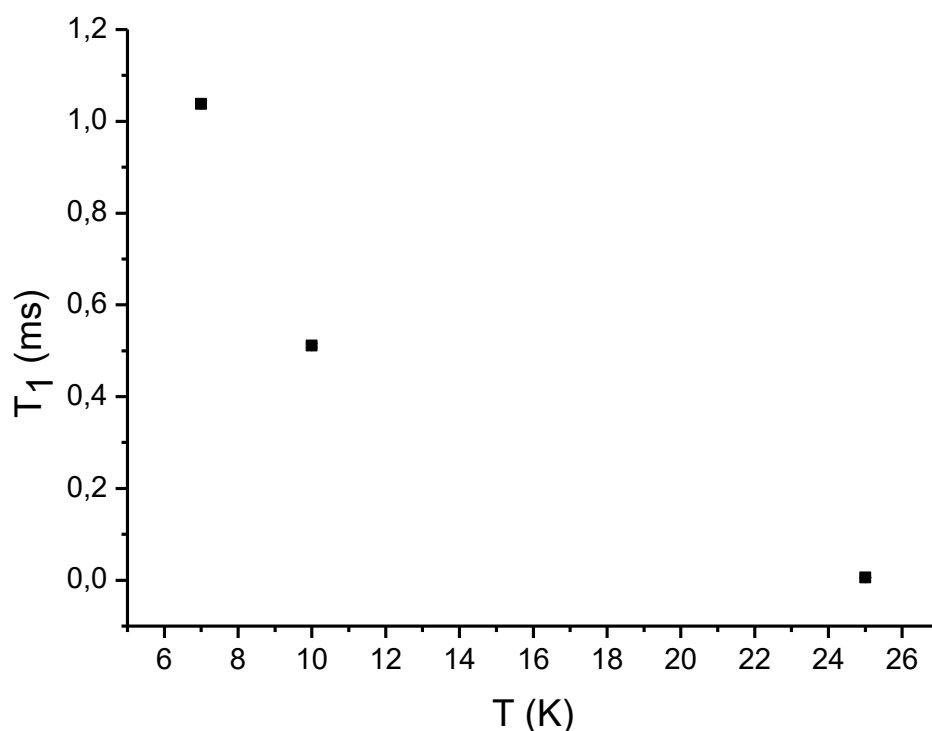


Figure 3.28: Temperature dependence of spin-lattice relaxation T_1 for **9** at 11400 G. Measured with inversion recovery sequence.

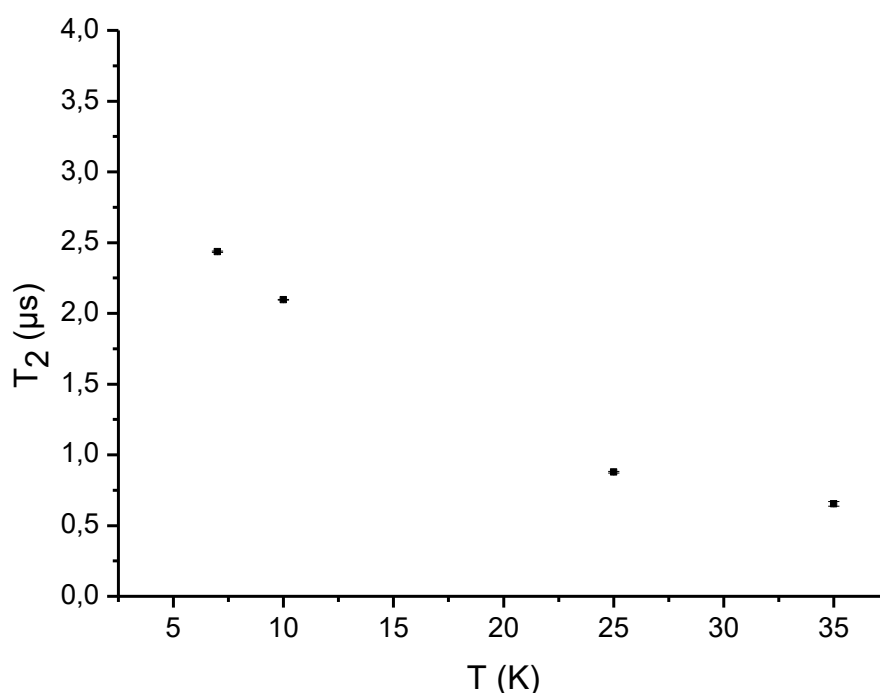


Figure 3.29: Temperature dependence of spin-spin relaxation T_2 for **9** at 11400 G. Measured with Hahn echo sequence.

The Tables 3.20 and 3.21 show the differences on T_1 and T_2 , using a complete deuterated media at different temperatures. Also de Q-band and the Hanh echo was measured shown in Figure 3.30 and Figure 3.31, respectively.

T (K)	A	+/-	T_1 (μ s)	+/- (μ s)	R^2
7	-0.29313	0.00182	996.21588	9.20243	0.97942
10	-0.16697	0.00131	422.54367	4.67686	0.97042
15	-0.1215	0.00139	162.25216	2.4829	0.95557
20	-0.09032	5,12E+01	24.34419	0.19484	0.98432
25	-0.01816	2,99E+01	9.04158	0.21982	0.87187

T (K)	A	+/-	T_2 (ns)	+/- (ns)	R^2
7	0.30321	0.00047	3585.88	8.02	0.99842
10	0.16246	0.00040	3645.10	13.58	0.99673
15	0.12276	0.00020	2882.31	6.51	0.99758
20	0.07714	0.00015	1852.89	4.31	0.99735
25	0.05720	0.00038	854.41	5.35	0.98637

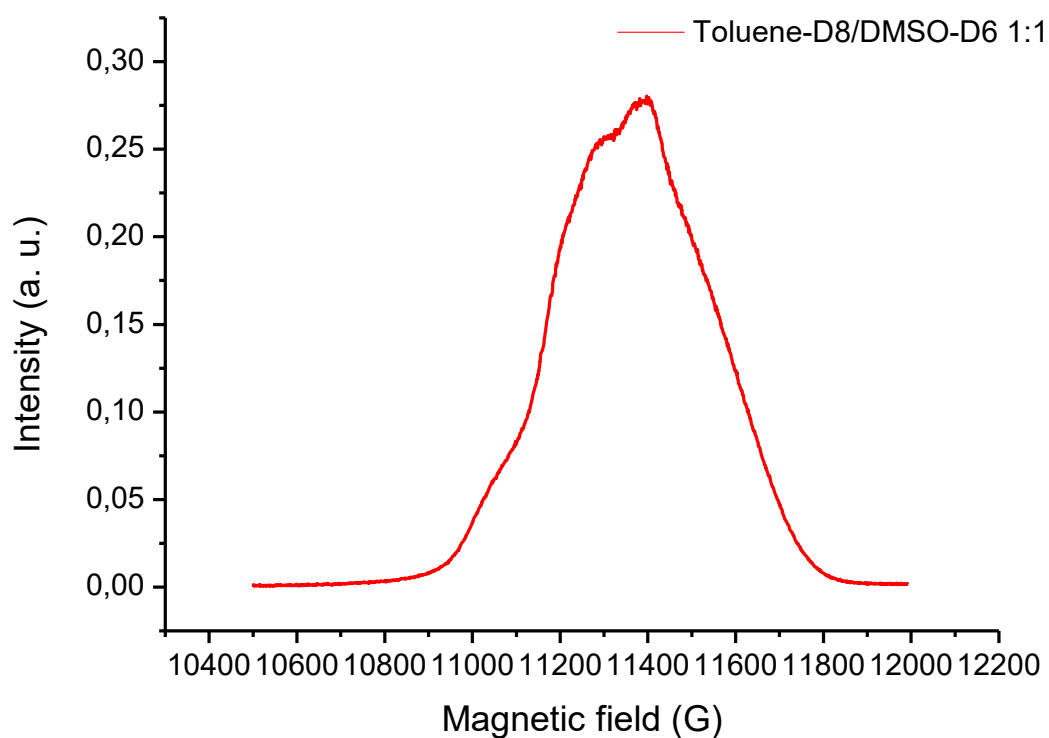


Figure 3.30: Q-band echo detected spectra of **9** in 1mM deuterated solutions at 35 GHz, 7 K, 10 ms repetition time, 50 shots per point.

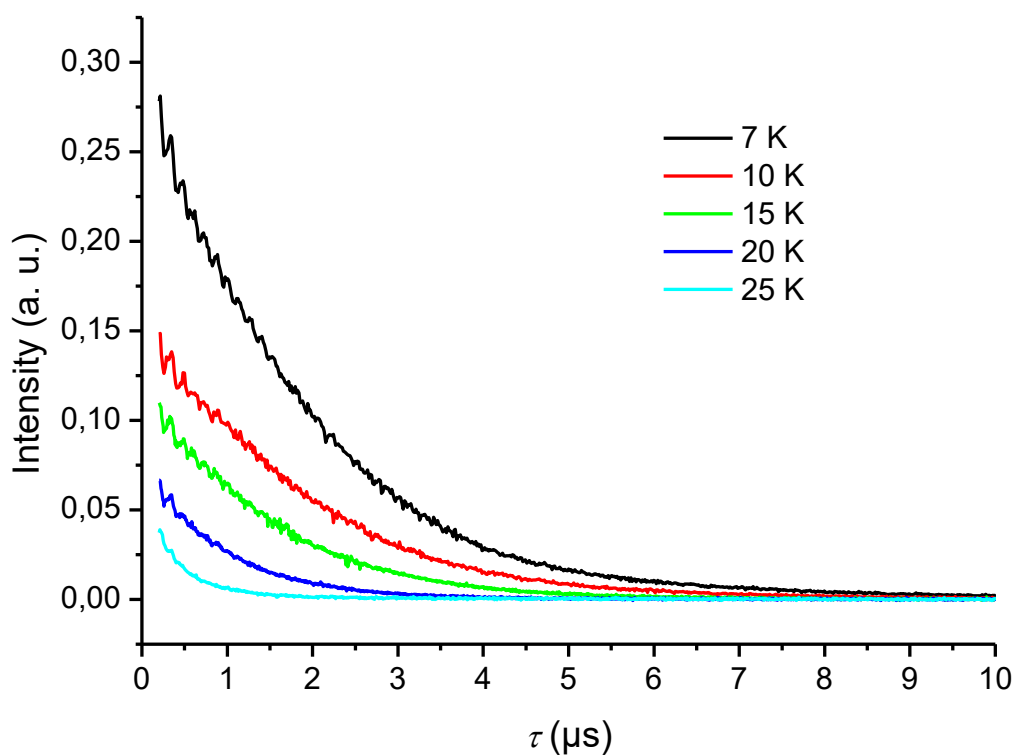


Figure 3.31: Hahn echo decay for **9** in Toluene-D8/DMSO-D6 at different temperatures at 11400 G. Modulation in decay is ESEEM due to deuterium (7.45 MHz at 11400 G).

As the results show, changing to a completely deuterated solvent, has an important change to the relaxation times of the pair CuNi, with increases of at least 1000 μs . This small modification also indicates that a change into a complete deuterated ligand, would probably increase the relaxation time T_2 .

The same experiments were done with **12** ($[\text{CuZn}]_2$) the analog of spin $\frac{1}{2}$ with no magnetic excited states. The Tables 3.22-3.25 and Figures 3.32 and 3.33 show the relaxation times T_1 and T_2 determined by monoexponential fit functions $y=A*\exp(-\tau/T_1)$ and $y=A*\exp(-2\tau/T_2)$ respectively.

Table 3.22. CuZn Toluene-H8/DMSO-D6 1:1 monoexponential fit T_1 at 12100 G

T (K)	A	+/-	T_1 (μs)	+/- (μs)	R^2
7	-0.49106	0.002	2679.68511	19.64203	0.98865
10	-0.37016	0.00177	1114.40866	8.05462	0.98737
25	-0.13257	0.00102	65.15272	0.77084	0.98299
50	-0.02538	5,83E+01	7.82661	0.31581	0.84309
70	-0.0084	5,42E+01	1.17608	0.0997	0.52873

Table 3.23. CuZn Toluene-D8/DMSO-D6 1:1 monoexponential fit T_1 at 12100 G

T (K)	A	+/-	T_1 (μs)	+/- (μs)	R^2
7	-0.16947	8,00E+01	2113.74.184	16.46123	0.98617
10	-0.1159	6,00E+01	933.54236	7.15642	0.98571
25	-0.04221	6,48E+01	47.70276	0.93139	0.9142
50	-0.01231	9,60E+01	2.36191	0.19293	0.38774

Table 3.24. CuZn Toluene-H8/DMSO-D6 1:1 monoexponential fit T_2 at 12100 G

T (K)	A	+/-	T_2 (ns)	+/- (ns)	R^2
7	0.57511	0.00108	3249.92	10.44	0.99591
10	0.41111	0.00078	3252.27	10.57	0.99581
25	0.15188	0.00019	2224.72	3.93	0.99857
50	0.05760	0.00026	797.76	3.51	0.99536
70	0.02495	0.00127	328.29	9.58	0.82367

Table 3.25. CuZn Toluene-D8/DMSO-D6 1:1 monoexponential fit T_2 at 12100 G

T (K)	A	+/-	T_2 (ns)	+/- (ns)	R^2
7	0.18613	0.00026	6034.29	13.11	0.9978
10	0.12292	0.00017	5155.04	10.80	0.99791
25	0.04057	0.00008	3130.04	8.17	0.99672
50	0.01216	0.00017	1328.17	20.27	0.89595

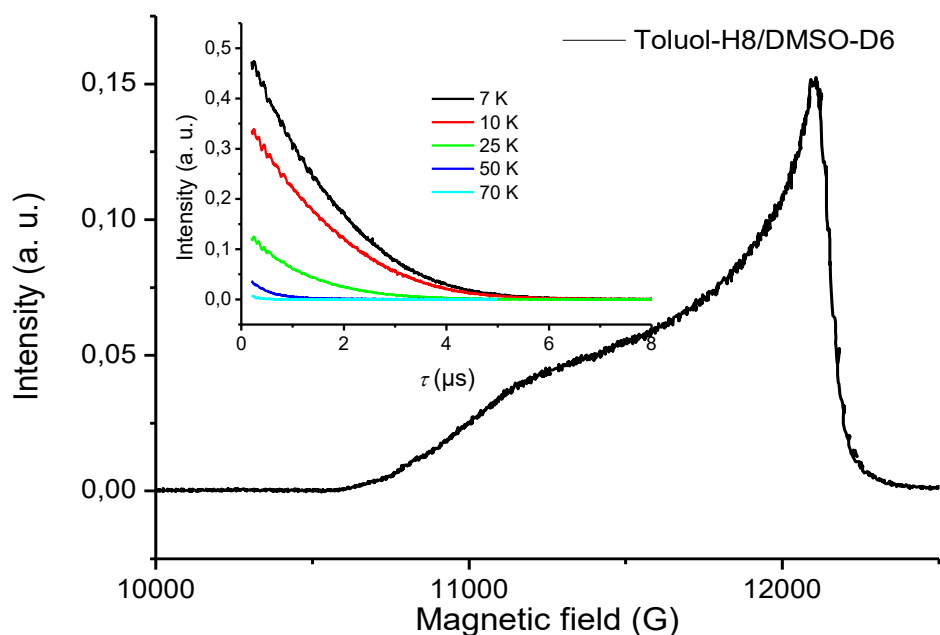


Figure 3.32: Q-band echo detected spectra of **12** in 1 mM solutions at 35 GHz, 7 K, 20 ms repetition time, 20 shots per point. (Inset) Hahn echo decay for Toluene-H8/DMSO-D6 at different temperatures at 12100 G. Modulation in decay is ESEEM due to deuterium (7.91 MHz at 12100 G).

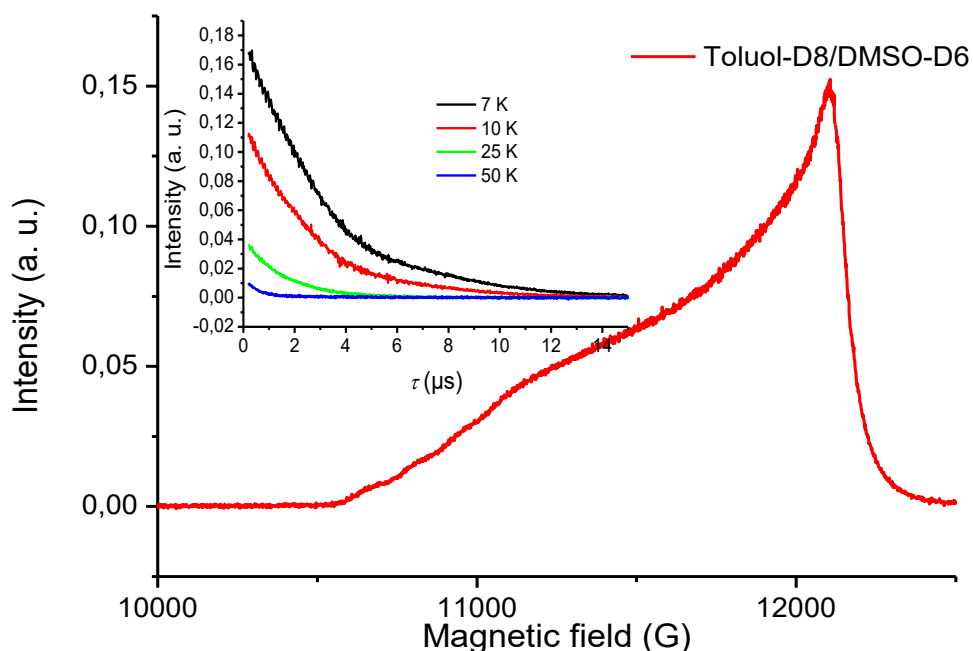


Figure 3.33: Q-band echo detected spectra of **12** in 1 mM deuterated solutions at 35 GHz, 7 K, 20 ms repetition time, 20 shots per point. (Inset) Hahn echo decay for Toluene-D8/DMSO-D6 at different temperatures at 12100 G. Modulation in decay is ESEEM due to deuterium (7.91 MHz at 12100 G).

Here, the change to pure spins $\frac{1}{2}$, gives better results for the relaxation time T_2 . Also the same behavior can be seen with regard to the change to deuterated solvents, with nearly doubling the relaxation times

Comparing both complexes in the complete deuterated media, the dimer CuZn has almost twice the value of the CuNi compound at 7K, 3585 ns for CuNi and 6034 ns for CuZn.

In both cases, the value for T_2 , related to the quantum coherence, approaches that required to perform quantum operations. To perform quantum computing, the coherence time of a qubit state must be about 10000 times longer than the time needed for operating with it³⁸. This relationship can be associated to a qubit figure of merit, Q , which represents the number of quantum operations that can be performed before losing phase coherence, so depends on T_2 and the time to do an individual quantum operation. The ratio of these is indeed the qubit figure of merit, which should be larger than 10.000 to allow for fault tolerant quantum computing⁶.

Taking the ratio of T_2 and the $\pi/2$ pulse length (20 ns), we arrive at a single qubit figure of merit $Q_M(\text{CuNi})$ of 180 and $Q_M(\text{CuZn})$ around 300. These values are still two orders of magnitude below the idealized Q of 10.000. We have seen that changing the conditions with are impact on T_2 , related to external interferences such as interactions with the surrounding particles or with lattice vibrations, has allowed already to increase the T_2 , hence, the figure of merit Q . It is plausible that this can be optimized, as has been seen for other spin based qubit systems.

3.5 Photochromic behavior

The photochromic behavior of all compounds was studied in solution ($5 \times 10^{-5} \text{M}$ in a mixture 1:1 of Toluene and DMSO) using a Xenon lamp with pass band filters and monitored by UV-Vis spectroscopy. The expected cyclization with its corresponding color change is represented in Figure 3.34.

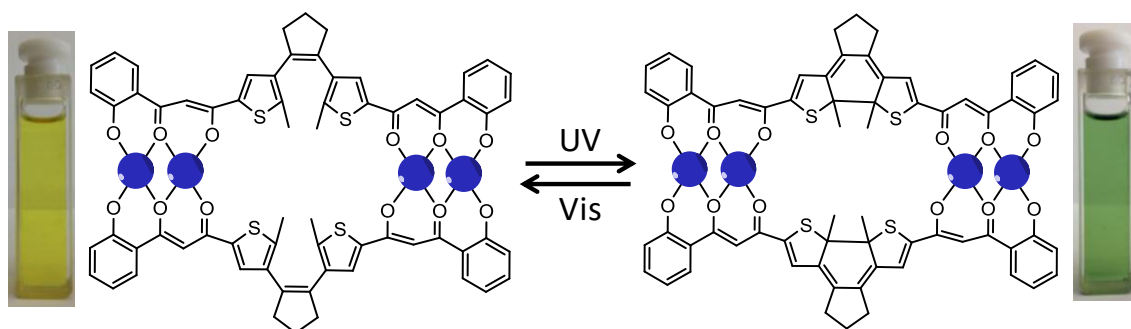


Figure 3.34: Cyclization of the complexes with their corresponding color change.

For all compounds, the UV-Vis spectrum is very similar. As a summary, in all cases for the open isomer, the bands corresponding to $\pi-\pi^*$ transition of the ligand appear around 282nm and depending on the compound, between 393 and 428 nm. The open form upon irradiation with UV developed a distinct absorption in the visible region, between 614 and 650 nm, due to the formation of the closed form. All the spectral bands are red shifted with respect to the analogous bands in the free ligand, except the one at 282nm, which is maintained during the isomerization processes.

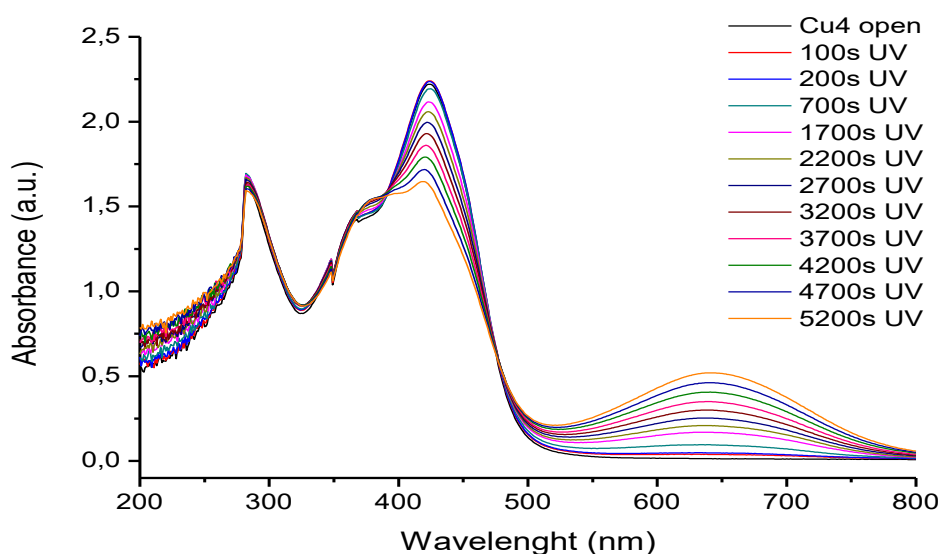


Figure 3.35: UV-Vis spectra of **5** ($[\text{Cu}_2]_2$) after irradiation with UV light ($<425 \text{nm}$).

Figure 3.35 shows the changes in the UV-Vis spectrum of compound **1** ($[\text{Cu}_2]_2$), after irradiation with UV light (<425 nm). The initial spectrum shows an intense band centered at 428 nm which decreases while a large band in the visible region centered at 642 nm, starts to appear. A PSS is reached in 5200s, very long comparing with the free ligand. Towards the end, a large shoulder at 395 nm becomes apparent.

Irradiation of the closed isomer with Visible light (>430 nm) did not produce the initial spectrum, leading to a new spectrum (Figure 3.36), where the band in the visible range indeed disappears, while the initial color of the solution is restored. However, the band at 428 nm is not recovered totally and the shoulder observed toward the end of the previous process continues to grow here as well.

Although both spectra have isosbestic points, the failure to recover the initial spectrum, is indicative of the degradation of the sample or of the presence of open ligands and closed ligands in the same molecule. The degradation could occur as a result of long exposition to UV irradiation, which can transform the photochromic unit into a new isomer irreversibly²¹. Another possibility is the dissociation of the complex, leading to free ligand in solution. This is supported by the new band appearing around 395 nm, which is close to the band of the free ligand (392 nm).

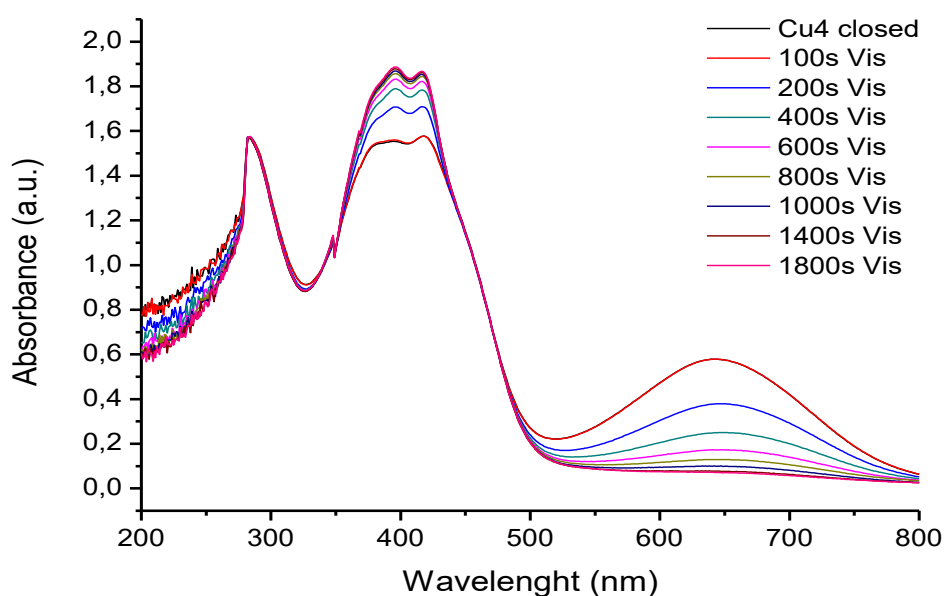


Figure 3.36: UV-Vis spectra of **5** ($[\text{Cu}_2]_2$) after irradiation with Visible light (>430 nm).

For compound **8** ($[\text{Zn}_2]_2$), a similar behavior is observed (Figure 3.37). For the open form, the large band at 411 nm with a shoulder at 390 nm, starts to decrease while the solution is irradiated with UV. The new band related to the extended conjugation appears at 629 nm. In this case, the peak at 411 nm is again not recovered after irradiation with visible light. In addition, the band in the visible region does not completely disappear. Also, the solution shows the characteristic green color of the closed form, even after long exposure to visible light (Figure 3.38)

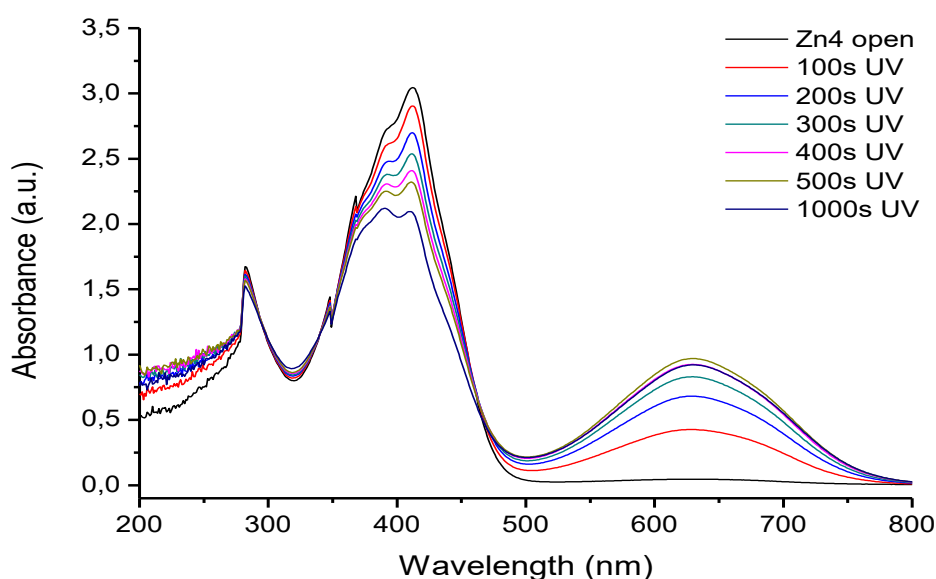


Figure 3.37: UV-Vis spectra of **8** ($[\text{Zn}_2]_2$) after irradiation with UV light (<425nm).

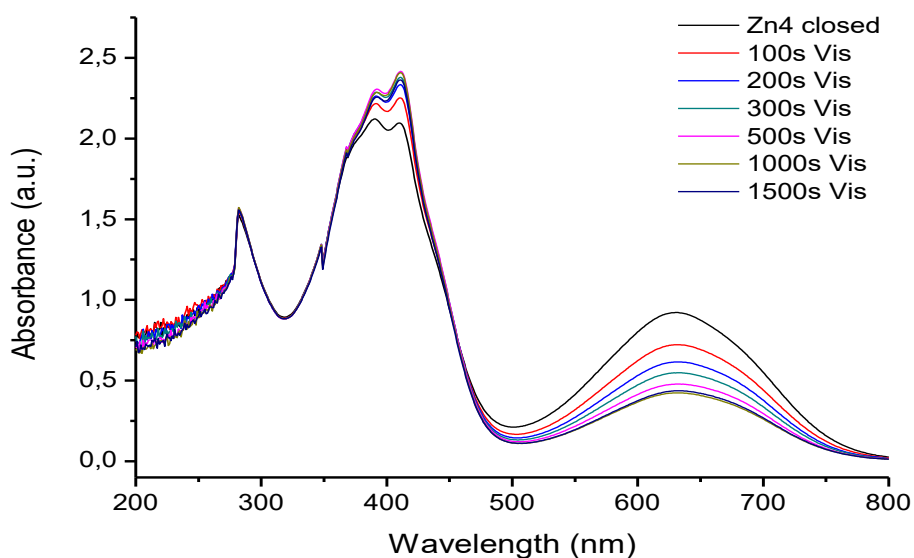


Figure 3.38: UV-Vis spectra of **8** ($[\text{Zn}_2]_2$) after irradiation with Visible light (>430nm).

The characteristic peak for compound **12** ($[\text{CuZn}]_2$), appears at 426 nm with a shoulder at 374 nm (Figure 3.39). After irradiation with UV, this shoulder does not change while the intense one decreases in intensity. The new band appears here at 650 nm, and is the more red shifted of the whole family of these compounds. Here, the reversibility of the process is larger than for the homometallic analogues, but also incomplete. The intensity of the initial band at 426 nm is not fully recovered (Figure 3.40).

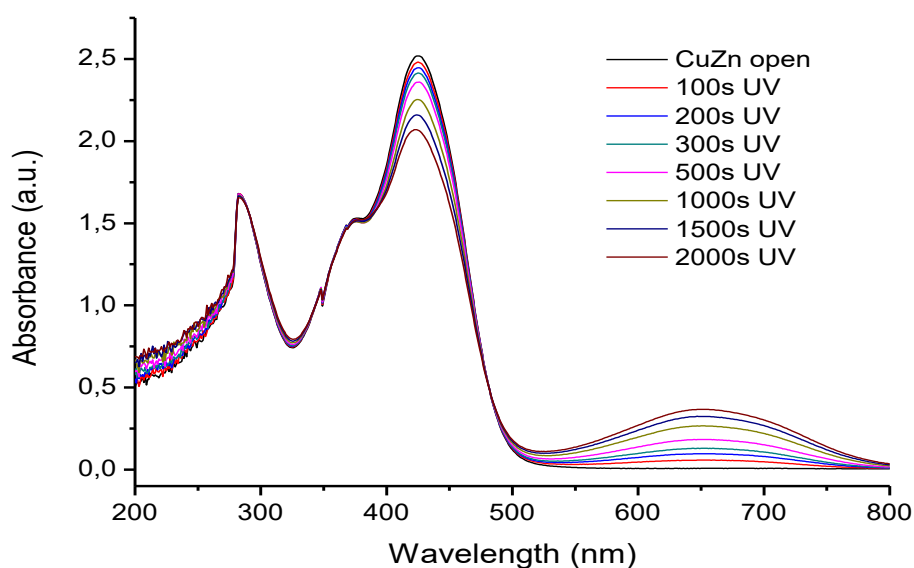


Figure 3.39: UV-Vis spectra of **12** ($[\text{CuZn}]_2$) after irradiation with UV light ($<425\text{nm}$).

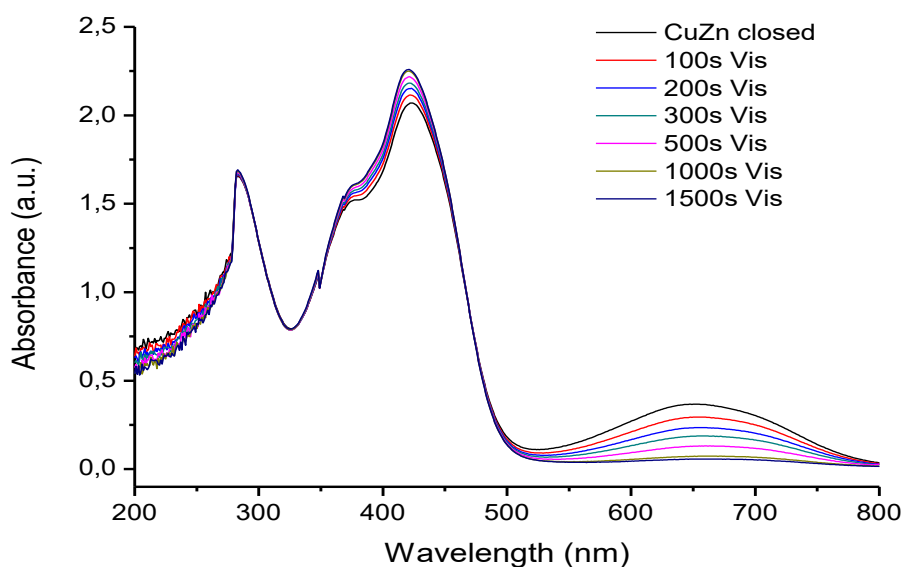


Figure 3.40: UV-Vis spectra of **12** ($[\text{CuZn}]_2$) after irradiation with Visible light ($>430\text{nm}$).

As mentioned in the beginning of this section, all the compound, homometalic and heterometallic, show approximately the same behavior.

The observed bathochromic shift in all the complexes of the bands corresponding to the π - π^* transition of the ligand, indicates an increase of the electron-withdrawing character of the chelating atoms due to the coordination with the metals.

Even though the metal to ligand charge transfer (MLCT) is not observed in the complexes, this band could be masked due to the afore mentioned bathochromic shift in addition with the exhibited broad band, compared with the free ligand.

Except for the zinc complex **8** ($[\text{Zn}_2]_2$), all compounds recover the initial color, typical of the open form, while the characteristic band around 420 nm related to the photochromic unit, changes in different ways, depending on the compound. In some cases the shoulder next to this band is the one that has more changes varying the intensity ratios. In other cases, the form of the spectrum is very similar after the cyclization and the opening ring processes compared to the original one, but the intensity of the larger band could not be recovered. All these changes can be seen in the Appendix I.

Since now, the structure of the closed isomers cannot be obtained, despite several attempts, such crystallizations in the dark with the closed isomer of the ligand in its PSS, HPLC experiments to separate the ligand isomers³⁹, or direct irradiations of single crystals⁴⁰, have been tried. However, a clear change of color (Figure 3.41) can be seen in the solid state, and different experiments are now under investigation to see if there are differences between the isomers.

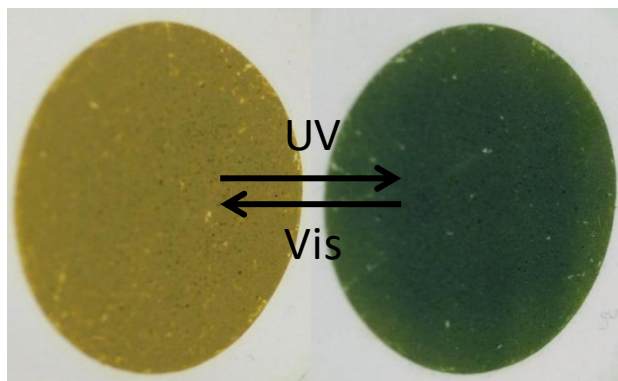


Figure 3.41: Color change of the tetranuclear complexes after irradiation with UV (<425 nm) and subsequently with visible light (>430 nm)

3.7 Conclusions

The family of both homo and heterometallic tetranuclear complexes presented in this chapter underscores a synthetic methodology based on conceiving in advance, thanks to the appropriate ligand design, the topology of the final functional entity. This has been demonstrated by different techniques, but maybe the most important in the case of the heterometallic systems, single crystal X-ray diffraction and magnetic measurements, are ideal methods to ascribe the metal topologies.

After the complete characterization concerning the heterometallic $[M'M\cdots MM']$ systems, we can confirm the presence of a total spin momentum in each pair, thus the utility of these compounds as pairs of qubits was been studied and evaluated by EPR measurements

As mentioned before, the qubit figure of merit Q , remains quite small. However, modifications on the surroundings of the pair of dimers, such as to the use of a complete or partially deuterated ligand, or the synthesis of one ligand similar with elements with negligible nuclear spin, shall increase the relaxation T_2 .

The fluorescence of the complexes was been studied, but any change was observed depending on the isomer. In this respect, the new ligand **H₄L3** could be useful, due to the naphthene group, which could be helpful if its emission band can be detected, just to compare the possible quench or enhance of that band when we have one isomer or the other.

Also, the obtaining of the pure closed isomer will serve to characterize better its properties, due to the degradation that have been seen during the photochromic reactions in solution.

3.8 Experimental

3.8.1 Ligands

1,2-bis-(5-methoxycarbonyl-2-methylthien-3-yl) cyclopentene (L4)

0.5 grams of **H₂L1** (1.4mmol) were dissolved in 20ml of dry methanol and 2.01ml of SOCl₂ (22.8mmol, excess) were added drop wise and the solution was stirred at reflux for 2 hours and then stirring overnight at r.t. After this, the solvent was removed in vacuo and the brown oil was dissolved in 20ml of ethyl acetate and washed several times to remove the HCl produced by de SOCl₂. The organic phase is separated, dried (Na₂SO₄) and evaporated, yielding a brown oil (0.52g, 98%). ¹H-NMR (400 MHz, CDCl₃) δ(ppm): 7.51 (s, 2H, Tph), 3.85 (s, 6H, Me), 2.79 (t, 4H, Cp), 2.07 (m, 2H, Cp), 1.91 (s, 6H, Me).

1,2-bis-(5-ethoxycarbonyl-2-methylthien-3-yl) cyclopentene (L5)

0.5 grams of **H₂L1** (1.4mmol) were dissolved in 20ml of dry ethanol and 2.01ml of SOCl₂ (22.8mmol, excess) were added drop wise and the solution was stirred at reflux for 2 hours and then stirring overnight at r.t. After this, the solvent was removed in vacuo and the brown oil was dissolved in 20ml of ethyl acetate and washed several times to remove the HCl produced by de SOCl₂. The organic phase is separated, dried (Na₂SO₄) and evaporated, yielding a brown oil (0.55g, 97%). ¹H-NMR (400 MHz, CDCl₃) δ(ppm): 7.50 (s, 2H, Tph), 4.3 (q, 4H, CH₂), 2.78 (t, 4H, Cp), 2.07 (m, 2H, Cp), 1.89 (s, 6H, Me), 1.35 (t, 6H, CH₃).

1,2-bis-(5-((2-acetylphenyl)-carboxylate)-2-methylthien-3-yl) cyclopentene (L2a)

0.4 grams of **H₂L1** (1.15 mmol) and a catalytic quantity (spatula tip) of DMAP were dissolved in 10ml of CH₂Cl₂ at 0°C. Once the solution was cooled, DCC (0.711g, 3.45 mmol) and 2'- hydroxyacetophenone (0.3g, 2.53 mmol) were added. The mixture was allowed to warm to r.t. and stirred for 12h. The mixture was filtered and the filtrate was washed with aqueous NHCO₃ 1M (3x6ml) and water (3x6ml). The organic phase was dried with Na₂SO₄ and solvent removal afforded a brown oil that was purified by column chromatography (silica gel with gradient elution (1:9; EtOAc:hexane to 100% EtOAc)) giving a light brown solid (0.62g, 92.4%) ¹H-RMN (400 MHz, [D₆]DMSO) δ (ppm): 7.95-7.87 (dd, 2H, Ar), 7.74 (s, 2H, Tph), 7.70-7.61 (td, 2H, Ar), 7.42 (t, 2H, Ar), 7.33

(d, 2H, Ar), 2.48 (t, 4H, Cp), 2.45 (s, 6H, Me), 2.05 (s, 8H, Me + Cp). MS (ESI+): m/z 585.14 ($[\text{C}_{33}\text{H}_{28}\text{O}_6\text{S}_2+\text{H}]^+$).

1,2-bis-(5-(3-oxo-3-(2-hydroxyphenyl)-propanoyl)-2-methylthien-3-yl) cyclopentene (H4L2).

L2a (1.678g, 2.87 mmol) was dissolved in anhydrous THF (50ml) at 0°C. tBuOK (7.18 ml of a 1M solution in THF, 7.18 mmol) was added and the mixture was mixed for 1 hour under N₂. The solution was filtered and the resulting solid was dissolved in 100 ml of water and was acidified with HCl till pH 1. The yellow-greenish precipitate was filtered and dissolved in hot acetone. The solution was cooled in the fridge, and yellow crystals appear in some days (1.1g, 66%). ¹H-RMN (400 MHz, CDCl₃) δ (ppm): 15.69 (s, 2H, OH enol), 11.96 (s, 2H, OH phenol), 7.66 (dd, 2H, Ar), 7.49 (s, 2H, Tph), 7.42 (dt, 2H, Ar), 6.9 (dd, 2H, Ar), 6.88 (td, 2H, Ar), 6.52 (s, 2H, CH enol), 2.86 (t, 4H, Cp), 2.15 (m, 2H, Cp), 2.05 (s, 6H, Me). MS (ESI+): m/z 585.1410 ($[\text{C}_{33}\text{H}_{28}\text{O}_6\text{S}_2+\text{H}]^+$)

1,2-bis-(5-((2-acetylnaphthyl)-carboxylate)-2-methylthien-3-yl) cyclopentene (L3a)

1.24 grams of **H₂L1** (3.6 mmol) and a catalytic quantity (spatula tip) of DMAP were dissolved in 50ml of CH₂Cl₂ at 0°C. Once the solution was cooled, DCC (2.28g, 10.8 mmol) and 1-hydroxy-2-acetonaphnone (1.46g, 7.9 mmol) were added. The mixture was allowed to warm to r.t. and stirred overnight. The mixture was filtered and the filtrate was washed with aqueous NHCO₃ 1M (3x15ml) and water (3x15ml). The organic phase was dried with Na₂SO₄ and solvent removal afforded a brown oil that was purified by column chromatography (silica gel with gradient elution (1:9; EtOAc:cyclohexane to 100% EtOAc)) giving a light brown solid (1.1g, 45%). ¹H-RMN (400 MHz, CDCl₃) δ (ppm): 7.93(d, 2H, Ar), 7.88 (d, 2H,Ar), 7.84 (s, 2H, Tph), 7.8 (2, 2H, Ar), 7.56 (t, 2H, Ar), 7.46 (t, 2H, Ar), 2.9 (t, 4H, Cp), 2.61 (s, 6H, Me), 2.17 (s, 6H, Me), 2.15 (m, 2H, Cp). MS (ESI+): m/z 685.14 ($[\text{C}_{41}\text{H}_{36}\text{O}_6\text{S}_2+\text{H}]^+$)

1,2-bis-(5-(3-oxo-3-(2-hydroxynaphthyl)-propanoyl)-2-methylthien-3-yl) cyclopentene (H4L3).

L3a (1g, 1.45 mmol) was dissolved in anhydrous THF (50ml) at 0°C. tBuOK (3.6 ml of a 1M solution in THF, 3.6 mmol) was added and the mixture was mixed for 2 hour under N₂. The solution was filtered and the resulting solid was dissolved in 100 ml of water and was acidified with HCl till pH 1. The yellow-greenish precipitate was filtered

and dissolved in hot ethyl acetate. The solution was cooled in the fridge, and yellow crystals appear in some days (0.4 g, 40%). MS (ESI+): m/z 685.10 ($[C_{41}H_{36}O_6S_2+H]^+$)

3.8.2 Coordination compounds.

[Cu₄L₂(py)₆]·**9(py) (5)**

A solution of **H₄L₂** (20 mg, 0.034 mmol) and tetrabutylammonium hydroxide (TBAOH, 0.136 mL, 0.136 mmol) in pyridine (15 mL) was added to a solution of CuBr₂ (15.19 mg, 0.068 mmol) in pyridine (15 mL). The resulting dark orange mixture was stirred for 2 h, filtered and the solution was then layered with hexane. After one week, orange crystals corresponding to the complex were collected (14 %, 11.5 mg). IR (KBr pellet, cm⁻¹): 3439 , 2917 , 2847 , 1600 , 1500 , 1443 , 1365 , 1326 , 1247 , 1195 , 1130 , 1030 , 1000 , 847 , 791 , 474 , 700 , 669 , 573. Anal., found (calc% for [C₉₆H₇₈Cu₄N₆O₁₂S₄]**·**2.65H₂O; **5**·2.65H₂O); C 59.89 (59.57), H 4.11 (4.34), N 3.98 (4.34).

[Co₄L₂(py)₆]·**9(py) (6)**

A solution of **H₄L₂** (20 mg, 0.034 mmol) and TBAOH (0.136 mL, 0.136 mmol) in pyridine (15 mL) was added to a solution of CoCl₂·6H₂O (16.16 mg, 0.068 mmol) in pyridine (15 mL). The resulting dark orange mixture was stirred for 2 h, filtered and the solution was then layered with ether. After one day, the complex was obtained as red crystals (10 %, 8.5 mg). Anal., found (calc% for [C₉₆H₇₈Co₄N₆O₁₂S₄]**·**2.3H₂O; **6**·2.3H₂O); C 60.26 (60.27), H 4.39 (4.35), N 4.43 (4.40). The IR spectrum was identical to the one obtained for complex **5**.

[Ni₄L₂(py)₆]·**9(py) (7)**

A solution of **H₄L₂** (20 mg, 0.034 mmol) and TBAOH (0.136 mL, 0.136 mmol) in pyridine (15 mL) was added to a solution of Ni(AcO)₂·4H₂O (16.2 mg, 0.068 mmol) in pyridine (15 mL). The resulting dark orange mixture was stirred for 2 h, filtered and the solution was then layered with ether. After three days, orange crystals were collected (13 %, 10.7 mg). Anal., found (calc% for [C₉₆H₇₈Ni₄N₆O₁₂S₄]**·**5H₂O; **7**·5H₂O); C 58.91 (58.89), H 4.43 (4.53), N 4.13 (4.29). The IR spectrum was identical to the one obtained for complex **5**.

[Zn₄L₂(py)₆]·9(py) (8)

A solution of **H₄L₂** (20 mg, 0.034 mmol) and TBAOH (0.136 mL, 0.136 mmol) in pyridine (15 mL) was added to a solution of Zn(AcO)₂ (9.26 mg, 0.068 mmol) in pyridine (15 mL). The resulting dark orange mixture was stirred for 2 h, filtered and the solution was then layered with hexane. After one week, the complex was obtained as green crystals (13 %, 10.7 mg). The IR spectrum was identical to the one obtained for complex **5**.

[Cu₂Ni₂L₂(py)₆]·9(py) (9)

A solution of **H₄L₂** (20 mg, 0.034 mmol) and TBAOH (0.136 mL, 0.136 mmol) in pyridine (15 mL) was added to a solution of Cu(NO₃)₂·3H₂O (8.21 mg, 0.034 mmol) and Ni(NO₃)₂·3H₂O (9.88 mg, 0.034 mmol) in pyridine (15 mL). The resulting dark orange mixture was stirred for 2 h, filtered and the solution was then layered with hexane. After four days, orange crystals corresponding to the complex were obtained (16 %, 13.2 mg). Anal., found (calc% for [C₈₆H₆₈Cu₂Ni₂N₄O₁₂S₄]·6H₂O; **9**·6H₂O·2py); C 56.34 (56.51) H 4.31 (4.41), N 2.88 (3.06). The IR spectrum was identical to the one obtained for complex **5**.

[Co₂Ni₂L₂(py)₆]·9(py) (10)

A solution of **H₄L₂** (20 mg, 0.034 mmol) and TBAOH (0.136 mL, 0.136 mmol) in pyridine (15 mL) was added to a solution of Ni(AcO)₂·4H₂O (8.71 mg, 0.035 mmol) and Co(AcO)₂·4H₂O (8.45 mg, 0.034 mmol) in pyridine (15 mL). The resulting dark orange mixture was stirred for 2 h, filtered and the solution was then layered with hexane. After four days, orange crystals were collected (12 %, 9.7 mg). Anal., found (calc% for [C₉₆H₇₈Co₂Ni₂N₆O₁₂S₄]·6H₂O; **10**·6H₂O); C 58.57 (58.29), H 4.12 (4.59), N 3.75 (4.25). The IR spectrum was identical to the one obtained for complex **5**.

[Co₂Cu₂L₂(py)₆]·9(py) (11)

A solution of **H₄L₂** (20 mg, 0.034 mmol) and TBAOH (0.136 mL, 0.136 mmol) in pyridine (15 mL) was added to a solution of Cu(AcO)₂·H₂O (7.4 mg, 0.037 mmol) and Co(AcO)₂·4H₂O (8.46 mg, 0.034 mmol) in pyridine (15 mL). The resulting dark orange mixture was stirred for 2 h, filtered and the solution was then layered with ether. After one day, the complex was obtained as orange crystals (13 %, 11 mg). Anal., found

(calc% for $[\text{C}_{96}\text{H}_{78}\text{Co}_2\text{Cu}_2\text{N}_6\text{O}_{12}\text{S}_4]\cdot 1.65\text{H}_2\text{O}$; **11** $\cdot 1.65\text{H}_2\text{O}$); C 60.27 (60.38), H 4.32 (4.29), N 4.50 (4.40). The IR spectrum was identical to the one obtained for complex **5**.

$[\text{Cu}_2\text{Zn}_2\text{L}_2(\text{py})_6]\cdot 9(\text{py})$ (12**)**

A solution of **H₄L₂** (20 mg, 0.034 mmol) and TBAOH (0.136 mL, 0.136 mmol) in pyridine (15 mL) was added to a solution of $\text{CuCl}_2\cdot 2\text{H}_2\text{O}$ (5.78 mg, 0.034 mmol) and ZnCl_2 (4.62 mg, 0.034 mmol) in pyridine (15 mL). The resulting dark orange mixture was stirred for 2 h, filtered and the solution was then layered with hexane. After one day, orange crystals corresponding to the complex were collected (16 %, 13.4 mg). Anal., found (calc% for $[\text{C}_{86}\text{H}_{68}\text{Cu}_2\text{Zn}_2\text{N}_4\text{O}_{12}\text{S}_4]\cdot 1.95\text{H}_2\text{O}$; **12** $\cdot 1.95\text{H}_2\text{O}\cdot 3.75\text{py}$); C 56.55 (56.94), H 3.76 (3.91), N 2.38 (1.94). The IR spectrum was identical to the one obtained for complex **5**.

$[\text{Ni}_2\text{Zn}_2\text{L}_2(\text{py})_6]\cdot 9(\text{py})$ (13**)**

A solution of **H₄L₂** (20 mg, 0.034 mmol) and TBAOH (0.136 mL, 0.136 mmol) in pyridine (15 mL) was added to a solution of $\text{NiCl}_2\cdot 6\text{H}_2\text{O}$ (8.08 mg, 0.034 mmol) and ZnCl_2 (4.62 mg, 0.034 mmol) in pyridine (15 mL). The resulting dark orange mixture was stirred for 2 h, filtered and the solution was then layered with ether. After one day, orange crystals were obtained (13 %, 10.7 mg). Anal., found (calc% for $[\text{C}_{86}\text{H}_{68}\text{Ni}_2\text{Zn}_2\text{N}_4\text{O}_{12}\text{S}_4]\cdot 5.2\text{H}_2\text{O}$; **13** $\cdot 5.2\text{H}_2\text{O}\cdot 2.75\text{py}$); C 55.69 (55.80), H 3.89 (4.34), N 2.98 (2.57). The IR spectrum was identical to the one obtained for complex **5**.

3.9 References

1. Aromí, G., Gamez, P. & Reedijk, J. Poly beta-diketones: Prime ligands to generate supramolecular metallocusters. *Coord. Chem. Rev.* **252**, 964–989 (2008).
2. Aguilà, D. *et al.* Heterodimetallic [LnLn'] Lanthanide Complexes: Towards a Chemical Design of 2-Qubit Molecular Spin Quantum Gates Heterodimetallic [LnLn'] Lanthanide Complexes: Towards a Chemical Design of 2-Qubit Molecular Spin Quantum Gates. (2014).
3. Aromí, G., Aguilà, D., Gamez, P., Luis, F. & Roubeau, O. Design of magnetic coordination complexes for quantum computing. *Chem. Soc. Rev.* **41**, 537 (2012).
4. Luis, F. *et al.* Molecular prototypes for spin-based CNOT and SWAP quantum gates. *Phys. Rev. Lett.* **107**, 1–4 (2011).
5. Ardavan, a. & Blundell, S. J. Storing quantum information in chemically engineered nanoscale magnets. *J. Mater. Chem.* **19**, 1754 (2009).
6. Bader, K. *et al.* Room temperature quantum coherence in a potential molecular qubit. *Nat. Commun.* **5**, 5304 (2014).
7. Lucas, L. N., Jong, J. J., Esch, J. H., Kellogg, R. M. & Feringa, B. L. Syntheses of Dithienylcyclopentene Optical Molecular Switches. *Eur. J. Org. Chem.* **2003**, 155–166 (2003).
8. Wissler, J., Mulder, A., Tampé, R. & Bolte, M. 1,2-Bis(5-chloro-2-methyl-3-thienyl)cyclopentene. *Acta Crystallogr. Sect. E Struct. Reports Online* **62**, (2006).
9. Duan, X. F., Zeng, J., Lü, J. W. & Zhang, Z. Bin. Insights into the general and efficient cross McMurry reactions between ketones. *J. Org. Chem.* **71**, 9873–9876 (2006).
10. Migulin, V. A. *et al.* Synthesis and characterization of nonsymmetric cyclopentene-based dithienylethenes. *J. Org. Chem.* **77**, 332–340 (2012).
11. Claisen, L. & Ergardt, E. F. *Chemische Berichte.* **22**, 1009 (1889).
12. Neises, B. & Steglich, W. Simple Method for the Esterification of Carboxylic Acids. *Angew. Chemie Int. Ed. English* **17**, 522–524 (1978).
13. Baker, W. Molecular rearrangement of some o-acyloxyacetophenones and the mechanism of the production of 3-acylchromones. *J. Chem. Soc.* 1381 (1933).
14. Mahal, H. S. & Venkataraman, K. 387. Synthetical experiments in the chromone group. Part XIV. The action of sodamide on 1-acyloxy-2-acetonaphthones. *J. Chem. Soc.* 1767 (1934).
15. Kobatake, S. & Irie, M. Single-Crystalline Photochromism of Diarylethenes. in *Bulletin of the Chemical Society of Japan* (2004).

16. Irie, M. Diarylethenes for Memories and Switches. *Chemical Reviews* **100**, (2000).
17. Eigler, D. M., Lutz, C. P. & Rudge, W. E. An atomic switch realized with the scanning tunnelling microscope. *Nature* **352**, 600–603 (1991).
18. Takeshita, M. & Irie, M. Reversible Fluorescence Intensity Change of a Diarylethene. *Chem. Lett.* 1123–1124 (1998).
19. Irie, M., Kobatake, S. & Horichi, M. Reversible Surface Morphology Changes of a Photochromic Diarylethene Single Crystal by Photoirradiation. *Science (80)*. **291**, 1769–1772 (2001).
20. Jong, J. J. D. de *et al.* Photochromic Properties of Perhydro- and Perfluorodithienylcyclopentene Molecular Switches. *European J. Org. Chem.* (2003).
21. Peters, A. & Branda, N. R. Limited photochromism in covalently linked double 1,2-dithienylethenes. *Adv. Mater. Opt. Electron.* **10**, 245–249 (2000).
22. Norrish, R. G. W. & Bamford, C. H. Photo-decomposition of aldehydes and ketones. *Nature* **140**, 195–196 (1937).
23. Schwack, W. & Rudolph, T. Photochemistry of dibenzoyl methane UVA filters Part 1. *J. Photochem. Photobiol. B Biol.* **28**, 229–234 (1995).
24. Yamaji, M. & Kida, M. Photothermal tautomerization of a UV sunscreen (4-tert-butyl-4'-methoxydibenzoylmethane) in acetonitrile studied by steady-state and laser flash photolysis. *J. Phys. Chem. A* **117**, 1946–1951 (2013).
25. Barrios, L. A. *et al.* Synthesis and properties of a novel linear [Ni₄L₂(py)₆] cluster: Designed ligand-controlled topology of the metals. *C. R. Chim.* **11**, 1117–1120 (2008).
26. Aromí, G. *et al.* Complexes of a novel multinucleating poly-beta-diketonate ligand. *Dalt. Trans.* 3586–3592 (2004).
27. Barrios, L. A. *et al.* Designed topology and site-selective metal composition in tetranuclear [MM'···M'M] linear complexes. *Chem. - A Eur. J.* **15**, 11235–11243 (2009).
28. Chilton, N. F., Anderson, R. P., Turner, L. D., Soncini, A. & Murray, K. S. PHI: A powerful new program for the analysis of anisotropic monomeric and exchange-coupled polynuclear d- and f-block complexes. *J. Comput. Chem.* **34**, 1164–1175 (2013).
29. Aromí, G. *et al.* Aggregation of [Cu₄(II)] Building Blocks into [Cu₈(II)] Clusters or a [Cu₄(II)] ∞ Chain through Subtle Chemical Control. *Chem. - A Eur. J.* **10**, 6476–6488 (2004).

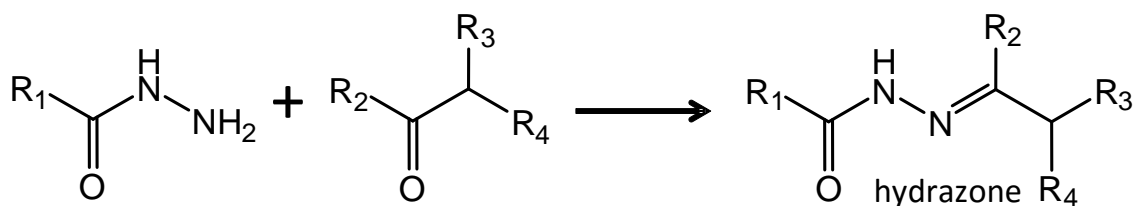
30. Thompson, L. K., Mandal, S. K., Tandon, S. S., Bridson, J. N. & Park, M. K. Magnetostructural Correlations in Bis(η^2 -phenoxide)-Bridged Macrocyclic Dinuclear Copper(II) Complexes. Influence of Electron-Withdrawing Substituents on Exchange Coupling. *Inorg. Chem.* **35**, 3117–3125 (1996).
31. Bryan, A. M., Long, G. J., Grandjean, F. & Power, P. P. Synthesis, structural, spectroscopic, and magnetic characterization of two-coordinate cobalt(II) aryloxides with bent or linear coordination. *Inorg. Chem.* **53**, 2692–8 (2014).
32. Walsh, J. P. S. *et al.* On the possibility of magneto-structural correlations: detailed studies of dinickel carboxylate complexes. *Inorg. Chem.* **53**, 8464–8472 (2014).
33. Titis, J. & Boca, R. Magnetostructural D correlation in Nickel(II) complexes: Reinvestigation of the zero-field splitting. *Inorg. Chem.* **49**, 3971–3973 (2010).
34. Morgenstern-Badarau, Rerat, M., Kahn, O., Jaud, J. & Galy, J. Crystal Structure and Magnetic and EPR Properties of the Heterobinuclear Complex $\text{CuNi}(\text{fsa})_2\text{en}(\text{H}_2\text{O})$. *Inorg. Chem.* **21**, 3050–3059 (1982).
35. Mitrikas, G., Sanakis, Y., Raptopoulou, C. P., Kordas, G. & Papavassiliou, G. Electron spin-lattice and spin-spin relaxation study of a trinuclear iron(III) complex and its relevance in quantum computing. *Phys. Chem. Chem. Phys. PCCP* **10**, 743–748 (2008).
36. Ardavan, A. *et al.* Will spin-relaxation times in molecular magnets permit quantum information processing? *Phys. Rev. Lett.* **98**, 057201 (2007).
37. Schlegel, C., Van Slageren, J., Timco, G., Winpenny, R. E. P. & Dressel, M. Origin of superhyperfine interactions in the antiferromagnetic ring Cr_7Ni . *Phys. Rev. B - Condens. Matter Mater. Phys.* **83**, 5–7 (2011).
38. Affronte, M. Molecular nanomagnets for information technologies. *J. Mater. Chem.* **19**, 1731 (2009).
39. Morimoto, M., Miyasaka, H., Yamashita, M. & Irie, M. Coordination assemblies of $[\text{Mn}_4]$ single-molecule magnets linked by photochromic ligands: Photochemical control of the magnetic properties. *J. Am. Chem. Soc.* (2009).
40. Irie, M., Lifka, T. & Uchida, K. Photochromism of Single Crystalline Diaruthenes. *Molecular Crystals and Liquid Crystals Science and Technology. Section A. Molecular Crystals and Liquid Crystals* (1997).

CHAPTER 4: EXPLORING THE SMM BEHAVIOR OF LANTHANIDE COMPLEXES CONTAINING PHOTOCROMIC LIGANDS

4.1 Introduction	154
4.2 Synthesis and characterization	155
4.2.1 Synthesis and crystal structure of of 1,2-bis-(5-(N'-(2-hydroxybenzylidene)hydrazide)-2-methylthien-3-yl) cyclopentene (H ₄ L7).....	155
4.2.2 Synthesis of 1,2-bis-(5-(N'-(pyridine-2-ylmethylene)hydrazide)-2-methylthien-3-yl) cyclopentene (H ₂ L8)	158
4.2.3 Phochromism of H ₄ L7and H ₂ L8	158
4.3 Synthesis and crystal structures of H ₄ L7 and H ₂ L8	160
4.3.1 Synthesis and crystal structure of [Ln ₂ L ₇ (CO ₃) ₂ Na ₆ Py ₁₀] (Ln: Tb (14); Dy (15))..	160
4.3.2 Synthesis and crystal structure of [Ln ₄ L ₈ Cl ₄ (H ₂ O) ₅]·nPy (Ln: Tb (16); Dy (17)).	163
4.3.3 Synthesis and crystal structure of [Ln ₄ L ₇ Na ₄ (H ₂ O) ₂ (CO ₃) ₂ (Py) ₆ (acac) ₄]·9Py (Ln: Tb (18); Dy (19)).	167
4.4 Introduction to magnetic properties of lanthanides	171
4.4.1 Magnetic properties of [Tb ₂ L ₇ (CO ₃) ₂ Na ₆ Py ₁₀] (14)	172
4.4.2 Magnetic properties of [Ln ₄ L ₈ Cl ₄ (H ₂ O) ₅]·nPy (16 and 17).....	173
4.4.3 Magnetic properties of [Ln ₄ L ₇ Na ₄ (H ₂ O) ₂ (CO ₃) ₂ (Py) ₆ (acac) ₄]·9Py (18 and 19).....	174
4.4.4 Single molecule magnet behavior	175
4.5 Coordination compounds with copper	177
4.5.1 Synthesis and crystal structure of [Cu ₂ L ₇ (Py) ₂](MeOH) (20)	177
4.5.2 Synthesis and crystal structure of [Cu ₂ L ₇ (Phen) ₂](H ₂ O) ₃ (21)	179
4.6 Magnetic properties of [Cu ₂ L ₇ (Py) ₂](MeOH) and [Cu ₂ L ₇ (Phen) ₂](H ₂ O) ₃	181
4.7 Photochromism behavior.....	182
4.8 Conclusions	184
4.9 Experimental	185
4.9.1 Ligands	185
4.9.2 Coordination compounds	186
4.10 References	189

4.1 Introduction

In the synthetic design of new coordination compounds it is of paramount importance the nature of the metal center that will be coordinated. The coordination number, the ionic volume, and the coordination geometry are crucial for such design. In terms of lanthanides, these ions can support different coordination numbers, presenting a large number of coordination geometries. Also the ionic radius here of importance, where the biggest value of 1.03 Å corresponding lanthanum and the shortest value to 0.86 Å for Lutetium¹ for the trivalent cations. Taking into account both variables, is possible, although challenging, to design ligands in order to adequately accommodate lanthanides. In that regard, porfirines²⁻⁵, crown ethers^{4,6,7} picolines^{8,9}, phenantrolines⁴ and salen¹⁰⁻¹² ligands, among others, have been used in the synthesis of coordinated compounds presenting lanthanide atoms. Another type of chelating group used to coordinate lanthanide atoms are those based on Schiff bases and their derivatives, like the hydrazones^{8,10,13-26}, which present of an N-N bond with different substituents, with at least one of them being an acyl group. These hydrazones can be thus functionalized very easy with other groups, such as aldehydes or ketones, allowing via Schiff base reaction^{27,28}, to obtain new chelating ligands in very good yields. The general synthesis to produce hydrazones is shown in Scheme 4.1.



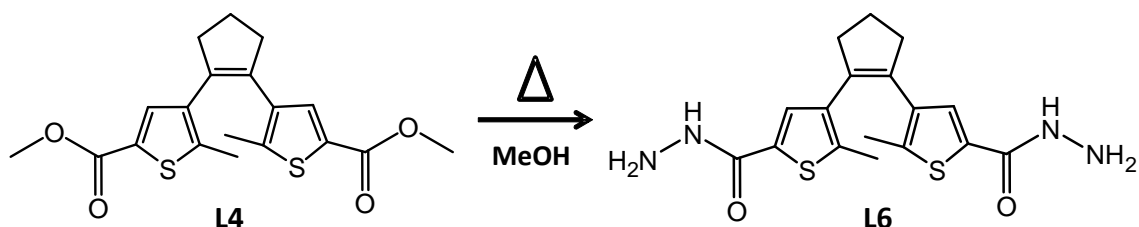
Scheme 4.1: General synthesis of hydrazones.

In this chapter, the synthesis and characterization of two new photoswitchable ligands taking advantage of this scheme is presented. Different coordination compounds of these ligands with some lanthanide atoms (Dy, Tb), have been prepared and tested via magnetic measurements, in order to prove their potential as single molecule magnets. Although the ligands present indeed the photochromic unit, the serendipity of the coordination reactions leads here to clusters which are not able to perform photocyclization. In contrast, the use of a transition metal, such as copper, gives coordination compounds able to perform photochromic reactions.

4.2 Synthesis and characterization

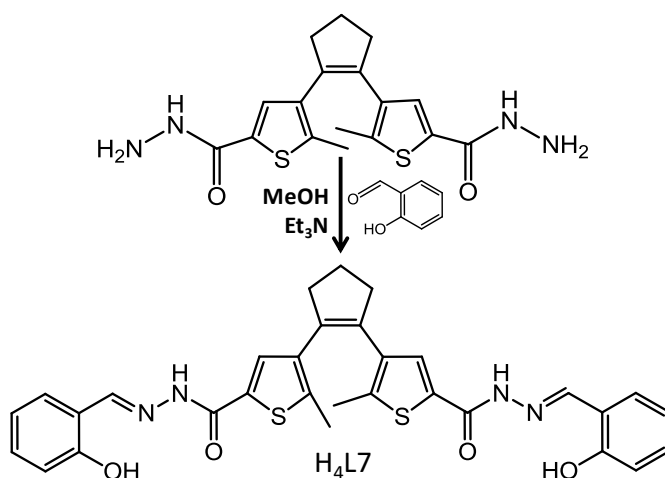
4.2.1 Synthesis and crystal structure of of 1,2-bis-(5-(N'-(2-hydroxybenzylidene)hydrazide)-2-methylthien-3-yl) cyclopentene (**H₄L7**)

Ligand **H₄L7** was designed to encapsulate two lanthanide atoms and keep them in one molecule while separated through a photochromic spacer. The first step was the synthesis of the carbohydrazone **1,2-bis-(5-hydrazide-2-methylthien-3-yl) cyclopentene (L6)**, which can be obtained via condensation of an excess of hydrazine with the previously presented species **L4**. The refluxed methanol mixture of both compounds, leads after three hours to **L6**, as a white powder. The general synthesis is shown in Scheme 4.2.



Scheme 4.2: Synthesis of **L6**.

The subsequently synthesis is the well-known Schiff base reaction^{27,28}, where an amine and a carbonyl group reacts by a nucleophilic addition, forming after dehydration, an imine. Here the reaction of **L6** with salicylaldehyde in refluxing methanol, in the presence of some drops of triethylamine (Et_3N) as a catalyst, gives **H₄L7** as white powder, which can be crystallized from DMF (Scheme 4.3).



Scheme 4.3: Synthesis of **H₄L7**

Figure 4.1 shows the molecular representation of **H₄L7**. The corresponding crystallographic data are summarized in Table 4.1. The system crystallizes in the orthorhombic $P2_12_12_1$ space group.

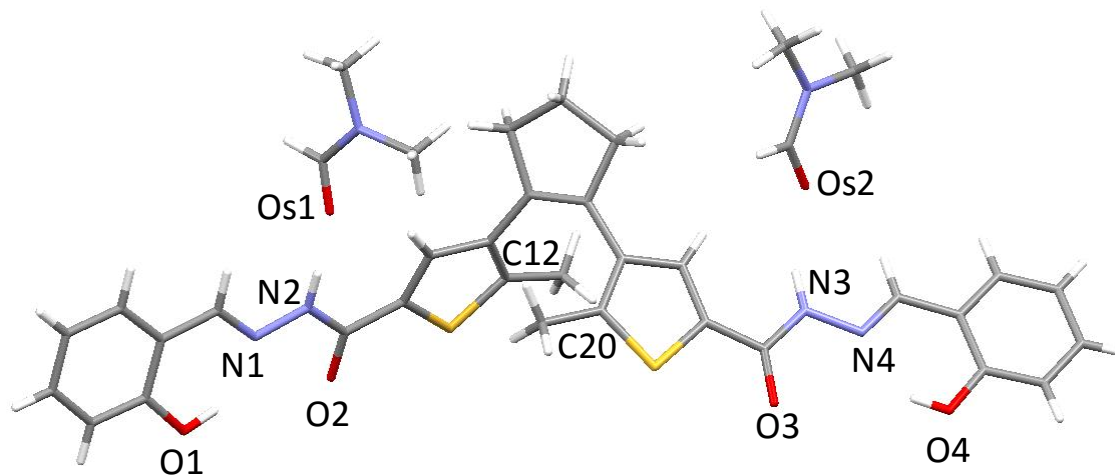


Figure 4.1: Crystal structure of **H₄L7**

Table 4.1. Crystallographic data for **H₄L7**

Formula	C ₃₇ H ₄₂ N ₆ O ₆ S ₂
M_r	730.89
a [Å]	12.868(8)
b [Å]	16.124(8)
c [Å]	18.277(9)
α [°]= β [°]= γ [°]	90
V [Å ³]	3782(3)
ρ [g cm ⁻³]	1.284
shape and colour	Yellow prism
Z	4
μ [mm ⁻¹]	0.193
reflns	6082
parameters	468
restrains	19
R_{int}	0.0326
R_1	0.0487
wR_2	0.1135
S	1.031

Ligand **H₄L7** presents intramolecular hydrogen bonds between the O-H moieties of the phenol groups and the nitrogen atoms of the imine, N1 and N4. In addition, **H₄L7**

crystallizes with two molecules of DMF in its lattice per asymmetric unit, creating hydrogen bonds with the N-H groups associated to N2 and N3.

These DMF molecules are the responsible of the efficient packing through the crystal, creating additional hydrogen bonds with neighboring of ligands and other DMF molecules while there is no presence of any aromatic stacking.

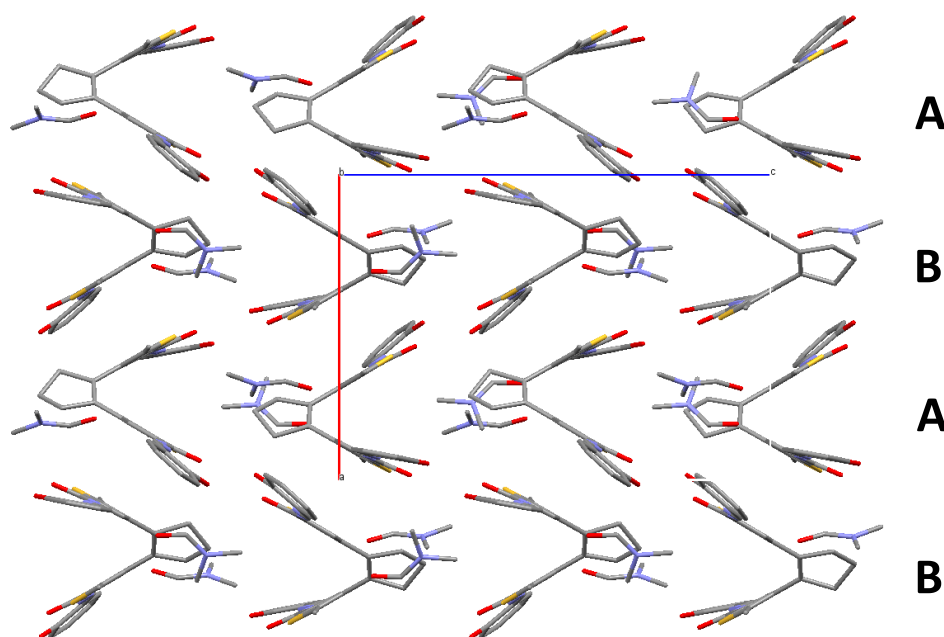


Figure 4.2: Crystal packing of **H₄L7** through the *b* axis.

The packing reveals two orientation of the molecules, disposed in layers (denoted by A and B in Figure 4.2), which are in opposite directions.

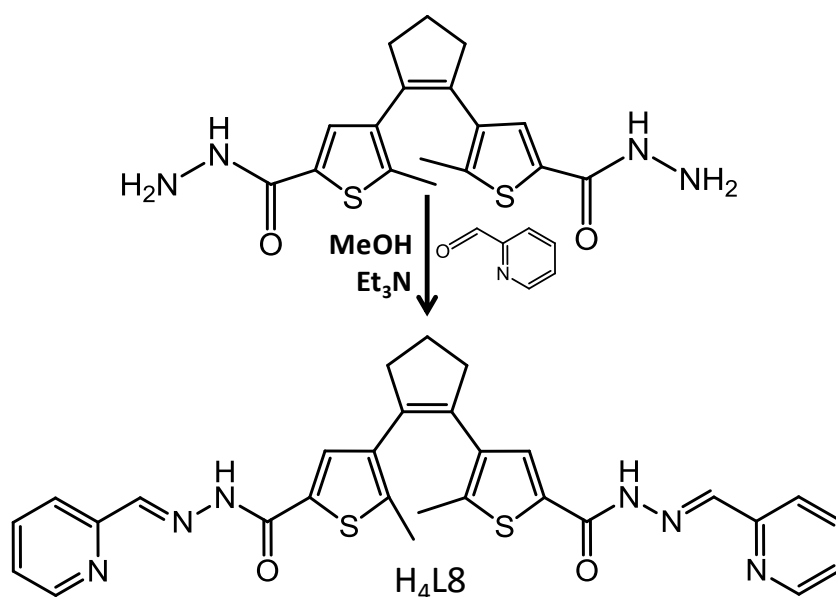
The central part, corresponding to the photochromic unit, presents the aryl thiophene rings in the antiparallel conformation, where the C12-C20 distance is shorter than 4 Å (3.503 Å), thus providing good conditions for the photocyclization process in the solid state. **H₄L7** presents a color change, passing from white to violet upon irradiation with UV light.

The crystal structure of **H₄L7** makes evident the two pockets present in the ligand, formed by the hydrazone and the phenol group. This cavity is large enough to encapsulate lanthanide ions, and as mentioned before, the hydrazone can be functionalized easily, for example by introduction of another donating group, such as a pyridine, as shown below.

4.2.2 Synthesis of 1,2-bis-(5-(N'-(pyridine-2-ylmethylene)hydrazide)-2-methylthien-3-yl) cyclopentene (**H₂L8**)

Following the same procedure for **H₄L7**, an using 2-pyridinecarboxyaldehyde instead of salicylaldehyde, a light grey powder of **1,2-bis-(5-(N'-(pyridine-2-ylmethylene)hydrazide)-2-methylthien-3-yl) cyclopentene (**H₂L8**)** is obtained following the precipitation with methanol and water. **H₂L8** also exhibits a change of color after irradiation with UV light, from light grey to violet.

The reaction of the hydrazone formation of **H₂L8** is shown in Scheme 4.4.



Scheme 4.4: Synthesis of **H₂L8**

4.2.3 Photochromism of **H₄L7** and **H₂L8**

The photochromic behavior of both ligands was studied in 5×10^{-5} M ethanolic solution. In both cases, after irradiation with UV light, the colorless solution turns deep violet and returns to the initial colorless upon irradiation with visible light. **H₄L7** is characterized by three intense bands at 213, 296 and 336 nm. Also a small band at 403 nm can be observed. All of them decrease in intensity with irradiation with UV while a broad band centered at 557 nm appears owing to the cyclization of the ligand. The inverse process occurs when the sample is irradiated with Visible light. Both processes are quite fast as shown in Figure 4.3. Eventhought the intense peak at 336 nm is not recovered at all, this

behavior can be possible explained as the result of the isomerization cis/trans by the hydrazone moiety²⁹.

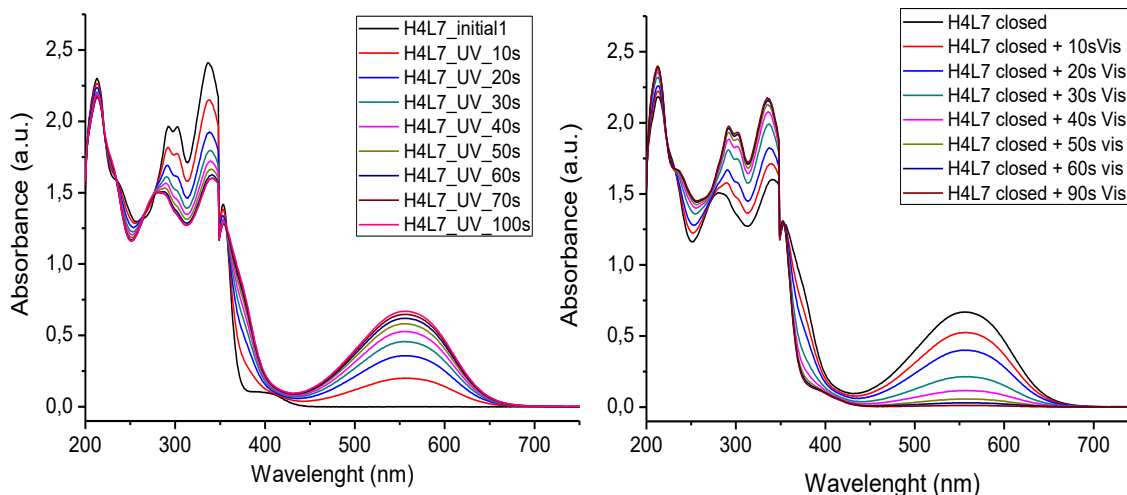


Figure 4.3: Left: Photocyclization of the open **H₄L7** ligand with UV light (<425nm). Right: Ring opening of the closed form upon irradiation with visible light (>430nm).

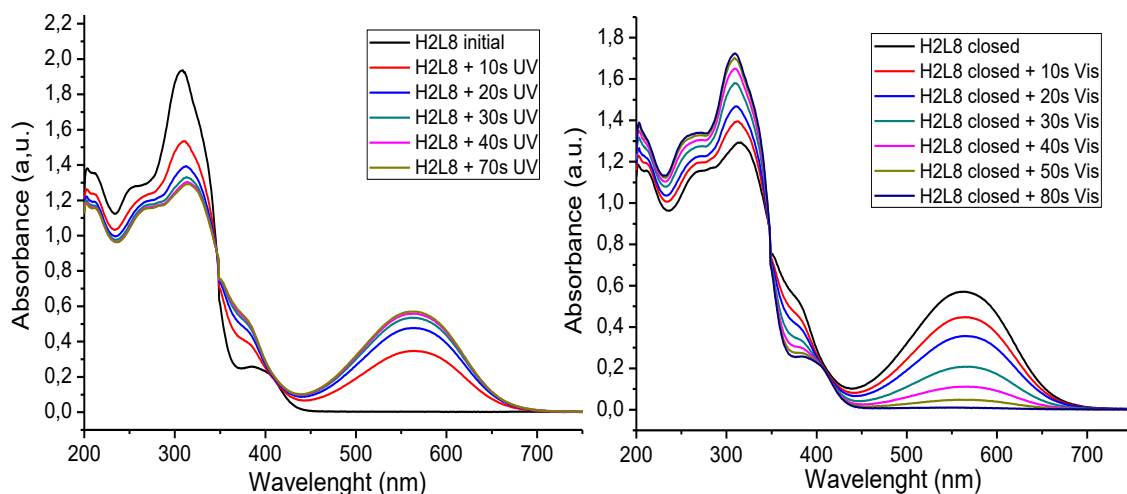


Figure 4.4: Left: Photocyclization of the open **H₂L8** ligand with UV light (<425nm). Right: Ring opening of the closed form upon irradiation with visible light (>430nm).

H₂L8 (Figure 4.4) has an intense and broad band at 308 nm with a small shoulder at 251 nm. It also presents a band at 208 nm and another at 396 nm, similar as ligand **H₄L7**. When the sample is irradiated with UV light, these bands decrease while a new broad band at 564 nm appears due to the cyclization. The ring opening process also seems to proceed completely upon irradiation with visible light. Both photochromic processes are

faster than in ligand **H₄L7** and also the small differences after the end of the complete cycle with the initial system can be due the possible isomerization cis/trans of the hydrazone moiety.

4.3 Synthesis and crystal structures of **H₄L7** and **H₂L8**

4.3.1 Synthesis and crystal structure of $[\text{Ln}_2\text{L7}_2(\text{CO}_3)_2\text{Na}_6\text{Py}_{10}]$ (Ln: Tb (**14**); Dy (**15**)).

The stoichiometry used was one equivalent of a nitrate lanthanide salt (of Tb or Dy) with one equivalent of ligand **H₄L7**, using four equivalent of base (NaH with an excess of 20%), to fully deprotonate the ligand, in pyridine, giving a yellow solution. After liquid-liquid diffusion, crystals of $[\text{Ln}_2\text{L7}_2(\text{CO}_3)_2\text{Na}_6\text{Py}_{10}]$ (Ln: Tb (**14**); Dy (**15**)) were formed (Figure 4.5). **14** and **15** crystallizes in the monoclinic space group $P2_1/n$. The asymmetric unit is formed by one ligand coordinated to one lanthanide, with one molecule of carbonate, three sodium ions and five coordinating pyridine molecules. One of these pyridine groups is disordered over two positions, almost in a perpendicular maner approximately in a 50% distribution. The presence of an inversion centre, allows to build-up the complete molecule. The lanthanide atom is surrounded by two different pocket cavities from **L7⁴⁻**. The rest of the coordination sphere is completed with oxygen atoms from the carbonate anions. The Ln(III) ions are thus described as eight coordinate (N_2O_6).

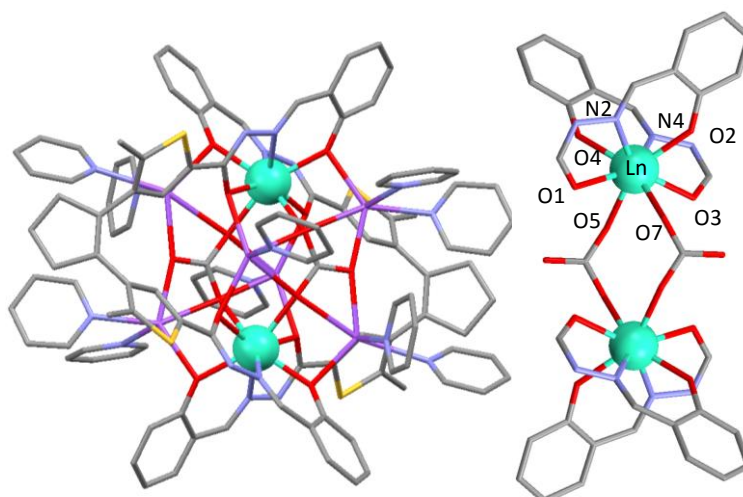


Figure 4.5: Representation of $[\text{Ln}_2\text{L7}_2(\text{CO}_3)_2\text{Na}_6\text{Py}_{10}]$ (left). The core of the cluster is represented in the right, showing the linkage with the carbonate. Hydrogen atoms were omitted for clarity.

There are not any solvent molecules in the lattice as pyridine is used as a solvent, it incorporates into the product via coordination through the sodium cations. The basic conditions used during the synthesis are important in the final structure of the compound ruling the reaction with the carbon dioxide presents in the air, forming carbonates. The crystal structure shows that the parallel configuration of the ligand seems to be the most stable compound. In that sense, sodium could be the responsible of this conformation because it acts as linker through the oxygen atoms presented in the structure and it links the ketone groups of the same molecule, forcing the parallel configuration, thus blocking the photochromism of these species. The distance between the reactive carbons is 5.268 Å

The corresponding crystallographic data of $[\text{Ln}_2\text{L7}_2(\text{CO}_3)_2\text{Na}_6\text{Py}_{10}]$ is summarized in Table 4.2.

Table 4.2. Crystallographic data of $[\text{Ln}_2\text{L7}_2(\text{CO}_3)_2\text{Na}_6\text{Py}_{10}]$		
	14	15
formula	$\text{C}_{57}\text{H}_{49}\text{N}_9\text{Na}_3\text{O}_7\text{S}_2\text{Tb}$	$\text{C}_{57}\text{H}_{49}\text{N}_9\text{Na}_3\text{O}_7\text{S}_2\text{Dy}$
M_r	1263.54	1269.15
Crystal system	monoclinic	monoclinic
space group	P21/n	P21/n
a [Å]	13.178(7)	13.177(15)
b [Å]	18.024(8)	18.070(2)
c [Å]	23.308(10)	23.209(3)
$\alpha = \gamma$ [°]	90	90
β [°]	96.558(2)	96.685(18)
V [Å ³]	5500.2(4)	5488.8(11)
Z	4	4
ρ [g cm ⁻³]	1.526	1.536
shape; colour	Yellow block	Yellow block
μ [mm ⁻¹]	1.447	1.902
reflns	12150	16029
parameters	757	744
restrains	19	240
R_{int}	0.071	0.0448
R_1	0.0419	0.0683
wR_2	0.110	0.1405
S	1.115	1.082

The packing of these compounds is very efficient as the Figure 4.6 shows, having little space to accommodate solvents molecules. Platon calculations reveal only 1.4% of possible space to place solvents (74.4\AA^3 from 5500\AA^3 of the unit cell).

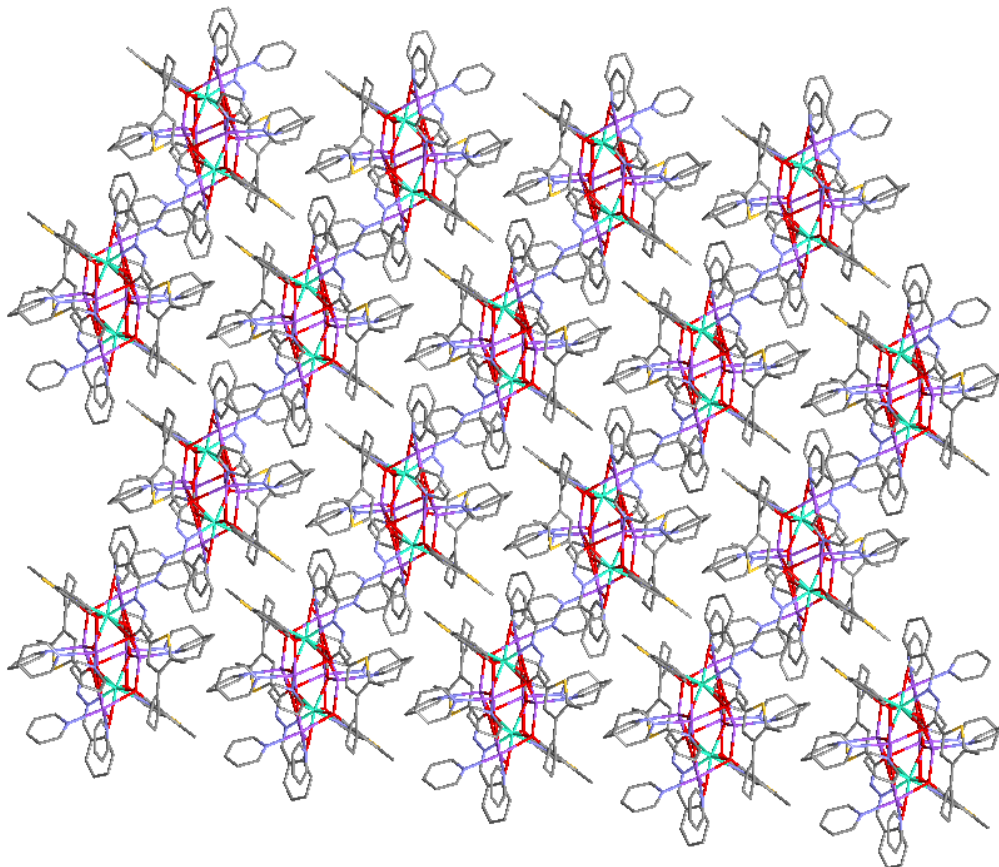


Figure 4.4: Crystal packing of $[\text{Ln}_2\text{L}_7_2(\text{CO}_3)_2\text{Na}_6\text{Py}_{10}]$

Selected bond and angles are shown in Tables 4.3, 4.4 and 4.5.

Table 4.3 Bond distances of $[\text{Ln}_2\text{L}_7_2(\text{CO}_3)_2\text{Na}_6\text{Py}_{10}]$			
Tb1-O1	2.274(3)	Dy1-O1	2.263(3)
Tb1-O2	2.419(3)	Dy1-O2	2.420(3)
Tb1-O3	2.404(3)	Dy1-O3	2.406(3)
Tb1-O4	2.271(3)	Dy1-O4	2.265(3)
Tb1-O5	2.349(3)	Dy1-O5	2.336(3)
Tb1-O7	2.369(3)	Dy1-O7	2.358(3)
Tb1-N1	2.537(4)	Dy1-N1	2.540(4)
Tb1-N4	2.536(4)	Dy1-N4	2.526(4)

Table 4.4 Angle values of **14**

O1-Tb1-O2	129.37(9)	O5-Tb1-O3	77.30(9)
O1-Tb1-O5	148.9(1)	O5-Tb1-O4	85.8(1)
O1-Tb1-N1	70.4(1)	O5-Tb1-O7	83.04(9)
O1-Tb1-O3	71.98(9)	O5-Tb1-N4	92.8(1)
O1-Tb1-O4	117.7(1)	N1-Tb1-O3	141.5(1)
O1-Tb1-O7	84.1(1)	N1-Tb1-O4	76.3(1)
O1-Tb1-N4	78.1(1)	N1-Tb1-O7	94.1(1)
O2-Tb1-O5	75.28(9)	N1-Tb1-N4	114.8(1)
O2-Tb1-N1	63.8(1)	O3-Tb1-O4	130.08(9)
O2-Tb1-O3	143.37(9)	O3-Tb1-O7	74.08(9)
O2-Tb1-O4	71.39(9)	O3-Tb1-N4	64.1(1)
O2-Tb1-O7	78.88(9)	O4-Tb1-O7	150.0(1)
O2-Tb1-N4	140.6(1)	O4-Tb1-N4	70.4(1)
O5-Tb1-N1	138.7(1)	O7-Tb1-N4	137.8(1)

Table 4.5 Angle values of **15**

O1-Dy1-O2	129.5(1)	O5-Dy1-O3	77.1(1)
O1-Dy1-O5	148.7(1)	O5-Dy1-O4	86.3(1)
O1-Dy1-N1	70.5(1)	O5-Dy1-O7	82.5(1)
O1-Dy1-O3	71.9(1)	O5-Dy1-N4	92.7(1)
O1-Dy1-O4	117.4(1)	N1-Dy1-O3	141.5(1)
O1-Dy1-O7	84.7(1)	N1-Dy1-O4	76.0(1)
O1-Dy1-N4	78.0(1)	N1-Dy1-O7	94.3(1)
O2-Dy1-O5	75.4(1)	N1-Dy1-N4	114.9(1)
O2-Dy1-N1	63.8(1)	O3-Dy1-O4	130.4(1)
O2-Dy1-O3	143.3(1)	O3-Dy1-O7	74.0(1)
O2-Dy1-O4	71.3(1)	O3-Dy1-N4	64.2(1)
O2-Dy1-O7	78.7(1)	O4-Dy1-O7	149.7(1)
O2-Dy1-N4	140.5(1)	O4-Dy1-N4	70.5(1)
O5-Dy1-N1	138.9(1)	O7-Dy1-N4	137.9(1)

4.3.2 Synthesis and crystal structure of $[\text{Ln}_4\text{L}_8\text{Cl}_4(\text{H}_2\text{O})_5] \cdot n\text{Py}$ (Ln: Tb (**16**); Dy (**17**)).

The use of ligand H_2L_8 with a 1:1 stoichiometry of lanthanide to ligand, using two equivalents of base to deprotonate the ligand (NaH with an excess of 20%), in pyridine, gives compound $[\text{Ln}_4\text{L}_8\text{Cl}_4(\text{H}_2\text{O})_5] \cdot n\text{Py}$ (Ln: Tb(**16**); Dy(**17**)) after liquid-liquid diffusion in hexanes (Figure 4.5).

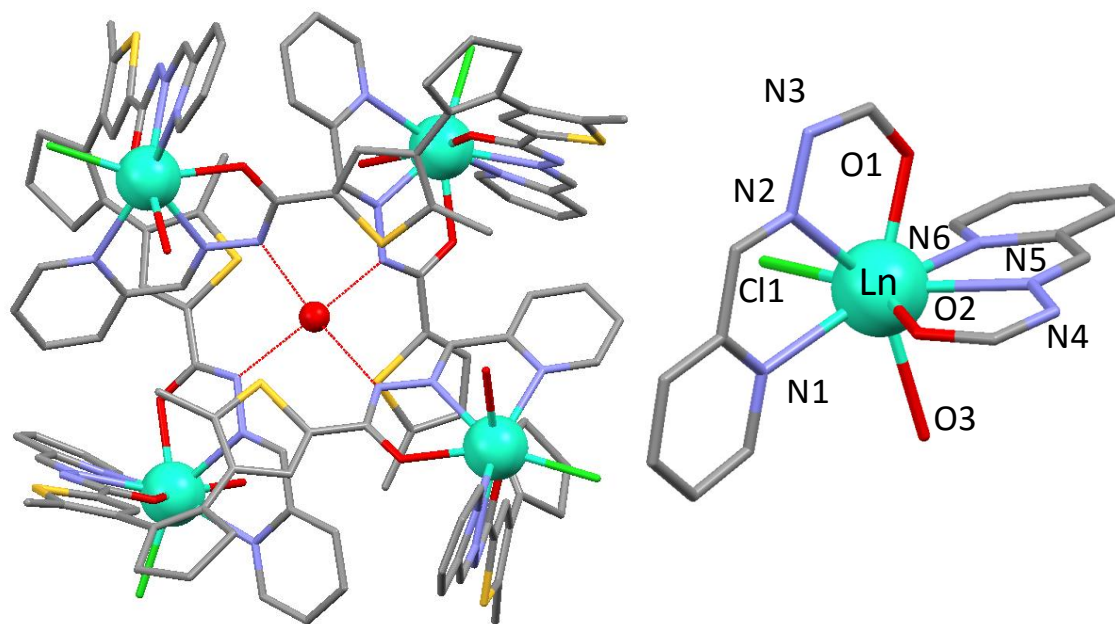


Figure 4.5: Crystal structure of $[\text{Ln}_4\text{L}_{84}\text{Cl}_4(\text{H}_2\text{O})_5]\cdot n\text{Py}$. The Ln core at the right.

$[\text{Ln}_4\text{L}_{84}\text{Cl}_4(\text{H}_2\text{O})_5]\cdot n\text{Py}$ crystallizes in the tetragonal space group I 41/a. The asymmetric unit of this compound is formed by one ligand, one lanthanide, one and $\frac{1}{4}$ of a water molecule, a chloride ion and two pyridine lattice molecules for **16** or one lattice pyridine for **17**. The lanthanide ions are surrounded by two coordination pockets from two hydrazone ligands (Figure 4.5, right), occupying six coordination sites, while the other two are filled by one chloride ion and one molecule of water. Once the symmetry operation is applied, the compound appears with four lanthanide atoms linked by four ligands L_{84}^{2-} . The configuration of the cluster shows the metals located at the vertices of a tetrahedron. The average distance between the lanthanide ions is 9.645 Å. The ligands are in the parallel configuration of the thiophenyl rings, which impede the photocyclization of the reactive carbons, the average distance between those carbons being 4.263 Å. This configuration causes each ligand arm to be oriented in two different ways, outside and inwards, respectively. The latter disposition of the ligands arms creates a cavity where a water molecule is placed, establishing hydrogen bonds with the nitrogen atoms (N4) of the hydrazone moiety not involved in the lanthanide coordination. The distance between this nitrogen and the oxygen of the water molecule is 2.9 Å.

The crystallographic data of both compounds is presented in Table 4.6.

	16	17
formula	$\text{C}_{39}\text{H}_{34}\text{ClN}_8\text{O}_{3.25}\text{S}_2\text{Tb}$	$\text{C}_{34}\text{H}_{29}\text{ClDyN}_7\text{O}_{3.25}\text{S}_2$
M_r	925.19	848.7
Crystal system	tetragonal	tetragonal
space group	I41/a	I41/a
$a = b$ [Å]	37.168(9)	36.841(13)
c [Å]	14.888(9)	14.839(10)
$\alpha = \beta = \gamma$ [°]	90	90
V [Å ³]	20567(12)	20140(2)
Z	16	16
ρ [g cm ⁻³]	1.093	1.120
shape; colour	Yellow needle	Yellow block
μ [mm ⁻¹]	1.540	1.652
reflns	6251	7214
parameters	437	425
restrains	90	101
R_{int}	0.0909	0.0684
R_1	0.0747	0.0800
wR_2	0.2171	0.2158
S	1.045	1.059

These compounds crystallize with one/two molecules of pyridine in the lattice. The packing (Figure 4.6) along the c axis, shows a beautiful distribution of the clusters creating holes as chanel, where surprisingly, no solvents can be seen, even platon calculations give 7841 Å³ of potential accessible voids for solvents. The whole structure is maintained through short electrostatic interactions, being the pyridine lattice molecule very important for this assembly. The pyridine group of the hydrazide creates short interactions with the cyclopentene too, and with the methyl group of the thiophene ring. In addition, short interactions are formed with the sulfur atom of the thiopenes with their neighbors, with distances of 3.45 Å. The concerned thiopenes are these disposed in the outside arms of the ligand. Selected bond distances and angles are shown in Tables 4.7, 4.8 and 4.9.

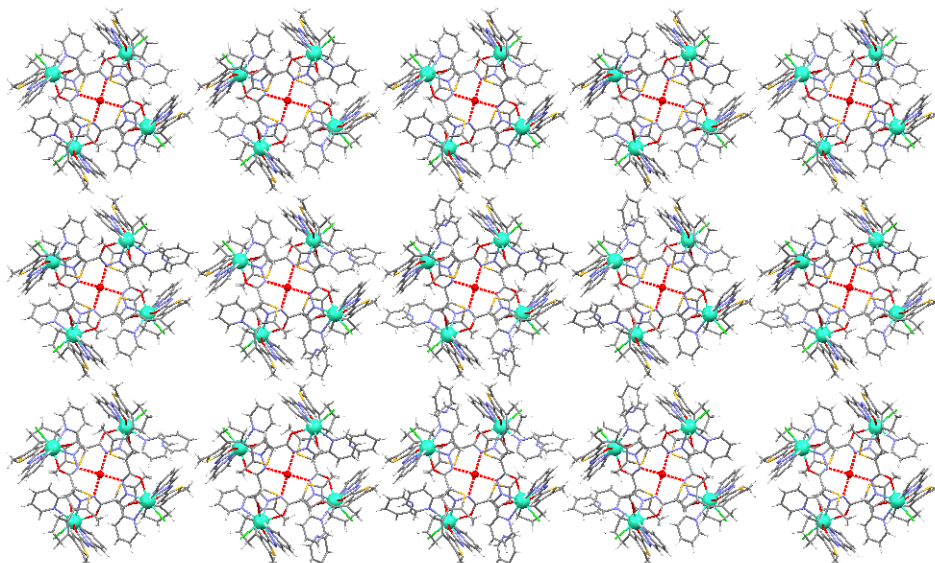


Figure 4.6: Crystal packing of $[\text{Ln}_4\text{L}_{84}\text{Cl}_4(\text{H}_2\text{O})_5]\cdot n\text{Py}$

Table 4.7 Bond distances of $[\text{Ln}_4\text{L}_{84}\text{Cl}_4(\text{H}_2\text{O})_5]\cdot n\text{Py}$

Tb1-Cl1	2.670(4)	Dy1-Cl1	2.630(5)
Tb1-O1	2.294(6)	Dy1-O1	2.257(7)
Tb1-O4	2.636(6)	Dy1-O4	2.618(7)
Tb1-N1	2.61(1)	Dy1-N1	2.59(1)
Tb1-N2	2.526(7)	Dy1-N2	2.479(9)
Tb1-O2	2.337(7)	Dy1-O2	2.333(7)
Tb1-N5	2.503(8)	Dy1-N5	2.539(8)
Tb1-N6	2.631(8)	Dy1-N6	2.608(9)

Table 4.8 Angle values for **16**

Cl1-Tb1-O1	94.1(2)	O4-Tb1-N2	141.9(2)
Cl1-Tb1-O4	99.8(2)	O4-Tb1-O2	83.1(2)
Cl1-Tb1-N1	81.9(2)	O4-Tb1-N5	79.1(2)
Cl1-Tb1-N2	87.2(2)	O4-Tb1-N6	83.0(2)
Cl1-Tb1-O2	150.4(2)	N1-Tb1-N2	63.1(3)
Cl1-Tb1-N5	146.5(2)	N1-Tb1-O2	69.4(3)
Cl1-Tb1-N6	83.9(2)	N1-Tb1-N5	130.0(3)
O1-Tb1-O4	150.6(2)	N1-Tb1-N6	156.1(3)
O1-Tb1-N1	127.2(3)	N2-Tb1-O2	73.7(2)
O1-Tb1-N2	64.1(2)	N2-Tb1-N5	114.5(2)
O1-Tb1-O2	97.4(2)	N2-Tb1-N6	135.1(2)
O1-Tb1-N5	75.1(2)	O2-Tb1-N5	63.1(3)
O1-Tb1-N6	72.8(2)	O2-Tb1-N6	125.6(2)
O4-Tb1-N1	80.7(3)	N5-Tb1-N6	62.6(3)

Table 4.9 Angle values for **17**

Cl1-Dy1-O1	93.9(2)	O4-Dy1-N2	142.3(3)
Cl1-Dy1-O4	98.6(2)	O4-Dy1-O2	84.3(3)
Cl1-Dy1-N1	80.7(3)	O4-Dy1-N5	79.7(3)
Cl1-Dy1-N2	86.8(2)	O4-Dy1-N6	83.0(3)
Cl1-Dy1-O2	149.2(2)	N1-Dy1-N2	63.0(3)
Cl1-Dy1-N5	147.4(2)	N1-Dy1-O2	69.4(3)
Cl1-Dy1-N6	84.1(2)	N1-Dy1-N5	130.3(3)
O1-Dy1-O4	150.7(3)	N1-Dy1-N6	155.9(3)
O1-Dy1-N1	127.4(3)	N2-Dy1-O2	73.4(3)
O1-Dy1-N2	64.5(3)	N2-Dy1-N5	114.6(3)
O1-Dy1-O2	98.2(3)	N2-Dy1-N6	134.7(3)
O1-Dy1-N5	75.6(3)	O2-Dy1-N5	63.4(3)
O1-Dy1-N6	72.0(3)	O2-Dy1-N6	126.6(3)
O4-Dy1-N1	81.0(3)	N5-Dy1-N6	63.3(3)

4.3.3 Synthesis and crystal structure of $[\text{Ln}_4\text{L7}_2\text{Na}_4(\text{H}_2\text{O})_2(\text{CO}_3)_2(\text{Py})_6(\text{acac})_4]\cdot 9\text{Py}$ (Ln: Tb (18); Dy (19)).

Since the stoichiometry of the previous reactions always leads to crystal structures with the photochromic unit in the unsuitable configuration to perform photocyclization, another strategy was used. In order to favor the open form of the photochromic unit, another chelating ligand was used as a means to block the lanthanide coordination positions thereby forcing the lanthanides to bind only one hydrazone pocket. Similar to Chapter 2, different blocking agents were used. Here, the use of nitrogen chelating ligands, such as bipyridine or phenanthroline in different ratios, was unsuccessful. However, the use of oxygen chelating agents, in particular the reaction with acetylacetonate, affords crystals. Unfortunately, refining of the structure reveals again the undesired configuration of the photochromic unit.

Thus, the reaction in pyridine of ligand **H₄L7** with lanthanide salts (Tb, Dy), in the ratio ½ respectively, in the presence of enough base to deprotonate the whole ligand (NaH with an excess of 20%), and with previously deprotonated acetylacetonate (acac), gives yellow crystals of $[\text{Ln}_4\text{L7}_2\text{Na}_4(\text{H}_2\text{O})_2(\text{CO}_3)_2(\text{Py})_6(\text{acac})_4]\cdot 9\text{Py}$ (Ln: Tb (18); Dy (19)) after slow liquid-liquid diffusion in hexane. The crystal structure is represented in Figure 4.7, as well as the immediate crystal environment of the metal centres.

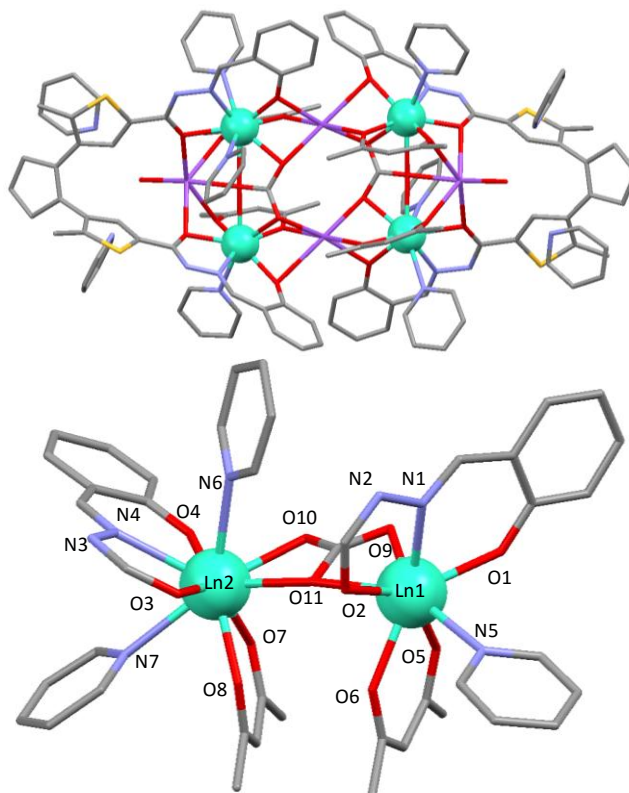


Figure 4.7: Crystal structure of $[\text{Ln}_4\text{L}_7\text{Na}_4(\text{H}_2\text{O})_2(\text{CO}_3)_2(\text{Py})_6(\text{acac})_4] \cdot 9\text{Py}$. The Ln core at the bottom.

The asymmetric unit of these new compounds is formed by one L_7^{4-} ligand, two lanthanide ions, two acylacetonate (acac) ligands, two sodium ions, one molecule of water, one carbonate anion and seven and a half molecules of pyridine.

The final compound is a tetramer of lanthanides, which can be treated as two dimers linked by two sodium centers through the phenolate and the carbonate molecule. Within the dimers, each lanthanide exhibits different coordination numbers. Ln1 has coordination number eight, formed by one hydrazide pocket, an acylacetonate molecule, to atoms of oxygen from the carbonate group (one of them shared with both lanthanides), and one pyridine molecule. In the case of Ln2, its coordination number is nine, with the same surrounding as Ln1 with an additional molecule of pyridine. Thus, Ln1 is N_2O_6 and Ln2 is N_3O_6 coordinated. Similar to the previous compounds, the basic conditions play a role in the cluster formation because is the source of the carbonates and the sodium ions link the ketone groups of the same ligand, forcing the parallel configuration of the photochromic unit. The distance between the reactive carbons is around 4.81\AA . The use of other bases did not give any measurable crystals.

The crystallographic data of both compounds is shown in Table 4.10.

Table 4.10 Crystallographic data of [Ln₄L₇Na₄(H₂O)₂(CO₃)₂(Py)₆(acac)₄]·9Py		
	18	19
formula	C ₇₈ H ₇₆ N _{11.5} Na ₂ O ₁₂ S ₂ Tb ₂	C ₇₈ H ₇₆ Dy ₂ N _{11.5} Na ₂ O ₁₂ S ₂
<i>M_r</i>	1794.44	1801.6
Crystal system	triclinic	triclinic
space group	P-1	P-1
<i>a</i> [Å]	14.4546(11)	14.4844(3)
<i>b</i> [Å]	16.3594(13)	16.4008(4)
<i>c</i> [Å]	18.6169(15)	18.5993(5)
<i>α</i> [°]	72.076(5)	72.1455(13)
<i>β</i> [°]	86.903(5)	86.8981(14)
<i>γ</i> [°]	72.452(5)	72.0414(12)
<i>V</i> [Å ³]	39990.1(6)	3996.69(17)
<i>Z</i>	2	2
<i>ρ</i> [g cm ⁻³]	1.494	1.497
shape; colour	Yellow rhombus	Yellow block
<i>μ</i> [mm ⁻¹]	1.887	1.984
reflns	15227	16977
parameters	965	933
restrains	696	1554
<i>R</i> _{int}	0.0827	0.0538
<i>R</i> ₁	0.0579	0.0436
<i>wR</i> ₂	0.1503	0.1225
<i>S</i>	1.065	1.091

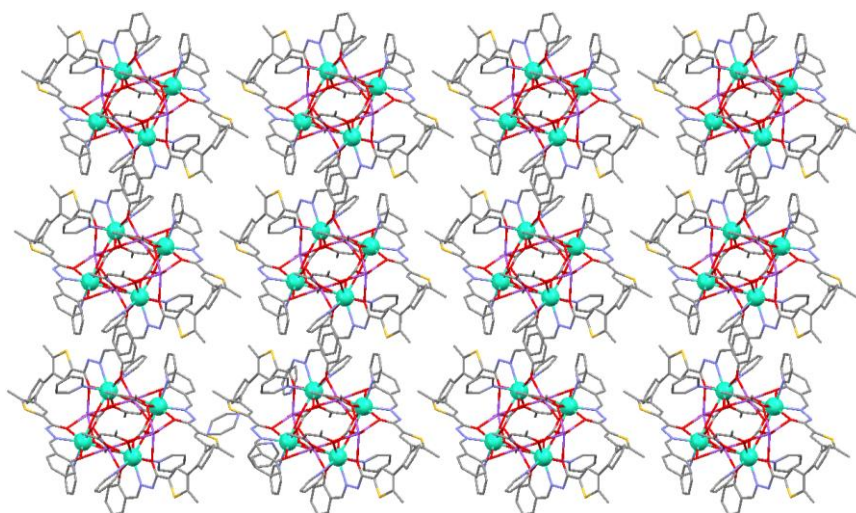


Figure 4.8: Crystal packing of Ln₄L₇₂ along b axis

The packing of these compounds features tetramers maintained through electrostatic interactions. The empty space is occupied by nine molecules in total in each unit cell, four of them forming hydrogen bonds with the water molecules coordinated to some of the sodium ions.

Table 11. Bond distances of
[Ln₄L₇Na₄(H₂O)₂(CO₃)₂(Py)₆(acac)₄]·9Py

18		19	
Tb1-O1	2.260(6)	Dy1-O1	2.250(4)
Tb1-O2	2.331(4)	Dy1-O2	2.326(3)
Tb1-O5	2.360(5)	Dy1-O5	2.338(5)
Tb1-O6	2.348(6)	Dy1-O6	2.348(3)
Tb1-O9	2.373(6)	Dy1-O9	2.353(4)
Tb1-O11	2.452(4)	Dy1-O11	2.441(3)
Tb1-N1	2.476(8)	Dy1-N1	2.472(6)
Tb1-N5	2.591(8)	Dy1-N5	2.574(5)
Tb2-O3	2.383(4)	Dy2-O3	2.358(4)
Tb2-O4	2.279(5)	Dy2-O4	2.271(5)
Tb2-O7	2.406(5)	Dy2-O7	2.378(5)
Tb2-O8	2.383(6)	Dy2-O8	2.398(3)
Tb2-O10	2.405(5)	Dy2-O10	2.396(3)
Tb2-O11	2.481(5)	Dy2-O11	2.471(3)
Tb2-N4	2.531(7)	Dy2-N4	2.509(4)
Tb2-N6	2.677(9)	Dy2-N6	2.677(6)
Tb2-N7	2.613(7)	Dy2-N7	2.583(5)

4.4 Introduction to magnetic properties of lanthanides^{30,31}

Compounds exhibiting magnetic anisotropy are characterized by a magnetic response which depends on the direction of the applied field, because the magnetic moment has a preferred orientation. The existence of spin-orbit coupling is crucial in such systems, because electrostatic interactions and exchange anisotropy cannot generate by themselves. The spin-orbit coupling interaction describes the coupling between an electron spin angular momentum and the magnetic moment generated by the movement of other electrons. The orbital angular momentum is higher in molecules containing heavy open shell atoms (like lanthanides), since they have more extended orbitals. The energie of the spin orbit coupling is expressed as:

$$H = \lambda L \cdot S$$

where L and S are the orbital angular momentum and spin operators respectively and λ is the spin-orbit parameter coupling. The λ sign depends on the number of electrons in the f orbitals, being positive when the number of electrons is less than seven, zero in the case of semi-filled layers and negative for a greater number of electrons. The sign of λ determines whether the states with L and S aligned in parallel ($\lambda > 0$) are stabilized or destabilized ($\lambda < 0$).

The effect of spin-orbit coupling in lanthanides is much more intense than in transition metals due to greater angular momentum of f orbitals with respect to that of the d orbitals and, to the absence of mixing of the magnetic orbitals with ligand orbitals, which tends to decrease the angular momentum. Thus the magnetic behavior of lanthanides is determined primarily by the repulsion between $4f$ electrons and by the spin-orbit coupling. At high temperatures, the magnetic susceptibility may be approximated by the behavior of the free ion from the following expression:

$$\chi = \frac{Ng_j^2\beta^2}{3kT}J(J + 1); \quad g_j = \frac{3}{2} + \frac{S(S+1)-L(L+1)}{2J(J+1)}$$

where g_j is a tabulated factor for each ion (the other parameters are presented in Chapter 1). The magnetic susceptibility at low temperatures deviates from this behavior if there are magnetic interactions between different ions and due to the splitting produced by the ligand field, which results in high anisotropic states split in energy.

4.4.1 Magnetic properties of [Tb₂L₇(CO₃)₂Na₆Py₁₀] (**14**)

The temperature dependence of the magnetic susceptibility of **14** was measured in a direct current (dc) magnetic field of 3000 Oe in the temperature range of 1.9–300 K. The temperature dependence of $\chi_M T$ is shown in Figure 4.9. The value of $\chi_M T$ at high temperatures for compound **14**, gives 22.56 cm³mol⁻¹K which is in reasonable agreement with the expected value of 23.6 cm³mol⁻¹K for two isolated Tb(III) ions (⁷F₆, L = 3, S = 3, g = 3/2).

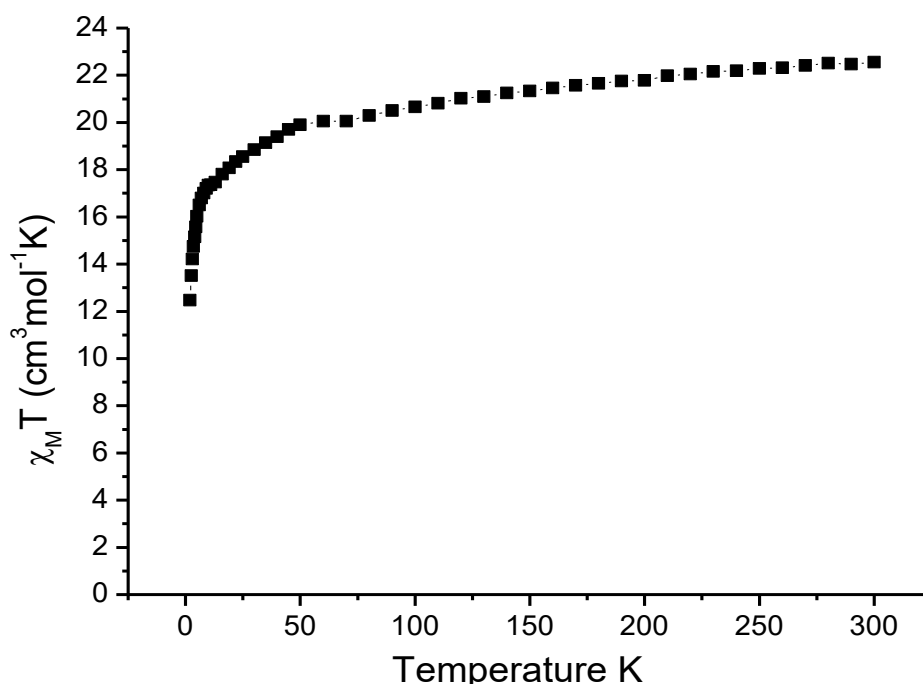


Figure 4.9: Plot of $\chi_M T$ vs T per mol of complex **14** at constant field.

14 shows a decrease of $\chi_M T$ on lowering the temperature, and at 50 K a slope change is observed with a more pronounced decrease. Below 10 K, the $\chi_M T$ product of the curve decreases abruptly to reach 12.45 cm³mol⁻¹K at 2 K. The ground state of a Tb(III) ion (4f⁸) is ⁷F₆ characterized by g_J = 3/2. The first excited state (⁷F₅) is separated by 2000 cm⁻¹ from the ground state. When the temperature decreases, the $\chi_M T$ curve decreases because of the progressive thermally depopulation of the crystal field levels of the J = 6 multiplet of the Tb(III) even in the absence of any exchange interaction, thus from 300 K to 50 K, the decrease of the $\chi_M T$ product is therefore principally attributed to the depopulation of the MJ states of the two Tb(III) ions. Below 10 K, the $\chi_M T$ evolution can be due also to intermolecular antiferromagnetic exchange interactions between both Tb(III) ions.

4.4.2 Magnetic properties of $[\text{Ln}_4\text{L}_8\text{Cl}_4(\text{H}_2\text{O})_5]\cdot n\text{Py}$ (**16** and **17**)

The temperature dependence of the magnetic susceptibility of **16** and **17** was measured in a direct current (dc) magnetic field of 3000 Oe for the **16** and in a field of 1000 Oe for **17**, both in the temperature range of 1.9–300 K.

The temperature dependence of $\chi_M T$ is shown in Figure 4.10. For each compound, the values found at 300 K, 55.04 and 44.61 $\text{cm}^3\text{mol}^{-1}\text{K}$ respectively for **17** and **16**, are close to that anticipated for four Ln(III) ions in the absence of exchange interactions (56.7 (Dy_4 , ${}^6\text{H}_{15/2}$, $L = 5$, $S = 5/2$, $g = 4/3$) and 47.2 (Tb_4 , ${}^7\text{F}_6$, $L = 3$, $S = 3$, $g = 3/2$)) and decreases as temperature is lowered with a more rapid fall below 50 K till values of 46.56 and 27.10 $\text{cm}^3\text{mol}^{-1}\text{K}$ for **17** and **16**, respectively. For these compounds, this behavior is originated from the crystal field effects, depopulation of the M_J sublevels and possible exchange interaction between the lanthanide ions.

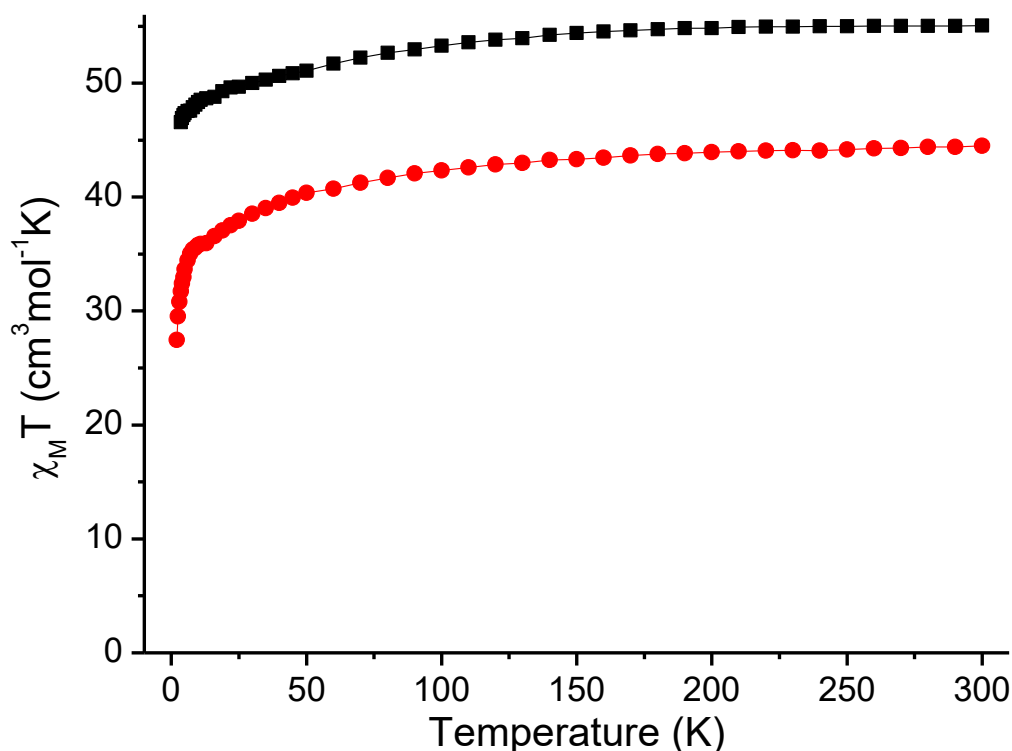


Figure 4.10: Plot of $\chi_M T$ vs T per mol of complex **16** (red line) and **17** (black line) at constant field.

4.4.3 Magnetic properties of $[\text{Ln}_4\text{L}_7\text{Na}_4(\text{H}_2\text{O})_2(\text{CO}_3)_2(\text{Py})_6(\text{acac})_4]\cdot 9\text{Py}$ (**18** and **19**)

The temperature dependence of the magnetic susceptibility of **18** and **19** was measured under a direct current (dc) magnetic field of 3000 Oe both in the temperature range of 1.9–300 K. The temperature dependence of $\chi_{\text{M}}T$ is shown in Figure 4.11.

The $\chi_{\text{M}}T$ values of 57.3 and 44.97 $\text{cm}^3\text{mol}^{-1}\text{K}$ at 300 K are slightly higher for the Dy compound while lower for the Tb compound than the intervals expected for the four corresponding, non-interacting Ln(III) centers. For both **18** and **19** the $\chi_{\text{M}}T$ product begins a very slow decrease at higher temperature, with the rate of decrease becoming steadily larger below 50 K. Similarly to the previous compounds, the sublevels of the anisotropic Ln(III) (Tb and Dy) ions are thermally depopulated when the temperature is lowered resulting in a decrease of the $\chi_{\text{M}}T$ product. Here, the $\chi_{\text{M}}T$ product at low temperatures is 33.64 and 20.11 $\text{cm}^3\text{mol}^{-1}\text{K}$ for **19** and **18**, respectively, lower than the tetramers containing ligand **H₂L8**. This behavior suggests a stronger interaction within the lanthanide dimers which indeed are closer to each other than within the compounds.

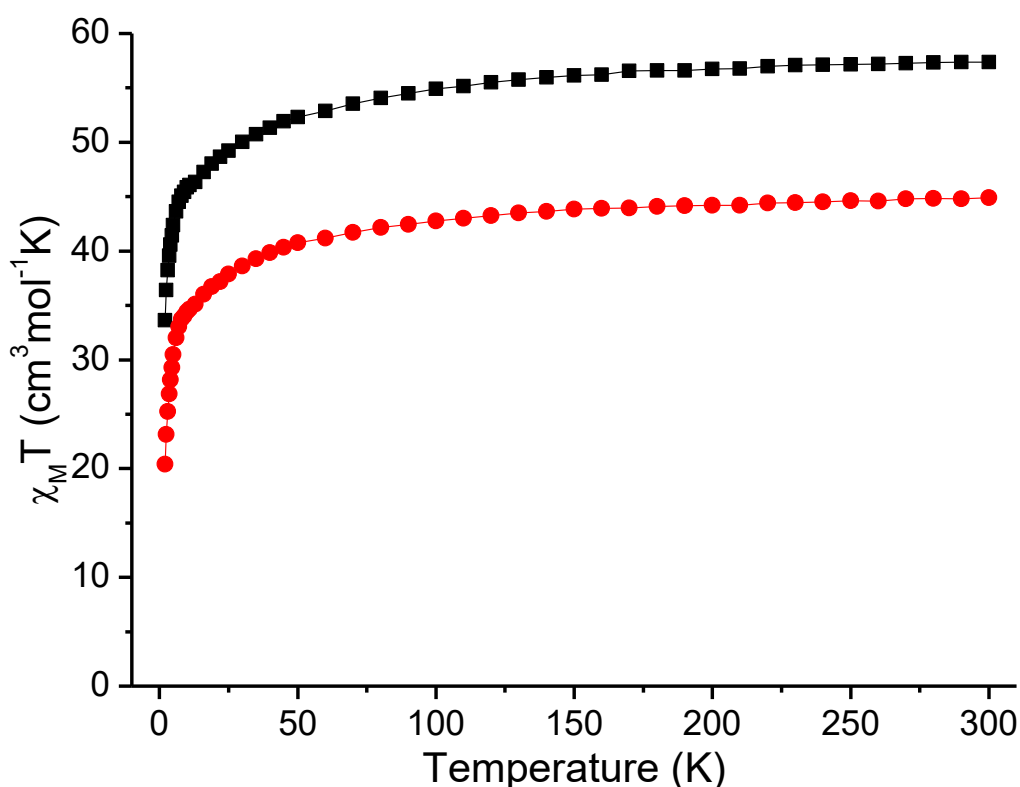


Figure 4.11: Plot of $\chi_{\text{M}}T$ vs T per mol of complex **19** (red line) and **20** (black line) at constant field

4.4.4 Single molecule magnet behavior

The dynamic magnetic properties of all compounds were investigated in order to prove the presence of single molecule magnet behavior. No obvious out-of-phase signal was observed when the ac susceptibility (χ'') was measured under zero dc magnetic field, except for the case of $[\text{Dy}_4\text{L}_8\text{Cl}_4(\text{H}_2\text{O})_5]\cdot\text{1Py}$ (**17**). The lack of slow relaxation in the other compounds is probably due to the presence of fast relaxation processes via quantum tunneling, frequently observed in lanthanide SMMs.

Frequency dependence of the χ'' signals were clearly observed at zero field measured at different temperatures for compound **17**. However, no maxima were observed down to 1.9K, even at 10 kHz (Figure 4.12, left).

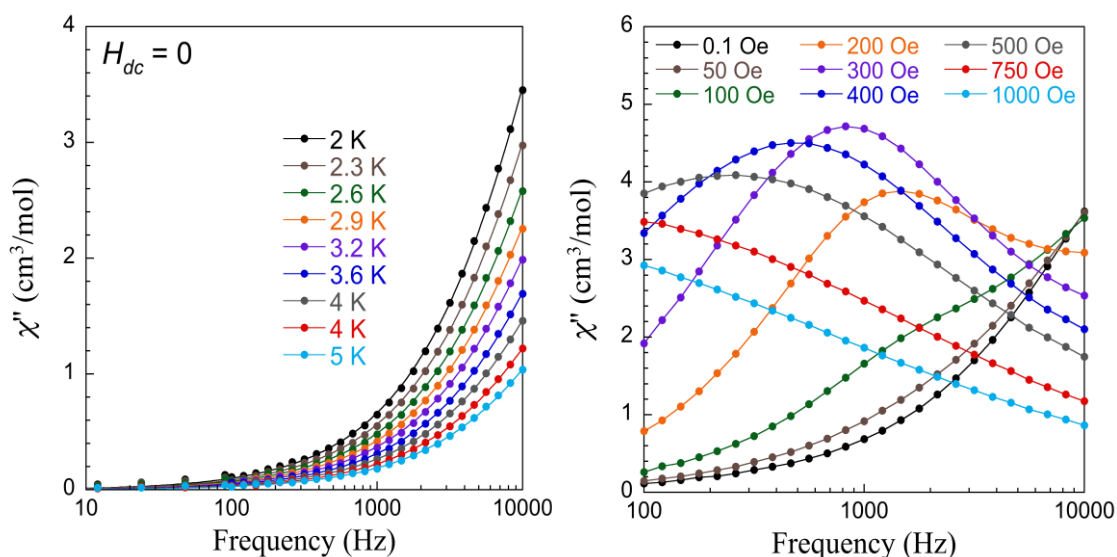


Figure 4.12: Left: Frequency dependence of χ'' for **17** measured from 2 K to 5 K. Right: Different applied dc fields at 2K.

Application of an external dc magnetic field results in a significant enhancement of χ'' around 250 Oe. This is the result of the cancellation of fast tunnelling at zero-field. The optimum applied dc field, where the maximum of the characteristic frequency was observed, was determined to be around 500 Oe (Figure 4.12, right). Measurements at two applied fields were done, 400 Oe and 750 Oe (Figure 4.13), in the temperature range of 1.9K to 10K and 2K to 20K, respectively for each applied field. Figure 4.13 shows how peaks shift to lower frequency as the temperature decreases, which is indicative of slow magnetization relaxation typical of SMM behavior.

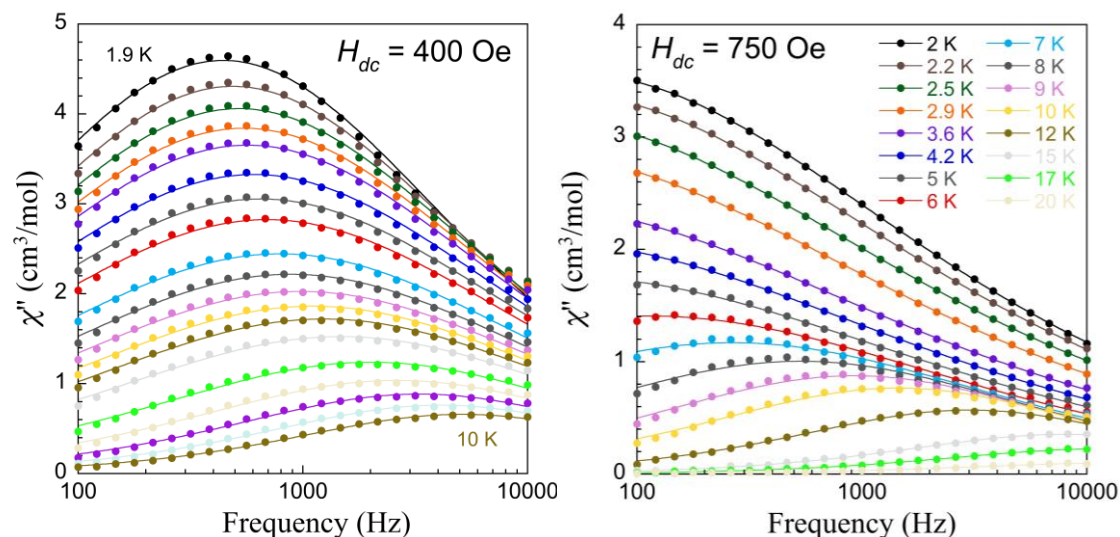


Figure 4.13: Out-of-phase χ'' magnetic susceptibility for **17** under two applied dc field of $H_{dc} = 400$ Oe and $H_{dc} = 750$ Oe.

Lines were fit to the Cole-Cole expression for the imaginary susceptibility allowing the extraction of the critical relaxation time τ and part of the data could be fitted to the Arrhenius law (Figure 4.14). Clearly, under zero field, the relaxation process is temperature independent and thus owing to a relatively fast tunneling. Under an applied field, the relaxation process through tunneling is significantly slowed down and a thermally-activated process becomes detectable. The fit of the 750 Oe set data at the four higher temperatures gives an activation barrier of 55K and a pre-exponential factor of 3.2×10^{-6} s. This relaxation behavior is ascribed to each Dy(III) ion, as no sign of significant exchange is observed at low temperatures.

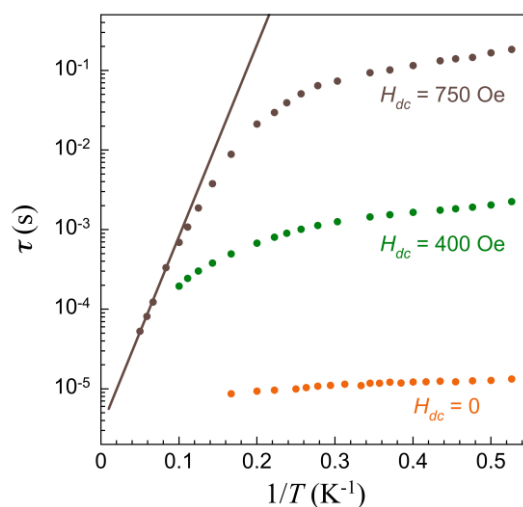


Figure 4.14: The three sets of τ plotted using the Arrhenius law.

4.5 Coordination compounds with copper

4.5.1 Synthesis and crystal structure of $[\text{Cu}_2\text{L7}(\text{Py})_2](\text{MeOH})$ (**20**)

The aim of preparing photoswitchable magnetic coordination compounds with H₄L7 was also attempted with Cu(II) compounds. The deprotonation of ligand H₄L7 using TBAOH in methanol followed by addition of copper bromide leads to a green precipitate. Subsequently addition of pyridine till complete dissolution of the precipitate leads to dark brown crystals of $[\text{Cu}_2\text{L7}(\text{Py})_2](\text{MeOH})$ (**20**) after several days by slow evaporation. The crystal structure of **20** is shown in Figure 4.15.

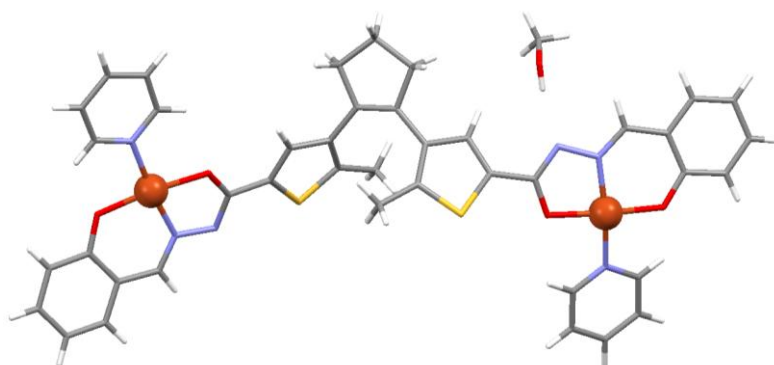


Figure 4.15: Crystal structure of **20**

20 crystallizes in the triclinic space group P-1. The asymmetric unit is composed by the deprotonated ligand L7^{4-} coordinating two copper atoms. These complete their coordination sphere with one pyridine molecule each. A methanol molecule is present as a lattice solvent, which is forming a hydrogen bond with the non coordinated nitrogen of the hydrazide moiety. Crystallographic data and selected bonds and angles are shown in Tables 4.12 and 4.13. Even though the coordination sphere of the copper seem to be square planar, the packing of the crystal reveals the presence of extended chains of this compound, formed through the axial position of one Cu ion, which interacts with the O4 of the phenolate group of a neighboring complex. The other Cu ion seems to remain in the square planar conformation due to the distortion of the possible axial bond with the O1 of its neighboring phenolate group from another complex. Almost all the angles of Cu1 through O4 are close to 90° whereas for Cu2, the angles with O1 are quite different, being 79.12° and 115.37° for the smallest and biggest angle respectively. This distortion can be seen in the left part of Figure 4.16.

The packing is formed by adjacent chains (Figure 4.16) thanks to a good stacking of the hydrazide groups. The reactive carbons are now in good disposition to undergo photocyclization, with distances between them of 3.423Å.

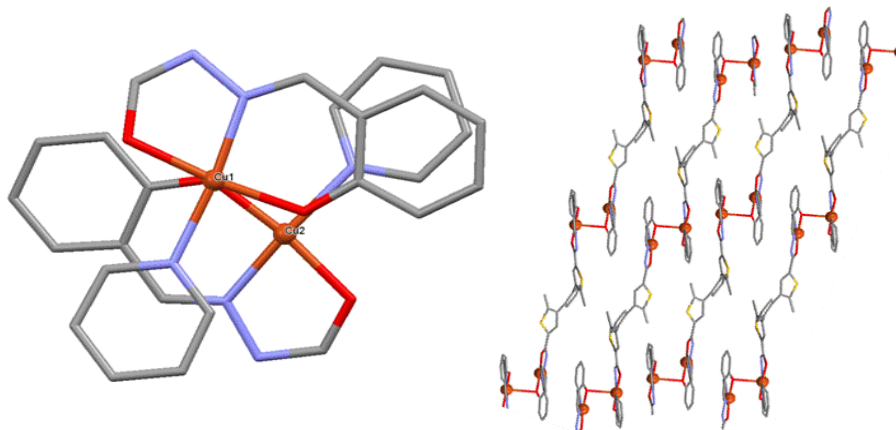


Figure 4.16: Left: Upper view through the Cu-O bond. Right: Packing of chains of compound **20**

Table 4.12 Crystallographic data of **20**

formula	C ₄₂ H ₃₄ Cu ₂ N ₆ O ₅ S ₂
<i>M_r</i>	897.98
Crystal system	Triclinic
space group	P-1
<i>a</i> [Å]	10.555(19)
<i>b</i> [Å]	13.171(3)
<i>c</i> [Å]	15.203(4)
<i>α</i> [°]	112.828(6)
<i>β</i> [°]	100.563(5)
<i>γ</i> [°]	90.268(4)
<i>V</i> [Å ³]	5500.2(4)
<i>Z</i>	2
<i>ρ</i> [g cm ⁻³]	1.563
shape;colour	Brown block
<i>μ</i> [mm ⁻¹]	1.280
reflns	5139
parameters	518
restrains	0
<i>R</i> _{int}	0.0254
<i>R</i> ₁	0.0398
<i>wR</i> ₂	0.0948
<i>S</i>	1.045

Table 4.13 Selected bond and angles of **20**

Cu1-O1	1.915(3)	O1-Cu1-O2	173.3(1)	N5-Cu1-O4	89.1(1)
Cu1-O2	1.951(2)	O1-Cu1-N1	93.2(1)	Cu1-O4-Cu2	94.6(1)
Cu1-N1	1.930(3)	O1-Cu1-N5	93.1(1)	O3-Cu2-O4	170.6(1)
Cu1-N5	2.001(4)	O1-Cu1-O4	88.8(1)	O3-Cu2-N4	81.4(1)
Cu1-O4	2.659(3)	O2-Cu1-N1	80.7(1)	O3-Cu2-N6	94.8(1)
Cu2-O3	1.953(2)	O2-Cu1-N5	93.2(1)	O4-Cu2-N4	92.6(1)
Cu2-O4	1.903(2)	O2-Cu1-O4	93.7(1)	O4-Cu2-N6	92.8(1)
Cu2-N4	1.935(4)	N1-Cu1-N5	173.6(1)	N4-Cu2-N6	165.0(2)
Cu2-N6	2.008(4)	N1-Cu1-O4	89.6(1)		

4.5.2 Synthesis and crystal structure of $[\text{Cu}_2\text{L7}(\text{Phen})_2](\text{H}_2\text{O})_3$ (**21**)

Following the same synthesis as **20**, now the addition of phenantroline and heating to 50°C, leads to a dark solution. After 1 hour of stirring, a green precipitate appears again. This precipitate was dissolved in DMF, and dark crystals of $[\text{Cu}_2\text{L7}(\text{Phen})_2](\text{H}_2\text{O})_3$ (**21**) appeared in two weeks by slow evaporation of the solution. The crystal structure is shown in Figure 4.17. **21** crystallizes in the monoclinic space group P21/n. Crystallographic data and selected bonds and angles are shown in Table 12 and 13.

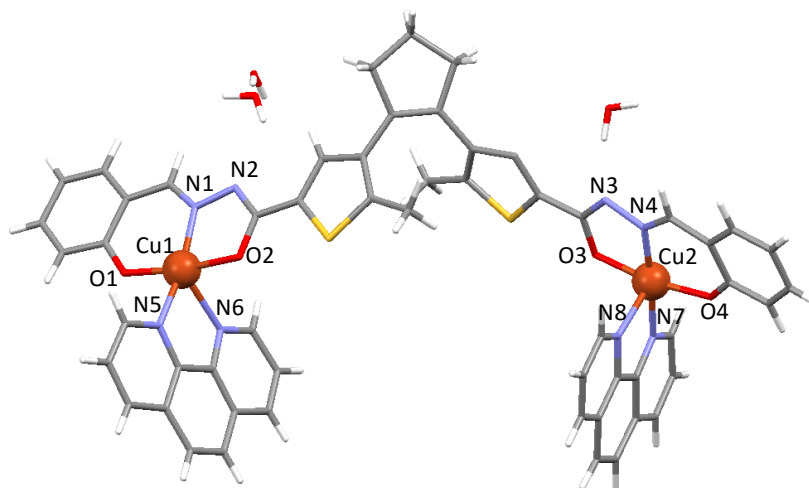


Figure 4.17: Crystal structure of **21**

The asymmetric unit is composed by one deprotonated ligand coordinating two copper ions through the hydrazone pocket and two molecules of phenantroline completing the coordination sphere in a square base pyramidal configuration. Three molecules of water are present as lattice solvents, two of them forming hydrogen bonds with the non coordinated nitrogen of the hydrazone.

The photochromic moiety presents the antiparallel configuration with a distance between reactive carbons of 3.468 Å. The crystal packing is well maintained through the stacking of the phenantrolines as shown in the left part of Figure 4.18. Indeed, this stacking is formed by discrete molecules which form two stacked arrays, creating a nice packing through the *b* axis.

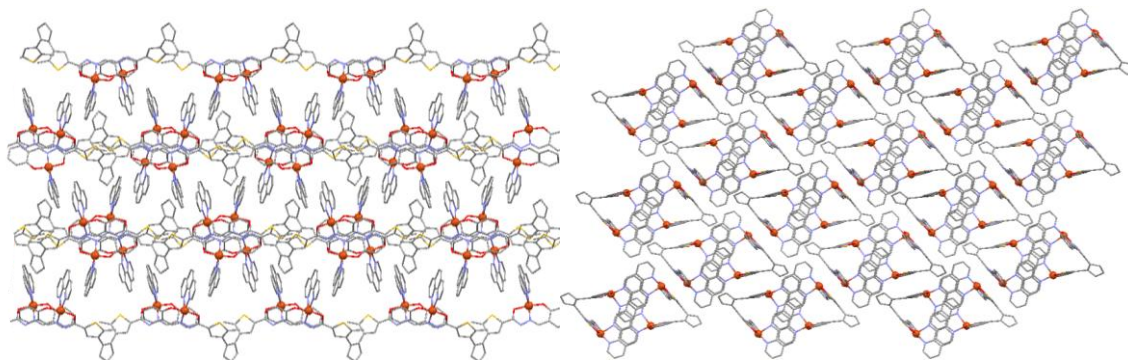


Figure 4.18: Different views of **21** trough the *a* axis (left) showing the stacking of the phenantrolines and trough the *b* axis (right).

Table 4.12 Crystallographic data of 21	
formula	C ₅₅ H ₄₅ Cu ₂ N ₈ O ₇ S ₂
<i>M_r</i>	1121.19
Crystal system	monoclinic
space group	P21/n
<i>a</i> [Å]	14.844(4)
<i>b</i> [Å]	15.911(4)
<i>c</i> [Å]	22.986(6)
$\alpha = \gamma$ [°]	90
β [°]	98.883(5)
<i>V</i> [Å ³]	5364(2)
<i>Z</i>	4
ρ [g cm ⁻³]	1.388
shape; colour	Brown block
μ [mm ⁻¹]	0.930
reflns	5015
parameters	679
restrains	728
<i>R</i> _{int}	0.0663
<i>R</i> ₁	0.0709
<i>wR</i> ₂	0.1754
<i>S</i>	1.030

Table 4.13 Selected bond and angles of **21**

Cu1-O1	1.887(5)	O1-Cu1-O2	172.4(2)	O3-Cu2-O4	169.1(2)
Cu1-O2	1.966(5)	O1-Cu1-N1	93.4(2)	O3-Cu2-N4	81.7(2)
Cu1-N1	1.950(7)	O1-Cu1-N5	85.8(2)	O3-Cu2-N7	93.9(2)
Cu1-N5	2.039(7)	O1-Cu1-N6	100.2(2)	O3-Cu2-N8	99.9(2)
Cu1-N6	2.285(6)	O2-Cu1-N1	81.0(2)	O4-Cu2-N4	94.6(2)
Cu2-O3	1.967(5)	O2-Cu1-N5	98.3(2)	O4-Cu2-N7	90.0(2)
Cu2-O4	1.899(5)	O2-Cu1-N6	87.1(2)	O4-Cu2-N8	90.8(2)
Cu2-N4	1.918(6)	N1-Cu1-N5	165.6(3)	N4-Cu2-N7	175.3(3)
Cu2-N7	2.006(6)	N1-Cu1-N6	116.9(3)	N4-Cu2-N8	100.1(3)
Cu2-N8	2.264(7)	N5-Cu1-O4	77.4(2)	N7-Cu2-N8	79.3(2)

4.6 Magnetic properties of $[\text{Cu}_2\text{L7(Py)}_2](\text{MeOH})$ and $[\text{Cu}_2\text{L7(Phen)}_2](\text{H}_2\text{O})_3$

Bulk magnetization measurements were done on samples of **20** and **21** between 2 and 300 K in a constant magnetic field of 1 T. The results are represented in Figure 4.20 in the form of $\chi_M T$ vs. T. The value of $\chi_M T$ at 300 K nearly corresponds to that expected for a molecule with two magnetically dilute Cu(II) centers ($0.75 \text{ cm}^3 \text{ mol}^{-1} \text{ K}$; $g=2.0$) with 0.85 and $0.83 \text{ cm}^3 \text{ mol}^{-1} \text{ K}$ for **20** and **21** respectively. This value remains almost constant upon cooling and starts to decrease noticeably below 20 K. This shows that the exchange between the copper ions is dominated by weak antiferromagnetic interactions. The fit of the susceptibility using the phy³² program provides a coupling constant of $J = -0.47 \text{ cm}^{-1}$ and $J = -0.45 \text{ cm}^{-1}$ using in both cases constant values of $g = 2.05$ and a TIP value of $200 \times 10^{-6} \text{ cm}^3 \text{ mol}^{-1}$.

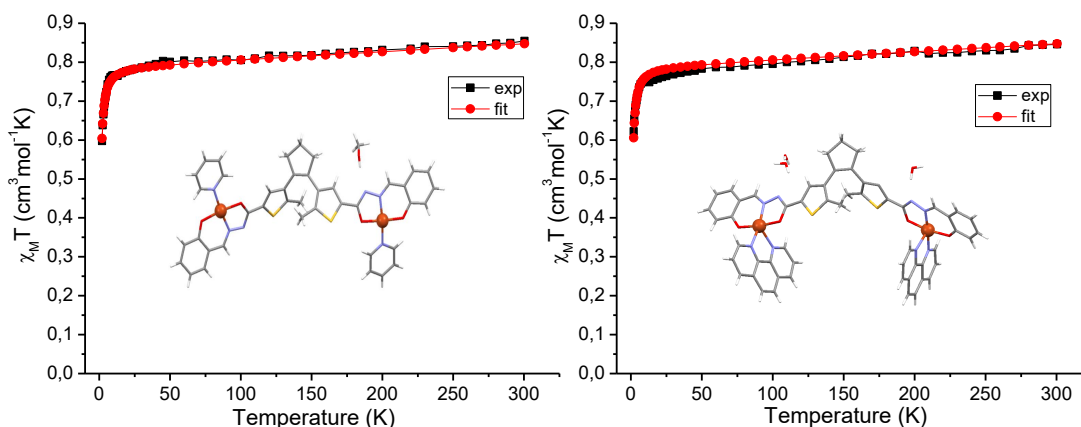


Figure 4.20: Susceptibility of **20** and **21**. The red lines are the fitting using the phy program

4.7 Photochromic behavior

Photochromic reactions were performed in $3.5 \times 10^{-5} \text{M}$ (DMF/methanol) solutions (Figure 4.21). **20** presents a sharp peak at 239 which can be ascribed to DMF. The other peaks appear at 259, 319, 335 and 391 nm, the latter with a shoulder at 407nm. All these bands are due to π - π transitions of the ligand. Irradiation of the sample with UV has a little influence on these bands, thus a broad band but not too intense appears around 569nm. This new band is due to the cyclization of the ligand causing a change of color from light brown to violet.

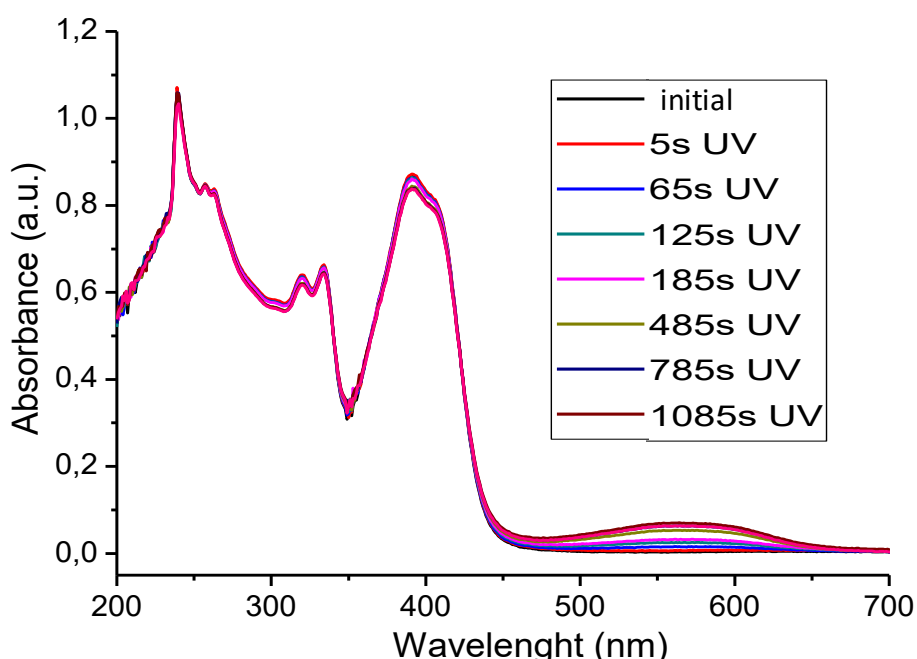


Figure 4.21: Photocyclization of the open **20** ligand with UV light (<425nm).

The process is totally reversible as shown in Figure 4.22. Irradiation of the violet solution with visible light returns the light brown color to the solution. All bands are totally recovered after 300s of visible light irradiation, which implies a faster process than the cyclization, the latter taking around 18 min to reach the completion. The photochromic process could not be followed in solid state, due to the dark color of the crystals, which prevents the observation of a detectable change of color.

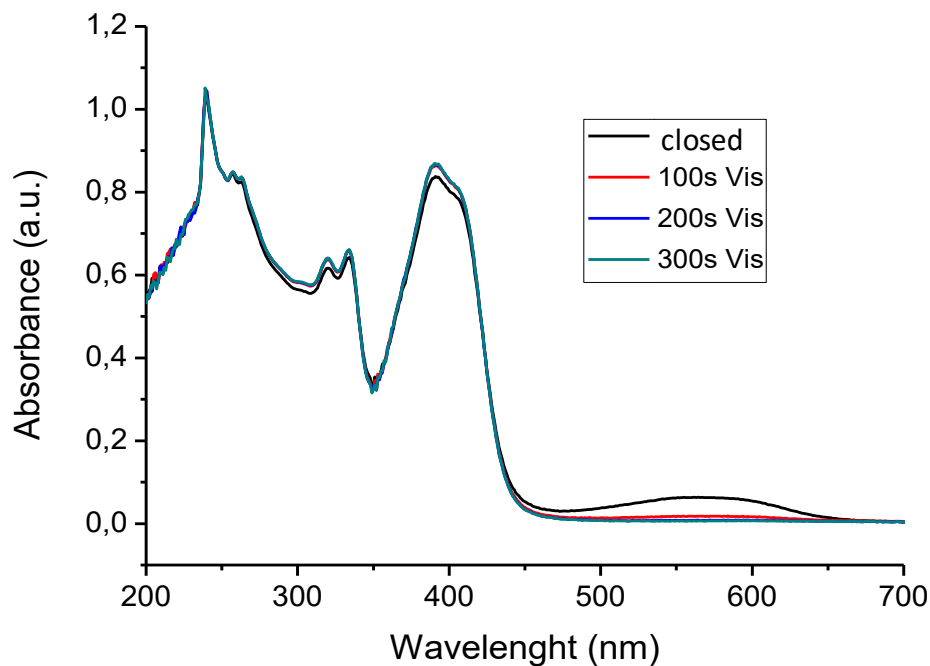


Figure 4.22: Ring opening of the closed form of **20** upon irradiation with visible light (>430nm).

Surprisingly, the photochromic process does not proceed for compound **21**. In a recent publication³³, the ability of metal atoms centers to tune the energy levels and the excited states of the photochromic system, was studied in order to explain the lack of photochromic behavior in some coordination complexes having diaryethenes. If the electronic coupling between the photochromic core and the metal centers is too strong, the energy transfer from the dithienylethene units to the metal moiety prevents the photoisomerization. This could be the explanation for the absence of photochromic activity in **21** and for the weakness of the corresponding response by **20**.

4.8 Conclusions

The breath of new ligands that can be reached starting from species **L6**, opens the possibility of building new coordination compounds with different magnetic applications. Indeed, hydrazones have been used in the synthesis of Single Molecules Magnets, iron and manganese compounds presenting spin crossover behavior or in biological fields, such as compounds able to interact with the DNA in tumor cells.

In this chapter, the synthesis of two new ligands with excellent photochromic behavior is shown. Both ligands are able to coordinate through their chelating pockets large atoms, like lanthanides but also transition metals with smaller atomic radii. However, the attempts to obtain lanthanide compounds with the photochromic unit in its antiparallel configuration, suitable to perform photocyclization have been unsuccessful. The various attempts have included the use of different stoichiometries, blocking agents and the most important factor, other bases. Nevertheless, single molecule magnet behavior can be observed in the tetramer dysprosium compound **[Dy₄L8₄Cl₄(H₂O)₅]·1Py (17)**.

The use of copper instead of lanthanide leads to two different complexes, crystal structure of which reveal the good configuration of the photochromic unit, thus the possibility to study their photocromic behavior in solution. The case of **[Cu₂L7(Py)₂](MeOH) (20)** is a possible good candidate for future magnetic characterization, since it shows reversible photocyclization.

4.9 Experimental

4.9.1 Ligands

1,2-bis-(5-hydrazide-2-methylthien-3-yl) cyclopentene (L6)

1.88 grams of **L4** (5 mmol) were dissolved in 20ml of dry methanol. To this solution was added an excess of hydrazine hydrate (10ml) and the solution was refluxed for 3 hours. The solution was cooled to r.t. and the former white precipitate filtered, washed with methanol several times and finally with ether, yielding a white powder (1.41g, 75%). ¹H-NMR (400 MHz, [D6]DMSO) δ(ppm): 9.55 (s, 2H, NH), 7.43 (s, 2H, Tph), 4.35 (s, 4H, NH₂), 2.72 (t, 4H, Cp), 2.00 (m, 2H, Cp), 1.84 (s, 6H; Me).

1,2-bis-(5-(N'-(2-hydroxybenzylidene)hydrazide)-2-methylthien-3-yl) cyclopentene (H₄L7)

0.7 grams of **L6** (1.86 mmol) were dissolved in 20ml of dry methanol and 0.39ml of salicylaldehyde (3.72 mmol) was added drop wise with some drops of Et₃N and the solution was stirred at reflux overnight. After cooling at r.t. the solution was filtered and the precipitate was washed with methanol and ether yielding a white powder (0.87g, 80.5%). ¹H-NMR (400 MHz, [D6]DMSO) δ(ppm): 11.95 (s, 2H, NHene), 11.05 (s, 2H, OH), 8.57 (s, 2H, NH), 7.73 (s, 2H, Tph), 7.52 (d, 2H, Ar), 7.27 (t, 2H, Ar), 6.84 (m, 4H, Ar), 2.82 (t, 4H, Cp), 2.06 (m, 2H, Cp), 1.88 (s, 6H, Me).). MS (ESI+) m/z: 585.14 [C₂₉H₂₆O₄N₄S₂+H]⁺.

1,2-bis-(5-(N'-(pyridine-2-ylmethylene)hydrazide)-2-methylthien-3-yl) cyclopentene (H₂L8)

0.7 grams of **L6** (1.86 mmol) were dissolved in 20ml of dry methanol with some drops of Et₃N and 0.45ml of 2-pyridinecarboxyaldehyde (3.72 mmol) was added drop wise and the solution was stirred at reflux overnight. After this, the solution was evaporated yielding a brown oil. 10ml of water and 50 ml were added. A precipitate appears and was filtered. This operation was repeated till the total dissolution of the oil. The portions were mixed and washed with water and ether, yielding a light grey powder (0.85g, 83.3%). ¹H-NMR (400 MHz, [D6]DMSO) δ(ppm): 11.95 (s, 2H, NHene), 8.6 (s, 2H, NH), 8.10 (m, 2H, Ar), 7.9-7.97 (m, 4H, Ar), 7.77 (s, 2H, Tph), 7.42 (m, 2H, Ar), 2.82 (t, 4H, Cp), 2.01-2.10 (m, 8H, Cp+Me). MS (ESI+) m/z: 555.16 [C₂₇H₂₄O₂N₆S₂+H]⁺.

4.9.2 Coordination compounds

[Tb₂L7₂(CO₃)₂Na₆Py₁₀] (14)

A solution of **H₄L7** (30 mg, 0.051 mmol) and NaH (10.2 mg, 0.255 mmol) in pyridine (10 mL) was added to a solution of Tb(NO₃)₃·xH₂O (14.9 mg, 0.034 mmol) in pyridine (10 mL). The resulting yellow solution was mixed for 2 hours, filtered and the filtrate was layered with toluene. After two days, yellow crystals were collected (17 mg, 42 yield %). IR (KBr pellet, cm⁻¹): 3434, 2956, 2917, 2847, 1608, 1543, 1515, 1465, 1378, 1195, 1139, 869, 760, 513.

[Dy₂L7₂(CO₃)₂Na₆Py₁₀] (15)

A solution of **H₄L7** (20 mg, 0.034 mmol) and NaH (5.48 mg, 0.136 mmol) in pyridine (10 mL) was added to a solution of Dy(NO₃)₃·xH₂O (29.58 mg, 0.068 mmol) in pyridine (10 mL). The resulting yellow solution was mixed for 2 hours, filtered and the filtrate was layered with ether. After five days, yellow crystals were collected (11 mg, 27 yield %). The IR spectrum was identical to the one obtained for complex **14**.

[Tb₄L8₄Cl₄(H₂O)₅]·2Py (16)

A solution of **H₂L8** (30 mg, 0.053 mmol) and NaH (4.24 mg, 0.106 mmol) in pyridine (10 mL) was added to a solution of Tb(Cl₃)₃·xH₂O (12.71 mg, 0.034 mmol) in pyridine (10 mL). The resulting yellow solution was mixed for 2 hours, filtered and the filtrate was layered with toluene. After one days, yellow crystals were collected (31 mg, 53 yield %). IR (KBr pellet, cm⁻¹): 3417, 2956, 2921, 2839, 1591, 1556, 1504, 1456, 1382, 1343, 1147, 1113, 1052, 865, 743, 695, 521.

[Dy₄L8₄Cl₄(H₂O)₅]·1Py (17)

A solution of **H₂L8** (20 mg, 0.036 mmol) and NaH (2.88 mg, 0.072 mmol) in pyridine (10 mL) was added to a solution of Dy(Cl₃)₃·xH₂O (12.21 mg, 0.036 mmol) in pyridine (10 mL). The resulting yellow solution was mixed for 2 hours, filtered and the filtrate was layered with toluene. After two days, yellow crystals were collected (15 mg, 25 yield %). The IR spectrum was identical to the one obtained for complex **16**.

[Tb₄L7₂Na₄(H₂O)₂(CO₃)₂(Py)₆(acac)₄]·9Py (18)

A solution of **H₄L7** (30 mg, 0.051 mmol) and NaH (10.2 mg, 0.255 mmol) in pyridine (10 mL) was added to a previous prepared solution solution of Tb(NO₃)₃·xH₂O (44.37 mg, 0.106 mmol), acetylacetonate (25.52mg, 0.212mmol) and NaH (10.19mg, 0.212 mmol) in pyridine (10 mL). The resulting yellow solution was mixed and heated (50°C) for 2 hours, filtered and the filtrate was layered with toluene. After one day, yellow crystals were collected (32 mg, 17 yield %). IR (KBr pellet, cm⁻¹): 3439, 2926, 2839, 1608, 1547, 1517, 1434, 1382, 1202, 1147, 1021, 830, 756, 526.

[Dy₄L7₂Na₄(H₂O)₂(CO₃)₂(Py)₆(acac)₄]·9Py (19)

A solution of **H₄L7** (30 mg, 0.051 mmol) and NaH (10.2 mg, 0.255 mmol) in pyridine (10 mL) was added to a previous prepared solution solution of Dy(NO₃)₃·xH₂O (35.41 mg, 0.106 mmol), acetylacetonate (25.52mg, 0.212mmol) and NaH (10.19mg, 0.212 mmol) in pyridine (10 mL). The resulting yellow solution was mixed and heated (50°C) for 2 hours, filtered and the filtrate was layered with toluene. After one days, yellow crystals were collected (21 mg, 11 yield %). The IR spectrum was identical to the one obtained for complex **18**.

[Cu₂L7(Py)₂](MeOH) (20)

A solution of **H₄L7** (20 mg, 0.034 mmol) and TBAOH (0.136 ml, 0.136 mmol) in methanol (10 mL) was added to a solution of CuBr₂ (15.22 mg, 0.068 mmol) in methanol (10 mL). The resulting green solution was mixed for 2 hours. After this, a precipitate appears and pyridine was added to the solution till complete solution of the precipitate and let to slow evaporation. After 1 day, dark brown crystals were collected (23 mg, yield 73%). IR (KBr pellet, cm⁻¹): 3442, 3065, 2926, 2839, 1608, 1500, 1469, 1343, 1195, 1139, 1078, 873, 752, 730, 695. Anal. Found (calc% for [C₄₂H₃₄Cu₂N₆O₅S₂·1.45H₂O]; **20**·1.45H₂O): C 55.9 (55.8), H 4.22 (4.11), N 9.25 (9.3).

[Cu₂L7(Phen)₂](H₂O)₃ (21)

A solution of **H₄L7** (20 mg, 0.034 mmol) and TBAOH (0.204 ml, 0.204 mmol) in methanol (10 mL) was added to a solution of CuBr₂ (15.22 mg, 0.068 mmol) in methanol (10 mL). The resulting green solution was mixed for 10 minutes and Phenantroline (13.75 mg, 0.068mmol) was added to the solution and was mixed for

30min while heating (50°C). After this, a precipitate appears and was filtered. This precipitate was dissolved in DMF. After two weeks, dark brown crystals were collected (18 mg, yield 42%). IR (KBr pellet, cm⁻¹): 3439, 3052, 2917, 2831, 1669, 1613, 1500, 1465, 1426, 1330, 1191, 1026, 943, 839, 721, 665, 562. Anal. Found (calc% for [C₅₅H₄₅Cu₂N₈O₇S₂·0.3H₂O]; **21**·0.3H₂O): C 58.11 (58.65), H 4.51(4.09), N 10.5 (10.01).

4.10 References

1. Kaim, W. *Advanced Inorganic Chemistry*. 5. Auflage. Von F. A. Cotton und G. Wilkinson. Wiley, Chichester 1988. XVII, 1455. *Angew. Chemie* **101**, 811–812 (1989).
2. Ishikawa, N., Sugita, M., Ishikawa, T., Koshihara, S. & Kaizu, Y. Lanthanide Double-Decker Complexes Functioning as Magnets at the Single-Molecular Level. *J. Am. Chem. Soc.* **125**, 8694–8695 (2003).
3. Zhu, X., Jiang, F., Poon, C., Wong, W. & Wong, W. Synthesis, Structure and Spectroscopic Properties of Lanthanide Complexes of N-Confused Porphyrins. *Eur. J. Inorg. Chem.* **2008**, 3151–3162 (2008).
4. Armelao, L. *et al.* Design of luminescent lanthanide complexes: From molecules to highly efficient photo-emitting materials. *Coord. Chem. Rev.* **254**, 487–505 (2010).
5. Xiong, R., Andres, J., Scheffler, K. & Borbas, K. E. Synthesis and characterisation of lanthanide-hydroporphyrin dyads. *Dalt. Trans.* **44**, 2541–2553 (2015).
6. Backer-Dirks, J. D. J. *et al.* Complexes of lanthanide ions with the crown ether 1{,}4{,}7{,}10{,}13{,}16-hexaoxacyclo-octadecane. *J. Chem. Soc. Dalt. Trans.* 2191–2198 (1980).
7. Magennis, S. W. *et al.* Crown ether lanthanide complexes as building blocks for luminescent ternary complexes. *Polyhedron* **22**, 745–754 (2003).
8. Das, S. *et al.* Molecular magnets based on homometallic hexanuclear lanthanide(III) complexes. *Inorg. Chem.* **53**, 5020–5028 (2014).
9. Aguilà, D. *et al.* Heterodimetallic [LnLn '] Lanthanide Complexes : Towards a Chemical Design of 2-Qubit Molecular Spin Quantum Gates Heterodimetallic [LnLn '] Lanthanide Complexes : Towards a Chemical Design of 2-Qubit Molecular Spin Quantum Gates. (2014).
10. Liu, C.-S. *et al.* A luminescent linear trinuclear DyIII complex exhibiting slow magnetic relaxation of single ion origin. *Dalt. Trans.* **40**, 9366 (2011).
11. Yang, Y. *et al.* Salen-Type Lanthanide Complexes with Luminescence and Near-Infrared (NIR) Properties. *J. Inorg. Organomet. Polym. Mater.* **23**, 1211–1218 (2013).
12. Nie, K., Gu, W., Yao, Y., Zhang, Y. & Shen, Q. Synthesis and Characterization of Salalen Lanthanide Complexes and Their Application in the Polymerization of rac-Lactide. *Organometallics* **32**, 2608–2617 (2013).
13. Carcelli, M. *et al.* Synthesis and characterization of new lanthanide complexes with hexadentate hydrazonic ligands. *Inorganica Chim. Acta* **358**, 903–911 (2005).

14. He, C. *et al.* Metal-tunable nanocages as artificial chemosensors. *Angew. Chemie - Int. Ed.* **47**, 877–881 (2008).
15. Lin, P. H., Burchell, T. J., Clérac, R. & Murugesu, M. Dinuclear dysprosium(III) single-molecule magnets with a large anisotropic barrier. *Angew. Chemie - Int. Ed.* **47**, 8848–8851 (2008).
16. Albrecht, M., Liu, Y., Zhu, S. S., Schalley, C. a & Fröhlich, R. Self-assembly of heterodinuclear triple-stranded helicates: control by coordination number and charge. *Chem. Commun. (Camb)*. 1195–7 (2009).
17. Albrecht, M., Yulia, Y., Exarchos, A., Nachev, P. & Fröhlich, R. 1 : 1 vs. 2 : 1 coordination of pentadentate hydrazone-type ligands to lanthanide(III) ions. Formation of cationic as well as dicationic complexes. *Dalton Trans.* 7421–7427 (2009).
18. Zhu, X., He, C., Dong, D., Liu, Y. & Duan, C. Cerium-based triple-stranded helicates as luminescent chemosensors for the selective sensing of magnesium ions. *Dalton Trans.* **39**, 10051–10055 (2010).
19. Thomas, J. a. Metal ion directed self-assembly of sensors for ions, molecules and biomolecules. *Dalt. Trans.* **40**, 12005 (2011).
20. Xue, S., Zhao, L., Guo, Y.-N., Zhang, P. & Tang, J. The use of a versatile o-vanilloyl hydrazone ligand to prepare SMM-like Dy₃ molecular cluster pair. *Chem. Commun.* **48**, 8946 (2012).
21. Tian, H. *et al.* A discrete dysprosium trigonal prism showing single-molecule magnet behaviour. *Chem. - A Eur. J.* **18**, 442–445 (2012).
22. Zou, L. *et al.* Phenoxido and alkoxido-bridged dinuclear dysprosium complexes showing single-molecule magnet behaviour. *Dalton Trans.* **41**, 2966–71 (2012).
23. Lin, P.-H., Korobkov, I., Burchell, T. J. & Murugesu, M. Connecting single-ion magnets through ligand dimerisation. *Dalton Trans.* **41**, 13649–55 (2012).
24. Anwar, M. U., Dawe, L. N., Tandon, S. S., Bunge, S. D. & Thompson, L. K. Polynuclear lanthanide (Ln) complexes of a tri-functional hydrazone ligand – mononuclear (Dy), dinuclear (Yb, Tm), tetranuclear (Gd), and hexanuclear (Gd, Dy, Tb) examples. *Dalt. Trans.* **42**, 7781 (2013).
25. Chandrasekhar, V., Hossain, S., Das, S., Biswas, S. & Sutter, J. Rhombus - Shaped Tetranuclear [Ln₄] Complexes [Ln = Dy(III) and Ho(III)]: Synthesis, Structure, and SMM Behavior. *Inorg. Chem.* (2013).
26. Hosseini-Monfared, H. *et al.* Syntheses, structures and magnetic properties of azido- and phenoxo-bridged complexes of manganese containing tridentate aroylhydrazone based ligands. *Polyhedron* **61**, 45–55 (2013).
27. Patai, S. The chemistry of the carbon-nitrogen double bond. *J. Mol. Struct.* **11**, 338 (1970).
28. Tidwell, T. T. Hugo (Ugo) Schiff, Schiff bases, and a century of β-lactam synthesis. *Angew. Chemie - Int. Ed.* **47**, 1016–1020 (2008).

29. Van Dijken, D. J., Kovaříček, P., Ihrig, S. P. & Hecht, S. Acylhydrazones as Widely Tunable Photoswitches. *J. Am. Chem. Soc.* **137**, 14982–14991 (2015).
30. Feltham, H. L. C. & Brooker, S. Review of purely 4f and mixed-metal nd-4f single-molecule magnets containing only one lanthanide ion. *Coord. Chem. Rev.* **276**, 1–33 (2014).
31. Gatteschi, D., Sessoli, R., Villain, J. *Molecular Nanomagnets*. (2006). doi:10.1017/CBO9781107415324.004
32. Chilton, N. F., Anderson, R. P., Turner, L. D., Soncini, A. & Murray, K. S. PHI: A powerful new program for the analysis of anisotropic monomeric and exchange-coupled polynuclear d- and f-block complexes. *J. Comput. Chem.* **34**, 1164–1175 (2013).
33. Harvey, E. C., Feringa, B. L., Vos, J. G., Browne, W. R. & Pryce, M. T. Transition metal functionalized photo- and redox-switchable diarylethene based molecular switches. *Coord. Chem. Rev.* **282-283**, 77–86 (2014).

CHAPTER 5: PHOTOCROMIC HELICAL ASSEMBLY OF Fe(II) FEATURING SCO

5.1 Introduction	196
5.2 Synthesis and characterization	197
5.2.1 Synthesis and design of 1,2-bis-(5-(2-pyrazol)-pyridin-2-methylthien-3-yl) cyclopentene (H ₂ L9)	197
5.2.2 Photochromic behavior and fluorescence of H ₂ L9.....	198
5.3 Synthesis and crystal structure of [Fe ₂ (L9) ₃] (ClO ₄) ₄ (22)	201
5.4 Photochromic properties of [Fe ₂ (L9) ₃](ClO ₄) ₄ (22)	205
5.5 Magnetic properties of [Fe ₂ (L9) ₃](ClO ₄) ₄ (22)	207
5.6 Solution studies.	209
5.6.1 Fluorescence of [Fe ₂ (L9) ₃](ClO ₄) ₄ (22)	209
5.6.2 Magnetic properties in solution of [Fe ₂ (L9) ₃](ClO ₄) ₄ (22)	211
5.7 Conclusions	217
5.8 Experimental	218
5.8.1 Ligands and precursors.....	218
5.8.2 Coordination complex	220
5.9 References	221

5.1 Introduction

In recent years the interest in spin crossover compounds (SCO)¹ has considerably increased, given their potential relevance as part of future electronic devices. This is in part because their electronic properties can be manipulated by means of external stimuli, such as temperature variations^{1,2}, external magnetic field³, light irradiation⁴⁻⁶, guest molecules⁷⁻⁹ or even changes in pressure¹⁰. The SCO phenomena can be observed within transition metals where the 3d electrons can be distributed in two different ways configurations (d^4-d^7)¹¹. The case of iron (II), d^6 , is the most studied², among others¹²⁻²¹

One of the main requirement to observe spin crossover is to have the correct ligand environment around the metal center. Indeed, the spin state is affected by the strength of the ligand field (Δ) of the ligands²². Ligands with a strong ligand field, split further the 3d orbitals e_g and t_{2g} , thus favouring the low spin state, while the inverse situation favours the high spin state (Figure 5.1). In that regard, ligands containing nitrogen donor atoms have been studied and used with very good results^{23,24}.

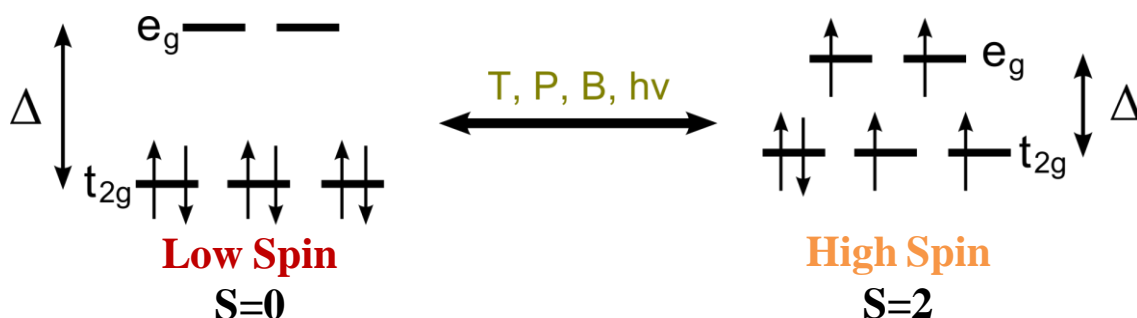


Figure 5.1: The two configurations of the Fe(II), d^6 , depending on the crystal field or by external stimulus.

In this chapter, the preparation of a photochromic ligand containing a pyridine-pyrazole based moiety, **H₂L9**, the synthesis of its iron complex and its characterization using different techniques is shown.

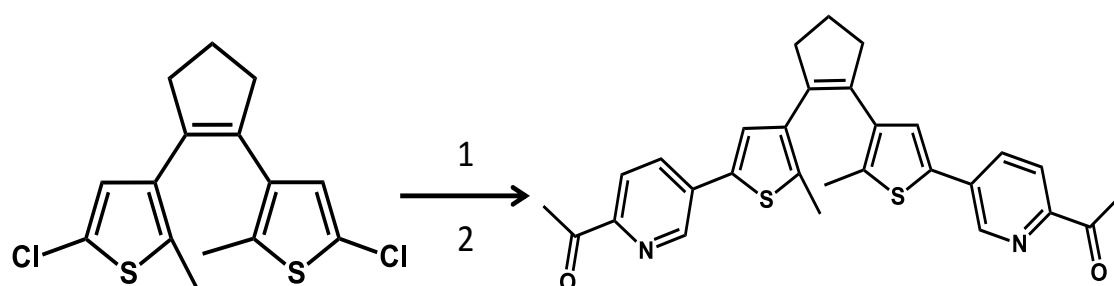
The introduction of the photochromic unit will serve as an additional way to modify the spin state of the complex, creating a multiresponse compound.

5.2 Synthesis and characterization

5.2.1 Synthesis and design of 1,2-bis-(5-(2-pyrazol)-pyridin-2-methylthien-3-yl) cyclopentene (**H₂L9**)

The purpose in preparation **H₂L9** is to obtain two cavities containing nitrogen donor atoms where later on, the stoichiometry of the coordination reaction with iron, will lead to dinuclear species with SCO properties. This can be achieved with pyridine/pyrazole moieties. We have thus prepared a new ligand containing the nitrogen pyridine atom in the *meta* position with respect to the connexion to the photochromic spacer and with the pyrazole ring in the *para* position.

The strategy followed for the synthesis of **H₂L9** starts with the introduction of two acetyl pyridine moieties into the photochromic building block **L0** via Suzuki cross coupling²⁵. First, **L0** was lithiated with *n*BuLi in THF at room temperature, and then treated with B(OBu)₃ to provide the bis(boronic ester). The crude material was used directly in the Suzuki reaction without any workup because it was found that it easily hydrolyses. For the Suzuki cross coupling reaction, Pd(PPh₃)₄ was used as palladium source, Na₂CO₃ as base, THF as solvent and several drops of ethylene glycol were added as cosolvent. The aryl halide used was 2-acetyl-5-bromopyridine^{26,27}, and after quenching of the reaction with diethyl ether and water, **1,2-bis-(5-(2-acetyl-5-bromopyridin)-2-methylthien-3-yl) cyclopentene (L9a)** was obtained in 49% yield (Scheme 5.1).



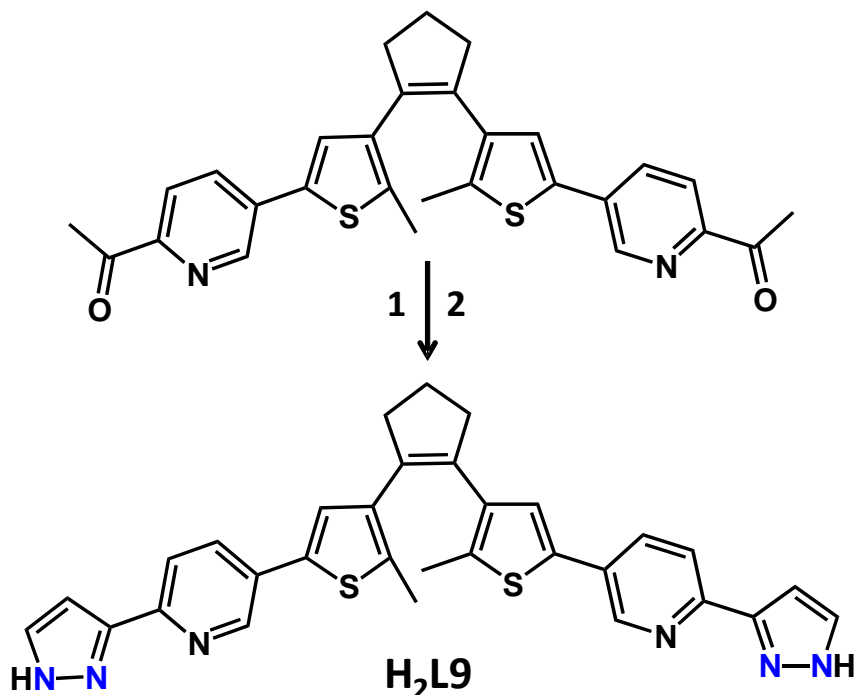
1: *n*BuLi, B(OBu)₃, THF

2: C₇H₆NBr, Pd(PPh₃)₄, Na₂CO₃, ethylene glycol, H₂O, THF, 60°

Scheme 5.1: Synthesis of **L9a**.

The preparation of the pyridine-pyrazole ligand is based on an earlier reported method²⁸. The first step is the reaction of an acyl derivative with *N,N*-

dimethylformamide dimethyl acetal. The resulting propenone is treated with hydrazine to generate the pyrazolyl ring, via a ring-closure step (Scheme 5.2).



- 1: N,N-dimethylformamide dimethyl acetal, refluxed
 2: $\text{NH}_2\text{-NH}_2$, EtOH, refluxed

Scheme 5.2: Synthesis of **H₂L₉**

5.2.2 Photochromic behavior and fluorescence of **H₂L₉**

H₂L₉ is very sensitive to light upon exposure to sunlight, it starts to react as witnessed by a color change, from colorless to deep violet. This change also translates into observed in the UV-Vis spectra of a methanolic solution of **H₂L₉**, where a small band in the visible region can be observed. The UV region is dominated by two bands, centered at 201 and 335 nm. The latter also presents a shoulder at 290 nm. All these bands are attributed to $\pi \cdots \pi^*$ transitions^{25,29}.

After irradiation with UV light (<425 nm), a big band centered at 551 nm starts to appear owing to the formation of the closed ring isomer where the π electrons are delocalized through an extended conjugated system, making the HOMO-LUMO gap smaller, thus the peak at 335 nm shifts to 551 nm.

This process is very fast and after 1 min, the PSS state is reached (Figure 5.2). The inverse process is slower than the cyclization. The initial isomer can be reached after 20min of visible light irradiation (>430 nm). The presence of the same isosbestic points during both processes is indicative of a pure sample (Figure 5.3).

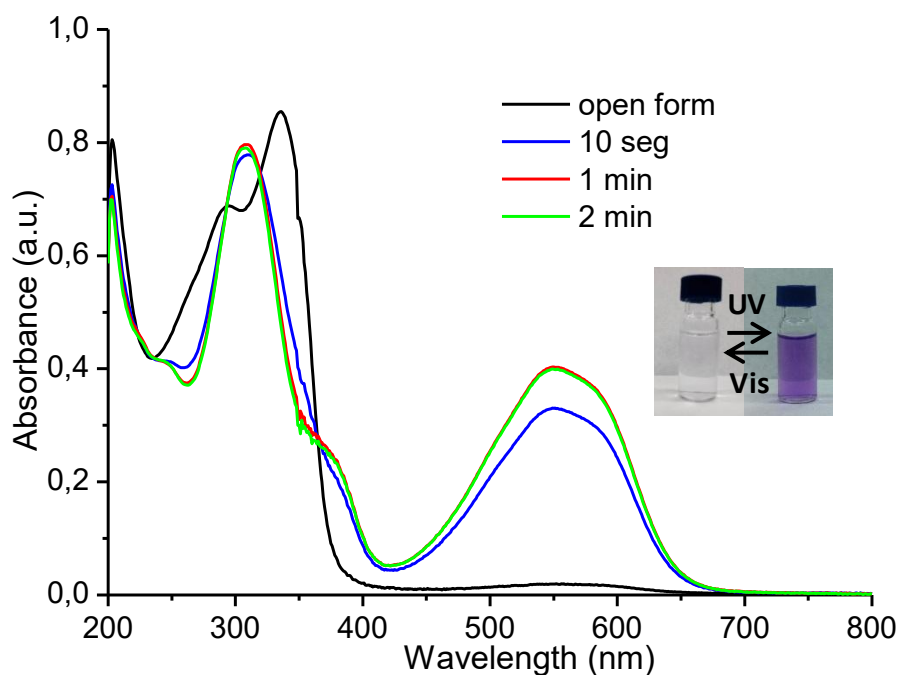


Figure 5.2: UV-Vis spectra of open $\text{H}_2\text{L9}$ upon irradiation with UV light (<425 nm).

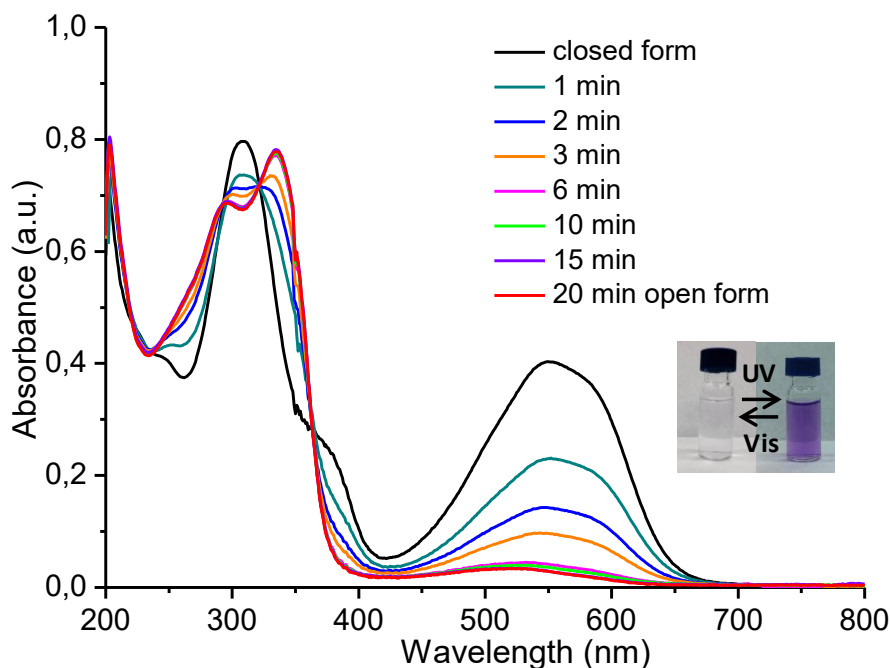


Figure 5.3: UV-Vis spectra of closed $\text{H}_2\text{L9}$ upon irradiation with Visible light (>425 nm).

The fluorescence behavior of **H₂L9** is different depending on the excitation wavelength used. In Figure 5.4, the emission spectrums of the ligand upon excitation with UV (left) and Visible light (right) are shown. **H₂L9** presents a broad band centered at 433 nm when it is excited with 290 nm light. This emission band shrinks dramatically when the sample is irradiated with UV light (<425), with a blue shift, down to 424 nm. This luminescence can be recovered completely after 900s of irradiation with Visible light (>430nm), which restores the initial spectrum corresponding to the open form.

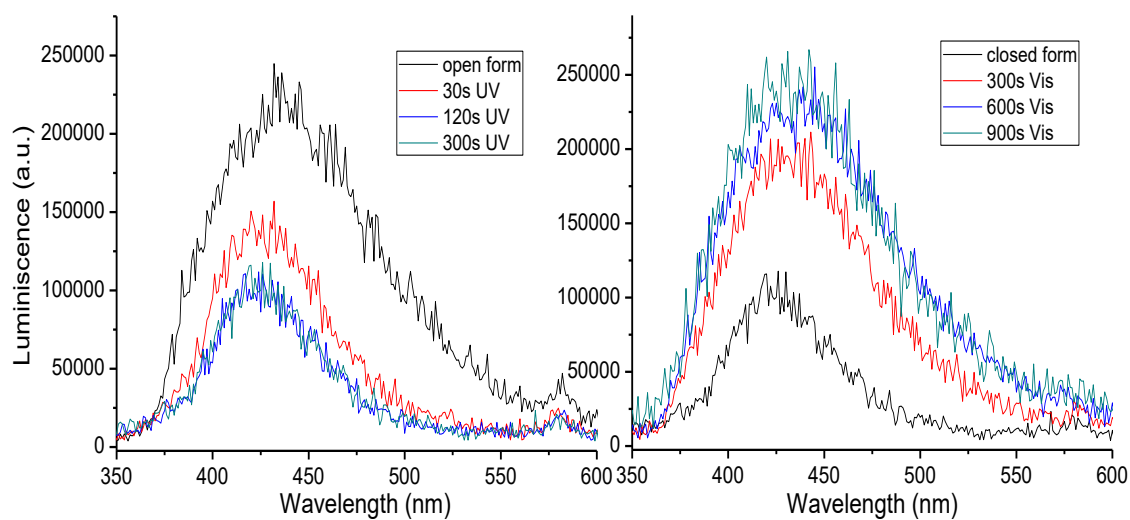


Figure 5.4: Fluorescence spectra, after excitation with 290nm, of **H₂L9** upon irradiation of UV light (left) and Visible light (right).

The fluorescence spectrum of **H₂L9** after excitation with 335 nm, shows a broad emission band centered at 430 nm which grows after UV irradiation, accompanied by a blue shift, down to 417 nm. The reverse process has a peculiarity. The original spectrum cannot be fully restored due to the excitation wavelength used, because this light is related to the photocyclization process, thus, the closed form is formed during the excitation process, which can be seen easily because the cuvette stays purple, even with large exposure times to Visible light (Figure 5.5, right).

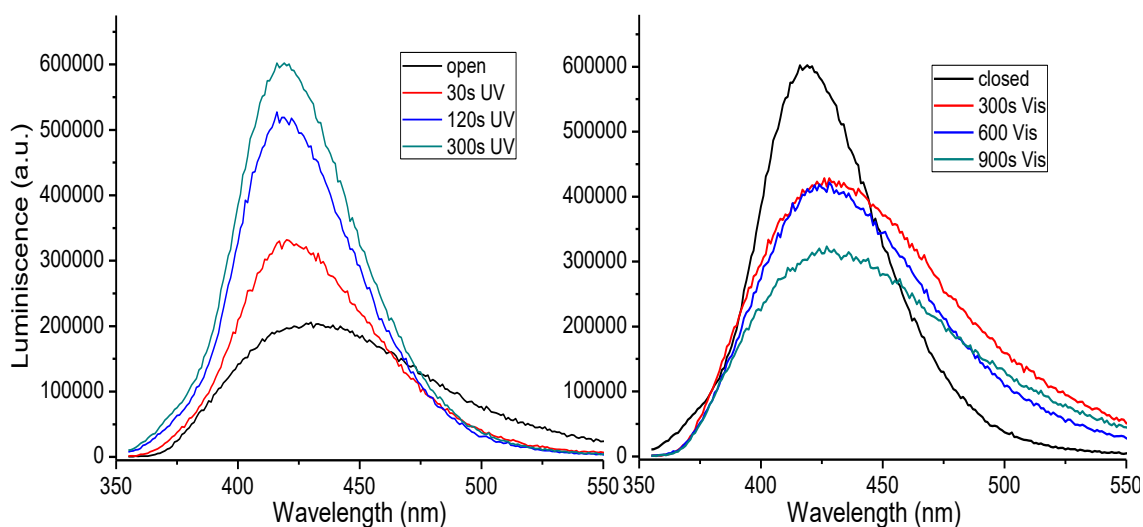


Figure 5.5: Fluorescence spectra, after excitation with 335nm, of **H₂L9** upon irradiation of UV light (left) and Visible light (right).

5.3 Synthesis and crystal structure of [Fe₂(L9)₃](ClO₄)₄ (**22**)

As we have explained before, the two cavities having nitrogen atoms of **H₂L9** could coordinate atoms of Fe(II).

Thus the reaction of two equivalents of Fe(ClO₄)₂·6H₂O with three equivalent of **H₂L9** in methanol, gives a deep red solution. Red crystals of **22** can be obtained after slow liquid diffusion in toluene in two weeks, as determined through single crystal X-Ray Diffraction.

Compound **22** crystallizes in the triclinic space group P-1, and the unit cell contains two cations of the complex in a helicate (Figure 5.6). The charge of the complex is compensated by eight molecules of perchlorate. Due to the quickly degradation of the crystal, the structure was solved using a mask, where most of the solvent which could not be refined, was extracted from the model, thus one must consider that some molecules of methanol, toluene and water are also present in the structure.

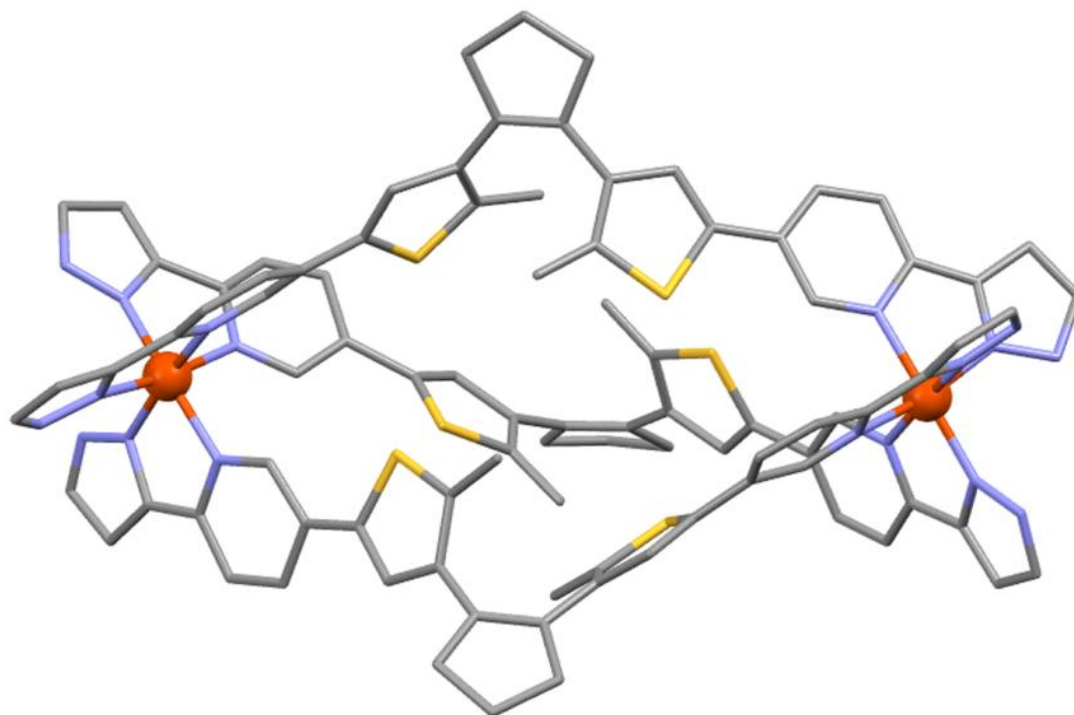


Figure 5.6: Crystal structure of the cation of **22**

Each complex cation is formed by three ligands **H₂L9** linking two atoms of Fe(II), in a helical configuration, thus furnishing an octahedral geometry and a FeN₆ coordination sphere for around each metal, as intended through the design of **H₂L9**. The structure was solved at 100K unveiling an average value for the Fe-N bond distances of 1.962 Å. This is a value typical for a low spin state of Fe(II)²². Indeed, the HS to LS transition involves an electron transfer from antibonding e_g orbitals to slightly bonding t_{2g} orbitals. The consequence is a shortening of the Fe-N bond lengths. The N-Fe-N angles may also be affected. The changes to the angles may be gauged by two parameters^{30,31,32}, Σ and Θ , which define the distortion and are an indirect indicator of the spin state of the metal. The parameter Σ relates to the N-Fe-N angles as it is the sum of the deviations from 90° of the 12 cis N-Fe-N angles in the coordination sphere (Figure 5.7, left). Σ is equal to 0 for an ideal octahedron and increases with the deformation. The other parameter Θ , relates to the trigonal twist angle in going from an octahedral symmetry towards a trigonal prismatic symmetry (Figure 5.7, right). The perfect octahedron has $\Theta = 60^\circ$ value, whereas the higher the value, the bigger the distortion. The parameter Θ is the sum of the deviation from 60° of the 24 twist angles.

In relation to the spin state of the molecule, the low spin state is characterized by less distorted octahedral symmetry, with lower values of Σ and Θ parameters.

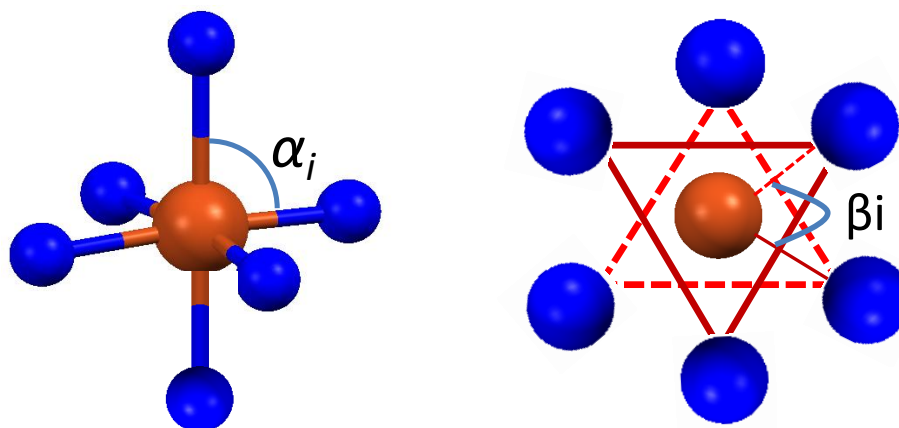


Figure 5.7: Definition of the structural parameters used to characterize the distortion of the FeN_6 octahedron. Σ on the left and Θ on the right.

The values of the distortion parameters are listed in Table 5.1 for each Fe(II) center of the asymmetric unit of complex **22** in addition to the corresponding parameters for the nine compounds that already exist in the literature with this coordination environment, i.e., with three chelating pyridine-pyrazole moieties linking the Fe(II) center.

Fe/Compound	Σ	Θ	T° (K)	Spin state	$d_{\text{Fe-N}}$ (Å)
Fe1	67,8	204	100	Low spin	1,97
Fe2	65,2	197	100	Low spin	1,965
Fe3	60	187	100	Low spin	1,959
Fe4	61,6	191	100	Low spin	1,962
Fe average	63,65	194,7	100	Low spin	1,962
DUMBUJ ³³	96	301	300	High spin	2,157
KAJXUQ ¹⁹	69,5	204,6	100	Low spin	1,988
LENXUY ³⁴	57,4	182	100	Low spin	1,984
NIHWIM ³⁵	127,1	329	100	High spin	2,207
NIHYEK ³⁵	87,9	207	100	High spin	2,18
PUHXOG ³⁶	85	252	300	High spin	2,114
REXBON ³⁷	64	189	100	Low spin	1,983
REXBUT ³⁷	90	270	300	High spin	2,133
REXCAA ³⁷	61,69	185	100	Low spin	1,987

Table 5.1: Values of Σ and Θ calculated with Olex 2.0 for compound **22** and different compounds presented in the literature.

Even though there are not too many reported examples, the values exhibited by compound **22** are consistent with these presented by the low spin compounds, thus, in the low range, as expected for a geometry closer to the perfect octahedron proper of the low spin state.

The three ligands of the helicate are in the correct configuration to undergo photochromic activity in the solid state, with an average of distance between the reactive carbons of 3.447 Å.

The packing of **22** features two layers of helicates (Figure 5.8). Those layers are interconnected by the pyridine-pyrazole moieties. The distances between the planes formed by the aromatic rings are displayed in Figure 5.8. The spaces between the clusters are occupied by perchlorate anions, some of which forming hydrogen bonds with pyrazol rings, and solvent molecules of methanol and toluene. The crystallographic data of **22** are shown in Table 5.2.

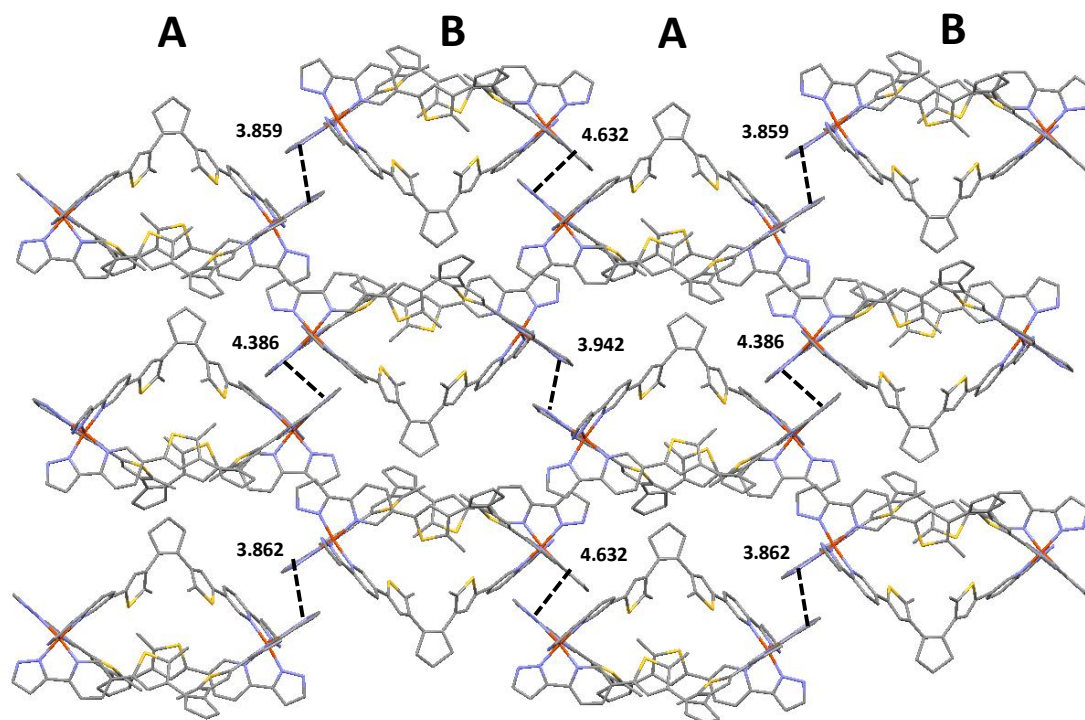


Figure 5.8: Crystal packing of **22**, showing the layers of helicates and the distances between the pyridine-pyrazole moieties in Å.

Table 5.2 Crystallographic data for **22**

formula	$C_{93}H_{78}Cl_4Fe_2N_{18}O_{16}S_6 + n\text{Solvents}$
M_r	2148 + nSolvents
Crystal system	Triclinic
space group	P-1
a [Å]	17.2103(12)
b [Å]	24.7227(15)
c [Å]	27.2192(17)
α [°]	89.981(4)
β [°]	89.999(5)
γ [°]	76.272(4)
V [Å ³]	11250.5(3)
Z	2
shape; colour	Red cubes
R_{int}	0.3361
R_1	0.1560
wR_2	0.3849
S	1.181

5.4 Photochromic properties of $[Fe_2(L9)_3](ClO_4)_4$ (**22**)

Irradiation of a methanolic solution of **22** with UV light (<425nm) caused a pronounced color change from light yellow to violet, which are characteristic of the respective chromophores in the open and closed isomers of **H₂L9**. Before UV-light irradiation, different $\pi-\pi^*$ transition bands of the open form of the ligand was observed with an extra band owing to a MLCT, at around 473 nm. Upon UV light irradiation, the bands centered at 264, 348 and 362nm start to decrease while new absorption bands appear around 305 and 562 nm (Figure 5.9). These bands were assigned to be $\pi-\pi^*$ transitions for the “closed” form of the ligand and a transition within the polyenic system of this form. Upon irradiation with visible light, the initial spectrum is recovered, showing that the photocyclization reaction is reversible (Figure 5.10).

Both processes show the same isosbestic points, indicative of a unique pathway without any type of secondary reactions. In addition, the band related to the coordination of the metal to the ligand is conserved (MLCT). The cyclization is faster than the opening ring reaction, the latter lasting 15 minutes before being complete.

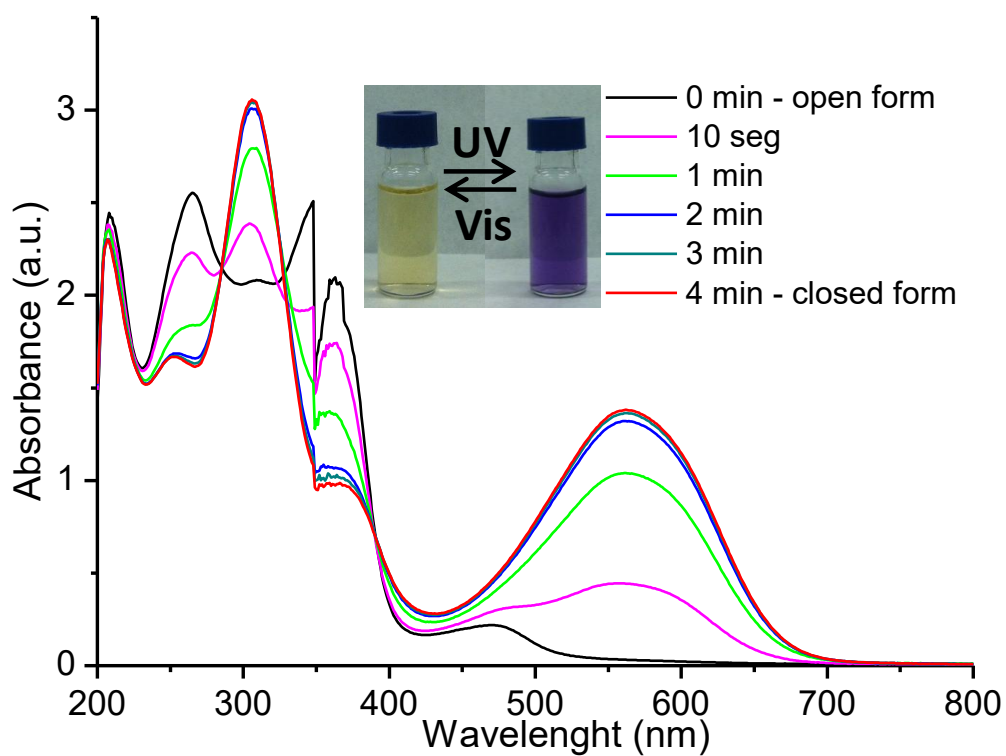


Figure 5.9: UV-Vis spectra of open **22** upon irradiation with UV light (<425nm).

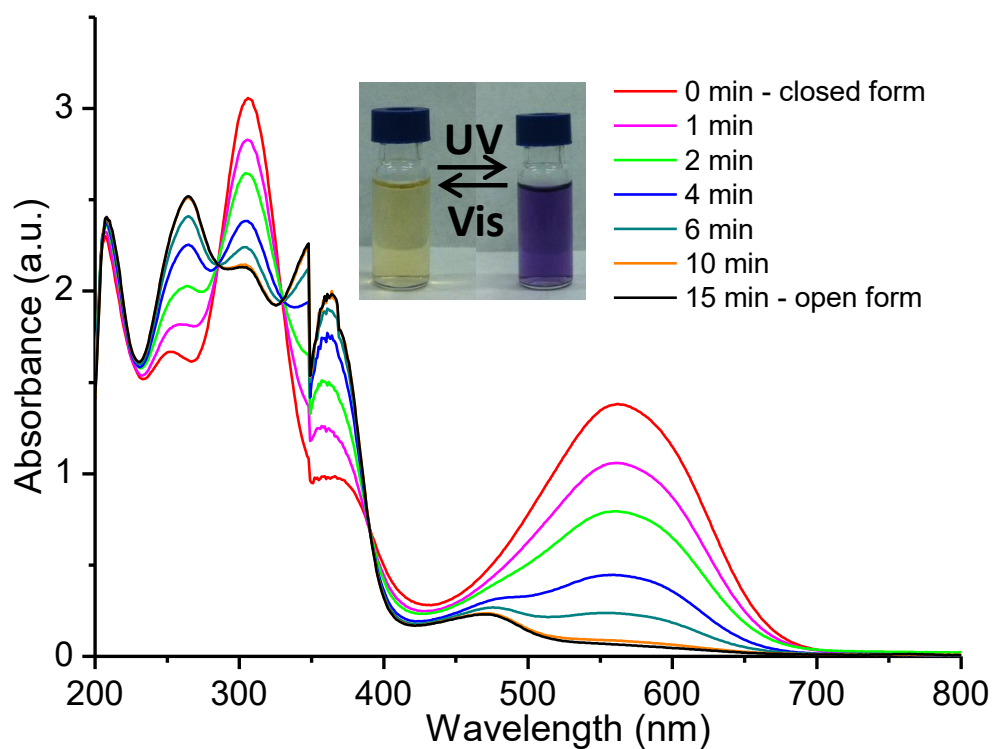


Figure 5.10: UV-Vis spectra of closed **22** upon irradiation with Visible light (>425nm).

The photochromic behavior in the solid state is very apparent when the sample is irradiated with UV light (<425nm), changing colors from orange to brown. The reverse process cannot be achieved even after long exposure to visible light (Figure 5.11). As mentioned above, the crystal lattice incorporates numerous molecules of solvent (toluene, methanol and water), many of which are lost upon air exposure. They may play an important role in the photochromic process, as shown in Chapter 2, related to the possible interactions between solvents and ligands. This could be at the root of the irreversibility of the process.

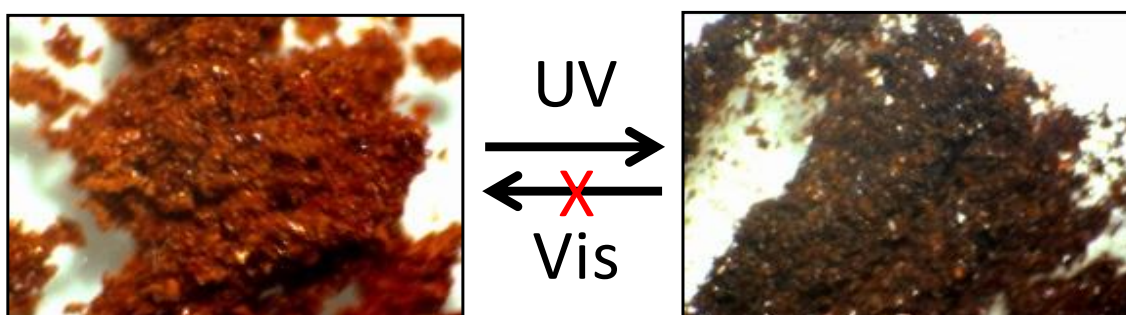


Figure 5.11: Photochromic behavior of **22** in the solid state.

5.5 Magnetic properties of $[\text{Fe}_2(\text{L9})_3](\text{ClO}_4)_4$ (**22**)

The temperature dependence on the magnetization for compound **22** has been studied on polycrystalline samples in the 2-400 K range. The $\chi_M T$ versus T plots is shown in Figure 5.12.

The curves of the initial **22** compound in the warming and cooling branches are superimposable. The $\chi_M T$ product at 400 K reaches a value of $5.8 \text{ cm}^3 \text{ mol}^{-1} \text{ K}$, which is in the range expected for two non-interacting high spin Fe(II) centres (HS, $S=2$, $6 \text{ cm}^3 \text{ mol}^{-1} \text{ K}$, for $g=2$). As the temperature decreases, the $\chi_M T$ value starts immediately to drop very gradually down to $1.8 \text{ cm}^3 \text{ mol}^{-1} \text{ K}$ at 50 K. This behavior is consistent with an incomplete spin crossover process, where part of the Fe(II) centers, remain on the high spin state. At very low temperature, a further decrease of the $\chi_M T$ is observed, caused either by zero field splitting (ZFS) of the remaining Fe(II) centres and/or by antiferromagnetic coupling between the afore mentioned Fe(II) centers. Thus, **22** exhibits a gradual and incomplete spin transition phenomena where the most part of the Fe(II) centers are in the low spin state at low temperature. A plateau around $3 \text{ cm}^3 \text{ mol}^{-1}$

1K would be indicative of a situation where a 50% of iron centres should be in the HS state and the other 50% in the LS state.

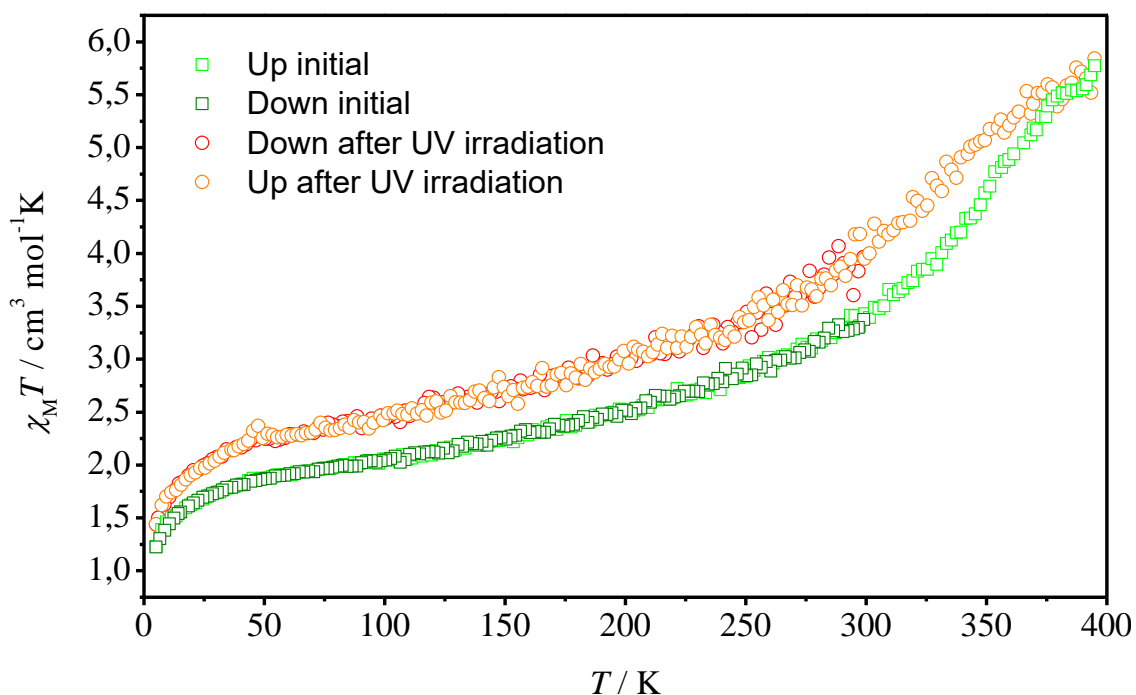


Figure 5.12: $\chi_M T$ versus T plot **22**. The initial compound is marked in green and the irradiated one in orange.

Subsequently, **22** was irradiated with UV light, causing a change of color from orange to brown. This change is also mirrored by the magnetic behavior of **22** (Figure 5.12). The magnetic curve has the same quantitative behavior regarding a gradual and incomplete spin transition, but the HS/LS ratio of Fe(II) centers is greater, as reflected by the values of the $\chi_M T$ in the whole range of temperatures. A shift of the SCO to lower temperatures is also apparent. In both processes the gradual character of the spin crossover is indicative of a low cooperativity of the system, also consistent with the incomplete value of the spin transition². The change in the magnetization caused by the cyclization of the ligands **H₂L9** of the assembly, may be related a change in the coordination sphere of the metal centres. Since the process favors high spin state, it is presumed that this new coordination sphere is more distorted than the initial one. The above results show that the new polydentate ligand **H₂L9** constitutes a new member of the family of diarylethenes ligands capable of producing spin crossover phenomena. The dinuclear system described here is unusual, since the few examples reported are mononuclear species.^{38,39}

Thus we reported here, the first example of a binuclear Fe(II) embedded in a helical assembly on this family of diarylethene ligands. Also, the synthetic procedure of the ligand gives the possibility to introduce new substituents in the pyrazole moiety, providing a wide array of new possible interactions in the crystal structure, such as the presence (or not) of hydrogen bonds or even better staking potential with the use of aromatic rings. Other possibility is the use of new counterions to compare if there are differences on the magnetic behavior.

5.6 Solution studies.

5.6.1 Fluorescence of $[\text{Fe}_2(\text{L9})_3](\text{ClO}_4)_4$ (22)

The design of new molecular systems combining SCO and other attractive functional properties, such as luminescence, that could sense the spin-state of its components, provides a valuable source of new hybrid materials^{40,41}. This could be the case of the helicate reported here, where as we have seen before, the SCO behavior summed to the luminescence and the photochromic activity of the compound, could be used to address the system externally and to exploit the synergy between different properties.

In order to explore its interaction with the thermal SCO, the fluorescence in solution of the system was measured at two different temperatures, 298 K and 77 K. In addition the photochromic behavior was also followed at both temperatures, through this technique. The fluorescence of the helicate was tested first with different excitation wavelengths. The 264 nm excitation light produces the best photoresponse fluorescence. The wavelengths corresponding to the maxima peaks in the UV-Visible spectrum, 348 and 362nm, affect the photochromic unit, thus the reversibility cannot be achieved in these conditions. Therefore, the 264nm wavelength can be used then to read the state of the isomer. First of all, the fluorescence was measured at room temperature (Figure 5.13), producing a broad peak centered at 430nm. The fluorescence can be switched off upon irradiation of the sample with UV light after 240s. The fluorescence can be recovered again using Visible light. 900s are needed to complete the ring opening process. The fluorescent was measured at 77K (Figure 5.14), leading to an increase of the signal intensity. In this case, the peak centered at 405 nm as a result of a clear blue shift.

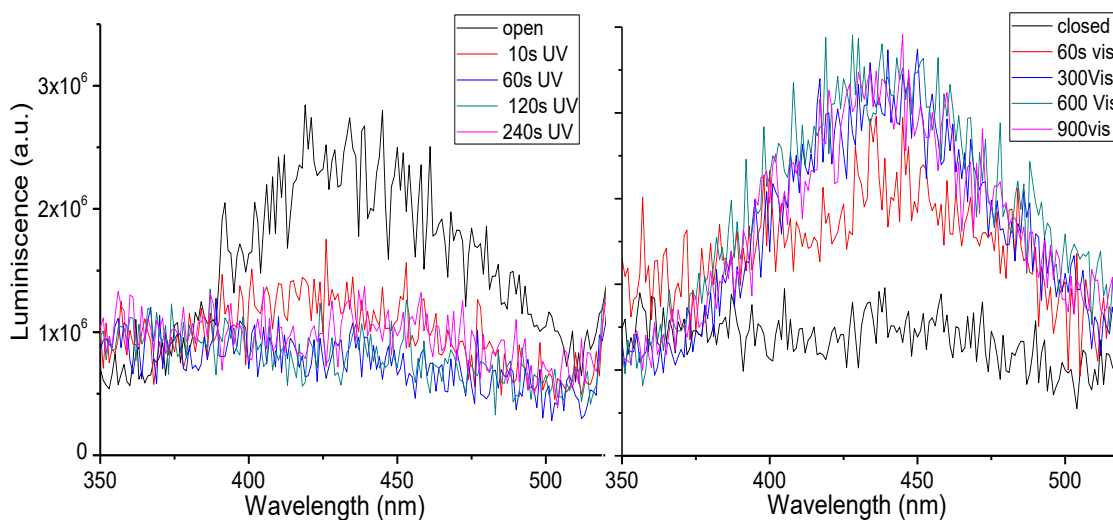


Figure 5.13: Fluorescence of **22** during photoisomerizations at r.t.

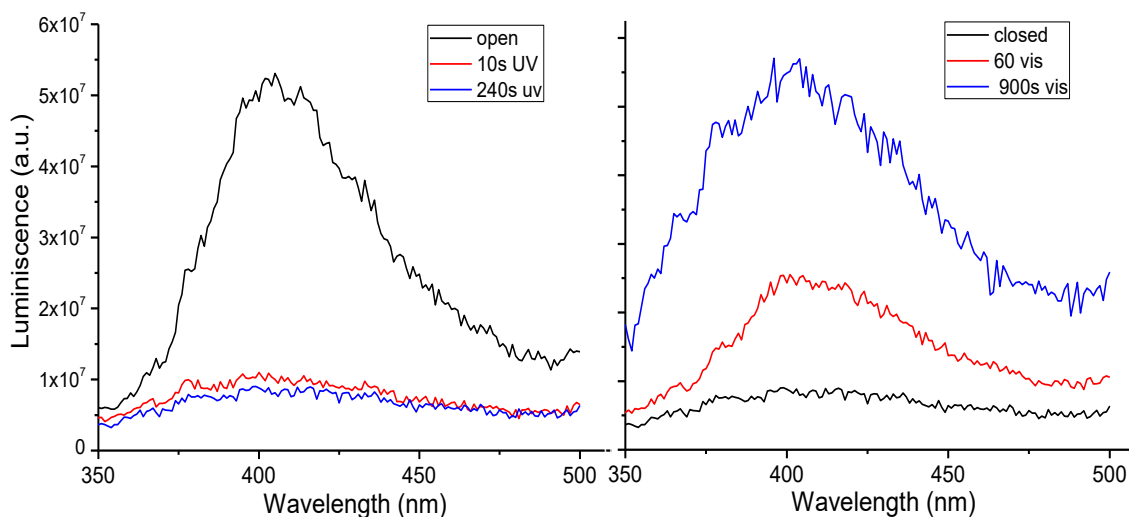


Figure 5.14: Fluorescence of **22** during photoisomerization at 77 K.

This hypsochromic effect (25nm shift), is indicative of the possible interactions between the magnetic properties of the Fe(II) centers and the fluorescent properties of the ligand⁴². This means that the spin state of the Fe(II) (almost fully LS at this temperature), affects the emission of the complex.^{42,43} These changes can be related to different energy states formed after SCO phenomena. In addition, the fluorescence of this state can be also turned off when the LS complex is irradiated with Visible light, similar behavior than the same process at room temperature. As Figure 10 (right) shows, the emission of the complex can be recovered after irradiation with Visible light.

All these changes that compound **22** can be featured in solution, make it a good candidate to be a hybrid compound with multiresponse behavior.

5.6.2 Magnetic properties in solution of $[\text{Fe}_2(\text{L9})_3](\text{ClO}_4)_4$ (22)

A very useful technique to study the magnetic behavior of Fe(II) compounds in solution, is the Evan's method^{44,45}. The Evan's method uses differences in the NMR chemical shift of a solvent caused by the presence of a paramagnetic species in the solution. It can be used to determine the magnetic moment of a paramagnetic compound and its number of unpaired electrons. Furthermore, the temperature dependence of the chemical shift difference can be used to determine the temperature-dependent magnetic moment at different temperatures. The Evan's method is often only performed at room temperature. Variable temperatures studies on the other hand, are very useful to study the SCO of iron compounds. These studies are limited by the freezing point of the solvent used in the experiment. For this, a necessary condition is to confirm the stability of the complex in solution. This was proved performing the UV-Vis experiments.

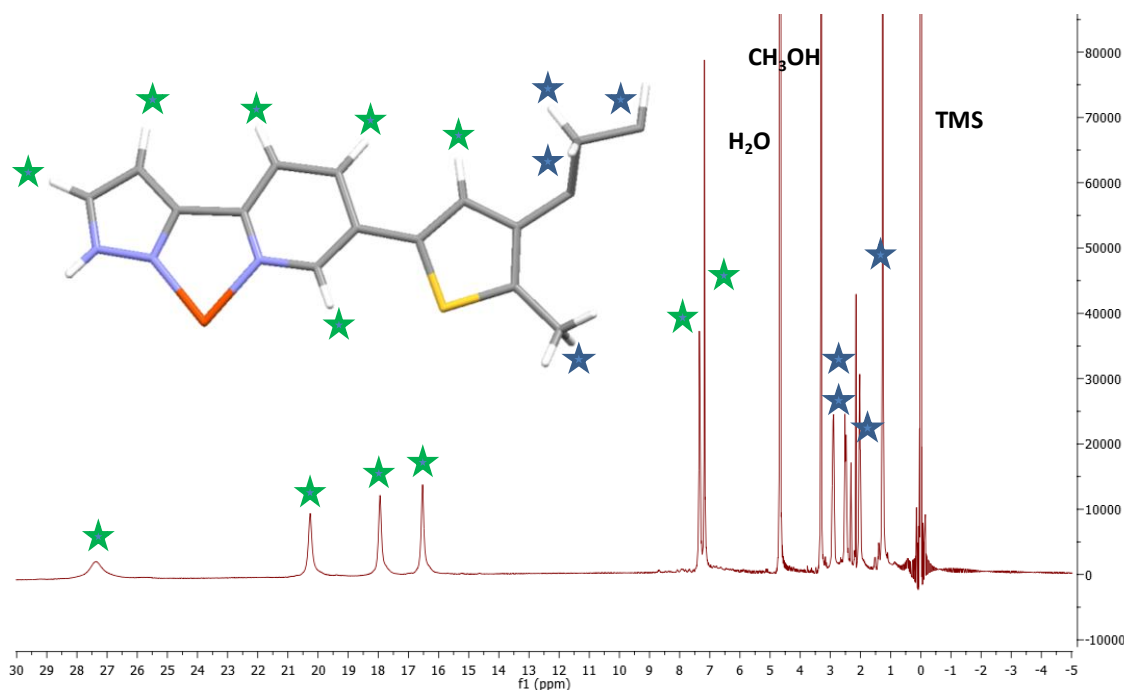


Figure 5.15: Paramagnetic ^1H -NMR of **22** at 318K in a 400MHz apparatus. The green stars are the aromatic peaks while the blue stars are the non-aromatic peaks. The higher displacements correspond to the protons which are closer to the iron center.

The paramagnetic ^1H -NMR spectrum of complex **22** (Figure 5.15), shows the expected symmetry of the compound in solution and allows to assign the peaks of the compound. Furthermore, this spectrum confirms the purity of the sample. The proton from the

nitrogen of the pyrazole is the only one not detected. It probably exchanges with water and it is not possible to see. To perform the Evan's method, an inset tube containing the same solvent of the experiment with the reference, here TMS, is introduced in the sample's NMR tube. The TMS shift from the inset should be different with respect to that of the sample as a result of the paramagnetic nature of the latter. The larger the difference, the larger the paramagnetic character of our sample. The separation in chemical shifts translates into a shift to the magnetic susceptibility, called paramagnetic shift. To calculate the paramagnetic shift, the next formula was used^{44,45}:

$$\chi_M = \frac{\chi_o \text{MW}(\text{solute})}{\text{MW}(\text{solvent})} + 3000 \frac{\Delta\nu}{4\pi\nu_o C} \quad \text{Eq. 1}$$

where χ_o is the diamagnetic molar susceptibility of the pure solvent ($-5,30\text{E}-07$ for CD_3OD), ν_o is the spectrometer frequency in Hz (600MHz); $\Delta\nu$ is the difference in chemical shifts between the TMS signals in the inner and outer tubes of the sample, in Hz; C is the concentration of iron compound in mol/L. The value of χ_M is then corrected for diamagnetic contributions.

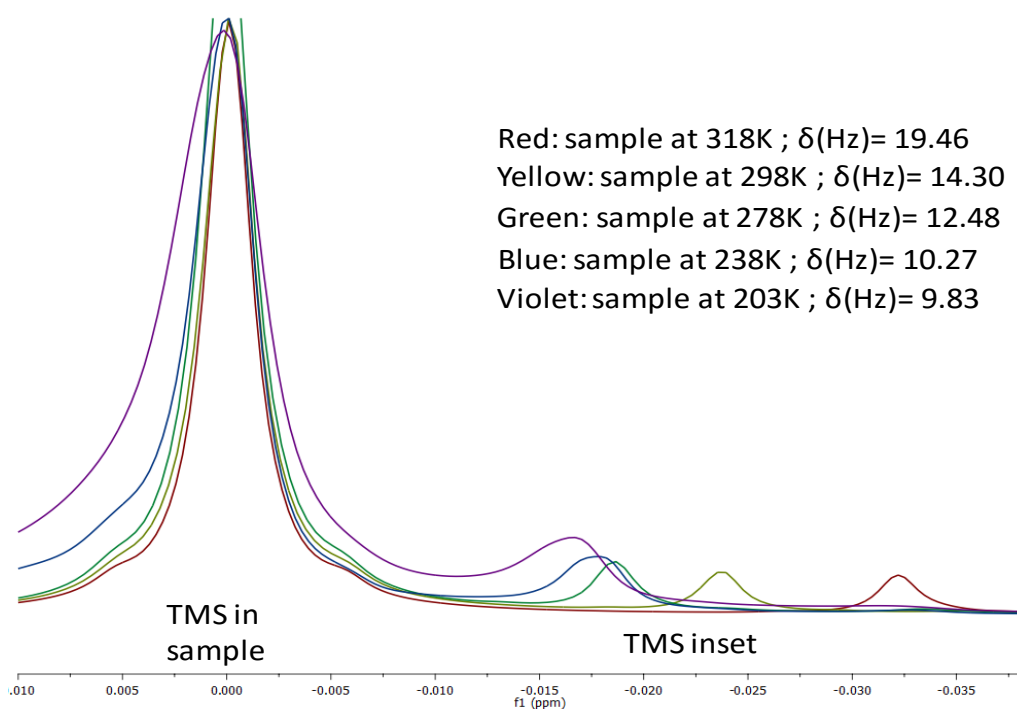


Figure 5.16: TMS displacements at different temperatures.

As Figure 5.16 shows, the introduction of the inset on the NMR tube, gives another signal corresponding to the TMS signal of the inset. The differences in chemical shifts are listed in Hz at different temperatures. When the sample is cooled, the difference in shifts corresponding to the TMS decreases, indicating that the iron centers are passing from a high spin to a low spin.

Applying Eq.1 for $C = 4.98 \times 10^{-4}$ mol/L the $\chi_M T$ values at different values after diamagnetic corrections are 5.65, 4.06, 3.09, 2.48, and 2.04 $\text{cm}^3 \text{mole}^{-1} \text{K}$ at 318, 298, 278, 238 and 203K respectively.

The orange solution was then irradiated with UV during 300s to perform the cyclization of the complex leading to a dark brown solution. The $^1\text{H-NMR}$ were performed again at various temperatures showing that the cyclization induces changes to the TMS shifts, consisting in a increase of the difference between the inset and the sample in all the cases (Figure 5.17). This suggests a higher paramagnetic character of the irradiated sample.

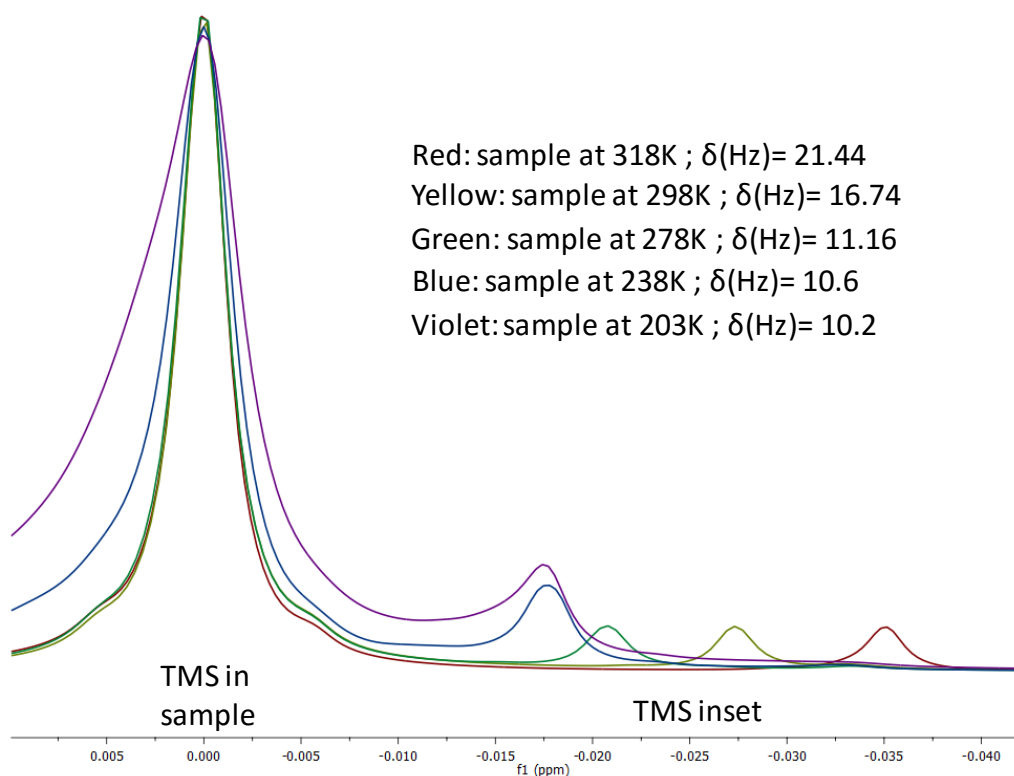


Figure 5.17: TMS displacements at different temperatures after irradiation with UV.

The corresponding of $\chi_M T$ are now 6.07, 4.65, 3.39, 2.54 and 2.1 $\text{cm}^3\text{mol}^{-1}\text{K}$ at 318, 298, 278, 238 and 203K respectively. Following these experiments, the sample was irradiated anew with visible light during 900s and the ^1H -NMRs were collected. Interestingly, similar values to the initial compound were obtained, accompanied with a return to the orange color, thus corroborating the reversibility of the process. In Table 5.3, the whole values of the shifts displacements with the corresponding susceptibility values are listed.

Helicate isomer (T/K)	Displacement (Hz)	$\chi_M T$
initial (318K)	19,46	5.65
initial (318K)+UV	21,44	6.07
initial (318K)+UV+Vis	19,69	5.70
initial (298K)	14,3	4.06
initial (298K)+UV	16,74	4.65
initial (298K)+UV+Vis	14,36	4.07
initial (278K)	11,6	3.09
initial (278K)+UV	12,48	3.39
initial (238K)	10,27	2.48
initial (238K)+UV	10,6	2.54
initial (238K)+UV+Vis	10,19	2.46
initial (203K)	9,83	2.04
initial (203K)+UV	10,2	2.10
initial (203K)+UV+Vis	9,9	2.06

Those results are consistent with the observations from the SQUID measurements and UV-Vis spectroscopy. However, the reversibility of the process was not observed in the solid state. The solution studies corroborate the robustness of the supramolecular assembly in solution, which was seen to persist for at least one month.

The rest of protons in the sample solution are also affected by the paramagnetic species, specially these belonging to the chelating pocket that are lying close to the metal centers. In Figures 5.18 and 5.19, there are comparisons of the complete spectrum at different temperatures. At high temperature (318K), the largest displacement reaches 29 ppm, while at low temperatures (203K), all the displacements are in the region expected for a diamagnetic species.

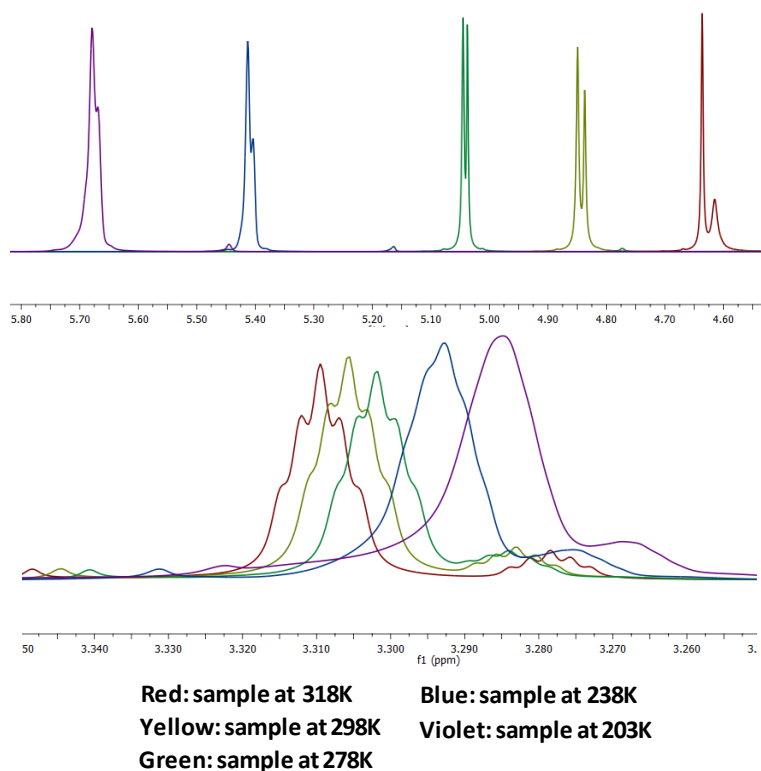


Figure 5.18: Displacement peaks of the solvent presented in the inset tube, water upper and methanol in the bottom depending on the temperature.

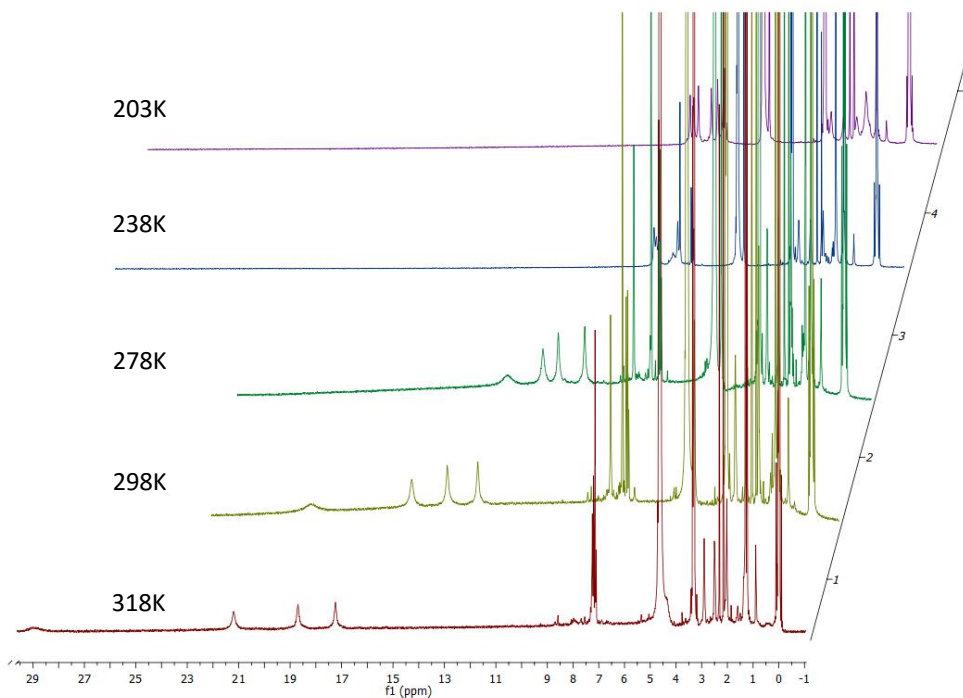


Figure 5.19: Displacement peaks depending on the temperature.

Comparing the solid state with the solution susceptibilities reveal a shift towards lower temperatures of the SCO in solution, with a more complete conversion to the LS state at low temperatures and surprisingly, a more abrupt transition (Figure 5.20). Interestingly, the influence of the photochromic process is more pronounced at high temperatures in solution. In the solid state, it seems to be more similar in the whole range of temperatures, although irreversible.

This behavior appears as a new example of the very rare phenomenon called anticooperativity. Recently, some reports have shown that certain forms of weak intermolecular interactions can cause anticooperative phenomena^{46,47}, which translates into incomplete SCO transitions in the solid state that are more gradual than predicted from the Boltzman equilibrium distribution. These effects are due to some form of intermolecular interactions, present in the crystal lattice but not in solution. Here, the weak intermolecular interactions cause some sort of barrier to the spin transition, which, contrary to the cases of cooperativity, are not propagated throughout the lattice, but have simply a local character. The consequence is thus, not an abrupt transition, but a more gradual one. The dissolution of the complex removes these effects, so the crystal field LS/HS energy difference is nearly the only contribution to the SCO phenomenon, thus yielding a conventional Boltzman-like HS to LS transition.

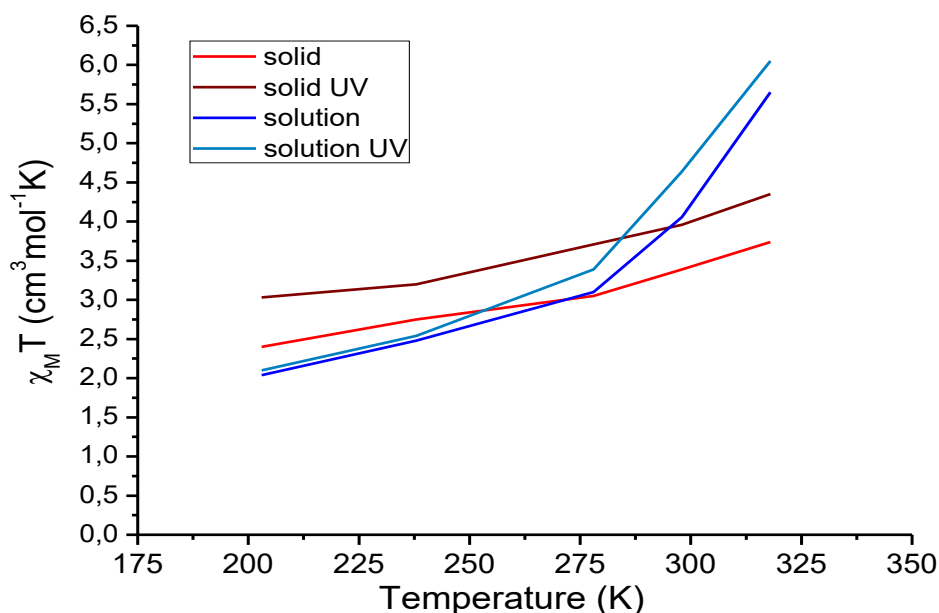


Figure 5.20: Comparative plot of the solid compound with the compound in solution, before and after irradiation with UV.

5.7 Conclusions

The strategy to obtain a spin crossover supramolecular assembly by ligand design has been successful with the preparation of a new coordination helicate $[\text{Fe}_2(\text{L9})_3](\text{ClO}_4)_4$ (**22**). The coordination pockets presented in ligand **H₂L9** are able to coordinate in an octahedral configuration two Fe(II) centers, that display spin crossover behavior as tested via different techniques.

To be emphasized are the techniques based on solution measurements, implemented thanks to the large stability of the helical coordination compound in methanol. This has allowed to prove the photochromic behavior of the assembly, shown to be an excellent switch with good fatigue resistance.

With regard to this switch ability, both isomers can be detected through their different characteristics, in the UV-Vis absorption and fluorescence spectra. The latter seems to be quenched when the closed isomer is presented, which gives a marker for the isomer present, in combination with the color change occurring upon cyclization.

The magnetic properties of the iron centers have been tested in the solid state and in solution, unveiling in both states a spin crossover behavior, more defined in solution due to the possible indication of an abrupt change in the paramagnetic behavior of the iron centers. This can be explained by the effects of the weak interactions that are involved in the anticooperativity phenomena in the solid state.

This work leaves the importance prospect of synthesizing new ligands, starting from the precursor **L9a**, whose ketone group can be functionalized with other pyrazol derivatives. It can also be part of other synthetic routes, such as the synthesis of new diketones, or the preparation of new hydrazone derivatives, which are commonly used for the synthesis of SCO compounds⁴⁸.

5.8 Experimental

5.8.1 Ligands and precursors

1,2-bis-(5-(2-acetyl-5-bromopyridin)-2-methylthien-3-yl) cyclopentene (**L9a**)

1 g (3 mmol) of **L0** was added in 20 mL of anhydrous THF under nitrogen in a round bottom flask and covered by aluminium foil. Subsequently, n-BuLi (2.5 ml of a 2.5M solution in hexanes, 6 mmol) was added and the slurry turns in a white-yellow precipitate. The mixture was stirred for 30 minutes and then 2.4 ml (8.9 mmol) of B(OBu)₃ were added. The slurry was kept under stirring during 1 h. Meanwhile, 1.05 g (5 mmol) of 2-acetyl-5-bromopyridine was dissolved in 20 mL of anhydrous THF under nitrogen flow. 0.196 g (0.2 mmol) of Pd(PPh₃)₄ were added to this solution and after 15 min of stirring 12.9 mL of Na₂CO₃ 2M and 6 droplets of ethylene glycol were added. The mixture was refluxed at 60°C for 3 h. Diethyl ether was added and a white-brown precipitate appears. It was filtered and washed with diethyl ether. The filtrate was washed with H₂O (5 x 20 mL), dried with Na₂SO₄, filtered and rotavaporated. The oil obtained was dissolved in diethyl ether, covered and left in the fridge till more precipitate was formed. The reaction yield was of 49% (0.78 g). ¹H-NMR (400 MHz, CDCl₃) δ (ppm): 8.79 (s, 2H, Ar), 8.01 (d, 2H, Ar), 7.83 (d, 2H, Ar), 7.18 (s, 2H, Tph), 2.87 (t, 4H, Cp), 2.71 (s, 6H, Me), 2.13 (m, 2H, Cp), 2.07 (s, 6H, Me). MS (ESI+) m/z: 499.15 [C₂₉H₂₆O₂N₂S₂+H]⁺. Single crystals of compound **L9a** were obtained by slow evaporation in THF (Figure 5.21). Crystallographic data for ligand **L9a** are listed in Table 5.4.

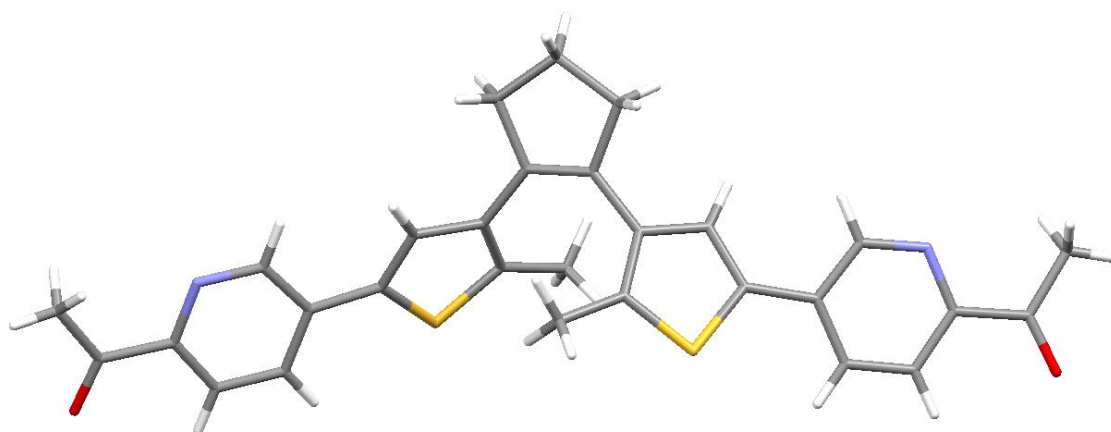


Figure 5.21: Crystal structure of **L9a**

Table 5.4. Crystallographic data for **L9a**

formula	C ₂₉ H ₂₆ N ₂ O ₂ S ₂
<i>M_r</i>	498.64
Crystal system	Monoclinic
space group	C 2/c
<i>a</i> [Å]	27.474(5)
<i>b</i> [Å]	11.855(2)
<i>c</i> [Å]	7.7211(16)
α [°]	90
β [°]	101.74(12)
γ [°]	90
<i>V</i> [Å ³]	2462.2(8)
<i>Z</i>	4
shape;colour	Blue block
<i>R_{int}</i>	0.0364
<i>R</i> ₁	0.0867
<i>wR</i> ₂	0.0909
<i>S</i>	1.060

1,2-bis-(5-(2-pyrazol)-pyridin-2-methylthien-3-yl) cyclopentene (H₂L9)

0.8 g of **L9a** (1.4 mmol) were added in 3 mL (22.6 mmol) of N,N-dimethylformamide dimethyl acetal and refluxed at 103 °C for 15 h. The reaction mixture was rotavaporated and a brown-red oil was obtained. 10 mL of EtOH were added and stirred a few minutes to dissolve the oil. 0.7 mL (14 mmol) of hydrazine monohydrate was added and the slurry was refluxed at 75 °C for 5 h. Water was added dropwise to the slurry until the precipitation of a powder is completed. The mixture was filtered. The reaction yield was almost quantitative (0.78 g). ¹H-NMR (400 MHz, Acetone) δ (ppm): 8.66 (s, 2H, Ar), 7.86 - 7.26 (m, 8H, Ar), 6.78 (s, 2H, Tph), 2.79 (t, 4H, Cp), 2.01(m, 2H, Cp), 1.93 (s, 6H, Me). MS (ESI+) *m/z*: 547.17 [C₃₁H₂₆N₆S₂+H]⁺.

5.8.2 Coordination complex

[Fe₂(L9)₃](ClO₄)₄ (22)

0.040 mmol of ligand **H₂L9** was dissolved in 10 mL of methanol and heated till complete dissolution. 0.026 mmol of Fe(ClO₄)₂ was dissolved in 10 mL of methanol with a spatula tip of ascorbic acid. The ligand solution was poured dropwise into metal ion solution. The mixture solution was stirred 1 hour and was finally filtered. The solution was divided into various fractions and placed in various tubes where toluene was introduced let the system diffuse. After complete diffusion, more toluene was added. After two weeks, red crystals of [Fe₂(L4)₃](ClO₄)₄ can be collected (mg 9.7, 37 yield %). IR (KBr pellet, cm⁻¹): 3396, 3134, 3013, 2913, 2839, 1621, 1600, 1565, 1513, 1473, 1391, 1252, 1091, 965, 921, 834, 782, 747, 617, 500. Anal. Found (calc% for C₉₃H₇₈Cl₄Fe₂N₁₈O₁₆S₆·1.2C₇H₈·5.25H₂O; **22**·1.2Toluene·5.25H₂O): C 51.62 (51.72), H 4.06 (4.2), N 10.55 (10.71).

5.9 References

1. Gütlich, P.; Hauser, A.; Spiering H. Thermal and Optical Switching of Iron (II) complexes. *Angew Chem Int Ed Engl.* 1994;33(20):2024-2054.
2. Gütlich P, Garcia Y, Goodwin H a. Spin crossover phenomena in Fe(II) complexes. *Chem Soc Rev.* 2000;29(6):419-427.
3. Bousseksou A, Varret F, Goiran M, Boukheddaden K, Tuchagues JP. Spin Crossover in Transition Metal Compounds III. In: Vol Berlin, Heidelberg: Springer Berlin Heidelberg; 2004:65-84.
4. Carbonera C, Sanchez CJ, Money VA, et al. Photomagnetic properties of iron(II) spin crossover complexes of 2,6-dipyrazolylpyridine and 2,6-dipyrazolylpyrazine ligands. *Dalt Trans.* 2006;(25):3058-3066.
5. Shih C-H, Sheu C-F, Kato K, et al. The photo-induced commensurate modulated structure in site-selective spin crossover complex trans-[Fe(abpt)₂(NCS)₂]. *Dalton Trans.* 2010;39:9794-9800.
6. Létard JF, Asthana S, Shepherd HJ, et al. Photomagnetism of a sym-cis-dithiocyanato iron(II) complex with a tetradentate N,N'-bis(2-pyridylmethyl)1,2-ethanediamine ligand. *Chem - A Eur J.* 2012;18(19):5924-5934.
7. Costa JS, Rodríguez-Jiménez S, Craig GA, et al. Three-way crystal-to-crystal reversible transformation and controlled spin switching by a nonporous molecular material. *J Am Chem Soc.* 2014;136(10):3869-3874.
8. Bao X, Shepherd HJ, Salmon L, Molnár G, Tong ML, Bousseksou A. The effect of an active guest on the spin crossover phenomenon. *Angew Chemie - Int Ed.* 2013;52(4).
9. Bartual-Murgui C, Salmon L, Akou A, et al. Synergetic effect of host-guest chemistry and spin crossover in 3D hofmann-like metal-organic frameworks [Fe(bpac)M(CN)₄] (M=Pt, Pd, Ni). *Chem - A Eur J.* 2012;18(2):507-516.
10. Shepherd HJ, Rosa P, Vendier L, et al. High-pressure spin-crossover in a dinuclear Fe(ii) complex. *Phys Chem Chem Phys.* 2012;14(15):5265.
11. J.Ribas. *Coordination Chemistry, Wiley VCH.*; 2008.
12. Pandurangan K, Gildea B, Murray C, Harding CJ, Müller-Bunz H, Morgan GG. Lattice effects on the spin-crossover profile of a mononuclear manganese(III) cation. *Chem - A Eur J.* 2012;18(7):2021-2029.
13. Harding DJ, Harding P, Phonsri W. Spin Crossover in Iron(III) Complexes. *Coord Chem Rev.* 2016;313(January):38-61.
14. Phonsri W, Martinez V, Davies CG, Jameson GNL, Moubaraki B, Murray KS. Ligand effects in a heteroleptic bis-tridentate iron(iii) spin crossover complex showing a very high T_{1/2} value. *Chem Commun.* 2016;52:1443-1446.

15. Zhang X, Wang Z-X, Xie H, Li M-X, Woods TJ, Dunbar KR. A cobalt(II) spin-crossover compound with partially charged TCNQ radicals and an anomalous conducting behavior. *Chem Sci*. 2015;7:1569-1574.
16. Martinho PN, Gildea B, Harris MM, et al. Cooperative spin transition in a mononuclear manganese(III) complex. *Angew Chemie - Int Ed*. 2012;51(50):12597-12601.
17. Bhar K, Khan S, Costa JS, et al. Crystallographic evidence for reversible symmetry breaking in a spin-crossover d 7 cobalt(II) coordination polymer. *Angew Chemie - Int Ed*. 2012;51(9):2142-2145.
18. Griffin M, Shakespeare S, Shepherd HJ, et al. A symmetry-breaking spin-state transition in iron(III). *Angew Chemie - Int Ed*. 2011;50(4):896-900.
19. Jones LF, Kilner CA, Halcrow MA. A Trinuclear Iron(III) Compound with an Unusual T-Shaped $[\text{Fe}_3(\mu_3\text{-O})]^{7+}$ Core. *J Clust Sci*. 2010;21(3):279-290.
20. Tang J, Costa JS, Smulders S, et al. Two-step spin-transition iron(III) compound with a wide [high spin-low spin] plateau. *Inorg Chem*. 2009;48(5):2128-2135.
21. Murray KS. Advances in polynuclear iron(II), iron(III) and cobalt(II) spin-crossover compounds. *Eur J Inorg Chem*. 2008;(20):3101-3121.
22. Hauser A. Ligand Field Theoretical Considerations. *Top Curr Chem*. 2004;51:49-58.
23. Halcrow MA. Iron(II) complexes of 2,6-di(pyrazol-1-yl)pyridines-A versatile system for spin-crossover research. *Coord Chem Rev*. 2009;253(21-22).
24. Malcolm A. Halcrow. *Spin-Crossover Materials: Properties and Applications.*; 2013.
25. Lucas LN, Jong JJ, Esch JH, Kellogg RM, Feringa BL. Syntheses of Dithienylcyclopentene Optical Molecular Switches. *Eur J Org Chem*. 2003;2003:155-166.
26. Abarca B, Ballesteros R, Ballesteros-Garrido R, Colobert F, Leroux FR. Triazolopyridines. Part 26: The preparation of novel [1,2,3]triazolo[1,5-a]pyridine sulfoxides. *Tetrahedron*. 2008;64(17):3794-3801.
27. Huo J, Arulsamy N, Hoberg JO. Facile synthesis and platinum complexes of 4',5,5''-trisubstituted-2,2':6',2''-terpyridines. *Dalt Trans*. 2011;40(29):7534-7540.
28. Salinas-Uber J, Vogels Y, Van Den Helder D, et al. Pyrazole-based ligands for the [copper-TEMPO]-mediated oxidation of benzyl alcohol to benzaldehyde and structures of the Cu coordination compounds. *Eur J Inorg Chem*. 2007;(26):4197-4206.
29. Jong JJD de, Jong JJD de, Lucas LN, et al. Photochromic Properties of Perhydro- and Perfluorodithienylcyclopentene Molecular Switches. *European J Org Chem*. 2003.

30. McCusker JK, Rheingold AL, Hendrickson DN. Variable-Temperature Studies of Laser-Initiated 5T2 → 1A1 Intersystem Crossing in Spin-Crossover Complexes: Empirical Correlations between Activation Parameters and Ligand Structure in a Series of Polypyridyl Ferrous Complexes. *Inorg Chem.* 1996;35(7):2100-2112.
31. Michael G. B. Drew, Charles J. Harding, Vickie McKee GGM and JN. Geometric control of manganese redox state. *J Chem Soc, Chem Commun.* 1995:1035-1038.
32. Marchivie M, Guionneau P, Létard JF, Chasseau D. Towards direct correlations between spin-crossover and structural features in iron(II) complexes. *Acta Crystallogr Sect B Struct Sci.* 2003;59(4):479-486.
33. Wei P, Yuan D, Zhu W, Zhang X, Hu B. Bis{tris[3-(2-pyridyl)-1 H - pyrazole]iron(II)} tetradecamolybdo(V,VI)silicate. *Acta Crystallogr Sect E Struct Reports Online.* 2010;66(2):m190-m191.
34. Yoneda K, Adachi K, Nishio K, et al. An [Fe^{II}₃O]⁴⁺ core wrapped by two [Fe^{II}L₃]⁻ units. *Angew Chemie - Int Ed.* 2006;45(1):5459-5461.
35. Shiga T, Noguchi M, Sato H, Matsumoto T, Newton GN, Oshio H. Triple-stranded ferric helices: a π-π interaction-driven structural hierarchy of Fe₅, Fe₇, and Fe₁₇ clusters. *Dalton Trans.* 2013;42(45):16185-16193.
36. Hao L, Liu T, Chen J, Zhang X. Bis{tris-[3-(2-pyrid-yl)-1H-pyrazole]iron(II)} dodecamolybdo(V,VI)phosphate hexahydrate. *Acta Crystallogr Sect E Struct Reports Online.* 2010;66(3).
37. Shiga T, Oshiro E, Nakayama N, et al. Dimerized spin-crossover iron(II) complexes as supramolecular anion capsules. *Eur J Inorg Chem.* 2013;(5-6):781-787. doi:10.1002/ejic.201201365.
38. Nihei M, Suzuki Y, Kimura N, Kera Y, Oshio H. Bidirectional photomagnetic conversions in a spin-crossover complex with a diarylethene moiety. *Chem - A Eur J.* 2013;19(22):6946-6949.
39. Milek M, Heinemann FW, Khusniyarov MM. Spin crossover meets diarylethenes: Efficient photoswitching of magnetic properties in solution at room temperature. *Inorg Chem.* 2013;52(19):11585-11592.
40. Garcia Y, Robert F, Naik AD, et al. Spin transition charted in a fluorophore-tagged thermochromic dinuclear iron(II) complex. *J Am Chem Soc.* 2011;133(40):15850-15853.
41. Shepherd HJ, Gural'skiy IA, Quintero CM, et al. Molecular actuators driven by cooperative spin-state switching. *Nat Commun.* 2013;4:2607.
42. Wang CF, Li RF, Chen XY, Wei RJ, Zheng LS, Tao J. Synergetic spin crossover and fluorescence in one-dimensional hybrid complexes. *Angew Chemie - Int Ed.* 2015;54(5):1574-1577.
43. Wen M, Mori K, Kamegawa T, Yamashita H. Amine-functionalized MIL-101(Cr) with imbedded platinum nanoparticles as a durable photocatalyst for hydrogen production from water. *Chem Commun (Camb).* 2014;50(79).

44. Yatsunyk LA, Walker FA. Structural , NMR , and EPR Studies of S (1 / 2) and S (3/2)Fe (III) Bis (4-Cyanopyridine) Complexes of Dodecasubstituted Porphyrins. *Inorg. Chem.* 2004 (43): 757-777.
45. Grant DH. Paramagnetic Susceptibility by NMR: The “Solvent Correction” Reexamined. *J Chem Educ.* 1995;72(1):39.
46. Scott HS, Ross TM, Chilton NF, et al. MOF111-Crown-linked dipyridylamino-triazine ligands and their spin-crossover iron(II) derivatives: magnetism, photomagnetism and cooperativity. *Dalt Trans.* 2013;42(47):16494.
47. Novikov V V., Ananyev I V., Pavlov AA, Fedin M V., Lyssenko KA, Voloshin YZ. Spin-crossover anticooperativity induced by weak intermolecular interactions. *J Phys Chem Lett.* 2014;5(3):496-500.
48. Zhang L, Xu G-C, Xu H-B, et al. Abrupt spin transition around room temperature and light induced properties in Fe(II) complexes with N4O2 coordination sphere. *Chem Commun (Camb).* 2010;46(15):2554-2556.

CHAPTER 6: CONCLUSIONS

6.1 Concluding remarks	230
------------------------------	-----

6.1 Concluding remarks

One of the main objectives of this thesis was the synthesis of new chelating ligands containing a photochromic unit able to change its conformation upon light irradiation. This isomerization should serve to modify the magnetic behavior of the new coordination compounds, formed upon reaction of transition metals or lanthanides, assembled within the photochromic ligands. With these aims, the synthesis of 5 new ligands has been achieved, which have been characterized successfully. Subsequently, the preparation of 22 coordination compounds with these ligands has been accomplished. The crystallographic study of these coordination compounds has been very important for the complete understanding of the magnetic and photochromic properties.

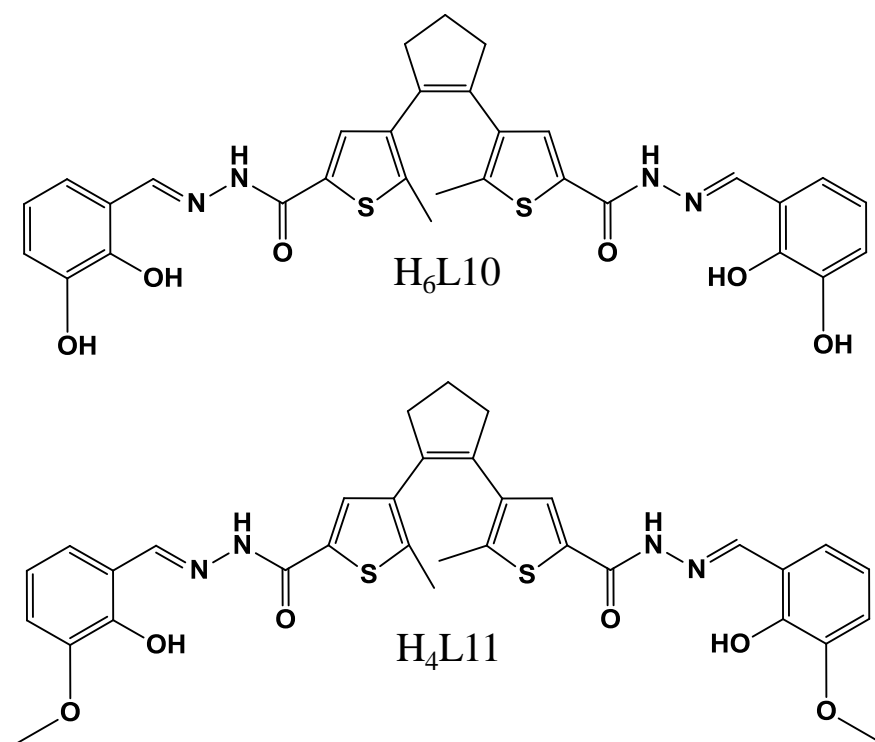
Regarding the crystal structures, in Chapter 2, the distinct photochromic properties of the complexes discussed was rationalized in light of the structural information. Thus, different behavior in photoconversion of two polymeric isomers, only differing in the packing through crystal lattice and the solvents present in the crystal was interpreted in terms of the structure. The solvents are important for the complete assembly of the crystal because they are in fact responsible of some of the weak intermolecular interactions within the crystal. These interactions, such as hydrogen bonds or p-p stacking, could influence the rearrangement of the matrix, hindering the photochromic activity, like in the case of the polymer containing water in its lattice described in that chapter. These results show that crystal design may constitute an interesting way for modulating the properties of the solid state photoactivity. All the discrete complexes presented in Chapter 1 exhibit an unsuitable configuration for the isomerization of the photochromic unit **H₂L1**. Nevertheless, the photochromic properties in solution were tested satisfactory thanks to the freedom degrees of the photochromic unit in that state. During the preparation of this thesis, part of this chapter has been published¹.

Although ligand **H₂L1** is not new, it has been the starting material for new ones. Two of them have been presented in Chapter 3, based on beta diketone moieties, **H₄L2** and **H₄L3**, which additionally, are functionalized with a phenol group. Those groups together form an excellent chelating pocket to introduce metal arrays. Importantly, those arrays can be formed as pair of heterometallic dimers, whose ground state exhibit in some cases $S=1/2$ systems, thus providing a pair of spins $1/2$ well defined within the

molecule. This feature can be exploited in the context of quantum computing by studying the quantum coherence of these spin. Indeed, coherence times of thousands of nanosecond can be measured at low temperature. With those numbers, the qubit figure of merit Q , remains however quite small. Modifications of the surroundings, such as the use of a complete or partially deuterated ligand, or the synthesis of one ligand similar with elements with negligible nuclear spin, shall increase the relaxation time. In addition, a more detailed study should be carried out on the photochromic activity in order to elucidate the species that are involved in the isomerization processes, in light of the differences seen in the reversibility of the mechanism. Other future studies shall deal with the possible modification of the exchange coupling within the dimer upon photocyclization. Indeed, the possibility of controlling the magnetic behavior with the photochromic moiety is still a challenge that can be studied using advanced techniques such as micro-squid devices and electron nuclear double resonance (ENDOR) measurements. The latter is specially useful to detect difference between the spins within the molecule, before and after the cyclization.

Two other new ligands, made from **H₂L1**, have been presented in Chapter 4. These have been synthesized via Schiff base condensation (**H₄L7** and **H₂L8**). Similar two the beta diketones, these ligands are able to perform fast and excellent photochromism, in addition to the cis/trans isomerizations that can undergo themselves. While those isomerizations have not been studied, they could be used as gate-reactivity, adding more versatility to these compounds. The chelating pockets of these ligands are very useful regarding to the coordination ability with lanthanides and transition metals. The necessary deprotonation of the ligand involves the use of bases, which here may be responsible for the unfavorable conformation of the photochromic ligand, leading to the parallel conformation and thus impeding the cyclization. Furthermore, single molecule magnet behavior has been observed in a dysprosium cluster. Therefore, obtaining a procedure to prevent the parallel position would be also useful for the modification of the SMM behavior. Furthermore, theoretical studies, would be useful for predicting of the photochromic properties of coordination compounds, in order to explain the low photo-activity of the copper compounds with the correct configuration of the ligand. Indeed, recent theoretical studies have shown the ability to predict the behavior, because these reactions proceed through excited states that involve orbitals from ligands and metals, and as a result the energy could be dissipated preventing the photocyclizations².

Towards the end of this thesis work, two new ligands have been synthesized, **H₆L10** and **H₄L11**, containing additional OH or methoxy groups, in the meta position of the outer aromating rings, using the same procedure described for the synthesis of **H₄L7** and **H₂L8**. These have been characterized by Mass Spectroscopy and ¹H-RMN. These two new ligands open the possibility to introduce additional metals centers or combinations of transition metals with lanthanides (Scheme 6.1). In addition, the antiparallel configuration of the photochromic unit can be obtained due to the new possible steric effects.



Scheme 6.1: Schematic representation of H₆L10 and H₄L11

Finally, in Chapter 5, the synthesis of a new photochromic ligand containing a pyridine-pyrazole moiety, **H₂L9**, has been tested for the preparation of a Fe(II) spin crossover helical system. Due to solvent loss from the structure of the helicate, the magnetic behavior and its photoactivity has been tested in solution. This has shown to be a good candidate as part of new hybrid devices, because of the excellent resistance to fatigue, the different fluorescent behavior and the SCO features. The versatility of the precursor of **H₂L9**, would lead to new photochromic ligands, not only for the SCO field, but also for the preparation of other types of molecular devices.

The work described along this thesis demonstrates the utility of chemistry design for preparing coordination compounds with the proper metal in order to obtain specific characteristics. All ligands presented in this thesis are symmetrical, however the synthesis of asymmetric ligands would be also very interesting. They would allow the combination of different magnetic behaviors within the same molecule, with important consequences, like the construction of well defined pairs of dissimilar qubits in one molecule. Indeed, the possibility to discriminate between them individually is a requisite for the fabrication of quantum logic gates for quantum information processing. The possibility to perform the photochromic behavior in the solid state is, indeed, an attractive challenge, requiring the study of the magnetic behavior in surfaces. As shown in Chapter 1, the possibility to change the backbone of the building block, opens a door to the preparation of a wide number of new chelating ligands, allowing the synthesis of a variety of coordination systems. Despite the fact this thesis is entirely related to the magnetic properties, other interesting fields, such as bioinorganic chemistry, electron transport or metal organic frameworks, are areas in which photochromic ligands could make the object of interesting studies. Indeed, studies related to the interaction of compounds **2**, **4** and **20** with DNA are now in course, in addition with the compound from a previously described photochromic ligand.

1. Jorge Salinas Uber, Marta Estrader, Corine Mathonière, Rodolphe Clérac, Olivier Roubeau and Guillem Aromí. Photochromic Performance of Two Cu(II)-One-Dimensional Solvatomorphs Controlled by Intermolecular Interactions. *Cryst. Growth Des.* (2016). doi:10.1021/acs.cgd.6b00556
2. Presa, A. *et al.* Non-Switching 1,2-Dithienylethene-based Diplatinum(II) Complex Showing High Cytotoxicity. *Inorg. Chem* (2016). doi:10.1021/acs.inorgchem.6b00362

APPENDIX I: UV-Vis spectra for 6, 7, 9, 10, 11 and 13

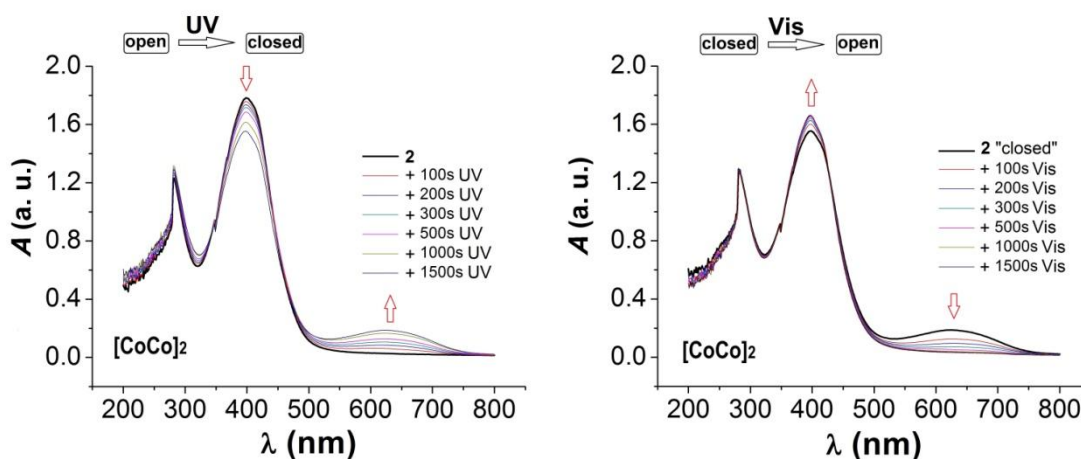


Figure A(I.1. Left: Electronic absorption spectrum of $[\text{Co}_4\text{L}_2(\text{py})_6]$ (**6**) –bold black line– in 5×10^{-5} M toluene/DMSO (1:1) solution and its evolution during irradiation with UV light ($\lambda < 425$ nm) over the course of 25 min. Bottom: Electronic absorption spectrum of the above photo-converted product –bold line– and its evolution upon irradiation with visible light ($\lambda > 430$ nm) during the course of 25 min.

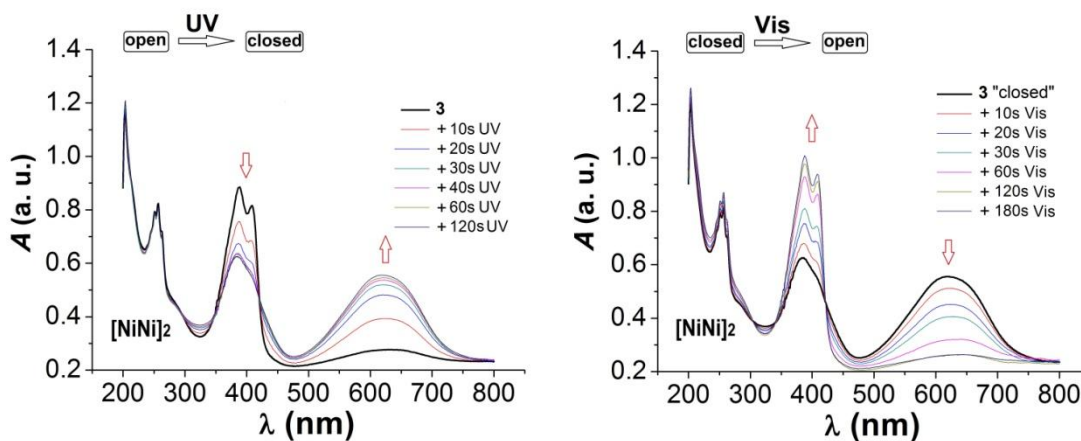


Figure A(I.2. Left: Electronic absorption spectrum of $[\text{Ni}_4\text{L}_2(\text{py})_6]$ (**7**) –bold black line– in 5×10^{-5} M toluene/DMSO (1:1) solution and its evolution during irradiation with UV light ($\lambda < 425$ nm) over the course of 2 min. Bottom: Electronic absorption spectrum of the above photo-converted product –bold line– and its evolution upon irradiation with visible light ($\lambda > 430$ nm) during the course of 3 min.

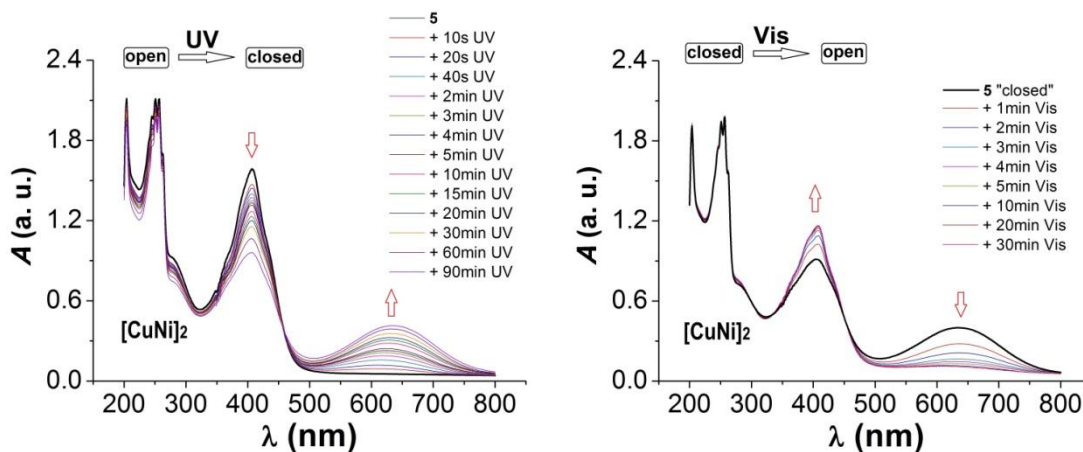


Figure A(I.3) Left: Electronic absorption spectrum of $[\text{Cu}_2\text{Ni}_2\text{L}_2(\text{py})_6]$ (**9**) –bold black line– in 5×10^{-5} M toluene/DMSO (1:1) solution and its evolution during irradiation with UV light ($\lambda < 425$ nm) over the course of 90 min. Bottom: Electronic absorption spectrum of the above photo-converted product –bold line– and its evolution upon irradiation with visible light ($\lambda > 430$ nm) during the course of 30 min.

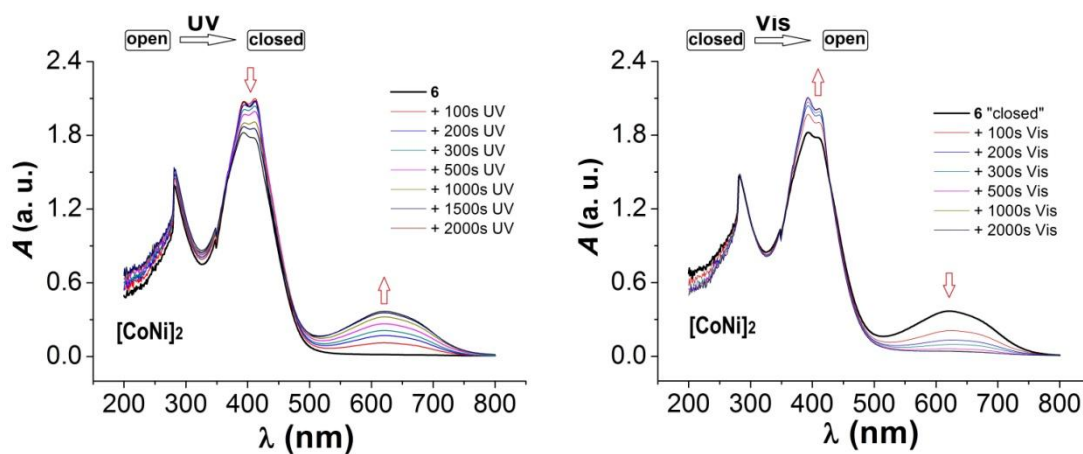


Figure A(I.4). Left: Electronic absorption spectrum of $[\text{Co}_2\text{Ni}_2\text{L}_2(\text{py})_6]$ (**10**) –bold black line– in 5×10^{-5} M toluene/DMSO (1:1) solution and its evolution during irradiation with UV light ($\lambda < 425$ nm) over the course of 33 min. Bottom: Electronic absorption spectrum of the above photo-converted product –bold line– and its evolution upon irradiation with visible light ($\lambda > 430$ nm) during the course of 33 min.

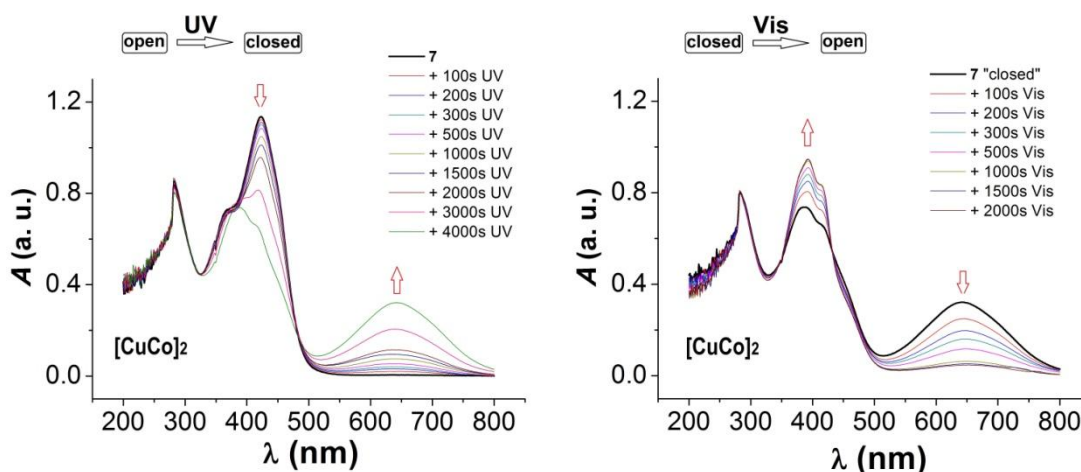


Figure A(I).5. Left: Electronic absorption spectrum of $[\text{Cu}_2\text{Co}_2\text{L}_2(\text{py})_6]$ (**11**) –bold black line– in 5×10^{-5} M toluene/DMSO (1:1) solution and its evolution during irradiation with UV light ($\lambda < 425$ nm) over the course of 66 min. Bottom: Electronic absorption spectrum of the above photo-converted product –bold line– and its evolution upon irradiation with visible light ($\lambda > 430$ nm) during the course of 33 min.

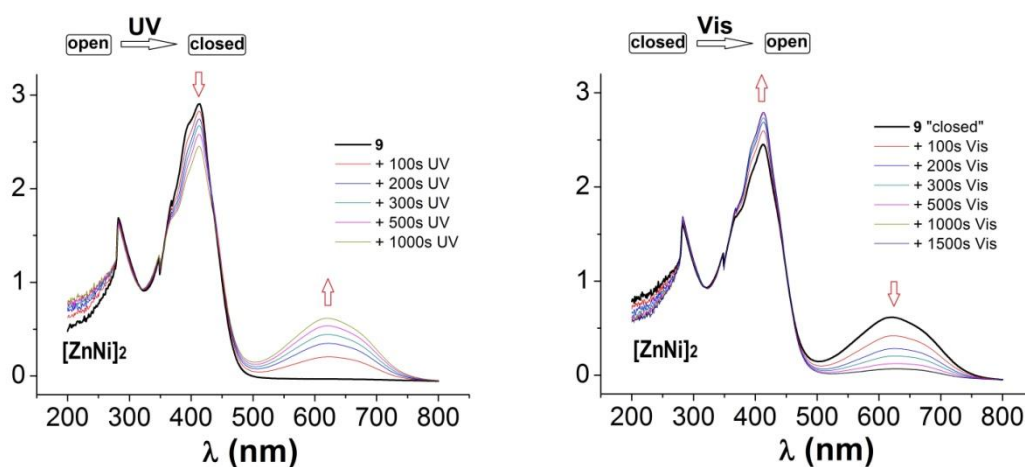


Figure A(I).6. Left: Electronic absorption spectrum of $[\text{Zn}_2\text{Ni}_2\text{L}_2(\text{py})_6]$ (**13**) –bold black line– in 5×10^{-5} M toluene/DMSO (1:1) solution and its evolution during irradiation with UV light ($\lambda < 425$ nm) over the course of 17 min. Bottom: Electronic absorption spectrum of the above photo-converted product –bold line– and its evolution upon irradiation with visible light ($\lambda > 430$ nm) during the course of 25 min.

APPENDIX II: Physical techniques

Infrared Spectroscopy

IR spectra for all compounds were recorded on KBr pellets, in the range 4000-400 cm⁻¹, with a Thermo Nicolet Avatar 330 FT-IR spectrometer.

Elemental Analysis

Elemental analyses (C, H, N) of compounds were performed with a Perkin-Elmer Series II CHNS/O Analyser 2400 at the Servei de Microanàlisi of the CSIC, Barcelona.

Metal analysis

Metal analyses were performed by inductively coupled plasma (ICP) spectrometry using a iCap6500 spectrometre at the Mikroanalytisches Labor Pascher.

¹H-NMR

H-NMR spectra were recorded with a Varian Mercury 400 MHz or Varian Inova MHz instrument at the Unitat de RMN at the Universidad de Barcelona. Chemical shifts are reported in δ (parts per million) relative to an internal standard of tetramethylsilane.

Mass Spectrometry

Positive/negative ion ESI mass spectrometry experiments were performed using a LC/MSD-TOF (Agilent Technologies) with a dual source equipped with a lock spray for internal reference introduction at the Unitat d'Espectroscopia de Masses of the Universidad de Barcelona.

UV-Vis spectrometry

Electronic absorption spectra were recorded with a cubet of 1cm light-pass using a Varian Cary 100 UV/Vis spectrophotometer with 1nm resolutions.

Fluorescence spectrometry

Fluorescence emission spectra were carried using a Horiba Jobin-Yvon SPEX Nanolog-TM and Cary spectrofluorimeters.

Magnetic measurements

Magnetic measurements were performed using a Quantum Design MPMS-XL SQUID magnetometer at the Unitat de Mesures Magnetiques of the Universitat de Barcelona or at the SAI Physical Measurements of the Universidad de Zaragoza using a similar apparatus.

Pulsed EPR experiments

CW X-Band EPR spectra were recorded on a Bruker EMX spectrometer ($\nu = 9.47$ GHz). Pulsed EPR measurements were performed with a home-built pulsed Q-band spectrometer ($\nu=35$ GHz). Temperatures between 7 and 275 K were obtained with an Oxford Instruments CF935 continuous flow helium cryostat. Typical pulse lengths were 20 ns ($\pi/2$) and 40 ns (π). For ESE-detected EPR spectra, the Hahn Echo pulse sequence ($\pi/2-\tau-\pi-\tau$ -echo) with fixed delay times of $\tau = 200$ ns at 7 K, was applied under sweeping the magnetic field. Phase memory times were measured also with Hahn echo sequence, here at a fixed magnetic field under variation of the delay time τ . For measuring spin lattice-relaxation times, the inversion recovery sequence ($\pi-T-\pi/2-\tau_{\text{fix}}-\pi-\tau_{\text{fix}}$ -echo) with $\tau_{\text{fix}} = 200$ ns and phase cycling was applied.

X-Ray Diffraction

X-ray data were collected with Bruker APEXII QUAZAR diffractometer with $\text{MoK}\alpha$ radiation ($\lambda = 0.7103$ Å) and equipped with a microfocus multilayer monochromator and with a Bruker APEXII CCD diffractometer on the Advanced Light Source beamline 11.3.1 at Lawrence Berkeley National Laboratory from a silicon 111 monochromator ($\lambda = 0.7749$ Å). Data reduction and absorption corrections were performed with SAINT¹ and SADABS¹. The structure was solved with and refined on F2 with the SHELXTL suite^{2,3} or OLEX2 suite⁴.

Raman Spectrometry

Raman spectra of microcrystalline samples were obtained using a Jobin-Yvon LabRam HR 800 spectrometer with a CCD camera cooled at -70 °C and an optical microscope Olympus BXFM. The Raman spectras were acquired with an excitation wavelength of 785 nm. The current employed was 185 mA with the minimum power available (10 % of the total) to prevent sample damaging.

Reflectivity

Surface reflectivity measurements were performed on a home-built system at different temperatures ranging from 10 to 300 K. This setup collects the light reflected by the sample (sum of direct and diffuse reflected light) that is analyzed by a high-sensitivity Hamamatsu 10083CA spectrometer. The spectra are compared to a white reference obtained with a NIST traceable standard for reflectance (SphereOptics, ref SG3054). The background, collected with the light source switched off, is subtracted from all

measurements. Different light emitting diodes (LEDs) operating between 385 and 1050 nm and bought from Thorlabs were used for excitation measurements.

1. Bruker AXS Inc., Madison, Wisconsin, USA.
2. Sheldrick, G. M. A short history of SHELX. *Acta Crystallogr. Sect. A* **64**, 112–122 (2008).
3. Sheldrick, G. M. SHELXTL.
4. Dolomanov, O. V., Bourhis, L. J., Gildea, R. J., Howard, J. a K. & Puschmann, H. OLEX2: A complete structure solution, refinement and analysis program. *J. Appl. Cryst.* **42**, 339–341 (2009).

APPENDIX III : List of Publications

- Jorge Salinas-Uber, Marta Estrader, Corine Mathonière, Rodolphe Clérac, Olivier Roubeau, and Guillem Aromí. Photochromic Performance of Two Cu(II)-One-Dimensional Solvatomorphs Controlled by Intermolecular Interactions. **Crystal Grown and Design** (2016). doi:10.1021/acs.cgd.6b00556
- Jordi Grau, Rosa F. Brissos, Jorge Salinas-Uber, Ana B. Caballero, Amparo Caubet, Olivier Roubeau, Luís Korrodi-Gregório, Ricardo Pérez-Tomás and Patrick Gamez. The effect of potential supramolecular-bond promoters on the DNA-interacting abilities of copper–terpyridine compounds. *Dalton Trans.*, 2015, 44
- Leoní A. Barrios, Jorge Salinas-Uber, Olivier Roubeau, S. J. Teat and Guillem Aromí. Molecular self-recognition: a chiral [Mn(II)₆] wheel via donor–acceptor pi-pi contacts and H-bonds. *Chem. Commun.*, 2015, 51
- Achareeya Cheansirisomboon, Jorge Salinas-Uber, Chiara Massera, Olivier Roubeau, Sujittra Youngme, and Patrick Gamez. One-Pot Multiple Metal–Organic Framework Formation: Concomitant Generation of Structural Isomers or of Drastically Distinct Materials *Eur. J. Inorg. Chem.* 2014.
- Jorge Salinas-Uber, Leoní A. Barrios, Olivier Roubeau and Guillem Aromí. A novel bis-b-diketonate ligand stabilizes a [Co(II)₈] cage that encapsulates a (μ-O)-H-(μ-O) moiety. *Polyhedron* 54, 2013.
- Leoní A. Barrios, Ivana Borilovic, Jorge Salinas-Uber, David Aguilà, Olivier Roubeau and Guillem Aromí. A new type of paddle-wheel coordination complex. [*Dalton Trans.*, 2013, 42].
- E. Carolina Sañudo, Jorge Salinas-Uber, Alba Pons Balagué, Olivier Roubeau and Guillem Aromí. Molecular [(Fe₃)–(Fe₃)] and [(Fe₄)–(Fe₄)] Coordination Cluster Pairs as Single or Composite Arrays. *Inorg. Chem.* 2012, 51, 8441–8446.
- Leoní A. Barrios, Guillem Aromí, Joan Ribas, Jorge Salinas-Uber, Olivier Roubeau, Ken Sakai, Shigeyuki Masaoka, Patrick Gamez, and Jan Reedijk. A Mixed-Valence [Mn(II)Mn(III)Mn(II)] Complex of a Linear Phenol-bis(pyrazole) Ligand with an S = 3 Spin Ground State. *European Journal of Inorganic Chemistry*, 2008, Issue 24 .

- Jorge Salinas-Uber, Yorick Vogels, Dave van den Helder, Ilpo Mutikainen, Urho Turpeinen, Wen Tian Fu, Olivier Roubeau, Patrick Gamez, and Jan Reedijk. Pyrazole-Based Ligands for the [Copper-TEMPO]-Mediated Oxidation of Benzyl Alcohol to Benzaldehyde and structures of the Cu coordination compounds. *European Journal of Inorganic Chemistry*, 2007; (26).

- Jorge Salinas-Uber, Ilpo Mutikainen, Urho Turpeinen, Patrick Gamez and Jan Reedijk. Formation of a silver (I) coordination compound whose crystal lattice is composed of three different types of 1D chains. *Inorganic chemistry communications*, 2007. Volume 10, Issue 12.

AGRADECIMIENTOS

Como muchos de los caminos en esta vida, no todo lo hacemos solos. Por lo tanto, no puedo acabar este trabajo sin agradecer el apoyo de toda la gente que me ha acompañado en esta bonita experiencia de 5 años.

Mis primeras palabras van para Guillem, a quien le agradezco la gran oportunidad que me brindó, junto a su confianza. Aun recuerdo el día que me ofreció este puesto, yo en casa, con mi cara de bobo, sin entender que había pasado. Acababa de pasar un tren de una única oportunidad y me había subido en él, sin saber lo que me esperaba, y me he encontrado con que ahora ya no tengo al Guillem que me llamo telefónicamente siendo jefe, sino que tengo a un Guillem al que considero un gran amigo. Por todo lo relacionado a lo no estrictamente profesional, también te doy las gracias. Para bien o para “bien”, Guillem esta acompañado de una de las mejores personas que conozco, Leo, a la que también agradezco todo su apoyo en esta etapa, por su alegría y compañía, pero sobre todo, por hacernos sentir a mi y a mis niñas, tan queridos. De química no se si hemos hablado, pero de cervecitas y guarapitas... ¡Os espero cada verano!

Existe también una persona en este camino, que puede parecer secundaria, pero para aquellos que me conozcan, saben que no es así. Patrick ha sido el causante de que me subiera a este tren, y le quiero agradecer toda su confianza hacia este Erasmus que se va a convertir en Doctor. Ya sabes, “see you on Monday”.

Agradecer de corazón a todos mis compañeros de despacho. A Jose, junto a Irene y la pequeña Sofía: ya en Leiden nos premiasteis con vuestra amistad y me alegro de que continuase del mismo modo aquí en Barcelona. A Gavin y MJ (MXoXo para los íntimos): os quiero con locura, no se que como ni cuando paso, pero ya sois imprescindibles in my life, os deseo lo mejor y siempre tendréis casita de Ador para lo que queráis. A Ivana: empezamos juntos en la séptima, y casi acabaremos juntos. Vas a ser una triunfadora, no lo dudo. Nadie vive la química como tú lo haces. Espero que la próxima vez que coincidamos, sonrias como cuando llegaste a Barcelona. Para Marta y su familia: gracias por esos momentos en el laboratorio y en el despacho. Tengo el “un porquet” como marca registrada de Marta Estrader. Un consejo: nunca juntes melón con hidratos de carbono, y el agua al comer, ni mirarla. Agradecer también a Carlos su amistad y compañía. Ahora que vuleves para la “terreta”, espero que nos podamos ver

más, ya que parece que nada cambió desde aquel primer día de carrera que nos perdimos buscando el aula de la primera hora. Espero que seas muy feliz en tu nueva etapa con Jimena y la pequeña Lucia.

Agradecer especialmente a la gente del GMMF. A David que me ha ofrecido su amistad y ayuda en todo momento: me quedo con las ganas de probar la creperie que no encuentras. A Santi, todo un descubrimiento. No te podrías haber quedado por Europa, tenias que irte “on brama la tonyina”. Espero que dejes de esquilar ovejas y disfrutes de la experiencia (en el fondo es envidia). A los pamplonicas, Dani y Leti, os echaré mucho de menos, en especial a Dani, con quien tanto tiempo he compartido las comidas de mediodia. A Vero, que me acogió al llegar y me acompañó durante los primeros momentos de esta etapa. A Raúl (pariguelo), que aún me debe una cervecita, que con los intereses, ya sube a un barril entero. A Lidia y Mariona, también queda una comida pendiente a cuatro. Será una buena excusa para poder volver a Barcelona. A todos vosotros, os doy todos mis animos con esto de realizar/acabar la tesis, con especial fuerzas para Mohanad. Todo pasará y la suma de todo será un fantastico recuerdo. Recuerdo también para todos los alumnos, masters, TFGs... Y finalmente agradecer el apoyo y consejos de Carolina, Albert y Nuria. Tambien os deseo lo mejor, porque sois grandes y eso es lo que hace a este grupo ser lo que es.

Para todos aquellos del departamento, que en algún momento hemos coincidido, os doy las gracias por vuestro apoyo, en especial a Lindley. Siempre esperaré tu invitación con “todos” los gastos pagados a Chile. A todos los técnicos que han hecho posible muchas de las medidas. Tambien a todas esas personas que me han adoptado como pupilo en sus laboratorios, como la gente de organica y todas las persona implicadas de los laboratorios de Burdeos y Tolouse. Tambien por las medidas realizadas en Stuttgart y las realizadas por Jordi Ribas. Mención especial para Olivier, al cual he molestado con mis preguntas sobre resolución de estructuras. Gracias por el tour por San Francisco, lo recuerdo con mucho cariño.

Para acabar, también a todas las personas que en un momento dado deje en Valencia para venirme a Barcelona, y que hablan con orgullo de mi. En especial el apoyo incondicional de mi familia, con mi madre al frente, y como no, a la “otra” familia, la Trapp, a la que siempre agradeceré que me acogieran como uno más de su familia. El orgullo es mio.

Finalmente, a mis dos amores, Tere y Nerea, sois el autentico motivo de todo lo que vivo. La fuerza y el motor para que todo siga adelante. Os quiero y siempre lo haré.

